Experimental and Computational Study of Soot Formation Under Diesel Engine Conditions

by

Ioannis Kitsopanidis

Bachelor of Science in Mechanical Engineering, 1998
Aristotle University of Thessaloniki, Greece

Master of Science in Mechanical Engineering, 2000
Massachusetts Institute of Technology

Submitted to the Department of Mechanical Engineering
in partial fulfillment of the requirements for the degree of

DOCTOR OF PHILOSOPHY

at the

MASSACHUSETTS INSTITUTE OF TECHNOLOGY
[September 2004]
July 22, 2004

MASSACHUSETTS INSTITUTE OF TECHNOLOGY
MAY 05 2005
LIBRARIES

© Massachusetts Institute of Technology. All Rights Reserved.

Author ....
Department of Mechanical Engineering
July 22, 2004

Certified by ....
Wai K. Cheng
Professor of Mechanical Engineering
Thesis Supervisor

BARKER

Accepted by ....
Ain A. Sonin
Chairman, Departmental Graduate Committee

To my family and friends

Experimental and Computational Study of Soot Formation Under Diesel Engine Conditions

by

Ioannis Kitsopanidis

Submitted to the Department of Mechanical Engineering
on July 22, 2004 in partial fulfillment of the requirements
for the degree of Doctor of Philosophy

Abstract

Past research has shown that during diesel combustion, soot is formed in local premixed fuel-rich regions. This project focuses on the fundamentals soot formation under fuel-rich conditions similar to those in diesel engine operation. Since these conditions cannot be easily reproduced in typical laboratory scale experiments, such as flat-flame burners, and since diesel engine data are difficult to interpret because of uncertainty in the local charge composition and thermal state, a new rapid compression machine (RCM) was built to study the phenomenon. The RCM provides a well-controlled and uniform engine-like thermal environment, where mixing and chemistry are decoupled. Fuel-rich mixtures of n-butane and air were primarily used in this study; aromatics, oxygenates and cetane improvers completed the test matrix. Line-of-sight absorption technique was used to investigate the details of soot evolution. The primary data set consisted of soot volume loading history for selected fuels at various equivalence ratios, temperatures and pressures. Based on existing sub-models, a detailed chemical kinetic calculation leading to soot particles was performed to study the relative importance of the underlying chemistry.

The results show that the initial soot volume grows exponentially with time, reflecting an "autocatalytic" mechanism. The growth rate depends strongly on temperature and pressure. The lower rates observed for richer mixtures can be attributed to lower temperatures after the end of the main heat release process, when most of the soot is formed. Soot yield increases steadily with fuel-air equivalence ratio and depends on fuel structure. Toluene addition to n-butane increases the final soot yield at constant fuel-air equivalence ratio (~1%/1% toluene by mol) but not at constant C/O ratio. Oxygenates totally suppress soot formation at or above 30% oxygen in fuel by mass. Since soot formation is kinetically limited at lower temperatures and soot precursors are not thermodynamically stable at higher temperatures, soot yield exhibits a bell-shape dependence on temperature with a maximum at approximately 1800-2000K. Thus different surface growth mechanisms prevail across the temperature range; the relative contribution of C_2H_2 over PAH to soot growth increases with temperature. Even though nucleation is mostly governed by PAH coalescence, it was found that the C_2H_2 route is not negligible under certain conditions. The kinetics of fuel-rich combustion was found to be sensitive to the fuel+HOO reaction. Suggestions are made for better correlation between model and experiments regarding ignition delay and rate of heat release.

While performing this study, insight was gained into RCM operation. Assuming uniform and homogeneous environment at the end of compression, was sufficient to model ignition delays under most conditions (2-10 ms), but not rate of heat release and maximum pressure. CFD analysis predicted non-negligible temperature stratification at the end of compression (~80% of mass within 50K). A multizone model, taking into account zones of constant mass and allowing heat transfer and flow into the crevice, was developed and improved the agreement significantly.

Thesis Supervisor: Wai K. Cheng
Title: Professor of Mechanical Engineering

Acknowledgements

Several people deserve my gratitude and first of all my thesis advisor, Prof. Wai Cheng. Without his dedication and guidance during the last 6 years this work would not have been possible. In addition, the advice of my thesis committee, Profs. Green, Heywood, Howard and Keck, made a profound impact on this work. Beyond my committee, I am grateful to Dr. Henning Richter for his willingness to join me in long meetings and share his great knowlwdge on soot formation kinetics and modeling

I would like to further thank the members of the MIT Engine and Fuels Research Consortium for their technical and financial support. I also feel very priviledged that Cummins Inc. sponsored my Ph.D. and I need to express my thanks to Dr. Wole Akinyemi for his continuous support and guidance.

Many thanks to the entire Sloan Automotive Lab community. My numerous labmates, who are impossible to list in this short paragraph, created a very pleasant working environment. A special thanks to Thane DeWitt, Sloan Automotive Laboratory Supervisor, who provided a substantial help throughout the entire project and especially during the design and construction of the rapid compression machine.

This work would not have been completed unless my stay in Boston was happy. I owe special thanks to my friends at home and especially those in Boston, who supported me with love and understanding. These people and the moments we had together will never be forgotten.

Finally, I would like to express my gratitude to my family. Without their love and support I would not have been able to follow my dreams.

Ioannis Kitsopanids,
Cambridge, MA, August 2004

Table of Contents

List of Figures

List of Tables

Nomenclature

ACRONYMS

CFD	computational fluid dynamics
CN	cetane number
DFT	density-functional theory
DME	di-methyl ether
EGR	exhaust gas recirculation
EHN	2-ethyl-hexyl nitrate
HCCI	homogeneous-charge compression ignition
LII	laser induced incandescence
LIF	laser induced fluoresence
LLNL	Lawerence Livermore national laboratory
LNT	lean NOx trap
LOS	line-of-sight
NTC	negative temperature coefficient
PAH	polycyclic aromatic hydrocarbons
PM	particulate matter
PMT	photomultiplier tube
RCM	rapid compression machine
SCR	selective catalyst reduction
SOF	soluble organic fraction
SY	soot yield

SYMBOLS

ϕ (phi)	fuel-air equivalence ratio
T	temperature
P	pressure
N	total volume concentration
ρ	density
K_B	Boltzmann constant
R	universal gas constant
Y	mass fraction
v	specific volume
u	internal energy
W	molecular weight

ω	rate of production of species
C_v	specific heat (constant volume)
C_p	specific heat (constant pressure)
m	refractive index
I	light beam intensity
p(D)	particle diameter distribution
n	particle number density
k_{ext}	extinction coefficient
C_{ext}	extinction cross section
Q_{abs}	absorption efficiency
Q_{sca}	scattering efficiency
D	diameter
λ	wavelength
f_v	soot volume fraction
ρ_s	soot particle density
W_C	carbon atomic weight
[C]	carbon concentration
Q_{conv}	heat transfer by convection
Q_{rad}	heat transfer radiation
A	area
h	heat transfer coefficient
w	velocity
L	characteristic length
ε	soot emissivity
σ	Planck constant
N_A	Avogadro number
μ	reduced mass
d	equivalent diameter
γ	collision efficiency

Chapter 1

Introduction

1.1 Motivation

The diesel engine, which is widely used today, is the most efficient power plant among all known types of internal combustion engines. This high fuel conversion efficiency originates from the essential features of its operating cycle: fuel injection controls the start of combustion, it operates fuel-lean and its load is varied by the amount of fuel injected per cycle [1]. By injecting the fuel directly into the cylinder right before combustion starts, spontaneous ignition of significant amounts of premixed fuel and air is avoided. Consequently, there is no knock constraint which is experienced in spark-ignited engines, and higher compression ratios can be employed. The lean operation of a diesel engine results in lower specific heat of the working fluid during expansion. The higher engine compression ratio and lower working fluid specific heat provide a considerable efficiency benefit of the diesel engine over other types of internal combustion engines. Moreover, controlling the engine load by varying the fuel flow, while keeping the airflow unthrottled, results in low pumping losses, which contributes to important efficiency gain especially under low load conditions.

The major efficiency benefits of diesel engines have recently drawn the attention of both automotive manufacturers and environmental agencies worldwide. The need for fuel economy and low emissions of CO_2, which is considered a greenhouse gas that scales with fuel consumption for a given fuel, has driven numerous research efforts towards further diesel engine development. However, there are still technical challenges to be addressed before diesels become the most widely used type of engine for transportation. The fuel-lean operation limits the maximum torque resulting in low specific power. The in-cylinder injection and high compression ratio increases the cost of the engine due to the high-pressure injection system and rugged construction requirements respectively. Even though turbocharged diesel engines and introducing sophisticated electronics were major technological achievements, the most important technical challenge of a diesel engine is to meet the emission standards. Hydrocarbon and CO emissions are not issues as in spark-ignition engines. The compression stroke allows only fresh air into the crevice volumes that could contribute substantially to hydrocarbon emissions. The overall fuel-lean mixture on the other hand, limits CO emissions to negligible levels. The major pollutants of a diesel engine are NO_X, and particulate matter (PM) which originate from combustion-generated soot particles. The source of NO_X and soot lies in the heterogeneous character of diesel combustion. Even though the overall fuel-air mixture is lean, direct injection results in locally fuel-rich and nearly stoichiometric regions just downstream the liquid spray and close to the diffusion flame boundary respectively. Soot particles are found in the premixed fuel-rich region and then burned substantially in the diffusion flame, where NO_X are formed due to the high local temperatures and available oxygen. The details of soot formation mechanism in a diesel combustion environment and the relevant processes affecting it are discussed extensively in the next chapter.

Apart from being toxic, NO_X are important ingredients in the photochemical smog reactions [2]. The health problems associated with inhaled PM are cancer, mutations, cardiopulmonary ailments and lung damage [3]. As a result, the US Environmental Protection Agency in North America and the European Commission in the EU have established strict standards for NO_X and PM emissions from all diesel-powered cars and trucks [4-5]. The evolution of regulated emission standards for NO_X and PM from heavy duty diesel engines in the US and EU are shown in Table 1.1 [6]. The allowable range of emissions imposed by the environmental agencies in the US has dropped by more than a factor of 5 over the last 15 years, and an additional order of magnitude drop is required within the next 5 years. The major challenge for the engine manufacturers is to meet simultaneously the mandated emission levels for both pollutants. The trade-off between engine-out PM and NO_x emissions has been a field of many recent studies in the diesel research community [7] and is clearly depicted in Figure 1.1. This trade-off is mostly attributed to the in-cylinder competition between NO_x formation and soot oxidation processes, which are both favoured by increasing temperatures.

Table 1.1 Regulated emission standards for heavy duty diesels [6].

USA[a]			**EU**[b]		
Year	**NO_x**	**PM**	**Year**[c]	**NO_x**	**PM**
1988	10.7	0.60	**1992**	8.0	0.61
1991	5.0	0.25	**1992**	8.0	0.36
1994	5.0	0.10	**1996**	7.0	0.25
1998	4.0	0.10	**1998**	7.0	0.15
2004	2.0	0.10	**2000**	5.0	0.10
2007	1.18[d]	0.01	**2005**	3.5	0.02
2010	0.2	0.01	**2008**	2.0	0.02

a. in g/bhp-hr
b. in g/kWh-hr
c. 1992/96 corresponds to Euro I and rest years to Euro II-V respectively.
d. In 2007 half of the fleet can still comply with the 2004 emission standard until 2009; the overall accounting leads to an effective emission standard of 1.18 g/bhp-hr for NO_x [8].

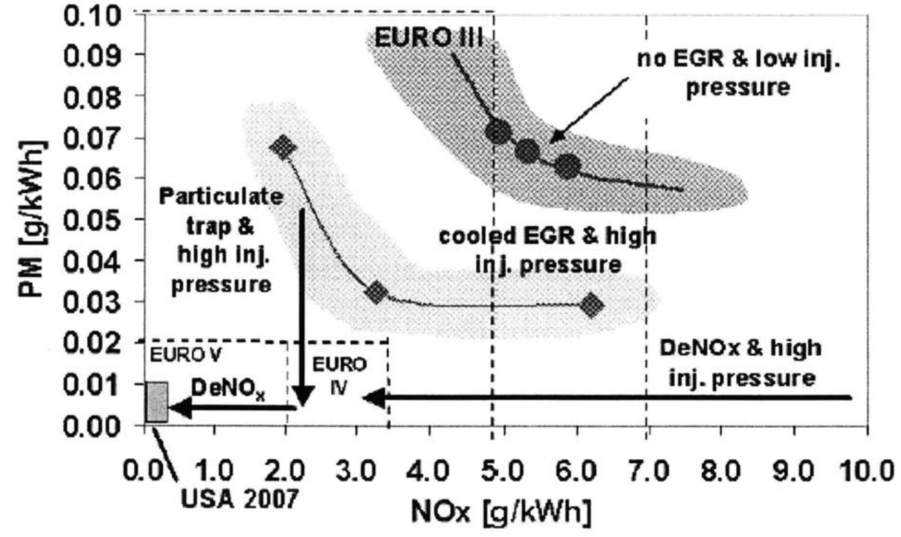

Figure 1.1 Trade-off between PM and NO$_x$ emissions from a heavy duty diesel engine [7].

The diesel engine industry was able to meet the increasingly stringent emission standards up to 2004 by focusing on combustion optimization and advanced subsystems aiming to reduce engine-out emission levels. Rapid fuel-air mixing for limiting soot formation was achieved by designing bowl-in pistons while lower maximum temperatures to avoid NO$_x$ were realized by retarding injection timing. Other advanced subsystems provided further improvements. Common-rail high-pressure fuel injection systems allowed for better injection control over the speed range; sophisticated injection strategies including multiple injections were employed. Significant amounts of cooled exhaust gas recirculation (EGR) in conjuction with variable geometry turbochargers to drive EGR at low loads had limited peak cylinder temperatures, and hence NO$_x$ levels, even further.

The imposed emission standards for 2007, especially the required ten-fold drop in PM levels, are however, very difficult to be met solely with in-cylinder strategies. Exhaust aftertreatment devices such as the diesel particulate filters [9], which have been an area of research for many years, seem to be a necessity for 2007 along with higher amounts of cooled EGR and/or more sophisticated in-cylinder fuel injection strategy for meeting the mandated two-fold drop in NO$_x$ levels [8]. The additional five-fold drop in NO$_x$ imposed by the US Environmental Protection Agency for 2010 is bound to require NO_x aftertreatment devices. Research on lean NO_x traps (LNT) and urea-based selective catalyst reduction (SCR) is still under way [10]. Alternative fuels such as Fischer-Tropsch [11], biodiesel [12], oxygenates [13] etc. are also areas of increasing research interest, although the advancement is not yet sufficient for practical implementation.

Since the source of pollutants is the combustion source itself, it is important to study the diesel combustion, especially the processes related to pollutant formation. Although h NO_x formation chemistry is, to a sufficient level well-established, the detailed knowledge of soot formation process remains as one of the major challenges within the combustion community. The transformation of the parent fuel molecules to soot precursors, the transition from the gas to the particulate phase and the growth of soot particles to engine-out PM of various sizes and chemical structures are very complicated processes, that are still not well understood. A fundamental study of soot formation under conditions similar to that found in diesel engine operation is a necessary step in order to shed some light into these processes. The findings of such study could provide valuable information to diesel engine manufacturers for optimizing engine performance and minimizing pollutant emissions.

1.2 Background

There are many reasons why soot formation chemistry has long been a field of active research efforts within the combustion community. Soot emissions reflect poor combustion and efficiency losses. In internal combustion engines, deposition of soot may have deleterious consequences on the maintenance and lifetime of such devices. However, what has really driven soot formation studies worldwide over the last decades were the adverse health effects and environmental impact associated with combustion-generated soot particles. More recently fuel-rich combustion, which leads to soot particle formation has drawn considerable attention in carbon black industry due to synthesis of fullerenes and carbon nanotubes, which have unique properties [14]. Hence, understanding fuel-rich combustion and soot formation is an active field today in combustion research. A review of the most common experimental and computational techniques in the soot formation research field is given in this section.

Characterization of combustion generated soot particles is difficult to achieve because of the physical and chemical complexity of the underlying processes. Most of the available information originates from laboratory flames having simple flow fields that permitted samples to be taken at different stages of particle formation. Such studies were able to give insight into the fundamental soot formation mechanisms. Many of them were carried out at MIT [15-18] and in particular the pioneering work done by Wersborg et al. [16] was able to quantify the critical processes of particle inception (often referred to as nucleation), surface growth and coagulation by using a molecular beam-sampling system combined with electron microscopy in a flat acetylene/oxygen subatmospheric flame. A series of experiments were conducted in General Motors research laboratories [19-24]. Harris et al. [24] evaluated the relative contributions of different species during the surface growth process in premixed ethylene/air flames. Since then, numerous studies, for example, work done by D'Alessio et al. [25] and Hanisch et al. [26], continued along the same lines using flat-flame burners. These studies gave even better insight to the relevant processes by using fast sampling techniques or optical methods capable of identifying critical species. Though these simple laboratory flames, which allowed sophisticated sampling tools to be employed, provided valuable information, they do not necessarily reflect the entire picture of soot formation process under the high-pressure, non-uniform and turbulent diesel combustion regime. With the advancement of combustion diagnostic tools and especially the optical methods, more recent soot formation research has focused directly on diesel engines since realistic engine conditions could be reproduced [27-33]. The work done by Dec at Sandia National Laboratories was pioneering in this field [34-40]. Many useful data, although qualitative in nature, were obtained with regard to soot distribution within the cylinder and the onset relative to the combustion event. However, not much further insight into the chemical processes was gained because of the uncertain environment: mixture and temperature non-uniformities, residual mass from previous cycles and coexistence of fuel droplets and vapor. Therefore, the data obtained lack clear quantitative interpretation. Shock tubes were also used for soot formation studies. The apparatus provided well-controlled conditions and uniform environment under fuel-rich [41-44] or even pyrolytic conditions [45-46]. Taking into advantage the discontinuity across a shock wave, a shock tube can increase instantaneously the pressure and temperature of a uniform mixture to levels comparable to a diesel engine. Then, valuable amount of data about the final amount of soot generated under certain conditions could be obtained. However, due to limitations to mixture properties allowed in shock tubes, heavy dilution (95-99.5% Ar) was required, resulting in very low fuel (and therefore soot) concentrations and negligible heat release. Since chemical kinetics do not necessarily scale linearly with species concentrations, such regime is not representative of a diesel engine combustion environment and extrapolation of these findings involve many uncertainties. A device which has been proven to be an excellent apparatus for studying hydrocarbon ignition phenomena under engine-like conditions is the rapid compression machine (RCM). It is a single-stroke device, which rapidly compresses a uniform mixture of fuel and air allowing for constant volume combustion. The RCM can combine the merits of a shock tube and a diesel engine by producing a well-controlled environment under diesel-like conditions. Details of the RCM design and operation are given in Chapter 3. Figure 1.2 summarizes the temperature and fuel carbon concentration regime of possible experimental setups. It is apparent that the temperature and fuel carbon concentration conditions achieved in a RCM is much more representative of a diesel engine compared to all other alternatives.

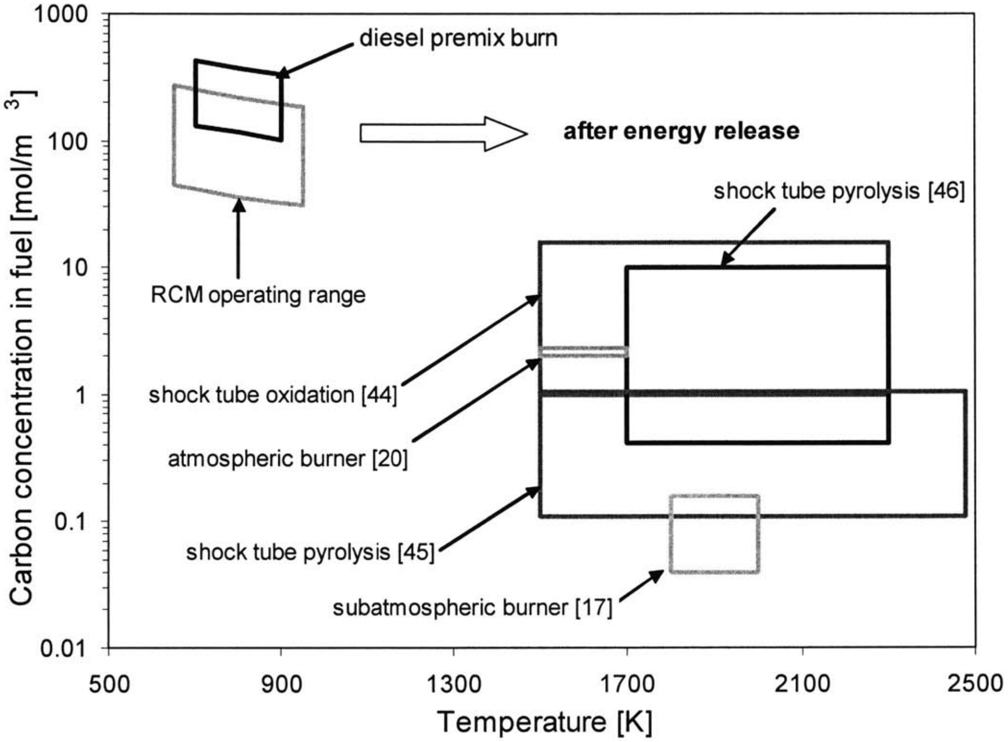

Figure 1.2 Typical conditions present in a diesel engine (local fuel-rich zone) and accomplished in flat-flame burners, shock tubes and RCMs.

Soot detection during a combustion process can be achieved either with direct sampling or optical techniques. Techniques like molecular beam sampling combined with electron microscopy have been very successful in identifying critical intermediates in burner type of experimental setups. Even though fast sampling methods were used directly in diesel engines [30], they are intrusive and, especially under high pressures, their ability to chemically freeze the sample is questionable. The advancement of laser technology, on the other hand, made available non-intrusive tools for combustion diagnostics. The most common technique used for soot detection are the line-of-sight (LOS) absorption [27-29, 31-32, 39-40] and the laser induced incandescence (LII) [34-37]. The latter method has been a valuable tool in non-uniform environment, like engines, giving a qualitative picture about soot distribution within the cylinder. To study soot formation kinetics however, it is necessary to continuously monitor soot quantitatively on time scale faster than a millisecond, therefore the LOS absorption technique appears to be advantageous over the incandescent methods.

In addition to experimental work, research efforts on soot formation have also included modeling of the underlying chemical processes. Empirical models describing the soot chemistry and its sensitivity to engine parameters such as temperature and fuel-air equivalence ratio have been extremely useful to the diesel engine research community. For example, models developed by Leung et al. [47] and Harris et al. [48] included formation and distruction reactions for soot mass (and sometimes soot particle number density) with rate constants calibrated against experimental data. These models were combined with computational fluid dynamics (CFD) codes to describe the complex diesel combustion. Such models proved to be valuable design tools for understanding the effects of combustion chamber geometry, temperature field, swirl, injection timing, EGR rate etc. on PM engine-out levels. However, the underlying chemistry could not be identified. Research moving towards detailed chemistry were encouraged by the increased computational power. Frenklach et al. [49] made the first step towards the quantitative modeling of species growth above the first aromatic ring on a fundamental basis. Since then many other models have been developed describing the growth of polycyclic aromatic hydrocarbons (PAH) with detailed chemistry and comparing against available experimental data. The models developed by Wang et al. [50], Richter et al. [51] Marinov et al. [52] and D'Anna et al. [53] are examples of these efforts, each of these giving different emphasis on the relative contribution of critical species like C_2H_2 and PAH in the nucleation and soot surface growth processes. More recently, some efforts have been extended to modeling the transition from the gas to the particulate phase using a sectional approach [54] or the method of moments [55]. The performance of these models have been evaluated under conditions close to diesel engine combustion. Figure 1.3 is a fuel-air equivalence ratio ϕ -temperature map of soot and NO formation, calculated based on Frenklach's PAH growth model, that is taken from Akihama et al. [56]. On the same map, the time history of actual fuel-air equivalence ratio and temperature realized in a diesel engine based on CFD analysis is depicted. Such maps, which can become very useful tools for designing the operation of diesel engine combustion in order to avoid both NO_X and soot formation, were first introduced by the experimental work done by Kamimoto et al. [57]. In the particular graph shown, the concept of smokeless combustion (dilution with more than 50% EGR) is evaluated and compared to typical diesel combustion (high smoke). Even though such maps were created under conditions of constant pressure and temperature (no heat release), all conditions and time scales involved were close to diesel combustion and therefore they are the first attempts to use detailed soot chemistry as a diesel combustion design tool.

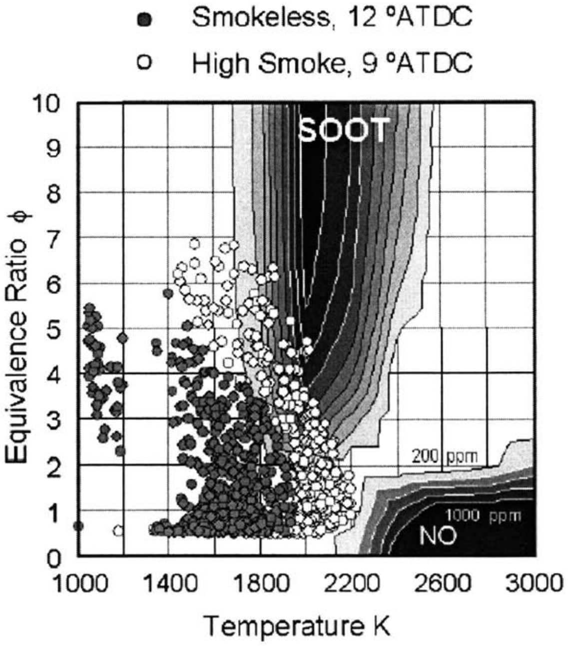

Figure 1.3 Fuel-air equivalence ratio-temperature map at the crank angle near the maximum heat release rate for two different diesel combustion concepts [56].

1.3 Objective

The objective of this research is to improve the fundamental knowledge base of soot formation kinetics under the thermal and pressure environment encountered in diesel engines. As described above, recent studies on soot formation have mostly focused on either diesel engines directly, where data interpretation is ambiguous due to the uncertain surrounding environment, or burners and shock tubes, where the temperature and species concentration regime is different from that in diesel combustion. The lack of fundamental soot kinetic data prevents the understanding of critical soot formation pathways. This understanding could lead to important soot reduction techniques and the development of physical models for design analysis.

This project aims to provide insight into the fundamentals of soot formation kinetics by combining experimental and computational approaches. In particular, the experimental objectives can be summarized as follows:

- Develop techniques to measure soot volume loading history under well-controlled conditions in diesel-like combustion regime.
- Observe the details of soot evolution and quantify the sensitivity of soot formation kinetics to combustion conditions and fuel structure.
- Supply a set of fundamental combustion data under diesel-like conditions for establishing quantitative kinetic mechanisms.

The computational objectives on the other hand extend to the following points:

- Combine existing chemical kinetic submodels and develop physical models to reflect the nature of the system.
- Calibrate not well-established parts of the model against the experimental data
- Determine the critical pathways for soot formation and evaluate their sensitivity

under diesel-like conditions.

The well-controlled environment of a RCM is used to provide engine-like conditions and soot evolution is monitored with the aid of the non-intrusive optical diagnostic method of LOS absorption. The outcome of this research aims to shed light into the critical processes underlying the soot formation chemistry in diesel engines. The findings could be a valuable reference data set for PM kinetics modeling that could be applied to diesel engine mixing and fueling strategy for lower PM levels.

Chapter 2

Soot Formation Fundamentals

2.1 Nature of Soot

Soot generated in combustion process is not uniquely defined in chemical or physical sense. Even though it looks black and consists mainly of carbon, it is quite different from graphite. Soot particles contain hydrogen, which is bounded to the carbon atoms. The amount of hydrogen in soot depends on the residence time of soot particles in the combustion environment with the aged particles having lower amount of hydrogen in them. Typically, C/H ratio is of the order of 8, which is much larger than that of the parent fuel molecule, which was a ratio of around 0.5. The carbon atoms are bonded together in hexagonal face-centered arrays in planes, commonly referred to as platelets. Platelets are arranged in layers to form crystallites, which combine together forming a 3-D spherule as shown in Figure 2.1, which was taken from Smith [73]. The average density of the soot particles is around 1.8 g/cm^3, which is lower than that of graphite because the spacing between the randomly disposed crystallites is slightly larger. Electron microscopy studies have shown that combustion generated soot particles, which are referred to as the elementary or primary particles, are nearly spherical with diameter often in the range of 20-30 nm; such particle contains around a million carbon atoms [59]. These primary particles usually exhibit a log-normal distribution in diameters and they aggregate together to form straight or branched chains, often referred to as clusters. The PM collected in a diesel engine exhaust has even more complicated structure and chemical composition than the aggregates. Elementary particles serve as nuclei where heavy hydrocarbons can be chemically or physically adsorbed later in the combustion event or during the exhaust stroke.

Figure 2.2, which was taken from Baumgard et al. [60], illustrates the nature of diesel engine exhaust particulates. The condensable material, which is often referred to as soluble organic fraction (SOF), because of the use of an extraction solvent to partition it from the more carbon-based core, constitutes approximately 25% of the mass and it has typically lower C/H ratio than the non-extractable part. In addition to heavy hydrocarbons, trace amounts of sulphur and inorganic oil additives also condense on these elementary soot particles [61]. Most studies about the hazardous health effects of PM consider this SOF, rather the core, to be mutagenic or tumorigenic [62].

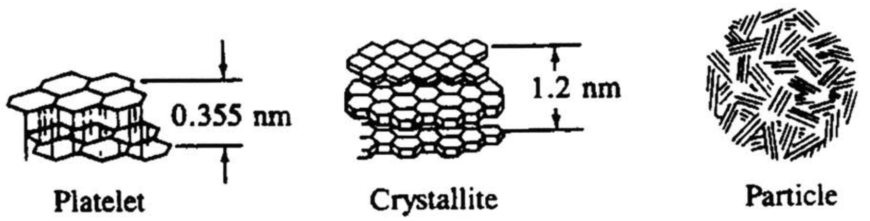

Figure 2.1 Structure of carbon particles [58].

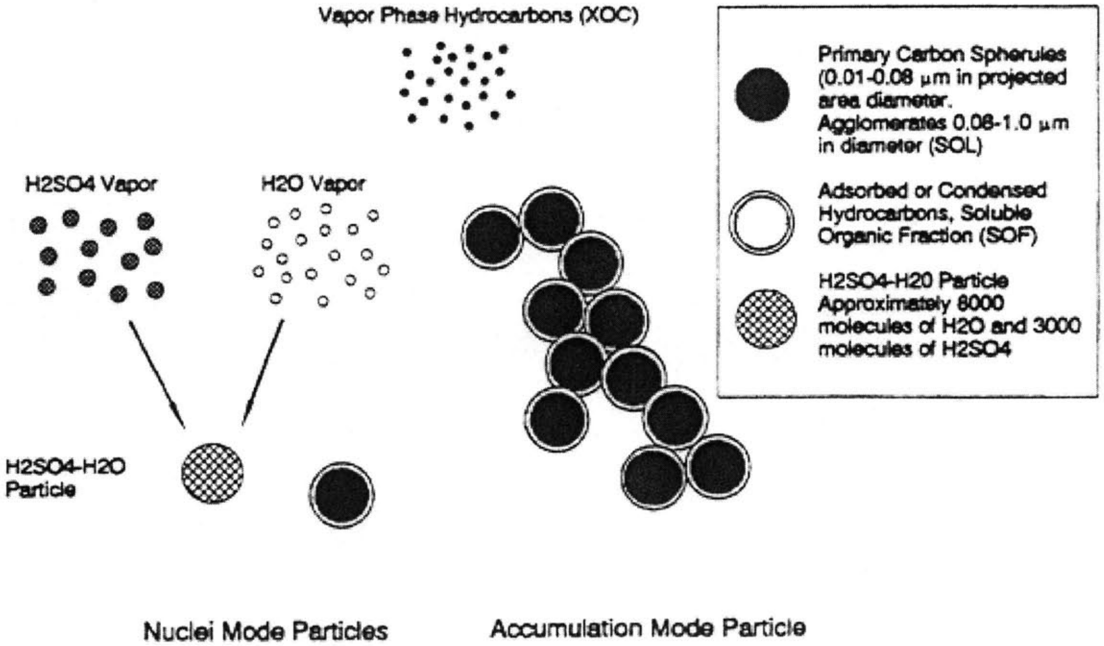

Figure 2.2 Schematic representation of diesel exhaust particles [60].

2.2 Soot Formation Process

The soot formation process involves the conversion of hydrocarbon fuel molecules containing a few carbon atoms into an agglomerate containing hundreds of thousands of carbon atoms with no unique chemical or physical structure. The gas-to-particulate phase transition encompasses very complex chemical and physical processes that are extremely hard to identify. A rough picture of soot formation in a homogeneous environment was taken by Bockhorn [63] and is shown in Figure 2.3.

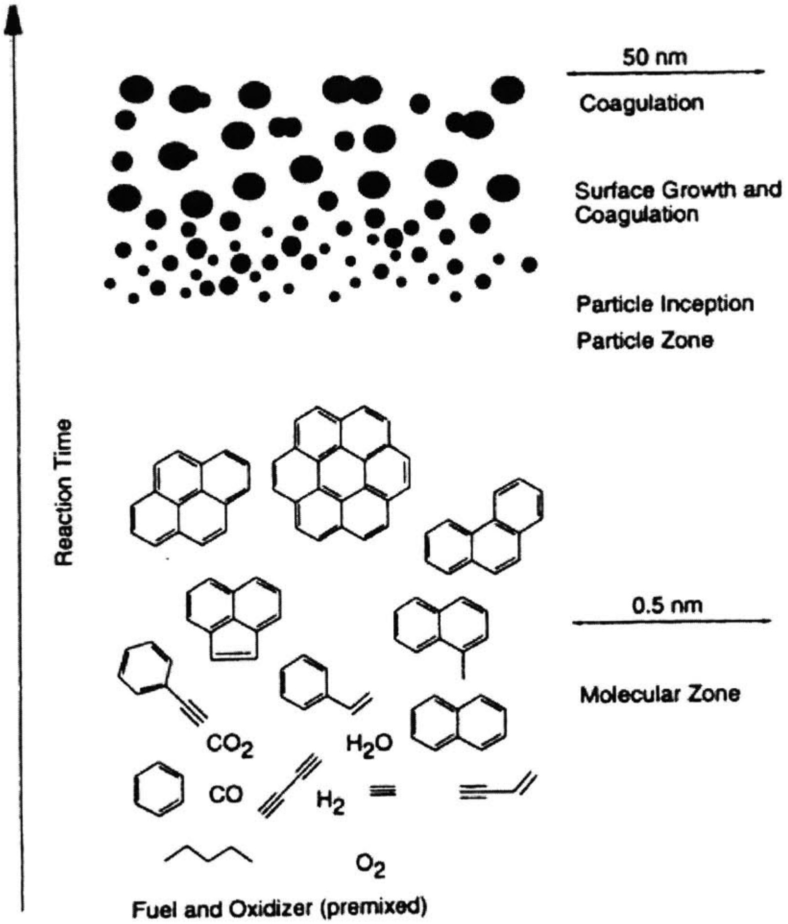

Figure 2.3 Rough picture of soot formation in homogeneous mixtures [63].

According to this picture, the hydrocarbon fuel breaks down into small hydrocarbons which in an oxygen-deficient environment lead to the formation of significant amounts of C_2H_2. Other species containing 2, 3 or 4 carbon atoms are formed from C_2H_2, which combine together into relatively stable aromatic rings. Further growth of the aromatic rings takes place mainly through reaction with C_2H_2 to form planar PAH. The PAH coalesces forming dimmers, trimmers and so on, before evolving into the particulate phase. Subsequent surface growth of the incipient soot particles determines the final amount of soot generated, while the particle size distribution is mostly determined by particle coagulation. An excellent review of the fundamentals of these processes was done by Richter et al. [64] and only a brief summary is given here. These processes are described more quantitatively in Section 6.3, where the kinetic model is described.

- *Formation of 1st aromatic ring*: The building block of large PAH and consequently of soot particles is the benzene ring, which exhibits relatively high thermodynamic stability. It has been stated that the formation of the first aromatic ring is critical in the subsequent soot formation process even when the parent fuel molecules are aromatic, which under some conditions may have decomposed. A great number of different chemical pathways leading to the first benzene ring has been discussed in the literature. Today, the propargyl radical (C_3H_3) recombination is recognized in the combustion community as the most efficient route. Other important paths include combination of butadienyl radical (n-C_4H_5) with vinyl (C_2H_3), vinyl-acetylene (C_4H_4) with C_2H_2, and but-en-yne radical (n-C_4H_3)[1] with C_2H_2 or C_2H_3. All the above routes include both recombination and cyclization. The formation of the first aromatic ring from poly-acetylenes, like tri-acetylene (C_6H_2) appears to be minor.
- *PAH growth and particle inception (nucleation)*: The addition of small units, from which C_2H_2 has drawn much attention, contributes to the growth of the first aromatic ring to PAH of growing size. Frenklach et al. [49] introduced the H-abstraction/

---

[1] n-C_4H_3 in this case refers to the isomer with the unpaired electron located at the edge of the chain so that after cyclization, the formation of a 6-membered ring is possible.

C_2H_2-addition mechanism, also referred to as HACA, which is illustrated in Figure 2.4. According to this mechanism the sole growth of PAH is due to C_2H_2. However, faster routes have been also suggested with building blocks greater than C_2H_2, like phenyl (C_6H_5) and cyclopentadienyl radical (C_5H_5) by Richter et al. [64] and acenaphthalene ($C_{12}H_8$) by D'Anna et al. [53]. The relative importance, however, of PAH-PAH reactions over the PAH-C_2H_2 route is widely accepted by the combustion community in the particle inception stage. At this stage heavy PAH molecules coalesce and form particles with molecular mass greater than 1500 amu and diameter of about 1.5 nm. Even though the particle inception involves the formation of a huge number of particles, the soot loading during this stage is considered to be insignificant.

- *Surface growth*: The bulk of the soot yield is generated by the surface growth process. This process involves the attachment of gas phase species to the surface of the particles and their incorporation into the particulate phase. Even though there may be some overlap, surface growth proceeds right after nucleation, which creates a significant surface area for gas phase species to condense on it. Surface growth involves chemical bonds between soot particles and the growth species, which implies radical sites on the soot particles or the growth species. The relative contributions of C_2H_2 and PAH on soot surface growth is the subject of current discussions in the combustion community.
- *Particle coagulation*: Coagulation refers to sticking collisions between particles during which the total soot mass remains the same while the average particle size increases. For small diameter particles, collision frequencies are high and isotropic so that the resulting particle retains a spherical shape statistically. The rapid surface growth at this stage also helps to "blanken-out" any irregular shapes. Past research

has shown that van der Waals forces may be significant at this stage [15] and since the sticking efficiency is high, the collisions theory limit is often used in these processes.

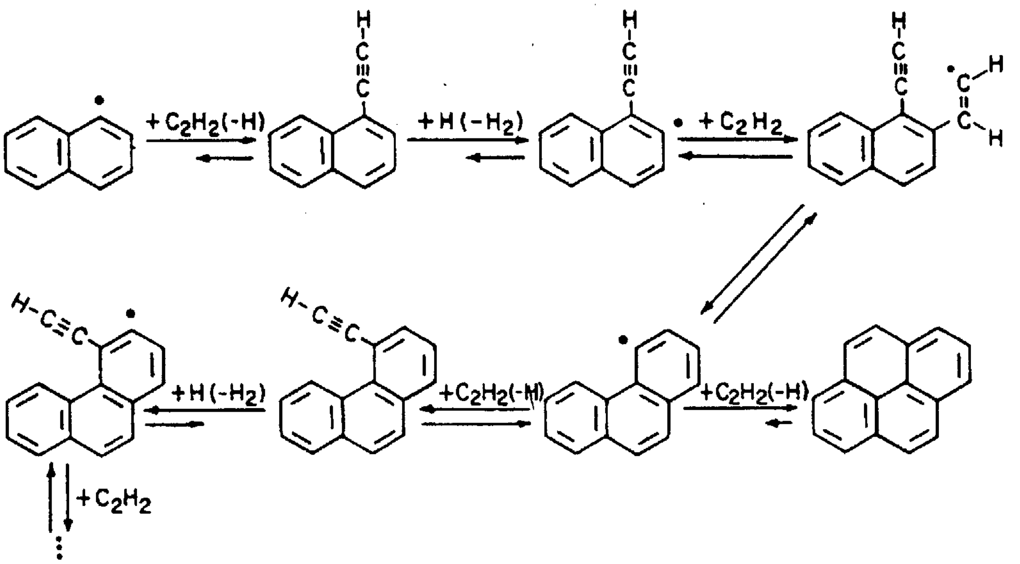

Figure 2.4 Example of HACA mechanism[49].

Although illustrated as discrete processes, there are overlaps among the above stages. Even in a perfectly homogeneous environment, surface growth and particle coagulation occur concurrently. Moreover, at any of these stages, oxidation of PAH or soot, mostly by OH radical, is taking place. Agglomeration, which involves the formation of clusters of particles without retaining their spherical shape, has been reported to start later when the particles are not very reactive chemically and surface growth cannot blanken-out any shape irregularities [66].

2.3 Soot Formation in Diesel Engines

The diesel combustion process is very complex due to its unsteady, heterogeneous and turbulent nature. This complexity makes a fundamental understanding of the location, the timing and the mechanisms of pollutant formation a real challenge. Among many reviews of diesel combustion and pollutant formation reported in the literature the work done by Kamimoto et al. [67] is especially succinct. In that study only the essential features of diesel combustion related to soot formation are summarized. Liquid fuel is injected just before the end of compression into hot air, where it starts evaporating and mixing. After a short ignition delay, premixed fuel-air auto-ignites and rapid heat release occurs. As more fuel is injected, combustion is then controlled by the rate of diffusion of air into the flame. According to the original diesel combustion description all fuel injected right after the premix burn, would be exclusively consumed in the diffusion flame. It was generally assumed that soot was exclusively formed in the fuel-rich side of the diffusion flame, where high temperatures prevailed and parent fuel molecule decompostion was possible. The initial premixed burn was not considered as a source of soot particles because it was thought to be stoichiometric. A much better insight into the processes involved in diesel combustion was gained by Dec et al. [68] via optical studies at Sandia National Laboratories and is summarized in [69]. Combining advent in-cylinder laser diagnostics, such as elastic scattering and LII, Dec observed soot in the central region of the jet just downstream the liquid fuel spray. Figure 2.5 shows a schematic of quasi-steady burning jet in a diesel engine based on the findings from in-cylinder laser measurements.

There are two major characteristics of this diesel combustion conceptual model that are worth noting:

- The fuel goes through a two-stage oxidation process even after the diffusion flame establishes; the first is at the fuel-rich premixed zone just downstream the liquid spray and the second at the diffusion flame in the periphery of the plume.
- Soot is formed in the fuel-rich premixed zone where fuel-air equivalence ratio was measured to range from 2 to 4; soot then grows in the center of the plume due to surface growth before part of it being oxidized in the diffusion flame.

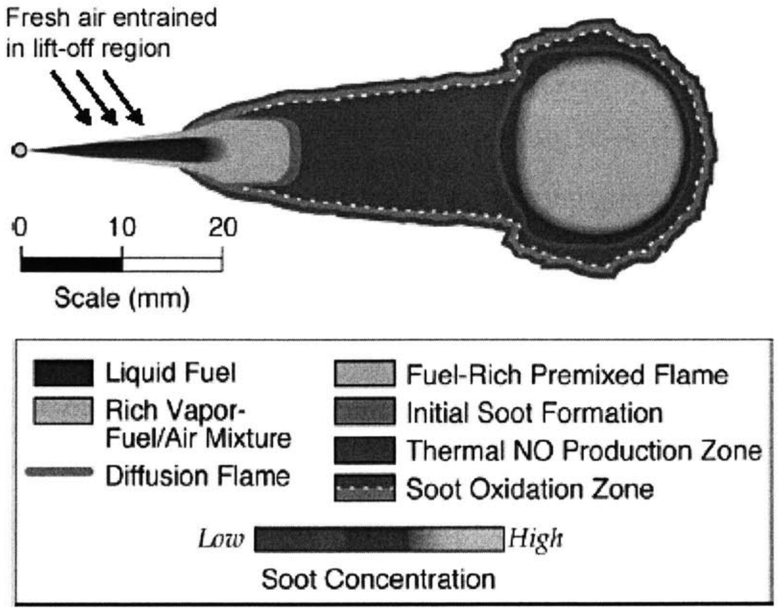

Figure 2.5 Schematic of a steady burning jet on the basis of laser measurements [69].

It is evident that understanding soot formation in diesel engines involves studying the kinetics of the fuel-rich premixed zone just downstream the liquid spray. Therefore, this is the region of diesel combustion that this research is focusing on using experimental and computational tools, in order to gain some insight into the soot formation fundamentals under conditions similar to diesel engine operation.

Chapter 3

Experimental Setup

3.1 Rapid Compression Machine

The RCM is a single-stroke device, which rapidly compresses a uniform mixture of fuel and oxidant to conditions similar to diesel engine operation. In a RCM, compression is induced by the piston movement, rather than a shock wave as in a shock tube. In contrast to an engine, the piston of the current RCM is locked in the compressed position to produce a constant volume environment. The mixture remains at these conditions for a longer period of time compared to a shock tube (~10 ms versus ~1ms); this time is only limited by heat losses. Right after the end of compression there is a short delay period of chemical origin that is characterized by the progress of near-isothermal processes. The chemical processes that precede ignition and rapid heat release are also referred to as preflame reactions. Combustion then takes place under constant volume condition and the rapid energy release results in significant pressure rise inside the combustion chamber. For the purpose of this study a new RCM was designed and built based on the Thornton design [70]. The schematic is shown in Figure 3.1.

The RCM is equipped with 4 fused silica windows 1.27 cm in diameter around the circumference of the combustion chamber and a fully transparent cylinder head for future imaging studies. The combustion chamber is cylindrical with 5.08 cm bore and 1.27 cm clearance height. Piston's position before the start of compression can be adjusted by changing spacers (not shown in Figure 3.1). The compression stroke then ranges from 15.24 cm to 20.32 cm, resulting in a compression ratio between 12.5 and 16.5.

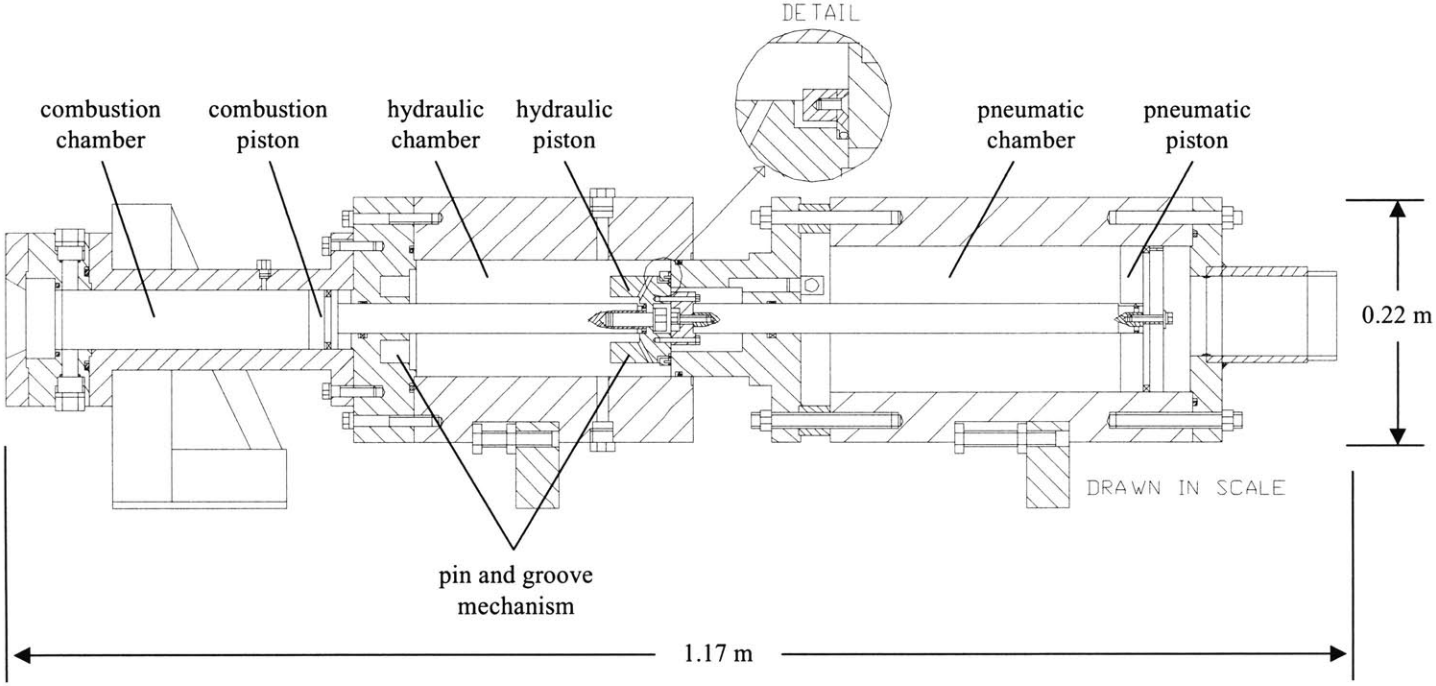

Figure 3.1 Schematic of the RCM

These values have taken into account the 3.1% crevice volume in the piston and windows at the end of compression. For purpose of this study, the stroke was set to its maximum value. These dimensions are representative of a diesel engine and similar to other RCM designs. What is different is the compression time, which was approximately 15 ms, (equivalent to approximately 2000 rpm engine speed) while in other designs it was over 20 ms. Table 3.1 summarizes the geometric features of different RCM designs along with the current MIT setup.

Table 3.1 Geometric features of different RCM designs

	MIT (old) [71]	**Leeds [72]**	**Lille [73]**	**MIT (new)**
Bore [cm]	5.08	4.6	5	5.08
Maximum stroke [cm]	10.92	23.2	19.9	20.32
Clearance height [cm]	0.6-2	2.27	2.2	1.27
Crevice [%]	N/A	N/A	N/A	3.1%
Compression time [ms]	20	22	20-80	15
Equivalent speed [rpm]	1500	1364	1500-375	2000
Optical access	no	yes	yes	yes

For the short compression times and relatively low temperature in most of the compression process, no significant chemical reactions took place before the end of compression, after which the chemistry was modeled by a simple constant volume process. Moreover, heat and mass (if any) losses during compression were minimized and to a good approximation there was an adiabatic core within the combustion chamber. Measuring pressure within the combustion chamber the core temperature at the end of compression was calculated from the initial conditions and the isentropic relationship of ideal gases:

$$\int_{T_{ini}}^{T_{comp,core}} C_p(T)\frac{dT}{T} = R\ln\left(\frac{P_{comp}}{P_{ini}}\right)$$

$C_P(T)$ in the above relationship is the average specific heat per mole of the mixture at temperature T and R is the universal gas constant. A Kistler 6125A piezoelectric pressure transducer was used to measure pressure within the combustion chamber during compression and post-compression period with 100 kHz sampling frequency.

As shows the combustion, hydraulic and pneumatic pistons were connected together by two shafts and move as a single piece. The hydraulic chamber was filled with silicon oil while the pneumatic chamber was vented to the atmosphere. After introducing the combustible mixture (as described below), the oil was compressed by high-pressure gas up to 90 bar to account for oil compressibility and possibly trapped air. The o-ring, shown clearly in the detail, sealed from the back chamber, which was vented to the atmosphere. The driving gas at the back of the 12.7 cm in diameter pneumatic piston was set at 17.5 bar. The gas is introduced with a large diameter pipe from a reservoir (not shown) ~50 times larger than the displaced volume in the pneumatic chamber so that no significant pressure drop (and hence driving force) occurred during the fast piston motion. The force balance between the driving gas and the pressurized oil was destroyed, by releasing the pressure in the hydraulic chamber. This was done by means of a fast solenoid valve, which allowed a very small quantity of oil (~1 cm^3) to be displaced. After the o-ring stopped sealing, oil flowed through the back of the hydraulic piston without being displaced out of the hydraulic chamber, and the piston rapidly accelerated. At this stage the piston motion was only restricted by moderate oil and shaft seals friction as well as pressure rise in the combustion chamber due to compression, which was though not significant until the very late stages of compression. The piston started decelerating when the pin of the hydraulic piston entered the groove. The clearance between the pin and the groove was just 0.7 mm in radius and hence the oil viscous forces built up and provide a significant resistance to piston motion. After reaching its final compression point, the piston was kept in place by the high pressure driving gas so that constant volume combustion can be realized. For the given driving pressure the piston could not bounce back if the pressure within the combustion chamber did not exceed 110 bar. Figure 3.2 shows the calculated piston velocity profile along with the experimental and calculated pressure trace during the compression process. The agreement is relatively good and the discrepancy must be due to heat losses. As stated above, the total compression time was not higher than 15 ms. Since maximum piston velocity was higher than 30 m/s, the moving mass big (~6 kg) and the deceleration length of the groove relatively short (2.54 cm), the inertia forces could be very high. To minimize the significant vibrations generated, a substantial RCM anchoring was required. More details about the RCM design and operation are given in Appendix A.

The mixture was prepared manometrically. The combustion chamber was evacuated, before mixture components were introduced. A Baratron 622A pressure transducer with accuracy of 0.1 Torr was used to accurately meter the quantities of the each mixture component. The combustion chamber, connecting lines and fuel reservoirs were all heated, insulated and temperature-controlled to accommodate liquid fuels, which require temperatures higher than their dew point at their given partial pressure in the mixture.

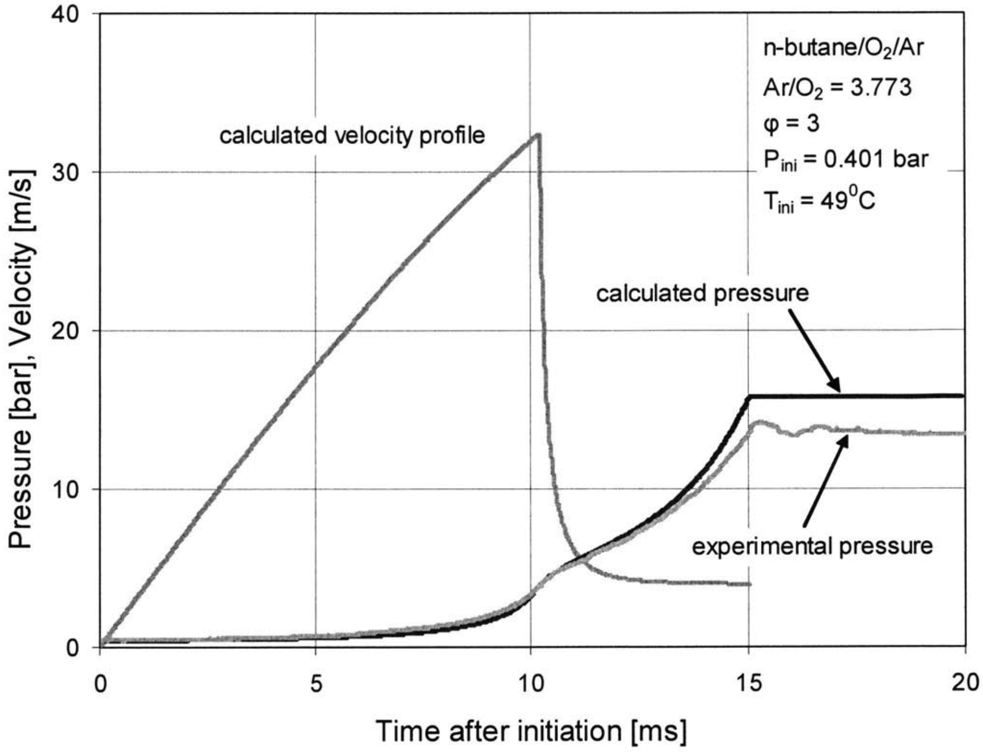

Figure 3.2 Comparison between experimental and calculated compression and velocity profile calculation.

Being able to test the combustion characteristics of mixtures under different conditions at the end of the compression is key to chemical kinetics studies. To do so, one can vary the stroke, the initial conditions or the specific heat of the mixture. The latter is accomplished by changing the diluent (N_2, Ar or CO_2) or even the diluent to O_2 ratio. For the purpose of this study, investigating fuel-rich mixtures, the diluent was always Ar and the Ar/O_2 ratio was set to 3.773, which is the same as N_2/O_2 in air so that realistic conditions can be reproduced. Ar was used instead of N_2 because its high specific heat ratio balanced out the low specific heat ratio of fuel-rich mixtures. A relatively wide range of conditions at the end of compression similar to a diesel engine (10-30 bar, 700-900 K) were accomplished by changing the initial conditions before compression commenced.

3.2 Diagnostic Method

As already stated in the introduction, the determination of real time soot concentration during the combustion process is based on the LOS absorption technique. The principle of this technique is shown schematically in Figure 3.3. When laser light passes through an absorbing media, like soot particles, light extinction occurs.

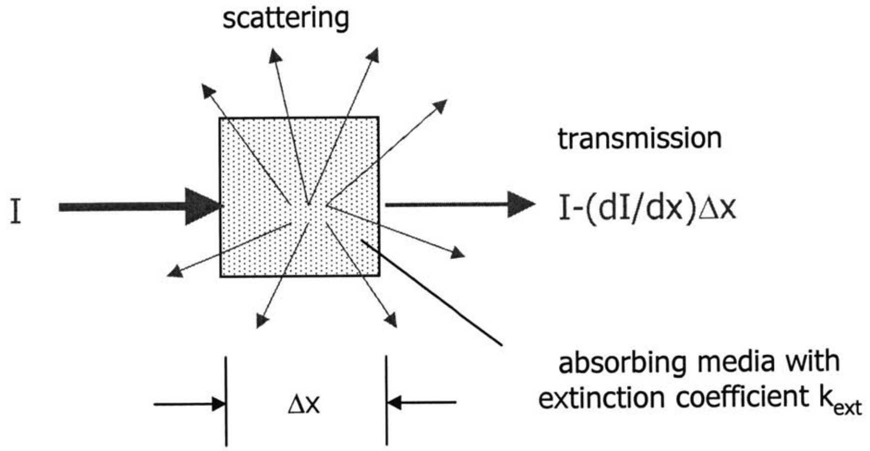

Figure 3.3 Line-of-sight absorption technique principle.

The extinction is the sum of light absorption and scattering and is described by Beer-Lambert's law:

$$dI = -I \cdot k_{ext} \cdot dx$$

where I is the intensity of the transmitted light beam passing through the absorbing media of length Δx and extinction coefficient k_{ext}. The extinction coefficient can be replaced by the product of the extinction cross-section C_{ext} and number density n of particles in the light beam path for any particle diameter distribution p(D):

$$k_{ext} = n \cdot \int_{0}^{\infty} p(D) \cdot C_{ext} \cdot dD$$

The extinction cross-section C_{ext} is defined as the extinction efficiency Q_{ext} multiplied by the projected area of soot particles to a plane perpendicular to the light beam. Therefore, assuming that all soot particles are spherical, the extinction coefficient is given by:

$$k_{ext} = n \cdot \frac{\pi}{4} \cdot \int_0^{\infty} p(D) \cdot D^2 \cdot Q_{ext} \cdot dD$$

The extinction efficiency Q_{ext}, which is a function of the particle size, the wavelength of the laser beam and the complex refractive index of the soot particles, consists of absorption and scattering components:

$$Q_{ext} = Q_{abs} + Q_{sca}$$

For the special case where particle diameter is much smaller than the wavelength of the incident light, $(\pi D)/\lambda \ll 1$, the Rayleigh scattering regime holds (we are interested in particle size $D \leq 30$ nm; the wavelength of the light used was 632.8 nm). Then for spherical particles, the absorption and scattering efficiencies are given by [74]:

$$Q_{abs} = 4\frac{\pi D}{\lambda} Im\left(\frac{m^2 - 1}{m^2 + 2}\right)$$

$$Q_{sca} = \frac{8}{3}\left(\frac{\pi D}{\lambda}\right)^4 \left|\frac{m^2 - 1}{m^2 + 2}\right|^2$$

Taking the ratio of the above two efficiencies, it can be deduced that for the Rayleigh regime the scattering efficiency is much smaller than the absorption efficiency:

$$\frac{Q_{sca}}{Q_{abs}} \propto \left(\frac{\pi D}{\lambda}\right)^3 \ll 1$$

Then the extinction of light can be solely attributed to absorption and the extinction coefficient becomes:

$$k_{ext} = n \cdot \frac{\pi^2}{\lambda} \cdot Im\left(\frac{m^2-1}{m^2+2}\right) \cdot \int_0^\infty p(D) \cdot D^3 \cdot dD$$

The integral in the above relationship is proportional to the mean particle volume, which combined with the number density of particles n, can give the total soot volume concentration f_v. After rearrangement, the above relationship reads:

$$k_{ext} = \frac{6\pi}{\lambda} \cdot Im\left(\frac{m^2-1}{m^2+2}\right) \cdot f_v$$

Substituting to Beer-Lambert's equation, the soot volume concentration can be calculated by:

$$\int_0^L f_v dx = \frac{\lambda \ln(I/I_0)}{6\pi Im\left(\frac{m^2-1}{m^2+2}\right)}$$

If the cloud of particles is homogeneous across the light path L, the above relationship can be integrated and it reduces to:

$$f_v = \frac{\lambda \ln(I/I_0)}{6\pi L Im\left(\frac{m^2-1}{m^2+2}\right)}$$

Even if the cloud of particles is not homogeneous but it consists of zones of different particle concentrations, the above relationship is still valid but then the soot volume concentration represents an average across the path of the light beam.

In order to reach to the above simple relationship that states that the soot volume concentration is proportional to the logarithm of light transmission, no particle size distribution was assumed. However, the following assumptions were made and explained below:

- *The particles are spherical.* Fast sampling studies followed by microscopy analysis have shown that soot particles are indeed spherical during the early stage of their formation. Small particles are very reactive and therefore their coalescent collisions are so rapid that they tend to "blanket-out" any shapes other than spherical [59]. The chain-like structures observed in diesel engine exhaust are believed to form after the end of the combustion event [1]. Past research in shock tubes has also shown that particles are initially spherical and when they collide they coalesce and fuse completely to form new spherical particles [66]. Since the current study focuses on the early stage of soot formation, it is highly unlikely that particles' shapes deviate substantially from the spherical shape at this stage.
- *The average particle diameter is much smaller than the wavelength of the incident light beam.* It has been reported that during the early stage of soot formation, particles are gigantic molecules with diameters less than 2 nm [59]. Microscopy studies suggest that the spherical building blocks of the aggregates observed in the exhaust of diesel engines are in the range 20-30 nm in diameter [59, 61]. By choosing a laser light wavelength in the visible range, it is assured that the particles are in the Rayleigh regime and scattering can be neglected. Therefore, for the purpose of this study the He-Ne laser was used with wavelength at 632.8 nm.
- *The refractive index of soot particles is known and remains constant during the course of combustion.* The refractive index of soot has only been determined in the bulk. Chang et al. [75] measured the complex refractive index based on dynamic light scattering to be 1.8-i0.58 at 10 mm above the burner surface and 1.62-i0.47 at 6 mm when the incident light's wavelength was 632.8 nm. Lee et al. [76] calculated the

complex refractive index based on multivariable dispersion model to be 1.9-i0.55 at 632.8 nm without finding any significant temperature effect at this wavelength. The maximum difference in the calculated soot volume concentration using any of the above refractive indices is ±6%. To be consistent with most recent studies the value suggested by Chang et al. [75] 10 mm above the burner was used in this study.

The schematic of the optical setup is shown in Figure 3.4. A 30 mW He-Ne laser beam passes through the combustion chamber, where it is attenuated by fuel-rich combustion generated soot particles. The attenuated beam after passing through lenses, pinholes and an interference filter, it is collected by an integrating sphere before being detected by a silicon photodiode.

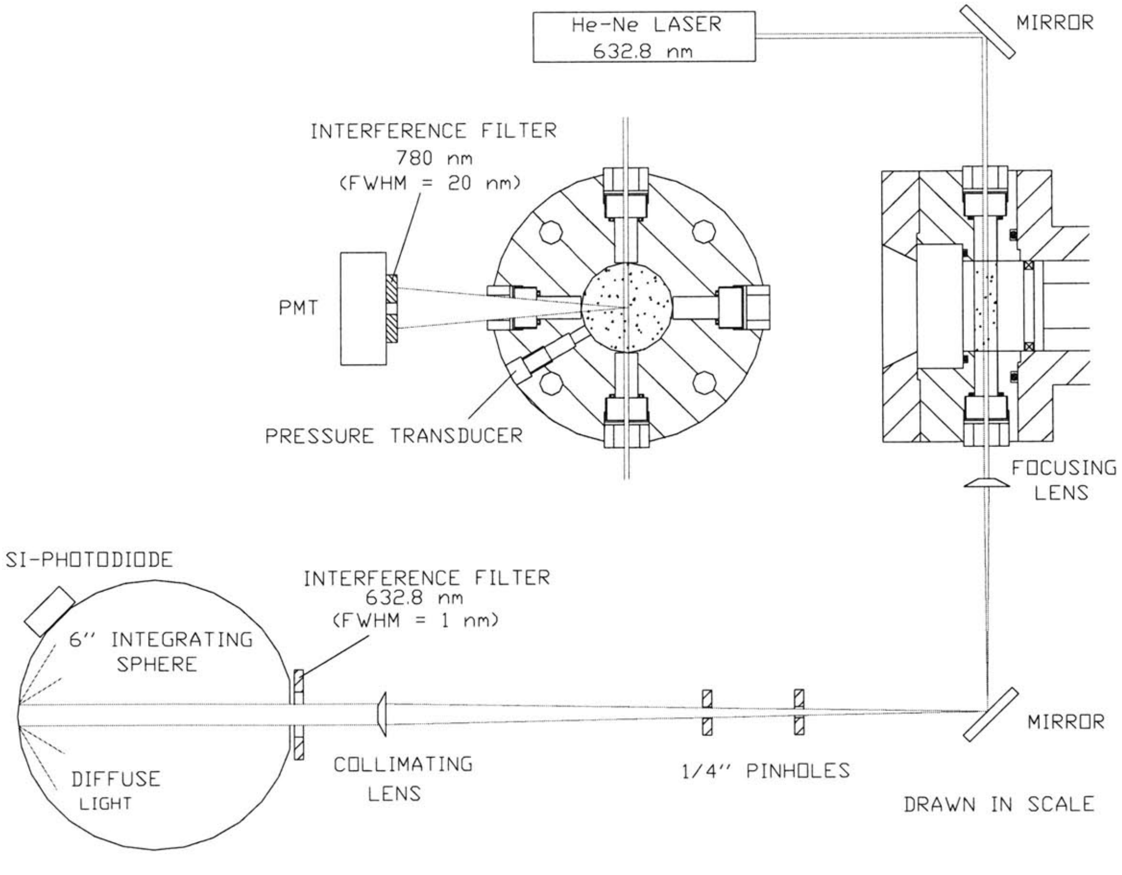

Figure 3.4 Schematic of optical setup

Mechanical vibrations and beam steering due to the change of refractive index in the combustion chamber during rapid temperature changes were the main sources of signal noise. The light beam could not remain exactly perpendicular to the combustion chamber windows and some light reflections could also be detected. The focusing lens expands the beam and the subsequent pinholes keep only the core of the beam blocking off the reflections and hence reducing the noise. The collimating lens collimates the light beam in front of the impact angle-sensitive interference filter. The integrating sphere collects the direct light beam even if it is subject to substantial deflections due to refractive index changes and/or mechanical vibrations and transforms it to diffuse light before being detected by the photodiode.

One significant source of error could be the superposition of laser light with combustion-generated light. During combustion natural emission of light takes place due to chemiluminescence and soot luminosity. The former arises from excited molecules decaying back to lower energy levels. In hydrocarbon flames such species are OH (310 nm), C_2 (516 nm), CH_2O (368-470 nm) and especially CH (390, 430 nm) [77]. Dec et al. [78] after conducting experiments in a diesel engine found out that chemiluminescence peaks at around 430 nm and is almost zero above 620 nm, with HCO speculated as the only possible species responsible at higher wavelengths. By using 632.8 nm laser light, this source of error can be almost eliminated. Soot luminosity, on the other hand, arises from soot particles, which act as gray bodies after being heated during combustion. The emission of this light has broadband spectrum and for typical rich combustion temperatures of 1800-2000K, the emissive power can be high at 632.8 nm and comparable to laser light coming out of the combustion chamber during the later stages since the latter is strongly attenuated by soot particles. To minimize soot luminosity detected by the photodiode, the interference filter used is very narrowband (FWHM[1] = 1 nm) and the integrating sphere has been moved far away from the combustion chamber (> 0.5 m) since luminosity drops with the square of the distance. This distance has been compromised by beam steering effects, which deflect the light. Figure 3.5 illustrates the error generated by soot luminosity on the detected signal under the same compression conditions. Curve A shows the transmission signal with the above described optical setup. Curve B shows the one obtained with a less narrowband filter (FWHM = 3 nm), with the photodiode much closer to the combustion chamber and without integrating sphere under the same operating conditions. It is clear that the signal is strongly distorted during the latter stages when laser light transmission is very small. It was found that at higher temperatures the error becomes even bigger. With the current optical setup, no light has been detected by the photodiode after running an experiment with the laser turned off indicating that no superposition of luminosity and incident laser light takes place.

---

1. Full width half maximum.

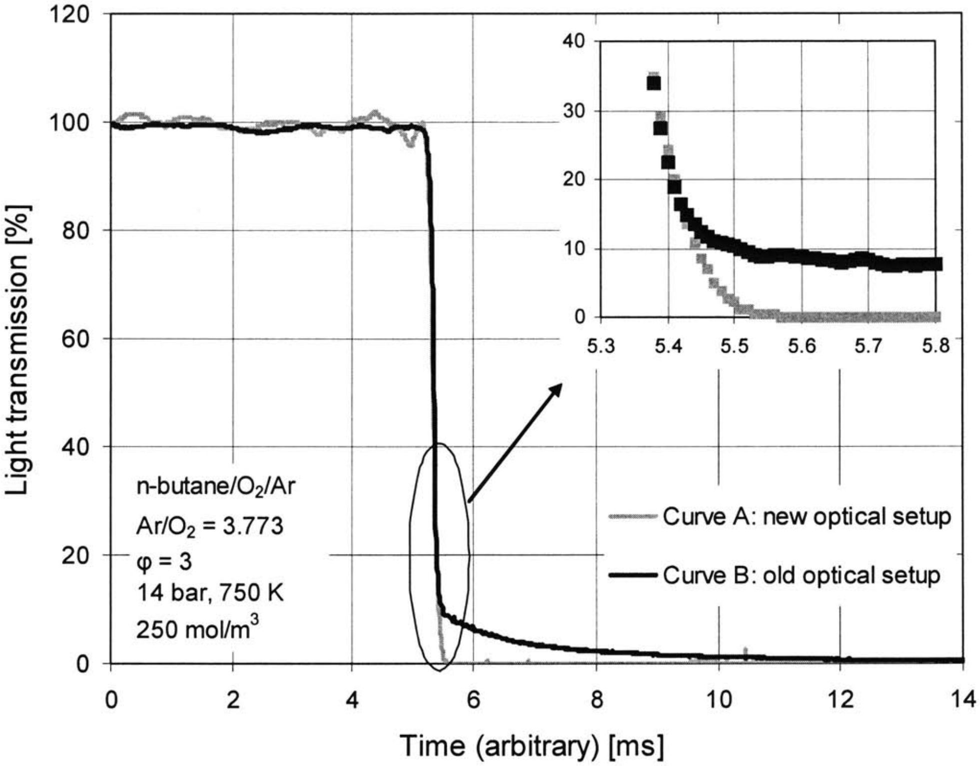

Figure 3.5 Effect of soot luminosity on transmission signal.

Many studies have been done on the nature of the species absorbing light at 632.8 nm. Microscopy studies claim that there are large molecules other than soot particles that may absorb light at this wavelength [17]. Other studies on the other hand claim that very young soot particles may even be transparent to light at this wavelength [53, 79]. Even though the distinction between soot precursors, which are gigantic molecules, and soot particles, is arbitrary, there does not seem to be any gaseous species absorbing light at 632.8 nm [80]. To test this assumption experimentally a photomultiplier tube (PMT) was placed above the top window of the RCM with an interference filter at 780 nm (FWHM = 10 nm) as shown in Figure 3.4. Laser light scattering is blocked and, as already explained above, no chemiluminescent light is emitted at this wavelength. The only light that can be detected comes from particle luminosity. Figure 3.6 shows the PMT detected signal along with the light transmission for the same case as Curve A of Figure 3.5. It is clear that the luminosity signal starts at the same time as light absorption suggesting that the absorbing media should be in the particulate phase.

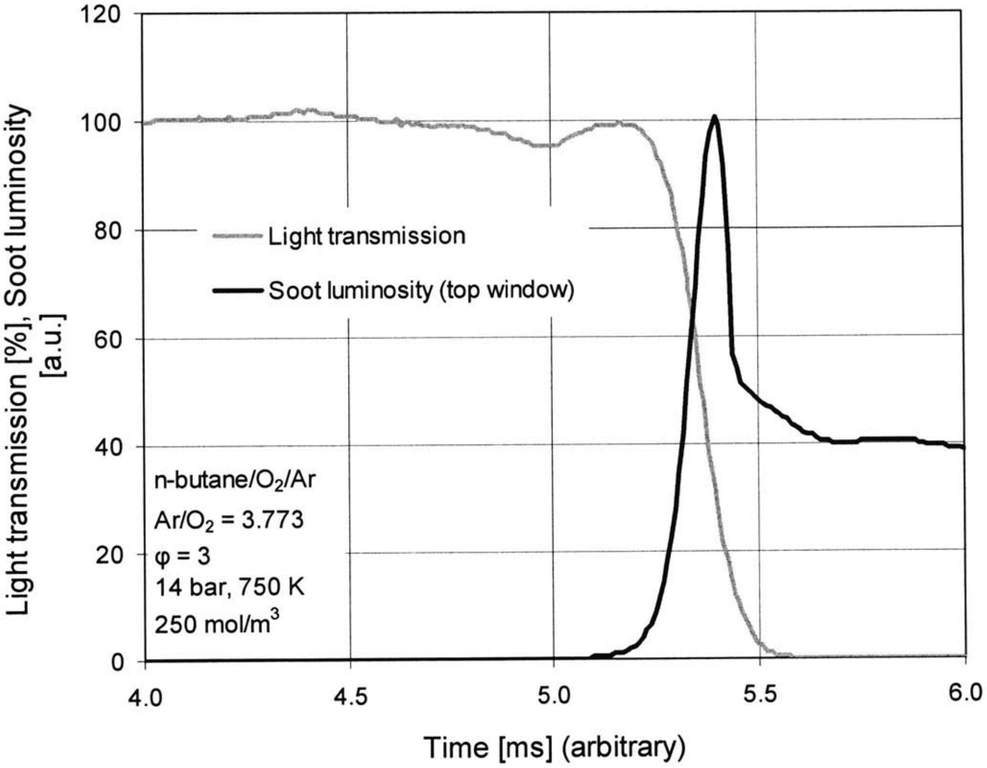

Figure 3.6 Soot luminosity (top window) and light transmission signals.

3.3 Sample Experimental Results

The primary experimental data comprised the pressure-time and LOS transmission-time records. Such data of 5 consecutive tests are exemplified in Figure 3.7 for a typical fuel-rich mixture. All tests were conducted with n-butane/O_2/Ar mixture, with Ar/O_2 = 3.773 and $\phi = 3$. The conditions at the end of compression were the same for all tests: P_{comp} = 14 bar, $T_{comp,core}$ = 765 K and total volume concentration N_{comp} = 250 mol/m^3. Looking closely at the pressure trace, one can see that the start of compression starts at t = 0 ms. At approximately 11 ms, the rate of pressure rise slows down as the pin of the hydraulic piston enters the groove, the resulting back-pressure decelerates the piston. The total traveling time of the piston before reaching its final compression point is approximately 15 ms. Right after that point there is a period of pre-ignition reaction, during which the rate of heat release cannot keep pace with the heat losses. Pressure drops slightly before the mixture igniting in two stages at approximately 8 ms later. These observations are consistent with what is reported in the literature for most hydrocarbon fuels. The energy release at this point is very rapid and it translates to pressure rise. The pressure drop from the peak value is due to heat transfer to the cold walls when the combustion is over. Note that the repeatability is remarkable and as far as the ignition delay is concerned, the variability is ±0.15 ms with 95% confidence level.

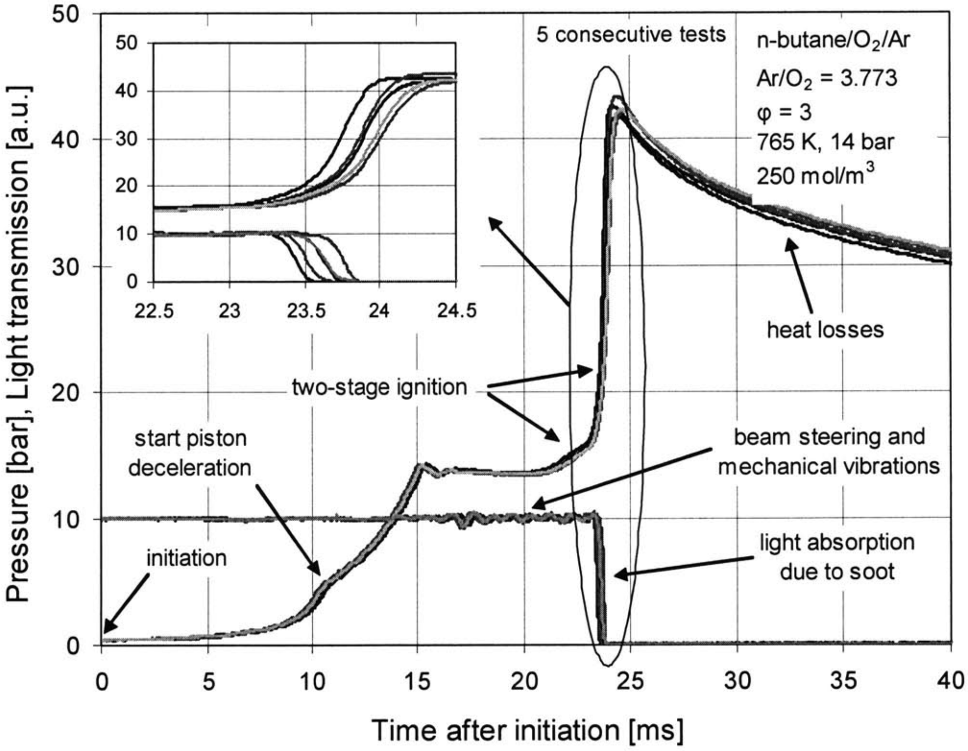

Figure 3.7 Typical data and repeatability.

Figure 3.8 shows clearly the ignition delay and combustion time constant, which are parameters of great importance in order to understand the oxidative characteristics of fuels. The ignition delay was defined as the time from the end of compression to the time where 10% of the pressure rise. This definition was used instead of the commonly used maximum rate of pressure rise because of the difficulty to define the pressure derivative in subsequent computational studies for some very fast heat release cases. From our data, we found that the two definitions give very similar results, which are offset by 5-10% (for delays not less than 2 ms), with that using our definition giving the lower value. A combustion time constant was used to describe the rate of heat release. It was defined as the time for the pressure to rise due to combustion from 20%-80% of its final value. A typical value was 0.5 ms and the variability was ±0.03 ms with 95% confidence level. On the same figure the 5%-20% pressure rise combustion time constant was defined describing the early stage of heat release. To our knowledge RCM rate of heat release data, which are particularly important to chemical kinetic model development, have been recently published only by Tanaka et al. [81] under very fuel-lean conditions.

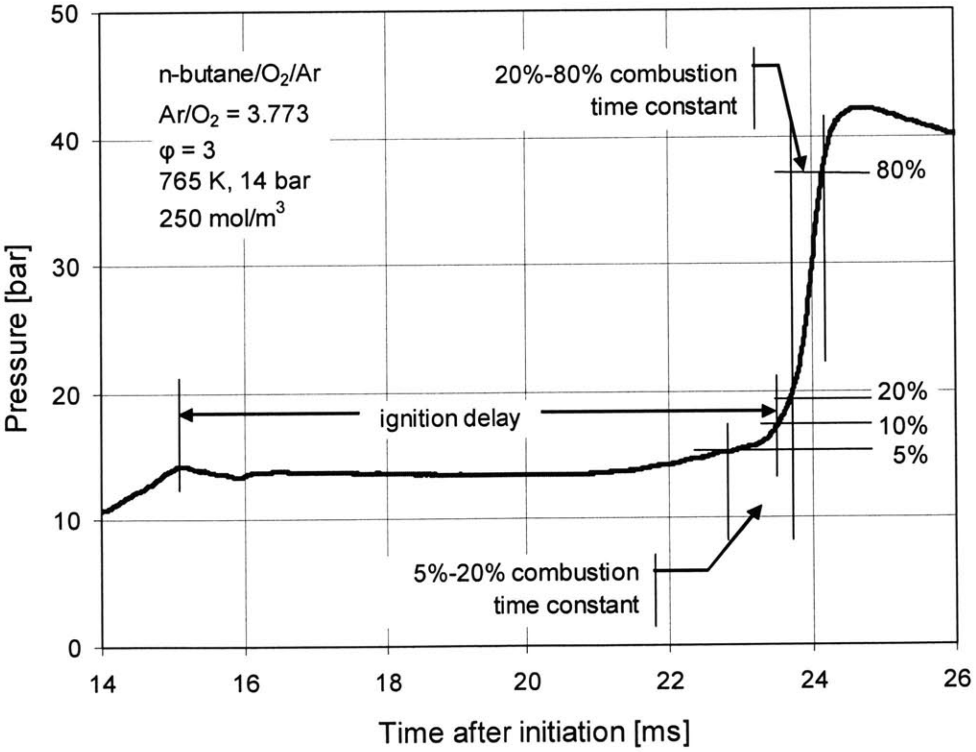

Figure 3.8 Combustion characteristics definitions.

The light transmission signal shown also in Figure 3.7, is a little noisy during ignition delay because of mechanical vibrations and light beam steering before dropping down to zero during combustion due to soot formation. Because of this noise the usable data range in this study was between 90% and 5% light transmission. The light transmission data were converted to soot concentration f_v according to the relationships given in the diagnostics section. It should be noted that 5% transmission does not mark the end of soot formation. Since the mixture is sufficiently rich, the combustion chamber can become almost opaque well before the process ends. Collecting the soot after the end of the experiment and converting it to soot concentration, it was found that depending on the operating conditions, not more than 10-15% of the soot formation process could be observed with the LOS method. Therefore, these experiments can provide valuable information about the critical initial stage of soot formation. Data points A of Figure 3.9 represent the soot yield (SY) obtained for the above case plotted in semi-log scale. SY, which is defined as carbon present in soot rationed to the total carbon content in the combustion chamber (which obviously comes from the fuel), can be calculated from f_v according to the relationship:

$$SY = \frac{\rho_s \cdot f_v}{W_C \cdot [C]_{comp}}$$

where $\rho_s = 1.8\,\mathrm{g/cm^3}$ and $W_C = 12\,\mathrm{g/mol}$ are soot density and atomic weight of carbon respectively; $[C]_{comp}$ is the molar carbon concentration at the end of compression.

From Figure 3.9 it is obvious that soot formation follows initially an exponential trend, which fits into the current understanding of the process. During fuel breakdown under rich conditions significant amounts of gaseous hydrocarbon (HC) species, like PAH and C_2H_2, with higher C/H ratio than the parent fuel molecules, are formed which act as building blocks to the surface growth of young soot particles. Soot particles promote the formation of bigger particles according to the global chemical reaction:

$$Soot + HC \rightarrow Soot$$

The rate of soot formation is then given by:

$$\frac{d}{dt}[Soot] = k(T) \cdot [HC] \cdot [Soot]$$

Integrating this rate equation an "autocatalytic" nature of soot formation is obtained. If we assume no significant temperature variation during the very early stage of soot growth:

$$[Soot] \propto \exp\left(k(T) \int [HC] dt \right)$$

That the initial soot volume fraction shows an exponential time dependence suggests that the HC concentration is nearly constant. Thus the generation of the soot precursors is in balance with their distruction (via condensing on the soot particles or via oxidation. However, in experiments with a low carbon loading, the supply of the precursors will eventually be exhausted; thus the trend should be exponential only initially. Data B of Figure 3.9 represents soot yield history at almost the same conditions as for Data A but at $P_{comp} = 10.5$ bar ($N_{comp} = 190$ mol/m^3) instead of 14 bar (250 mol/m^3). It is obvious that soot formation is only initially exponential and then it continues at an increasignly slower rate. Since the initial soot formation turns out to be exponential under most conditions tested, a soot time constant can be defined. This time constant can be used to compare the sensitivity of initial soot formation rates to combustion parameters like temperature, pressure, fuel-air equivalence ratio and fuel structure. This is possible since

RCM repeatability is very good, as Figure 3.7 suggests. With 95% confidence level, the variability of the ignition delay, combustion and soot time constant are ±2%, ±12% and ±13% respectively.

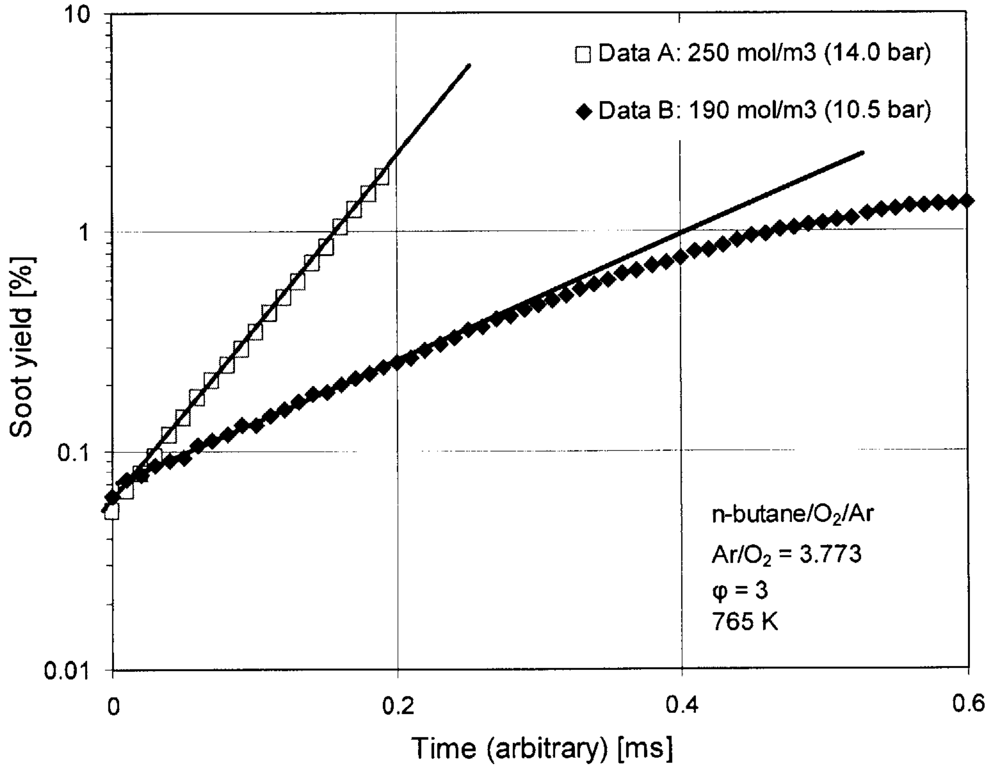

Figure 3.9 Effect of total volume concentration on soot formation history.

Illustrative experimental data of the effect of temperature on ignition delay, combustion and soot time constant are shown in Figure 3.10, Figure 3.11 and Figure 3.12 respectively. The initial conditions were varied so that at the end of compression $N_{comp} = 250\,\text{mol/m}^3$ and $T_{comp,core} = 722, 741, 765, 787, 839, 894$ and 931K. In all cases n-butane/O_2/Ar mixtures were used, with Ar/O_2 = 3.773 and $\phi = 3$. The ignition delay of n-butane plotted in Figure 3.10 in Arrhenius graph shows a typical hydrocarbon autoignition behavior observed in the past by other researchers. At lower temperatures the ignition delay drops rapidly with increase in temperature. At intermediate temperatures, the delay stays fairly constant or even increases showing clearly the well-known negative temperature coefficient (NTC) zone. At high temperatures, it drops rapidly again. The trends of combustion and soot time constants shown in Figure 3.11 and Figure 3.12 respectively (in Arrhenius form too) also depict the importance of temperature on chemical kinetics. Data of both time constants give a quantitative picture about how fast combustion and soot formation proceed and supplemented by additional data under different conditions, which are reported in the next chapter, can provide a better basis for chemical kinetic modeling of such complex processes.

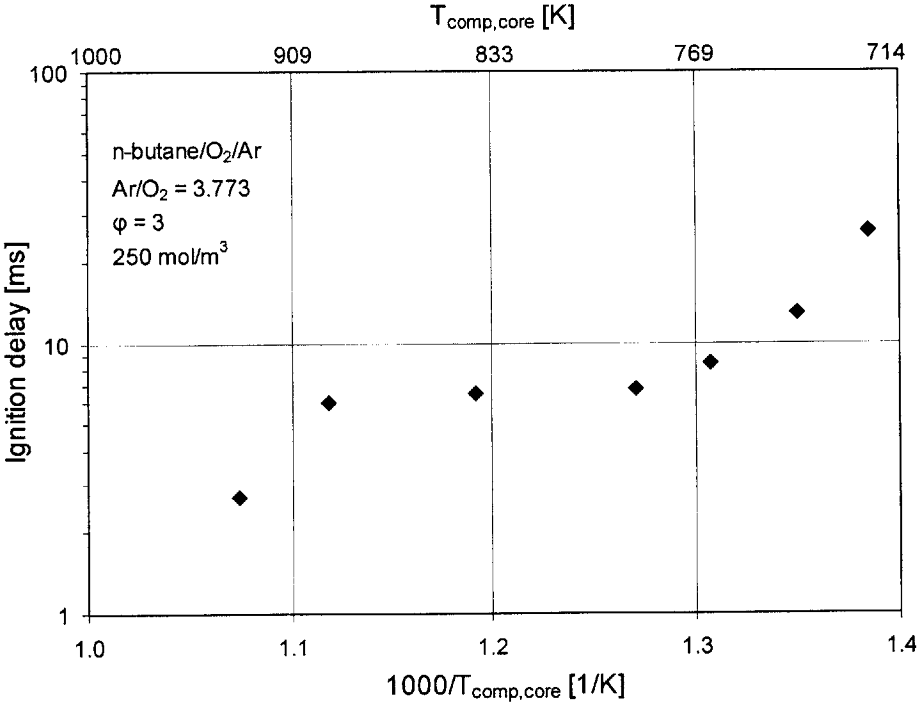

Figure 3.10 Effect of compressed core temperature on ignition delay.

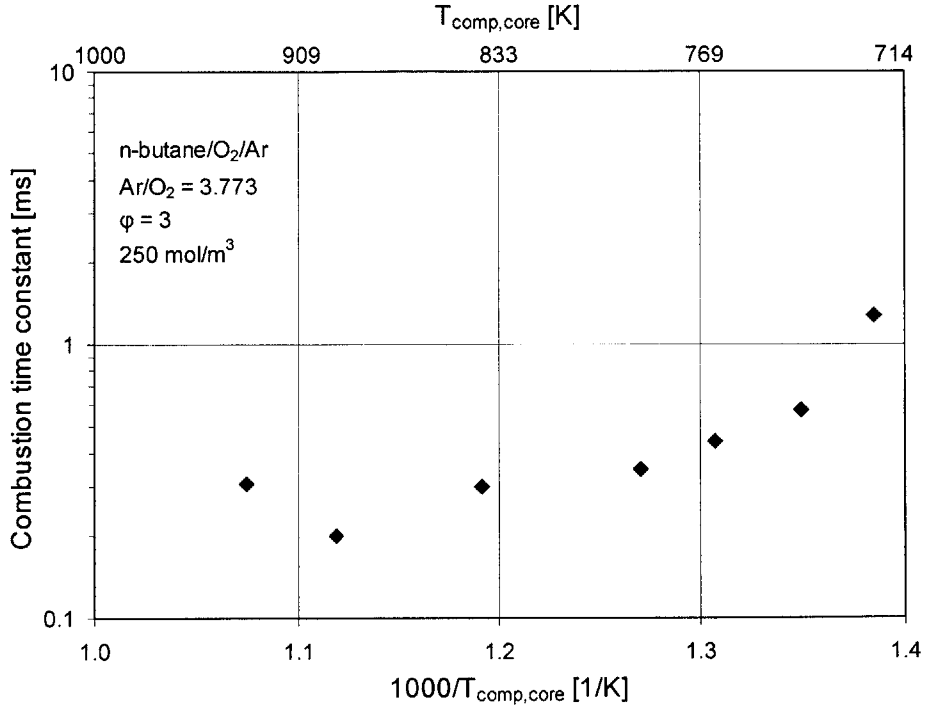

Figure 3.11 Effect of compressed core temperature on combustion time constant.

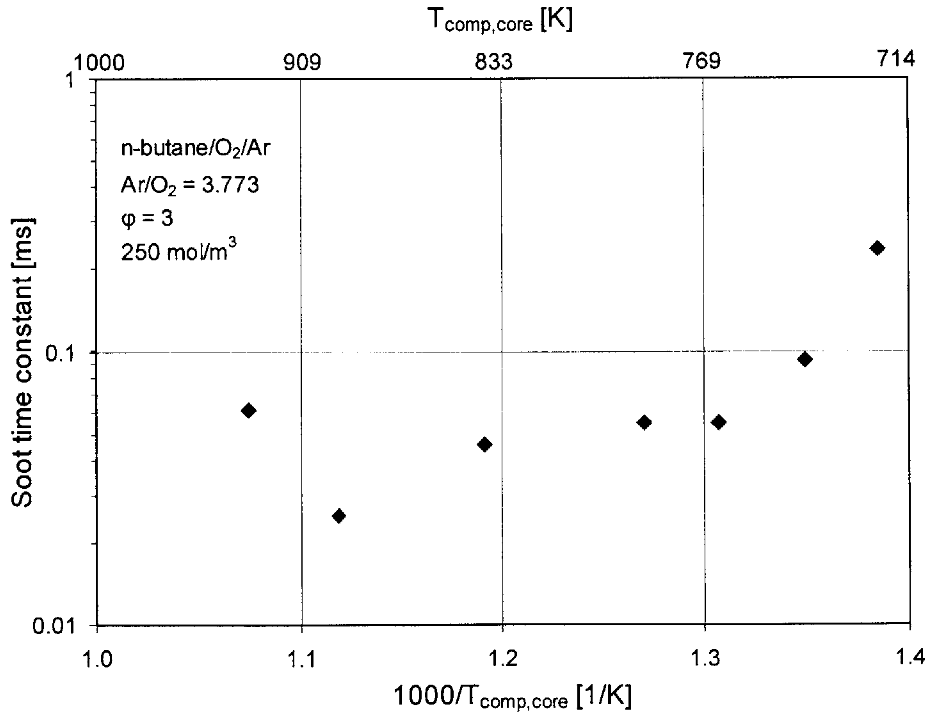

Figure 3.12 Effect of compressed core temperature on soot time constant.

3.4 Test Matrix

It is the objective of this study to gain fundamental insight into the soot formation process under diesel engine conditions. Therefore, the mixture and the thermal environment just before the start of combustion were designed accordingly. At the end of compression, core temperatures varied between 680-950 K and total volume concentrations between 190-500 mol/m^3 (corresponding to approximately 9-33 bar compression pressure). The fuel-air equivalence ratio was chosen to be fairly high, so that the fuel-rich premixed zone, speculated to be responsible for soot formation, could be reproduced. Consistent with previous optical studies, the fuel-air equivalence ratio varied between 2 and 5. The fuel used in most of the experiments was n-butane. Mixtures of n-butane with toluene or di-methyl-ether (DME) or 2-ethyl-hexyl-nitrate (EHN) were also tested under some particular conditions. N-butane was selected as the base fuel because it shows typical hydrocarbon characteristics (e.g. NTC and two-stage autoignition). Also it is a fuel with relatively low reactivity so that under most conditions no significant reactions take place before the end of the compression. Toluene, apart from having the simplest molecular structure of the alkylated benzenes, has also been suggested as a surrogate for describing combustion of aromatics in diesel and aviation jet fuels. DME is a very simple oxygenate, which is appealing to diesel engines because of its tendency to suppress soot formation. Furthermore there are available chemical kinetic models for all above molecular structures, although not validated under the current operating conditions that the data could be compared to. From the practical point of view since they are gases under ambient conditions (apart from toluene, which has though sufficient vapor pressure), mixture metering is straightforward and condensation at the walls during compression can be avoided. To test the effects of a CN improver on soot formation, the base fuel was also doped with very small amounts of EHN for a limited number of experiments. Previous studies utilized different diluent/O2 ratios of Ar, N_2 and CO_2 in order to achieve different compression conditions starting from the same initial conditions before compression. In this study in order to investigate the impact of fuel-air equivalence ratio or temperature or concentration alone on fuel-rich combustion and soot formation, a single diluent was used. Compressed gas temperatures and pressures were varied by changing the initial conditions. Furthermore, to simulate engine conditions as close as possible, the diluent/O_2 ratio was kept constant and equal to 3.773 (ratio of N_2/O_2 in air). Thus, unlike most shock tube and flow reactor studies, the mixture was not diluted. Ar was used as the diluent instead of N_2 in this study because with its higher specific heat ratio, the temperatures and pressures at the end of compression of the rich mixtures could be raised to the desirable levels. The test matrix used in this study is summarized in Table 3.2.

Table 3.2 Test matrix used in this study

Test parameter	**Range**
Fuel	Mixtures of n-butane, toluene, DME, EHN
Fuel-air equivalence ratio	2 - 5
Compressed core temperature	680 - 950 K
Total volume concentration (pressure)	190 - 500 mol/m^3 (9 - 33 bar)
Diluent	Ar
Diluent/O2	3.773

Chapter 4

Ignition Delay Study

4.1 Introduction

Hydrocarbon fuel ignition characteristics have long been a field of both experimental and computational efforts due to their relation to practical combustion systems. Numerous experimental studies conducted in RCM [71, 73, 81-85], shock tubes [86-88], and flow reactors [89-90] have provided valuable data sets under different regimes of operation. Shock tubes were mostly used to study short ignition delays (of the order of 1 ms) of highly diluted mixtures under high temperatures and pressures. Flow reactors involved studies at low pressures and the mixture may also be diluted. There is recent interest in high pressure, intermediate temperature ignition characteristics of hydrocarbons since these conditions are encountered in most practical combustion systems such as internal combustion engines. The operations of diesel and homogeneous-charge compression-ignition (HCCI) engines rely on the auto-ignition of hydrocarbons under this regime [81]. The end-gas in spark-ignition engines, which is responsible for engine knock, is also subjected to similar conditions [71]. The RCM has been proven to be an excellent apparatus for studying hydrocarbon ignition phenomena under engine-like conditions. Due to its precisely controlled conditions, the interpretation of the data is unambiguous and therefore proposed chemical kinetic mechanisms can be tested.

One objective of this study was to use a RCM to obtain new data on oxidation and spontaneous ignition of fuel-rich mixtures (fuel-air equivalence ratio between 2 and 5) at intermediate temperatures (700-900 K) and high pressures (10-35 bar). These conditions are of great importance since they are those found in diesel engines and they govern the ignition delay. Mixtures of n-butane, toluene and DME with air were used since they could represent the fuel used in diesel engines while having simple molecular structures. Most of the data will be compared to and augment those found in the literature. The three independent variables used in the experiments, apart from the fuel itself, were fuel-air equivalence ratio, and compression temperature and total mole concentration (from which pressure can be defined). Apart from studying features of general interest regarding hydrocarbon autoignition experimentally, the study aimed to test detailed chemical kinetic mechanisms and evaluate their performance. Such chemical kinetic modeling efforts could provide further insight into the major oxidation pathways of hydrocarbons, which could help understand better the conditions preceding formation of soot.

4.2 Chemical Kinetic Model

Since the experiments were conducted over a wide range of compression temperatures, the chemical kinetic model employed should have included both the low and the high temperature paths of hydrocarbon oxidation. The mechanism developed by Lawrence Livermore National Laboratories (LLNL) and that described in Ref. [91] was used. The complete mechanism consists of 857 species and 3605 reactions. Since this model corresponds to iso-octane oxidation, species and reactions larger than n-butane were removed to decrease computational time. This simplification resulted in no effect on computed ignition delay times and the model consisted of only 265 species and 1403 reactions. To model the autoignition of n-butane/toluene or n-butane/DME mixtures, the toluene and DME sub-models were added to the base kinetic model described above. These models have been also developed by LLNL and are described in [92] and [93] respectively. The resulting mechanisms consisted of 341 species and 1646 reactions for n-butane/toluene and 281 species and 1471 reactions for n-butane/DME. Since fuel-rich mixtures were used, additional chemical pathways involving PAH, which eventually lead to soot, in principle should have been included. A PAH and a soot model, which are discussed extensively in Chapter 6, were added to test the effect on ignition delay and no variation was observed, therefore these models were not used for the purpose of the autoignition study.

The Senkin application of Chemkin-II was used for computing the time histories of species, pressure and temperature assuming an adiabatic and homogeneous system [94]. The calculation started after the end of compression. The volume was fixed and experimental compression pressure and computed core temperature (as already described in Chapter 3) where used as the starting conditions. Keeping the model simple facilitates understanding of the chemical processes involved, but implies that three major assumptions were made: (a) an adiabatic core exists and determines the ignition delay, (b) no significant reactions take place before the end of compression and (c) heat transfer is negligible during the ignition delay. The validity of these assumptions is discussed below.

It has been shown that the temperature field within the RCM is not entirely uniform [95]. Even though assuming a homogeneous mixture for heat release studies may lead to inaccuracies, past research has shown that a significant adiabatic core does exist [96]. Hence, spatial uniformity of temperature and species concentration during ignition delay is assumed. The implications of non-uniformities in the temperature field on ignition delay and rate of heat release are studied extensively in Chapter 5. The core temperature is the highest temperature within the combustion chamber and determines the autoignition of the mixture as long as the conditions do not correspond to the NTC region. As shown in the experimental results section below, for the conditions employed in this study, instead of a clear NTC region, the ignition delay reaches a plateau with increasing temperature under certain conditions. Therefore, for the purpose of this study, the core temperature sufficiently represents the thermal environment of the combustion chamber and determines the ignition delay. Recent studies have also shown that there may be reactions occurring before the end of compression [84, 97]. Even though the compression time of this RCM and the reactivity of n-butane are much lower than those used in the cited studies the effects of pre end-of-compression reactions on ignition delay have been evaluated. Assuming an adiabatic core during compression, the volume of the core can be calculated from the pressure data in a similar way as the core temperature described in Chapter 3. The resulting calculated volume is different from the combustion chamber volume in that it does not only contract due to mechanical compression but at the same time it is also subjected to some expansion. The boundary layer gas contracts while being cooled by the wall and therefore the core expands adiabatically. Therefore, the resulting contraction of the core during compression is lower than that dictated by the compression ratio. Calculating the core volume from the pressure data, it was found that the effective compression ratio was reduced to approximately 15 instead of being 16.5. Then the computed core volume can be used as an input to the model instead of using simple constant volume relationships. In this case the starting conditions do not correspond to the end of compression but to the conditions during compression where temperature and pressure are high enough so that important reactions start occurring with appreciable rates. To evaluate the impact of pre end-of-compression reactions on ignition delay, it was found that under most conditions starting the simulation 3 ms before the end of compression was sufficient. Similarly, to study heat transfer effects during the ignition delay, the core volume was calculated from the pressure data during that period too. Due to the short time scale of the experiments, it is believed that heat transfer cannot affect the core directly; however the core temperature drops adiabatically as it expands due to the contraction of the boundary layer gas. The temperature drop for a given pressure drop is expected to be rather small though, because the mixtures used in this study were fairly rich and hence the specific heat ratios quite low. To exemplify this, using the adiabatic relationship for the core mentioned above, the core temperature drop from the end of compression to the start of combustion, was estimated. For a typical experiment with $\phi = 4$, $T_{comp,core} = 725\,\mathrm{K}$ and $P_{comp} = 27\,\mathrm{bar}$, the measured pressure drop during the delay (which was measured 6.7 ms) did not exceed 0.5 bar. Using a specific heat ratio of 1.24 the core temperature drop could not be more than 3 K.

Figure 4.1 shows in a log-log scale the ignition delays calculated using constant and variable core volume relationships as described above. The two methods predict very similar ignition delays between 2 and 10 ms. The constant volume assumption overestimates ignition delay for very short delays (pre end-of-compression reactions) and underestimates it for very long delays (heat transfer effects). The majority of our data (more than 80%) laid between 2-12 ms and therefore the constant volume assumption is deemed to be accurate enough. The modeling results shown in the next section are produced with constant volume relationships so that the chemical features of the model can be clearly studied. However, some of them need to be interpreted taking into account the findings of Figure 4.1.

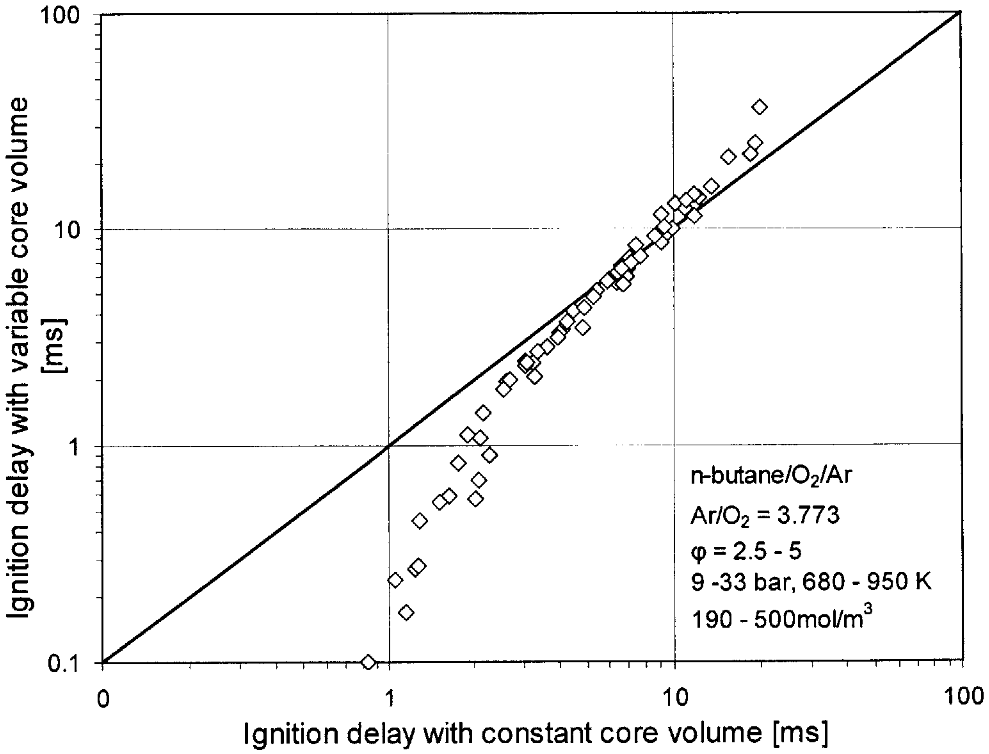

Figure 4.1 Ignition delay calculated with constant and variable core volume relationships.

4.3 Experimental Results

The experimentally observed effect of the core temperature at the end of compression on ignition delay for $\phi = 2.5$ and $N_{comp} = 250$ and 500 mol/m^3 is shown in Figure 4.2 as symbols. On the same graph the corresponding model results (discussed in the next section) are also shown as lines. Figure 4.3, Figure 4.4 and Figure 4.5 show the results obtained as the mixture gets richer, i.e. $\phi = 3.0$, 4.0 and 4.5 respectively for different total compressed volume concentrations. Note that for richer mixtures the maximum compression temperatures achieved were lower since pre-compression heating was limited to approximately 150^{0}C.

From this extensive set of experimental data it turns out that the ignition delay characteristics of n-butane/O_2/Ar mixtures could be grouped into three temperature zones. For lower temperatures the ignition delay drops rapidly with increase in temperature. At intermediate temperatures, the delay stays fairly constant (or even slightly increases) showing a weak NTC behavior. At high temperatures, it drops rapidly again. The temperature boundary between these zones depends on concentration but the behavior is at least qualitatively similar. This behavior is typical of alkane oxidation and it has been observed in the past for similar fuels and under other conditions by many researchers [73, 84-86].

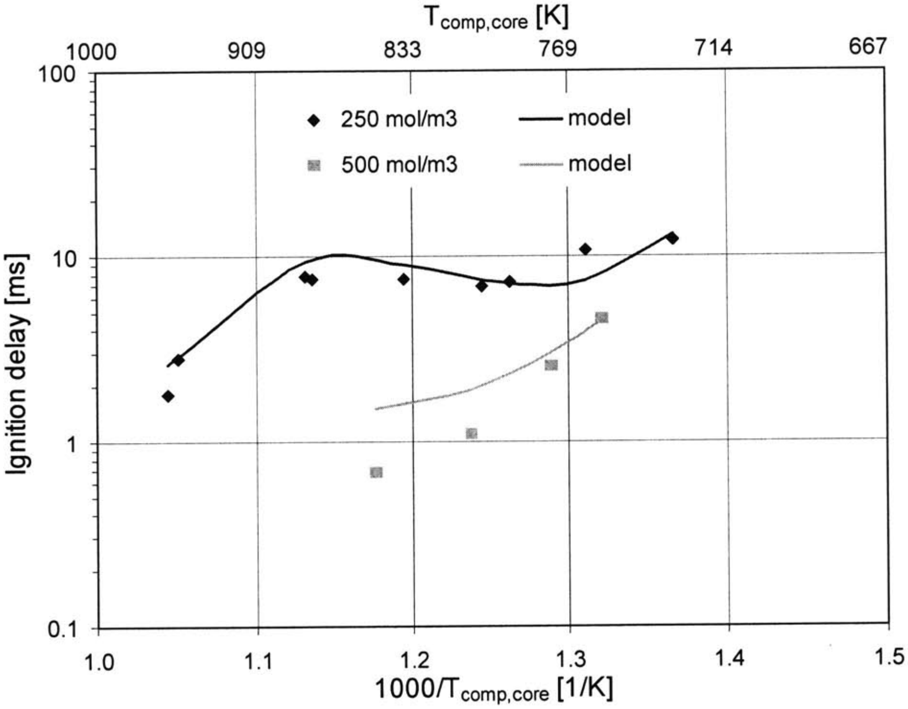

Figure 4.2 Experimental data (dots) and modeling results (lines) of n-butane/O_2/Ar mixtures (Ar/ O_2 = 3.773) for ϕ = 2.5 .

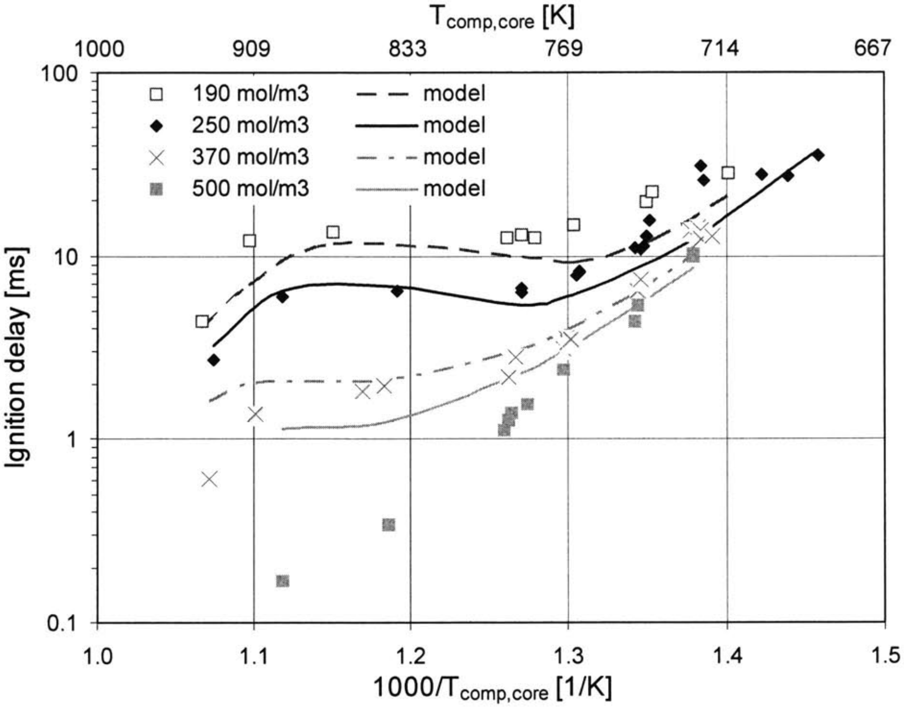

Figure 4.3 Experimental data (dots) and modeling results (lines) of n-butane/O_2/Ar mixture (Ar/O_2 = 3.773) for $\phi = 3.0$.

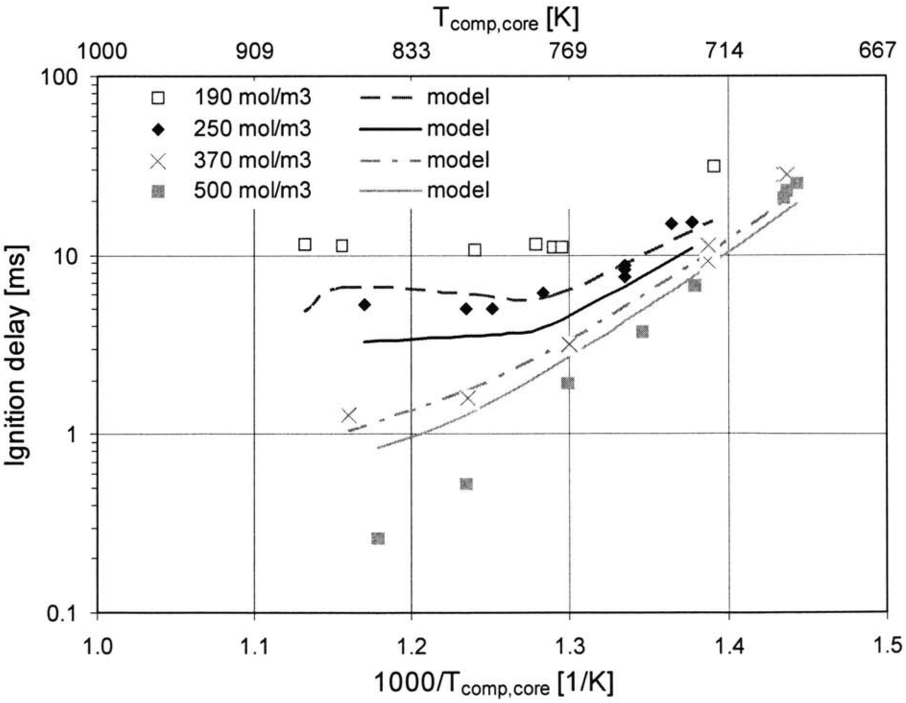

Figure 4.4 Experimental data (dots) and modeling results (lines) of n-butane/O_2/Ar mixture (Ar/O_2 = 3.773) for $\phi = 4.0$.

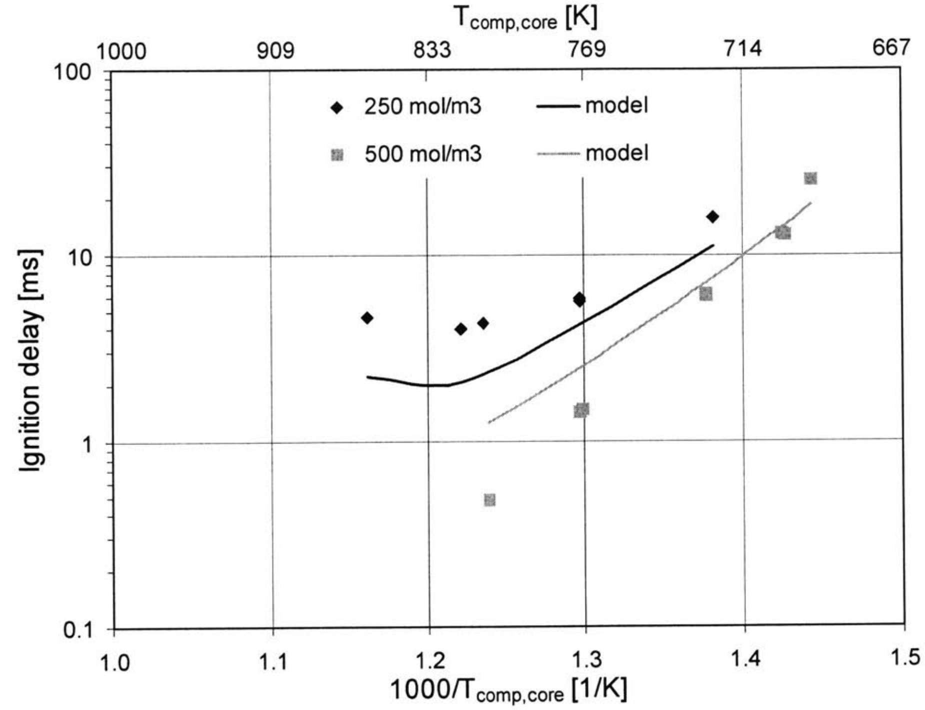

Figure 4.5 Experimental data (dots) and modeling results (lines) of n-butane/O_2/Ar mixture (Ar/ $O_2 = 3.773$) for $\phi = 4.5$.

Figure 4.6 shows a schematic of the main hydrocarbon oxidation characteristics for both low and high temperature paths. The low temperature mechanism includes more paths, like ether formation, not included in the schematic since they are of minor importance. Most chemical kinetic models include the general features of this diagram [91, 98-100]. A detailed description is given in [91, 97, 101] and only a brief summary is given here. At lower temperatures alkyl radicals (R) produced from parent fuel molecules (RH) by decomposition or H-atom abstraction react with O_2 to form alkyloperoxy radicals (ROO). The most likely path for the latter radicals is to go through isomerization (internal H-atom transfer) forming hydroperoxy alkyl radicals (QOOH), and after one more O_2 addition, to form hydroperoxyalkylperoxy radicals (OOQOOH). These radicals go through another isomerization forming carbonyl hydroperoxides (O=R'OOH) and OH radicals and then the former decompose giving carbonyl radicals (O=R'O) and OH. The last two steps initiate branching since two very reactive OH are formed. This chemical pathway is responsible for the first stage of hydrocarbon ignition. As temperature increases equilibrium causes ROO to decompose back to O_2 and R shutting down this route. Then O_2 reacts again with R but now abstracting an H-atom forming hydroperoxy radicals (HOO), which are also formed by O_2 addition to H-atoms along with a collision partner giving the required energy to overcome the high energy barrier. Then HOO form the relatively unreactive at intermediate temperatures hydrogen peroxides (HOOH), by recombination or attack on the fuel. The concentration of HOOH builds up and during this period temperature may lengthen the ignition delay and the NTC behavior is observed. As temperature increases HOOH decompose giving two OH radicals, which act as branching agents. Since this decomposition is pressure dependent, ignition delay shortens with pressure. At these temperatures H can also react directly with O_2 creating two more reactive radicals. At these high temperatures R radical decomposition also happens which finally leads to beta scission products. Hence, ignition delay starts dropping again with temperature.

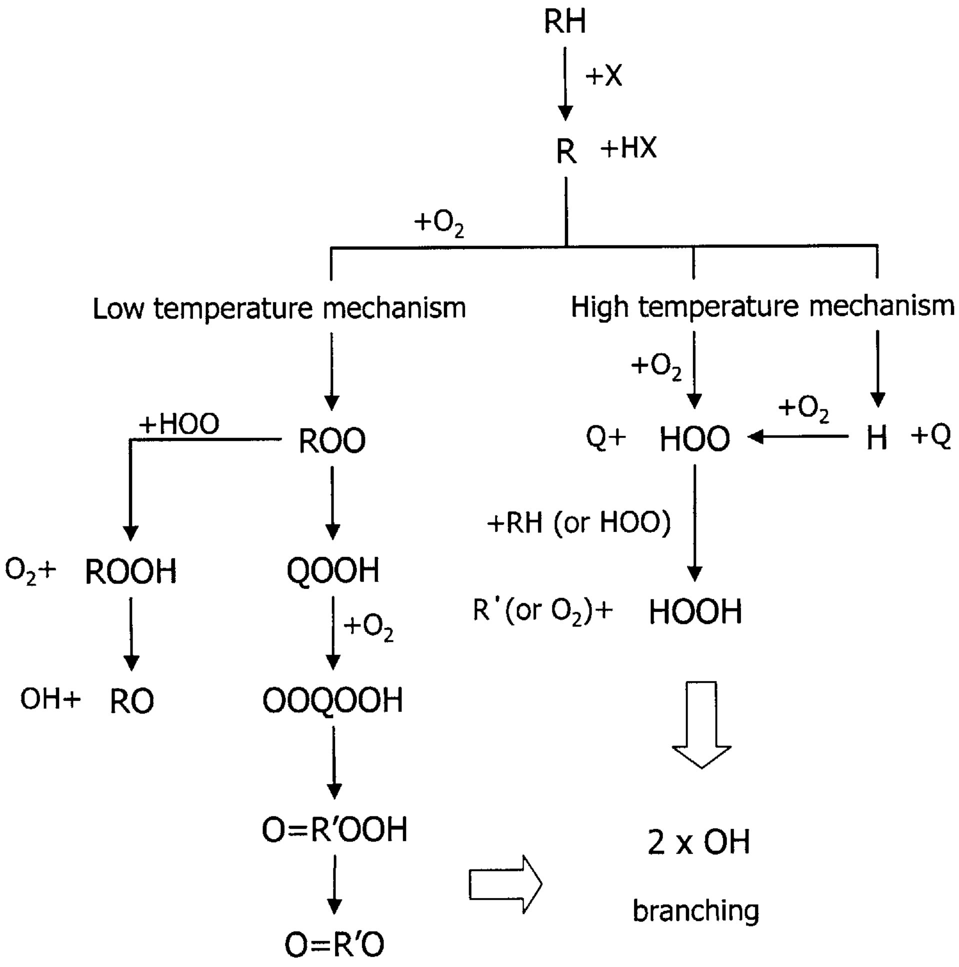

Figure 4.6 Schematic of main hydrocarbon oxidation pathways (see text for nomenclature).

It is evident from the data that lower pressure (which scales with total molecule concentration) increases ignition delays over the entire temperature range and amplifies the NTC region. This is clearly shown in Figure 4.7 for low and high concentrations (250 and 500 mol/m^3 respectively) and different fuel-air equivalence ratios. Similar observations for alkanes were also made by other studies but since the pressure was always lower compared to the current study the NTC region was always observed (less prominent though at higher pressures) [73, 84-86]. Such behavior can be attributed to the reactions that involve change in the number of molecules in the low temperature mechanism [97]. In particular, the reactions forming ROO and OOQOOH lead to a smaller number of molecules, and hence lower pressure. Therefore, an increase in pressure shifts the equilibrium strongly towards the formation of ROO radicals. Then, decomposition back to R and O_2 occurs at even higher temperatures (shift of NTC zone), where the high temperature mechanism (HOOH decomposition) is about to kick off (less prominent NTC region).

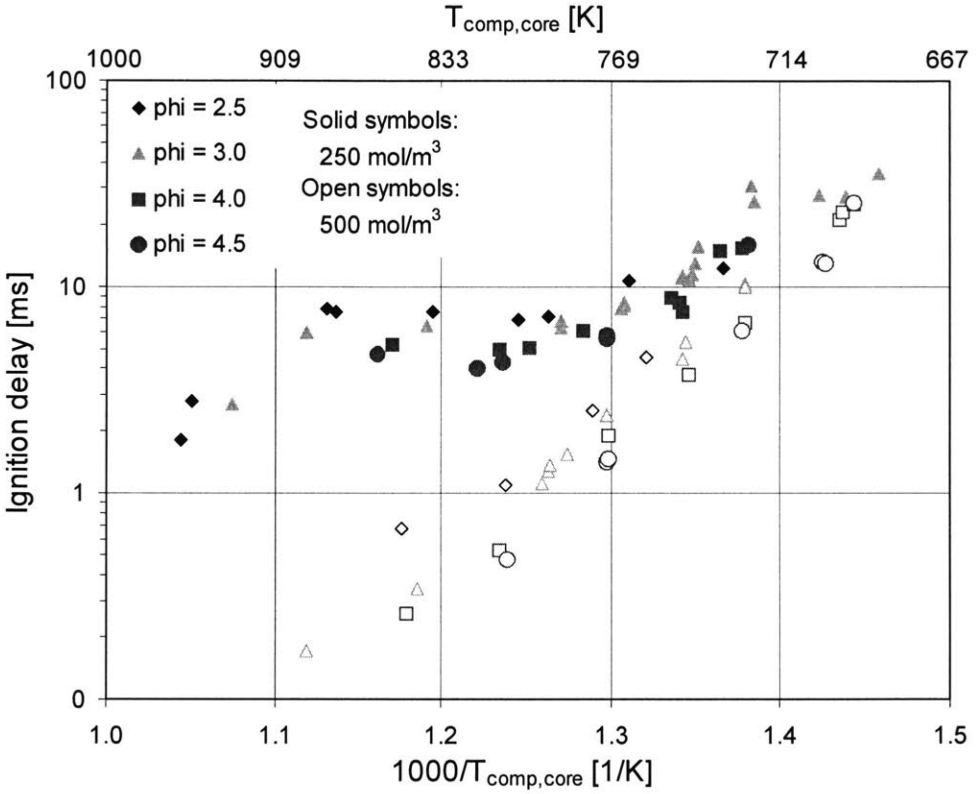

Figure 4.7 Experimental data of n-butane/Ar/O_2 mixture (Ar/O_2 = 3.773) for 250 and 500 mol/ m^3.

Figure 4.8 shows the effect of fuel-air equivalence ratio on ignition delay for two different concentrations along with the corresponding computational results for approximately the same compression temperature of the core (770 K, ±5 K). It is clear that the ignition delay becomes shorter as fuel-air equivalence ratio increases for the range studied here. Similar results have been obtained by other limited studies of fuel-air equivalence ratio effects on ignition delay but at less fuel-rich mixtures [73, 86], even though sometimes the compression conditions were not kept strictly constant [83]. The reason for such behavior could be also attributed to the equilibrium shift of the reaction that kicks off the low temperature mechanism, i.e. the addition of O_2 to R forming ROO. When conducting tests at different fuel-air equivalence ratios, the compression conditions, i.e. pressure and temperature and therefore gas concentration were kept constant. Since the total number of molecules was the same, a richer mixture would comprise more RH and less O_2 molecules. But for every O_2 molecule removed, 3.773 Ar molecules were also removed. So when the mixture got richer the RH molecules increased more in absolute terms[1]. Assuming that R radicals are roughly proportional to the initial RH concentration, it becomes apparent that increasing fuel equivalence ratio results in a shift of equilibrium of the reaction in question towards the products, i.e. the acceleration of the low temperature mechanism. Therefore, the mechanism of fuel equivalence ratio effect on ignition delay is similar to that of pressure.

---

[1] $N = N_{RH} + N_{O_2} + N_{Ar} = N_{RH} + 4.773N_{O_2}$

Since the total number concentration N is fixed, it follows:

$\Delta(N_{RH}) > |\Delta(N_{O_2})|$

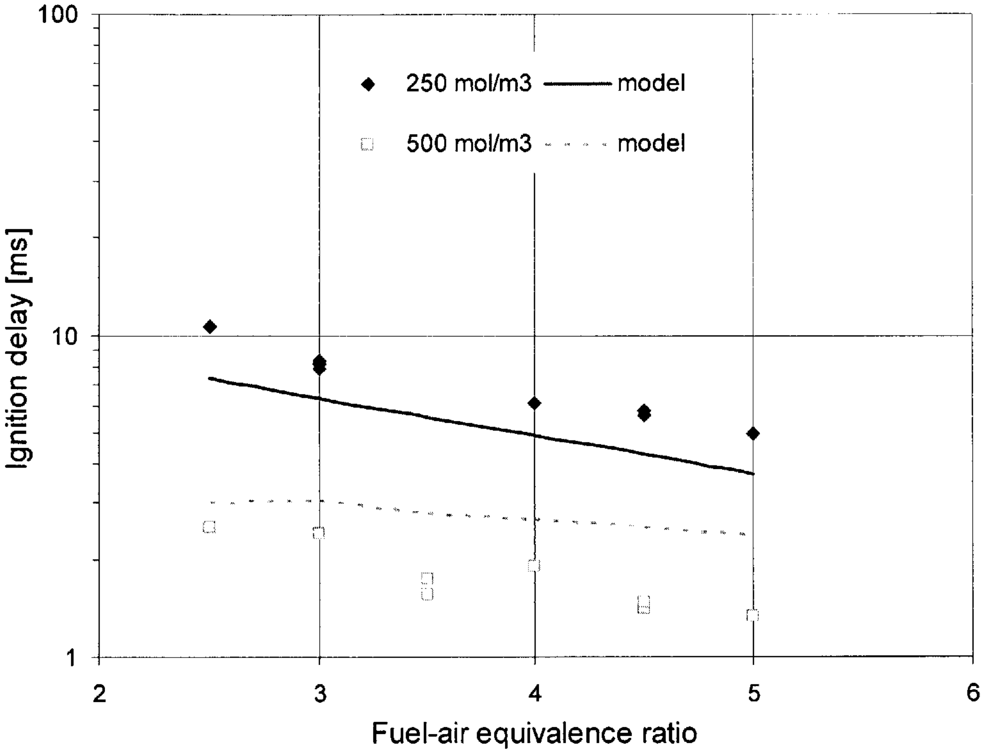

Figure 4.8 Experimental data and modeling results of n-butane/Ar/O_2 mixture (Ar/O_2 = 3.773) for 770 K (± 5K).

Minetti et al. [85] has done a similar study on n-butane autoignition for lower total volume concentrations (120 to 180 mol/m^3) and stoichiometric mixtures. To achieve different temperatures at the end of compression in that study, the diluent was changing from pure CO_2 (lower temperatures) to pure Ar (higher temperatures). Even though the heat capacity of the mixture changes, the effect of diluent on ignition delay was found to be of minor importance as long as the compression conditions and the diluent to oxygen ratio are the same[1]. Some of these data are plotted in the same graph with current's study data for richer mixtures ($\phi = 3$ and 4) and at very similar total volume concentration (190 mol/m^3) in Figure 4.9. All data seem to follow similar trends and are in accordance to the picture of hydrocarbon ignition described above. The equivalence ratio shortens the ignition delay

---

[1] It has been calculated that exchanging Ar with CO_2 increases the ignition delay by less than 5%.

and along with pressure it shifts the NTC zone to higher temperatures, where it is not very prominent.

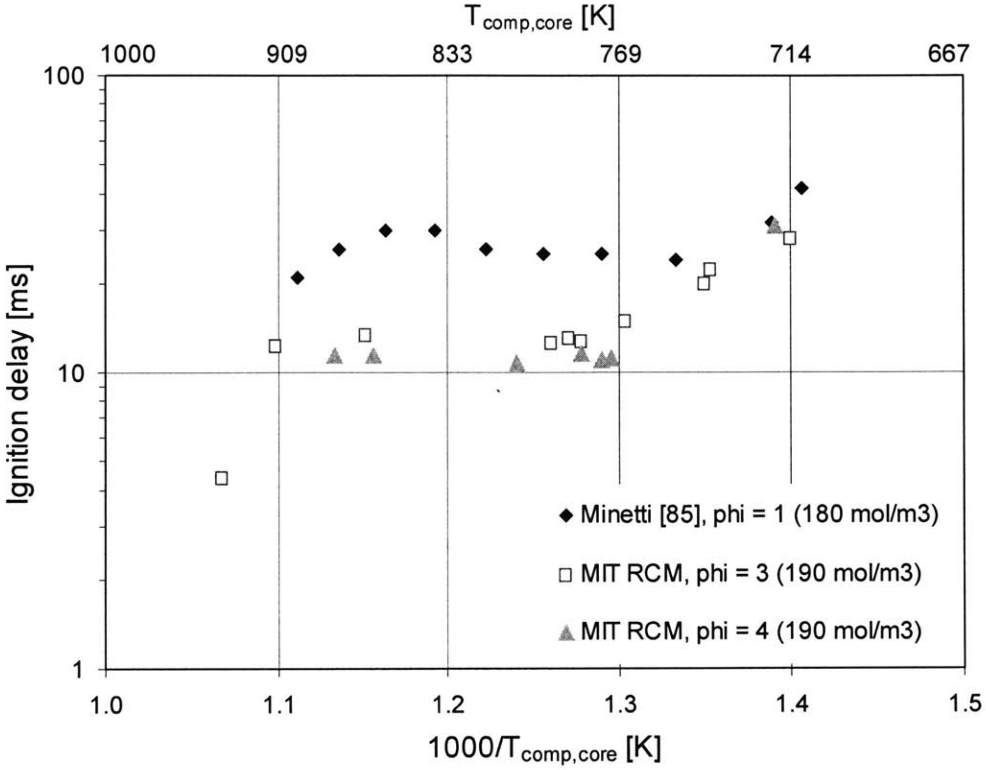

Figure 4.9 Experimental data from MIT and Lille RCM of n-butane/diluent/O_2 mixture (diluent/O_2 = 3.773) for 180-190 mol/m^3.

The typical two-stage auto-ignition of alkanes observed in most studies was also observed here [73, 84-85]. However, as past research has shown for n-butane, the first-stage is longer and less prominent compared to longer-chain alkanes, therefore it is not always readily observed [84]. Since the first-stage is related to the NTC region, at high pressures, equivalence ratios and at high and lower temperatures, it is hardly perceptible. Yet, it is very clear at intermediate temperatures, lower pressures and less fuel-rich mixtures. It should be also noted that when the ignition delay becomes sufficiently small some of the first-stage heat release might be taking place before the end of compression, while when it becomes too long, heat transfer may suppress the heat released during that first-stage. Figure 4.10 shows the effect of temperature on the autoignition behavior of n-butane for $N_{comp} = 190\,\text{mol/m}^3$, $\phi = 3$ and $T_{comp,core} = 911, 787$ and 739 K. Each test corresponds to each of the three temperature zones described above (see also Figure 4.3). It is obvious that the first-stage is not observed at high and low temperature tests but it is very pronounced at intermediate temperatures.

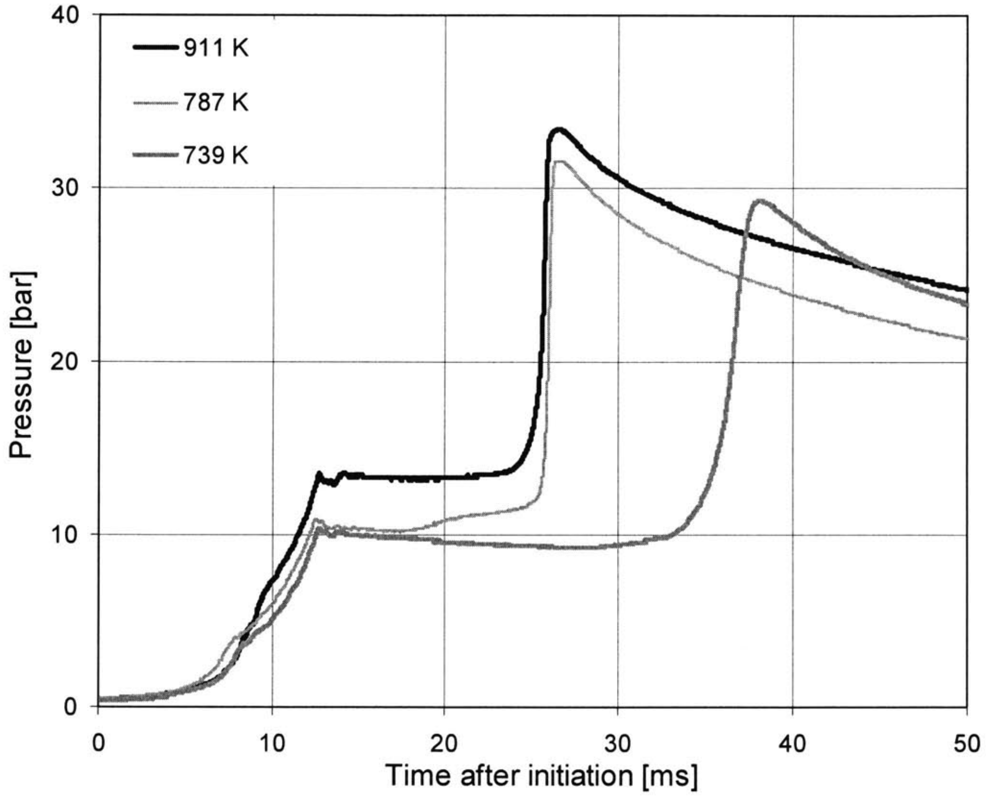

Figure 4.10 Two-stage ignition of n-butane/Ar/O_2 mixtures (Ar/O_2 = 3.773) for $\phi = 3$ at 190 mol/m^3.

Figure 4.11 and Figure 4.12 show the effect of adding toluene and DME respectively to the base fuel on ignition delay for some illustrative cases. Figure 4.11 shows ignition delay data of n-butane/toluene mixtures for 350 and 500 mol/m^3 as a function of toluene mol fraction in the fuel. The fuel-air equivalence ratio was set to 3 and the initial conditions were adjusted so that the core temperature at the end of compression was 770 K (±2 K). As expected, ring structures are more difficult to be ruptured than normal paraffins since the low temperature mechanism described in Figure 4.6 is absent and therefore the ignition delay increases as the mole fraction of toluene in the fuel increases. The cetane number (CN) of toluene is 2.6 as opposed to 22.5 for n-butane. Similar data are plotted in Figure 4.12 for n-butane/DME mixtures. Two sets of data are plotted: 450 mol/m^3, $\phi = 3$, $T_{comp,core} = 715\,\mathrm{K}$ (±3 K) and 250 mol/m^3, $\phi = 3.5$, $T_{comp,core} = 745\,\mathrm{K}$ (± 3K). DME is known to have high CN (approximately 57) and since it exhibits low temperature chemistry, it accelerates the ignition delay. The data are plotted as a function of the mass fraction of oxygen in the fuel since it is customary to do so for oxygenated fuels in the diesel engine literature because it has been reported that for 30%, combustion generated soot particles drop to zero [102]. Note that for this mixture, 35% of oxygen in the fuel by mass corresponds to pure DME.

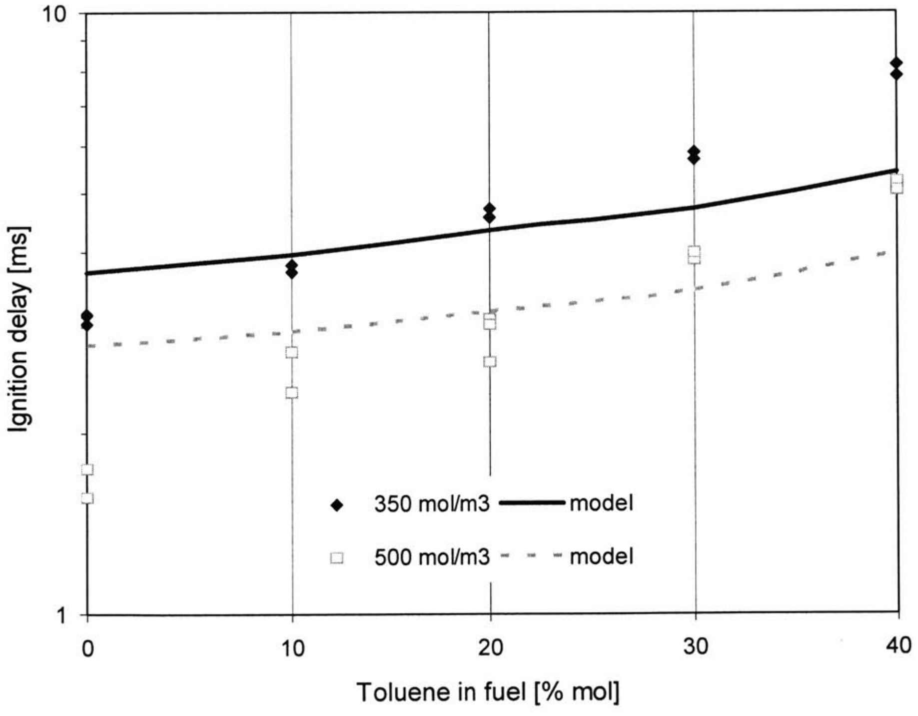

Figure 4.11 Experimental data and modeling results of n-butane/toluene/Ar/O$_2$ mixture (Ar/O$_2$ = 3.773) for 770 K (±2 K) and $\phi = 3$.

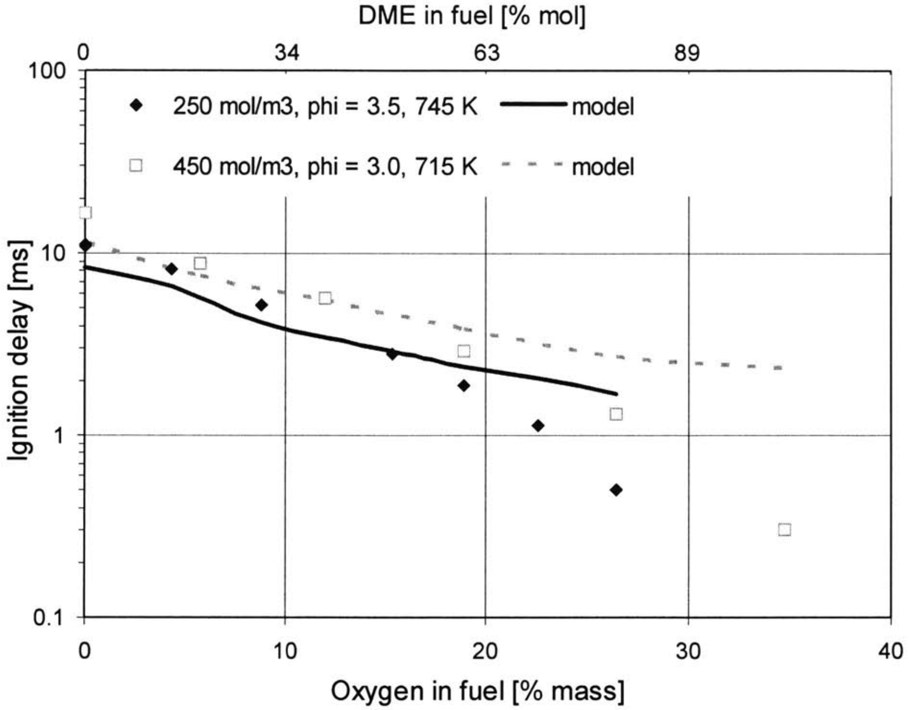

Figure 4.12 Experimental data and modeling results of n-butane/DME/Ar/O_2 mixture (Ar/O_2 = 3.773).

4.4 Modeling Results

The computed ignition delay results are shown along with the experimental data in the figures of the previous section. To keep the model simple, constant core volume has been assumed. However the findings of Figure 4.1 need to be taken into account for very short (<2 ms) and very long ignition (>10 ms) delays. The chemical kinetic models were developed by LLNL as explained above but two adjustments were made in order to achieve a better agreement with the data and are explained below. The first one concerns OOQOOH isomerization and the second H-atom abstraction from the fuel with HOO.

In the original version of the model described in [91] the activation energy of OOQOOH isomerization reaction R23 was set 3 kcal/mol lower (out of approximately 25 kcal/mol) than that of ROO isomerization to QOOH R12^1. The reasoning is based on the fact that the H-atom transferred is attached to a C-atom bound to a OH group and therefore it should be transferred readily. As an illustration Figure 4.13 shows the agreement between the experimental data and the original model prediction for 250 mol/m^3 and $\phi = 3$. The model predicts a much shorter ignition delay for the whole temperature range. In a later version of the model [103], the activation energy of R23 was set equal to that of R12 in order to achieve better agreement with the experimental data even though this modification is not physically sound (as explained above the second reaction should have a lower barrier). This modification improves the prediction of present study's experimental data too as Figure 4.13 shows. The improvement concerns the low and intermediate temperatures since the R23 path is only active at this temperature range. At higher temperatures though the model still predicts shorter ignition delay. A thorough sensitivity analysis was carried out in order to identify the chemical pathways leading to autoignition at different temperature ranges. A typical case with $\phi = 3$ and 250 mol/m^3 was investigated at 686 K, 765 K and 894 K. The activation energy of each of the reactions involved was increased by 3 kcal/mol and the sensitivity of the ignition delay was recorded. Some results are depicted in Figure 4.14. Paths known to be active at high temperatures like R and ROO decomposition (the other high temperature route $R+O_2 = Q+HOO$ is not active for small hydrocarbons like n-butane in the present model) increase the ignition delay at high temperatures without affecting the low temperature chemistry. The effects are fairly small though. In addition, the latter path requires modification in species thermal properties to show a trend (modification of forward or reverse rate constant only). Significant paths at low temperatures like ROO and OOQOOH isomerization or ROOH decomposition have no impact at high temperatures as expected. Looking at H-atom abstraction from the parent fuel molecules, it was found out that H abstraction with HOO affects significantly the ignition delay at high temperatures with the impact diminishing as the tempera-

---

1. R23 and R12 correspond to the reaction notation followed by the authors of the original model.

ture drops. H-atom abstraction from the fuel with HOO is dominant only under high-pressure, high-temperature conditions because then HOO is abundant and can proceed regardless its high activation energy compared to other abstraction reactions (e.g. $E_{act,HOO} \cong 20$ kcal/mol, $E_{act,OH} \cong 1.5$ kcal/mol). The importance of this reaction has been also reported for fuel-rich mixtures by Westbrook and Dryer [104]. Coupled with HOO formation and HOOH decomposition, it can be part of a chain-branching loop:

$H+O_2+M = HOO+M$	high pressure
$RH+HOO = R+HOOH$	fuel-rich mixture
$HOOH+M = OH+OH+M$	high temperature

According to this scheme one radical (H) with a parent fuel molecule and an oxygen result in three very reactive radicals (R and two OH).

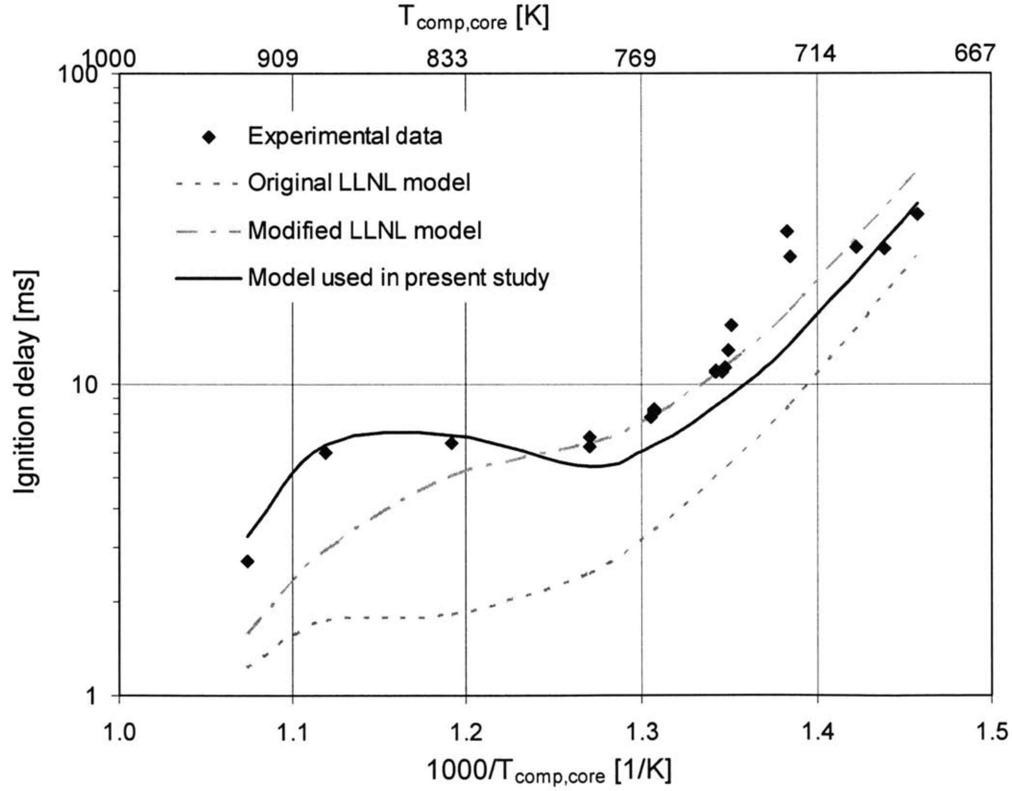

Figure 4.13 Ignition delay predictions of n-butane/Ar/O_2 mixture (Ar/O_2 = 3.773) with different kinetic models for 250 mol/m^3 and $\phi = 3$.

Since H-atom abstraction has also a small impact on low temperature ignition delay, the activation energies of OOQOOH and QOOH isomerizations do not need to be the exactly the same in order to achieve good correlation with the data. In the present study, the activation energy difference between these two isomerizations was set to 1.5 kcal/mol, which is between the two figures suggested in the previous models, while the activation energy of H-atom abstraction from the fuel by HOO was increased by 3 kcal/mol. The resulting model agreement is shown in Figure 4.13 and it is better than the previous models at the whole temperature range especially if heat transfer was taken into account for long ignition delays. The calculated ignition delay results shown in the previous section correspond to the model with these two modifications.

The trends of ignition delay with fuel-air equivalence ratio, the NTC region and the effect of pressure on NTC region are reproduced by the model reasonably well. Also, the trends on ignition delay by adding toluene and DME to the base fuel are sufficiently predicted. The prediction deteriorates slightly as the mixture gets even richer, suggesting that there may be other chemical paths becoming more active under such conditions, which have not been extensively studied so far. As stated in the modeling assumptions section, the agreement is expected to become worse for ignition delays higher than 10 ms (due to heat transfer) and lower than 2 ms (due to pre end-of-compression reactions). Taking into account the results of Figure 4.1, the predictions under such conditions are expected to become even better if variable core volume was taken into account.

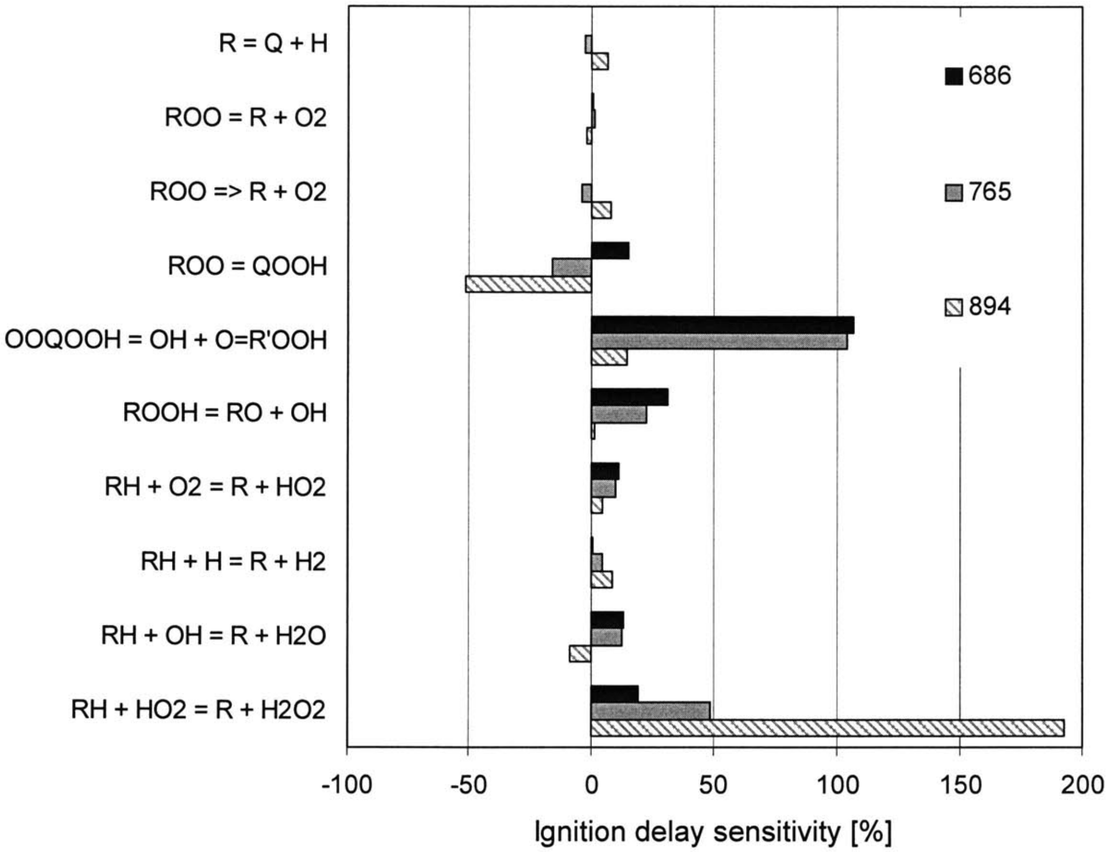

Figure 4.14 Ignition delay sensitivity analysis of n-butane/Ar/O_2 mixture (Ar/O_2 = 3.773) for 250 mol/m^3 and $\phi = 3$.

Chapter 5

Rate of Heat Release Study

5.1 Introduction

Numerous experimental studies of hydrocarbon oxidation have been conducted using either a RCM or a shock tube focusing on the ignition delay characteristics of various fuels. Such experimental data, like those reported in Chapter 4, encouraged computational efforts resulting to both detailed [91] and reduced [100] chemical kinetics models, some of which have been already mentioned. These models predict accurately enough the experimentally observed ignition delays and seem to describe the relevant chemistry sufficiently well. However, only a limited number of data have been reported in the literature on heat release rates. Such data are of particular interest because energy release rates could determine species formation and consumption rates. Especially in practical combustion systems like engines, where competing processes are involved, heat release rates could provide some insight into the dominant chemical pathways. The performance of most chemical kinetic models on the rate of heat release has barely ever been tested. They have been validated only under certain conditions of low pressure in highly diluted isothermal burners, where species concentrations can be directly measured with sufficient accuracy [105]. There are essentially two reasons why the literature lacks heat release data especially at high-pressure conditions. First, the kinetic rates under such conditions could be too high to be measured accurately. Second, uncertainties in the mixture and temperature environment could determine the measured rates. Even though such uncertainties are eliminated in a shock tube, this device apart from often using diluted mixtures, it is not capable of keeping a constant volume environment when pressure increases.

A RCM, as opposed to an engine, with its well-controlled conditions could overcome to some extent these uncertainties. However, recent studies have reported that the temperature field after the end of compression of a RCM might not be entirely uniform. Clarkson et al. [95] imaged the temperature field after the end of compression of a RCM using 2-D LIF of acetone and Griffiths et al. [106] measured it with 1-D Rayleigh scattering. Both studies, which were performed in the same RCM, concluded that due to the transport to the wall boundary layer by the roll-up vortex, there must be a cooler core in the center of the combustion chamber that may be depressed by 60 K. Griffiths et al. [72] performed CFD calculations that predicted a similar temperature stratification. Lee et al. [107] also predicted a lack of temperature uniformity at the end of compression generated by the piston motion shearing gas off the wall and creating a roll up vortex. However, the corner vortex remained confined very close to the wall without penetrating much into the center of the combustion chamber. A possible explanation of this could be the different RCM designs and especially the lower bore/stroke ratio used in Griffiths' RCM.

One objective of this study was to provide rate of heat release data for fuel-rich hydrocarbon mixtures under high-pressure conditions, where the rates are fast, using a RCM. Understanding heat release rates under fuel-rich conditions is essential for gaining insight into and modeling the soot particle formation process. These rates were compared to available chemical kinetic models and the effects of temperature stratification within the RCM, on their predictive capability was assessed. A thorough sensitivity analysis was carried out and the most important chemical pathways during hydrocarbon oxidation were identified. The relevant contribution of these pathways for fuel-lean and fuel-rich mixtures was also evaluated.

5.2 Singlezone Approach

The singlezone approach assumes that the core extends to the entire combustion chamber of the RCM. In the other words, the charge is spatially uniform and there is no temperature stratification across the chamber volume. Furthermore, no heat transfer to the cold cylinder walls is considered. Similarly to the ignition delay study, the Senkin application of Chemkin-II was used for computing the time histories of species, pressure and temperature right after the end of compression assuming an adiabatic and homogeneous system. The volume was fixed and experimental compression pressure and computed temperature (as already described in Chapter 3) where used as the starting conditions for the simulations. These assumptions were also made for ignition delay prediction, which was described in Chapter 4. The resulting correlation with the experimental data turned out to be fairly good since the core largely determined the autoignition behavior of the mixture. In this section the validity of this assumption was tested for the rate at which combustion proceeded, right after autoignition.

Figure 5.1 shows the correlation of both combustion time constants (5%-20% and 20%-80% pressure rise) between experimental data and singlezone model predictions. The predicted time constants are much lower than the experimental and especially the 20% to 80% constant is at least an order of magnitude off. This discrepancy is believed to be too high to be solely attributed to the chemical kinetic model.

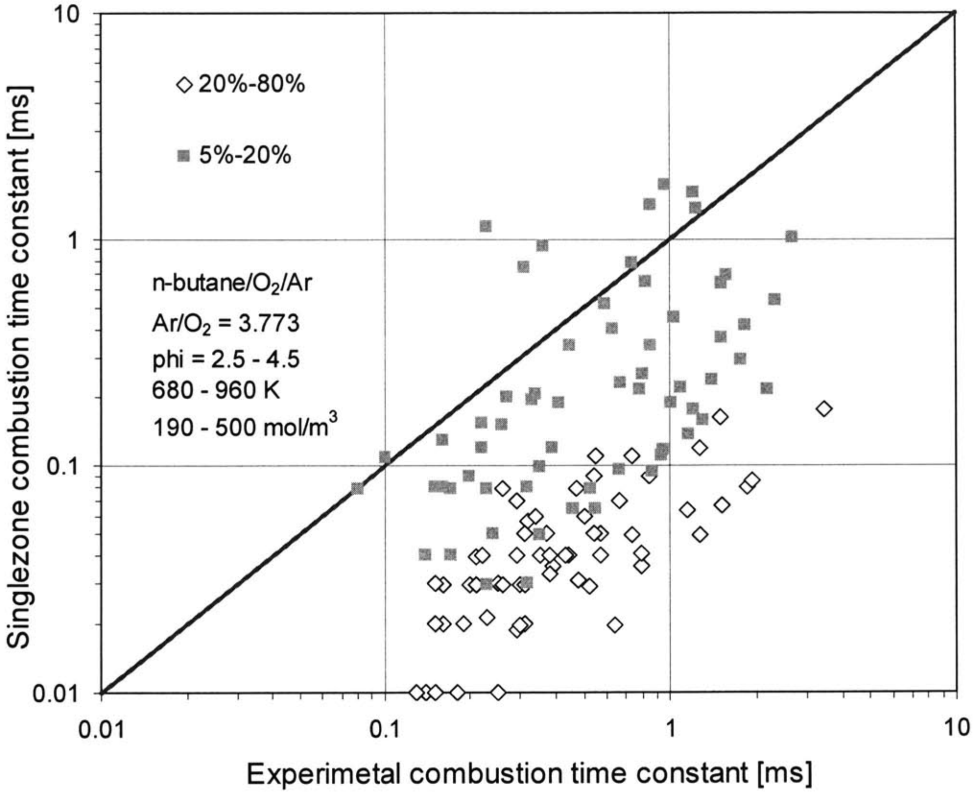

Figure 5.1 Combustion time constant correlation between singlezone model predictions and experimental data for most conditions tested.

One possible reason for such discrepancy could the temperature stratification resulting from the heat transfer process. As already discussed in the introduction previous studies have reported that the temperature field at the end of compression of a RCM might not be uniform. Then, temperature zones igniting at different timings could cause a slow pressure rise. The effect of thermal stratification on the measured pressure is mostly predominant when the singlezone heat release is very fast and the ignition delay is very sensitive to temperature. In other words, temperature non-uniformities could determine the pressure rise if:

$$\frac{\tau_{heat-release}}{\left(\frac{d\tau_{delay}}{dT}\right)\Delta T_{non-uniformity}} \ll 1$$

The numerator in the above relationship represents the singlezone heat release time constant (e.g the 20%-80% pressure rise) and the denominator, the ignition time difference between the first and last zones within the combustion chamber. Even though there should be a significant thermal feedback between the ignited and non-ignited zones due to compression, which would accelerate the pressure rise (as long as the system is not in the NTC regime), the above relationship could give an estimate of whether thermal stratification influences the measured pressure rise. This thermal feedback is the reason why the left hand side must be lower than unity for the non-uniformities to be significant. Figure 5.2 shows experimental data depicting the sensitivity of ignition delay to temperature. It is apparent that at around 800 K small temperature differences of 10 K could change the ignition delay by as much as 1 ms, with the effects being even more pronounced at lower temperatures. The heat release time constant under such conditions from Figure 5.1 is of the order of 0.1 ms or less. Therefore from the above relationship, non-uniformities of even less than 10 K could possibly affect the measured pressure rise. Along the same lines, temperature non-uniformities could limit the maximum pressure reached at the end of combustion. Charge at lower temperatures igniting later than the core could chemically freeze if it was pushed towards the wall or squeezed into the crevice as the ignited gas expands. Figure 5.3 shows the correlation between the predicted and experimental maximum pressure supporting this argument. The experimental maximum pressure is approximately 20% lower than the predicted. This discrepancy can be hardly attributed to uncertain species thermal properties. Even though the thermal properties of the species in the soot model were approximate, their mole fractions were too low to affect significantly the energy balance. Hence, the degree of temperature non-uniformities for this particular RCM design needed to be assessed, as it may be a determining factor in the measured rate of pressure rise and maximum pressure.

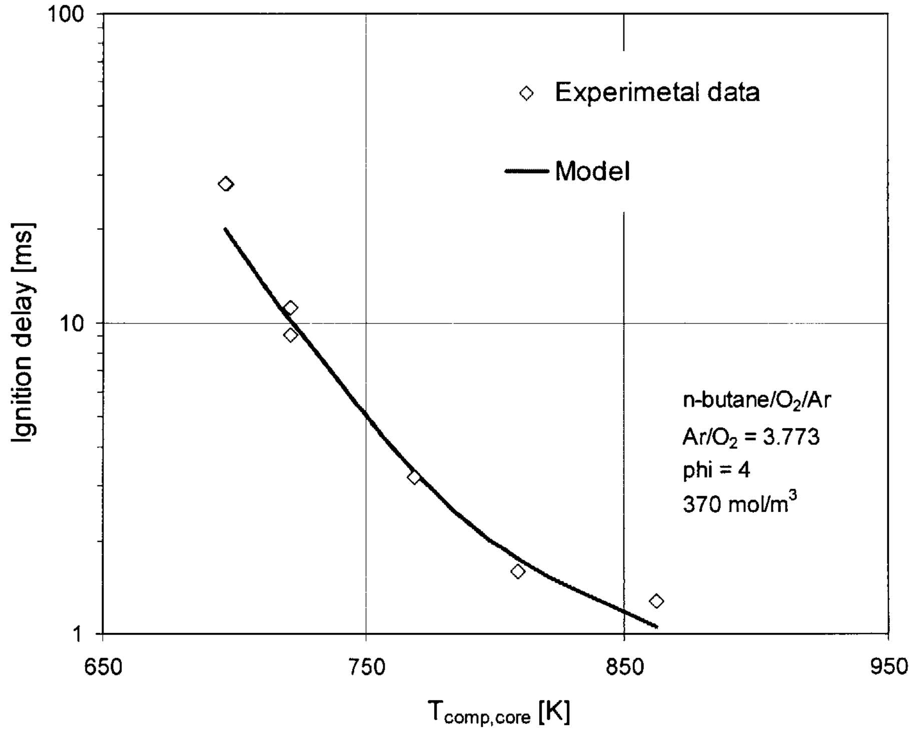

Figure 5.2 Ignition delay sensitivity to compressed core temperature.

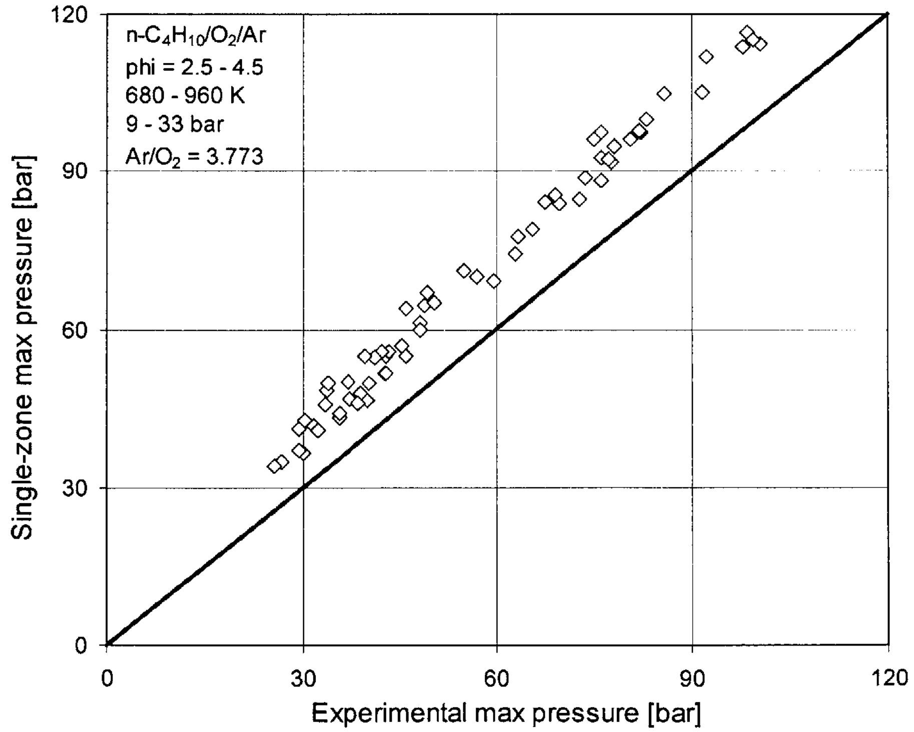

Figure 5.3 Maximum pressure correlation between singlezone model predictions and experiments for most conditions tested.

5.3 CFD Analysis

Even though charge spatial uniformity within the RCM can be claimed based on the accurate mixture preparation process before the start of compression, thermal non-uniformities could be most likely induced by the turbulent nature of the rapid compression. Scraping the boundary layer off the wall by the piston during the compression resulting in a vortex penetrating into the core has been previously reported [107]. To assess the extent of charge thermal stratification at the end of compression in the RCM, the compression process was modeled using the KIVA-3 CFD code [108] under non-reacting conditions. The code was used in its original form ($k-\varepsilon$ turbulence model, law of the wall boundary layer) and the speed was set to 2000 rpm, which corresponds to 15 ms compression time. The exact combustion chamber geometry including the piston crevice, which was 3.1% of the total volume at the end of compression was reproduced with a simple 2-D mesh. Axisymmetry was assumed allowing a good resolution near the walls. To adequately resolve the boundary layer a grid spacing of 0.08 mm was employed in the boundary layer (in the direction perpendicular to the walls), while the mesh points were more coarsely spaced in the core region. The grid details used in this study are depicted in Figure 5.4.

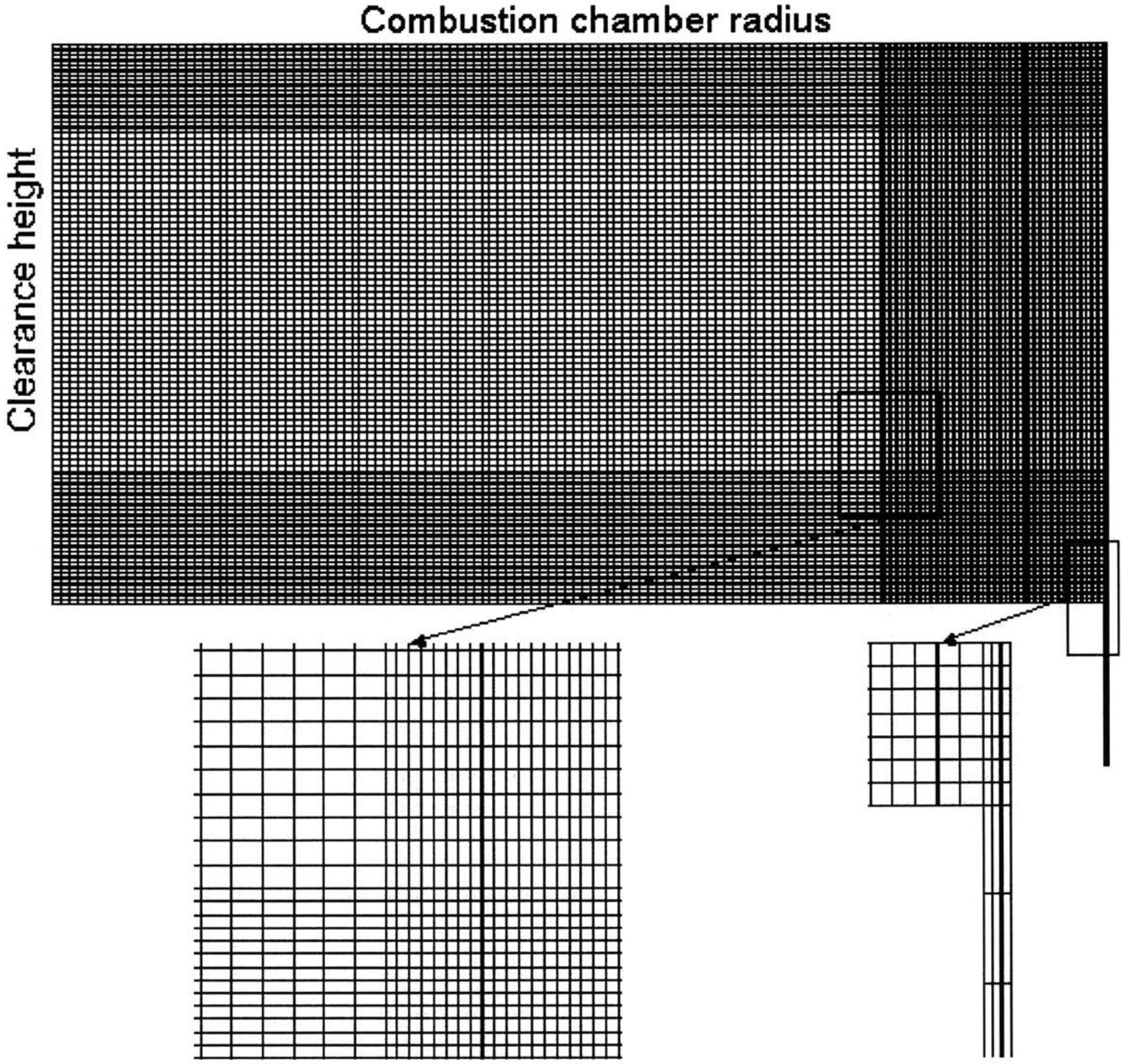

Figure 5.4 Grid at the end of compression for the RCM

Before analyzing the temperature distribution obtained at the end of compression, the correlation between the experimental and predicted compression pressure for non-reacting mixtures was checked. Figure 5.5 shows the agreement for 5 cases using different inert gas compositions, while keeping the diluent/O ratio at 3.773, like in air and constant initial conditions: 0.5 bar, 293 K. The figure illustrates that the compression pressure is sufficiently reproduced.

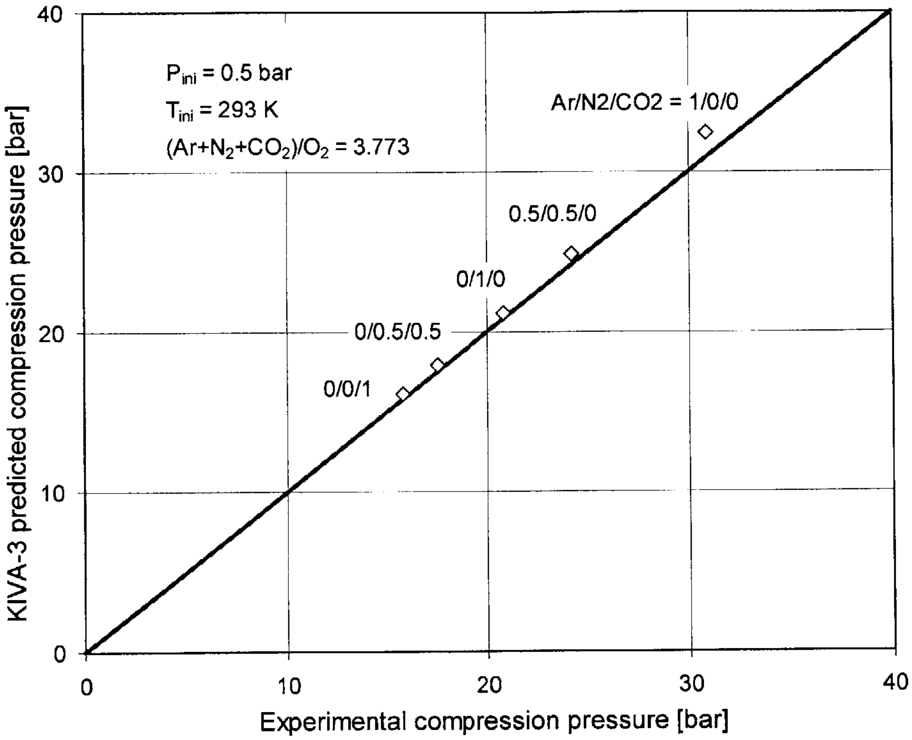

Figure 5.5 Compression pressure correlation between KIVA-3 predictions and experiments for non-reacting mixtures.

Figure 5.6 shows the temperature distribution obtained at the end of compression for air using the above initial conditions. The 90% boundary layer is less than 0.7 mm and the roll-up vortex seems to penetrate well into the core. The velocity vectors displayed also in Figure 5.6 explain the shape of the temperature contours and vortex penetration for the particular RCM geometry. Since the stroke is relatively long and the crevice volume quite small, the vortex cannot be contained inside or stay close to the crevice. Sensitivity analysis performed on the combustion chamber geometry found out that the temperature field and the vortex shape are very sensitive to the stroke and the crevice volume. Shorter strokes resulted in a much smaller vortex confined very close to the wall. Crevices big enough to contain the entire roll-up vortex created a more uniform temperature field as previously reported [71]. The effects of combustion chamber geometry on the resulting temperature field at the end of compression as calculated with CFD are reported in Appendix B. The sensitivity of all above KIVA-3 results to grid spacing was also studied. One parameter that was found to be sensitive to grid dimensions was the penetration of the roll-up vortex into the combustion chamber. Figure 5.7 shows the penetration length as a function of grid spacing by the wall normalized to the length obtained with the coarser grid tested (0.3 mm). It is obvious that using grid spacing by the wall of 0.08 mm is sufficient. This is the grid spacing employed throughout the entire study.

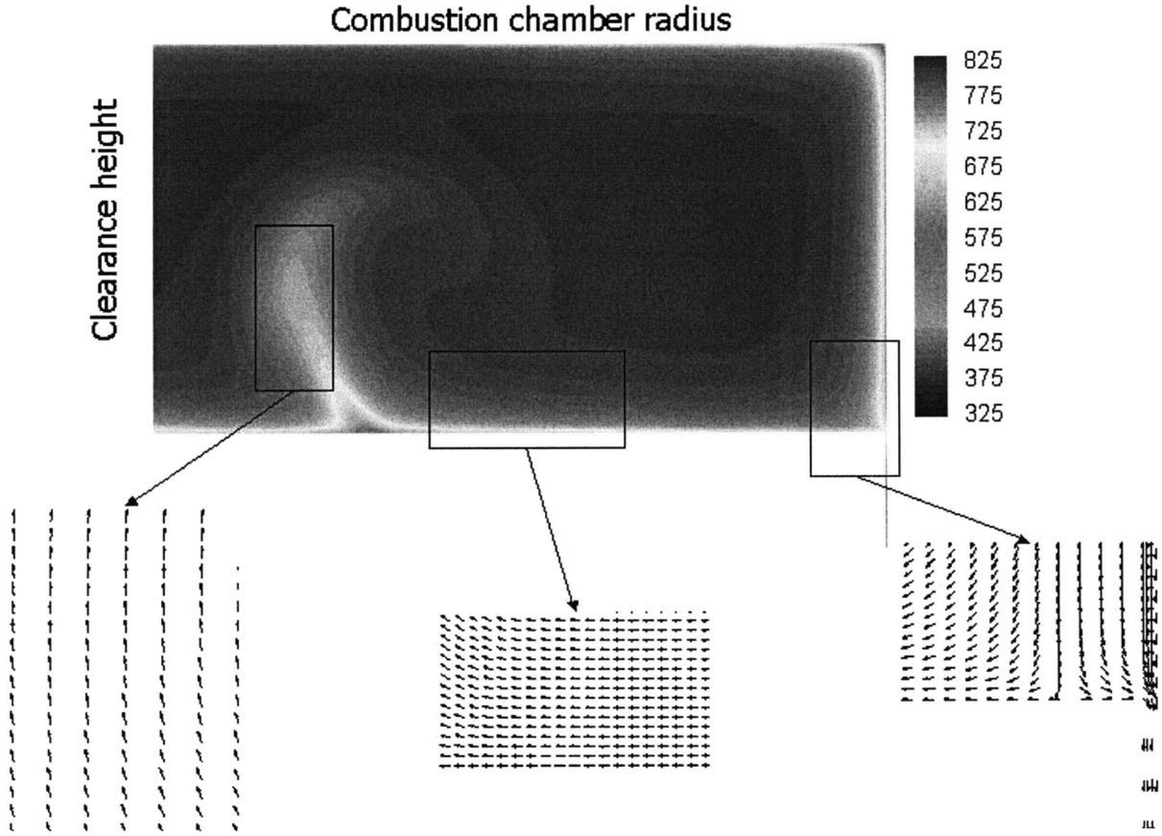

Figure 5.6 KIVA-3 prediction of temperature and velocity field at the end of compression.

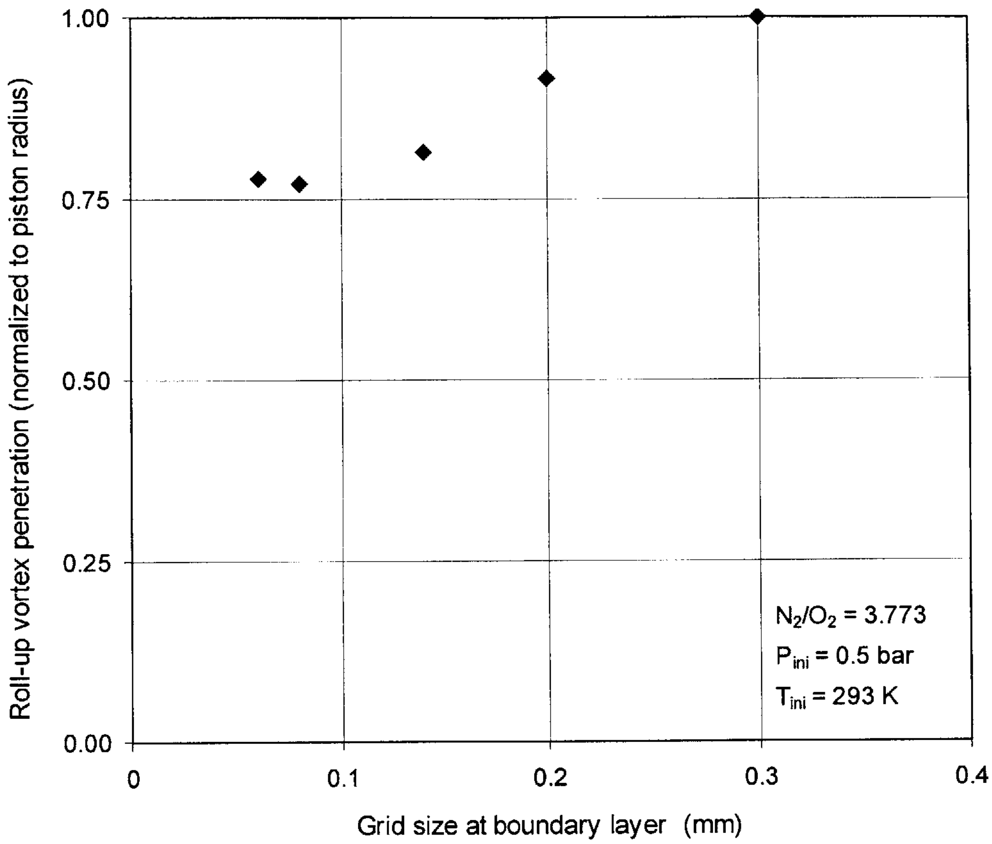

Figure 5.7 KIVA-3 sensitivity to grid size.

The resulting picture of the temperature distribution was converted into a temperature-mass distribution and is depicted in Figure 5.8 with a solid line. There is a core containing approximately 80% of the mass, which is almost adiabatic extending to a 50 K temperature range. Around 13% of the mass is at a much lower temperature very close to the wall and the rest 7% is squeezed inside the crevice. Even though the temperature-mass distribution suggests that there is a significant amount of mass at almost the same temperature, the rapid heat release rates and the high sensitivity of ignition delay to temperature at the conditions studied here, imply that multiple ignition zones are very likely to occur. Therefore, to study heat release rates in a RCM, a simple singlezone model is not sufficient and a more sophisticated model including temperature-mass distribution needs to be incorporated.

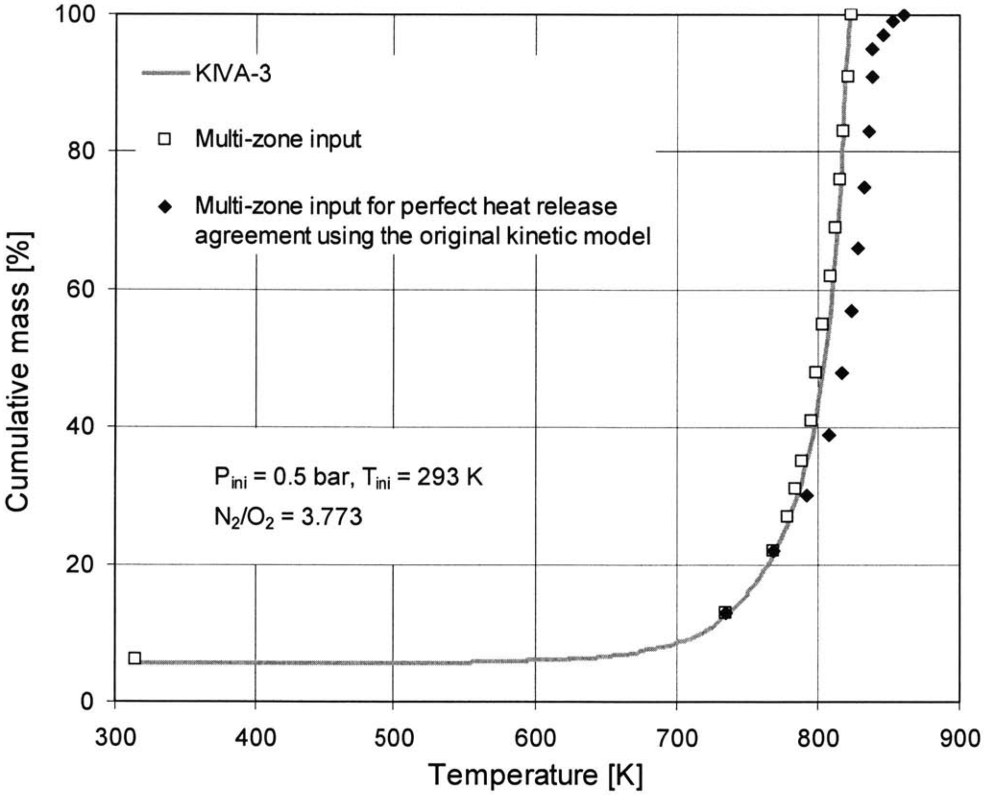

Figure 5.8 KIVA-3 prediction and zone discretization of temperature-mass distribution at the end of compression.

5.4 Multizone Approach

Considering temperature non-uniformities across the combustion chamber volume of the RCM introduces substantial complexity to the analysis. A comprehensive model combining CFD analysis and chemical kinetics during the entire compression process should be in principle developed. However, the simultaneous calculation of fluid dynamics and chemical kinetics is beyond the current computational capability especially for detailed chemistry involving species up to soot particles used in the present study. Aceves et al. [109] gave a great overview of the capabilities of current computers with respect to the actual problem that needs to be solved. Most recent related research has been reported in the HCCI literature. The RCM is essentially an HCCI engine working at fuel-rich conditions (in this study) with the piston locked at the end of compression. In view of the fact that not significant reactions take place before the final stages of compression, most modeling efforts uncoupled CFD and chemistry. The CFD code predicts the temperature distribution during the major part of compression and then the chemical kinetics solver takes over. The output of the CFD code is discretized in temperature zones, which are treated as individual well-stirred reactors by the chemical kinetics solver, allowing work transfer between them.

The multizone approach followed in this study is very similar to that proposed by Yelvington et al. [110]. The only differences concern the KIVA-3 temperature distribution scaling method and the heat transfer and crevice models, which are described in detail below. Yelvington's method was an extension of Aceves' method in that a faster numerical solver is utilized evaluating analytical derivatives (as opposed to finite differences) using the DAEPACK software library.

An overview of the entire multi-zone model employed in this study is shown in Figure 5.9. From the conditions before the start of compression and the measured compression pressure, the core temperature can be calculated assuming an adiabatic core and using the isentropic relationship of ideal gases as explained in Chapter 3. Since KIVA-3 simulation is computationally intensive, only one calculation was performed and the temperature distribution for each test was scaled linearly with core and wall temperature according to the relationship:

$$T_j = T_{wall} + (T_{core} - T_{wall}) \frac{T_{KIVA,j} - T_{KIVA,wall}}{T_{KIVA,core} - T_{KIVA,wall}} \qquad j = 1, N_{zones}$$

In the above relationship T_j is the temperature at the end of compression of zone j and T_{wall} and T_{core} the wall and core temperatures respectively for a specific test. All kiva temperatures are produced from the single KIVA-3 run using air at 293 K and 0.5 bar before the start of compression. As a compromise of good resolution and computational time, the temperature-mass distribution predicted by KIVA-3 simulation was discretized in 15 zones. The details are shown in Figure 5.8 with open symbols along with the exact KIVA-3 distribution. Based on the assumption reported in previous studies and justified for not very short ignition delays in Chapter 4, the charge is chemically frozen up to the end of compression. After the end of compression the multizone model takes over, which includes a non-adiabatic and chemically reactive mixture. The set of equations solved for each zone j are the following:

Energy equation:

$$\bar{c}_{v,j}\cdot\frac{dT_j}{dt}+v_j\cdot\sum_{i=1}^{K}(\dot{\omega}_{ij}\cdot W_{ij}\cdot u_{ij})+Q_{conv,j}+P\frac{dv_j}{dt}+Q_{rad,j}=0$$

Species equations:

$$\rho_j\cdot\frac{dY_{ij}}{dt}-\dot{\omega}_{ij}\cdot W_{ij}=0 \quad i=1,Kspecies$$

Ideal gas law:

$$P-\rho_j R\left(\sum_{i=1}^{K}\frac{Y_{ij}}{W_{ij}}\right)T_j=0$$

Volume conservation (entire system):

$$\sum_{j=1}^{N}\frac{m_j}{\rho j}=const$$

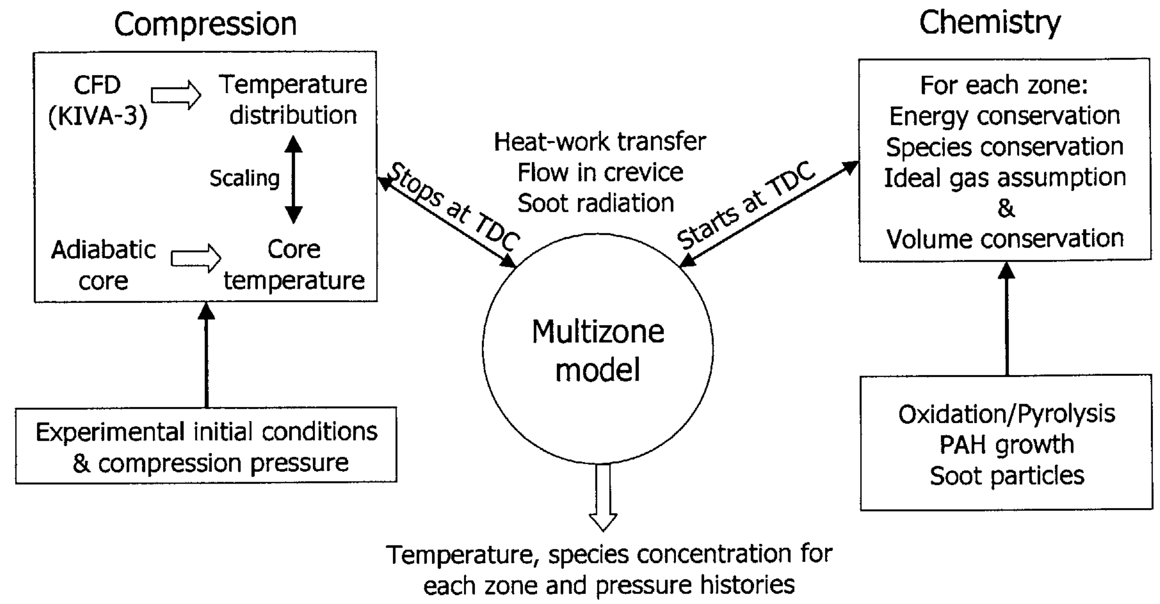

Figure 5.9 Multizone model overview

The heat transfer and crevice models are better explained in the schematic shown in Figure 5.10. Each zone has constant mass and is separated from its neighbor zones by mass-less pistons. As the energy equation shows, apart from work transfer the zones are also allowed to interact with each other by means of heat transfer too. The details of heat transfer depend on the location of each zone in the combustion chamber. The combustion chamber is divided into two areas: the main combustion chamber and the crevice. The crevice considered here is twice as big as the geometric crevice in order to account for the charge in direct contact with the cold walls but still in the main combustion chamber. As the core zones expand upon ignition, they push the rest zones towards the crevice. As soon as a zone enters the crevice, it starts exchanging heat with the wall (instead of its neighbor zones), its heat transfer coefficient increases and it chemically freezes. There is a gain and a loss energy component due to heat transfer for all zones outside the crevice:

$$Q_{conv,j} = h_j A_j (T_j - T_{j+1}) - h_{j-1} A_{j-1} (T_{j-1} - T_j)$$

Note that the second term is missing for the core zone and $T_{j+1} = T_{wall}$ for all zones inside the crevice. The zone area A_j is calculated assuming that all zones are cylindrical. The heat transfer coefficient is approximated by the Woschni correlation:

$$h_j = 3.26 L_j^{-0.2} P^{0.8} T_j^{-0.55} w_j^{0.8}$$

The characteristic length L_j is the volume to surface area of each zone. The velocity is set to 2 m/s and 4 m/s for outside and inside the crevice respectively. These are approximate figures based on the predicted velocity field by KIVA-3 at the end of compression.

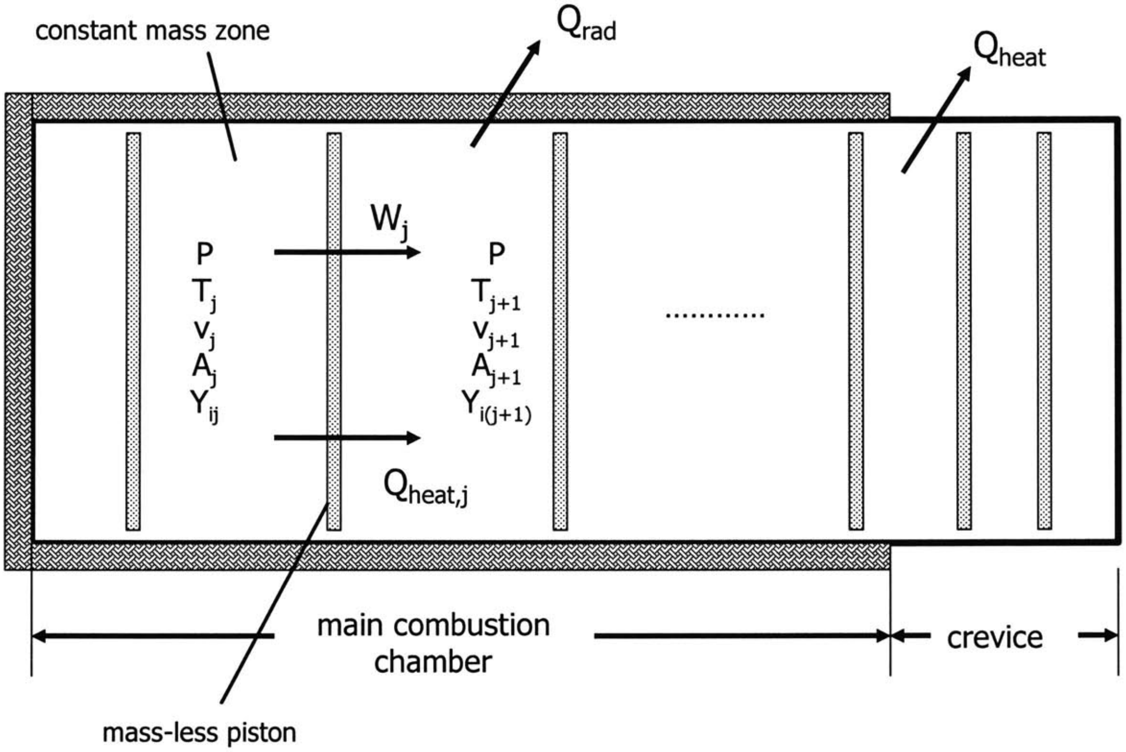

Figure 5.10 Multizone model details

To test the heat transfer model, the experimental and predicted pressure histories were compared after the end of compression for non-reacting mixtures. Figure 5.11 shows the correlation for different inert gases like CO_2, N_2 and Ar. The molar ratio of inert gas to oxygen was set to 3.773 like in air. The calculated core temperature is also shown on the graph. The heat transfer process seems to be sufficiently well predicted with this simple model especially when the core temperature at the end of compression is close to the temperature range of interest in this study (~800 K).

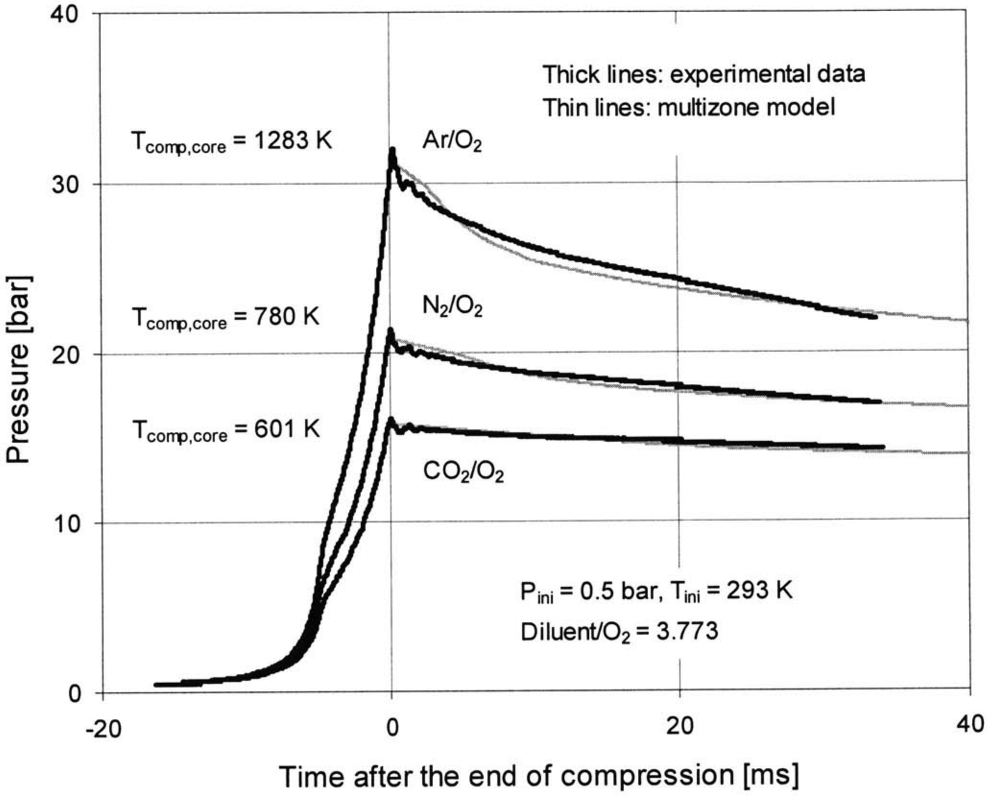

Figure 5.11 Heat transfer-crevice model validation

The fuel-rich mixtures used in this study lead to soot formation, hence heat transfer by soot particle radiation should be in principle included in the model. The radiation term of the energy equation is given by:

$$Q_{rad,j} = \varepsilon_j \sigma A_{rad,j} T_{p,j}$$

In the above relationship, ε_j is the soot emissivity, σ the Planck constant, $A_{rad,j}$ the heat exchange area due to radiation and $T_{p,j}$ the soot particle temperature, which is assumed to be the same with the surrounding gas temperature since the particles are small. For very low particle number concentrations $A_{rad,j}$ can be approximated by the total particle surface area. However, $A_{rad,j}$ is lower than the total particle surface area for high number concentrations since part of the radiation cannot escape. The upper limit in that case would be the total surface area of the combustion chamber, which is obtained by projecting on it all combustion generated soot particles. The soot emissivity is related to the extinction coefficient according to [111]:

$$\varepsilon_j = 1 - \exp(-k_{ext,j} D)$$

where D is the combustion chamber diameter. The extinction coefficient $k_{ext,j}$ has been defined in Section 3.2

$$k_{ext,j} = \frac{6\pi}{\lambda} Im\left(\frac{m^2 - 1}{m^2 + 2}\right) f_{v,j}$$

where $m = n - ik$ is the complex refractive index of soot, λ the wavelength and $f_{v,j}$ the soot volume fraction. Taking the spectral average extinction coefficient according to [112], the above relationship reads:

$$k_{ext,j} = 3.72 f_{v,j} C_0 T_j / C_2$$

where $C_0 = 3.63$ (for an average refractive index suggested by Lee and Tien) and $C_2 = 1.4388$ cmK.

The relationship between soot emissivity and $f_{v,j}$ is graphically shown in Figure 5.12 for a typical temperature of 2000 K. It is apparent that soot emissivity is very close to unity for soot volume fractions greater than 30 cm^3/m^3. Since the final soot volume fraction in most experiments is larger than 100 cm^3/m^3, it is sufficient for simplicity to assume that the soot emissivity is unity during the whole soot formation process. Since the charge is discretized in zones, the soot radiation term is included in the energy equation of the outer zone only forming substantial amounts of soot. To sum up, the parameters shown in the radiation term take the following values:

$$\varepsilon_j = 1.0$$

$$\sigma = 5.67$$

$$T_{p,j} = T_j$$

$$A_{rad,j} = min(A_{cc}, A_p)$$

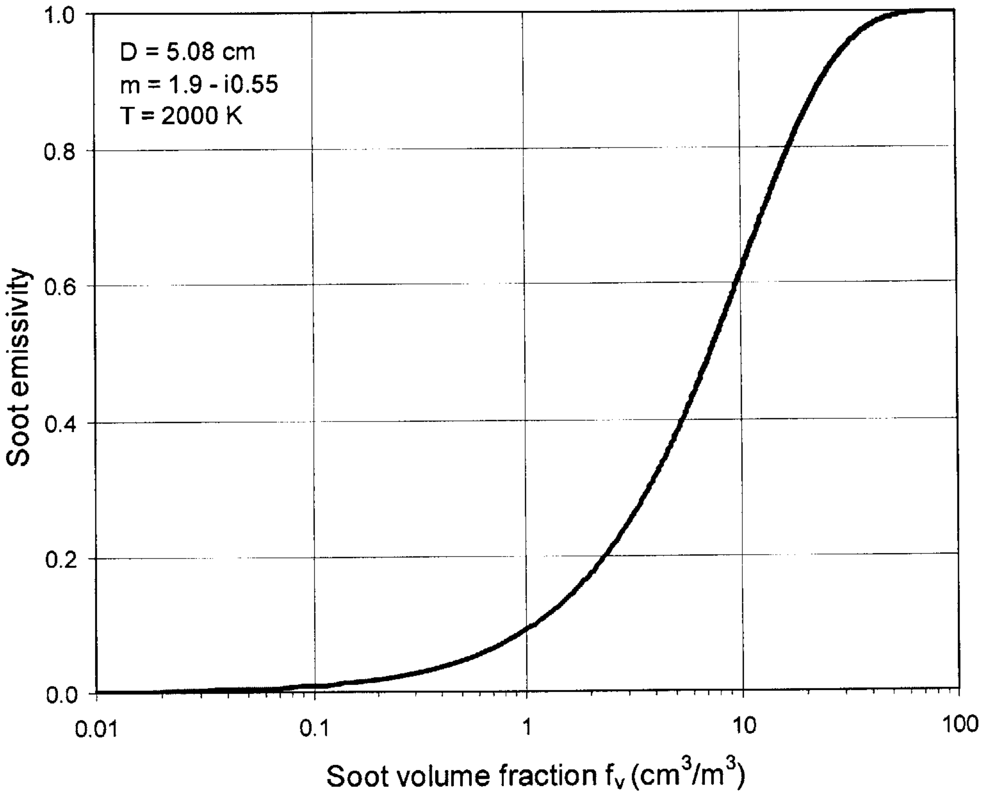

Figure 5.12 Soot emissivity dependence on soot volume fraction

5.5 Multizone Model Results

The entire multizone model consists of chemically reactive systems, heat transfer by convection and radiation and flow into the crevice. A sample problem, including 498 species, 5734 reactions and 15 zones, is solved within one hour on a 3.2 GHz Pentium IV computer running Linux.

A typical case pressure history ($\phi = 4$, compression conditions: 750 K, 250 mol/m^3) predicted by the model is shown in Figure 5.13 and compared against the singlezone model output. On the same graph, the experimentally obtained pressure trace is also depicted. Since the ignition delay was not exactly the same, to clearly compare the rate of pressure rise, the 50% pressure rise points have been matched. The agreement between the experiment and the model has improved significantly as far as both maximum pressure and rate of heat release when the multizone model is used. The discrepancy in the early stage of heat release is discussed below. Figure 5.14 and Figure 5.15 show predicted zone temperatures and their cumulative volumes respectively. Figure 5.14 clearly demonstrates that even though the rate of heat release of each individual zone is fast, the overall pressure rise is slow because of different ignition timings. As pointed in the single-zone section however, there is a substantial thermal feedback between the burning-expanding and unburned-compressed zones, which accelerates the rate. Some zones do not ignite because of their low temperature at the end of compression or due to the high heat transfer coefficient assigned next to the wall. As Figure 5.15 shows, after the ignition of the core zones, the zones closer to the walls are pushed towards the crevice where they may chemically freeze and as a result, the maximum pressure is lower and the rate of pressure drop after the end of combustion increases. To realize the contribution of each individual term in the energy equation, the magnitudes of chemical energy release, work and heat transfer (both by convection and radiation) of the first-igniting zone are shown in Figure 5.16 for the typical case studied in Figure 5.13. Initially there is a balance between convective heat losses and chemical energy release. Upon ignition the dominant term in the energy equation is the chemical energy release. Therefore, the rate of heat release of each individual zone is determined exclusively by chemistry. Then, there is some work transfer to the other zones because of expansion and later from the other igniting zones. Soot radiation reaches a maximum rapidly when the particle surface area equals the combustion chamber area and then drops to zero when substantial amounts of soot are formed in a zone closer to the walls blocking radiation escaping from the zone shown.

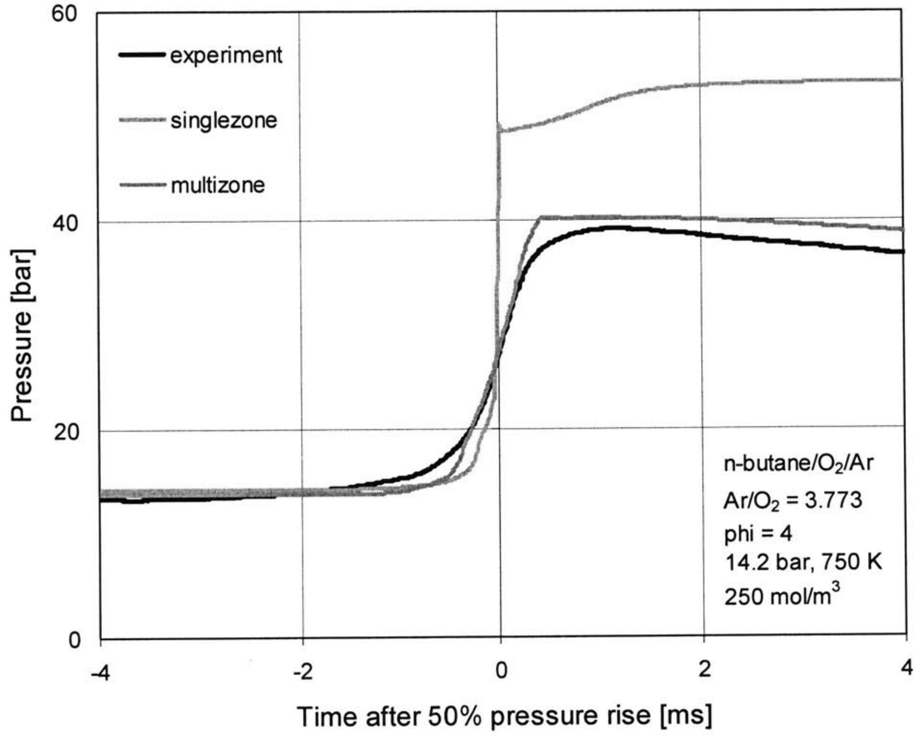

Figure 5.13 Pressure history prediction with single- and multizone model along with the corresponding experimental data

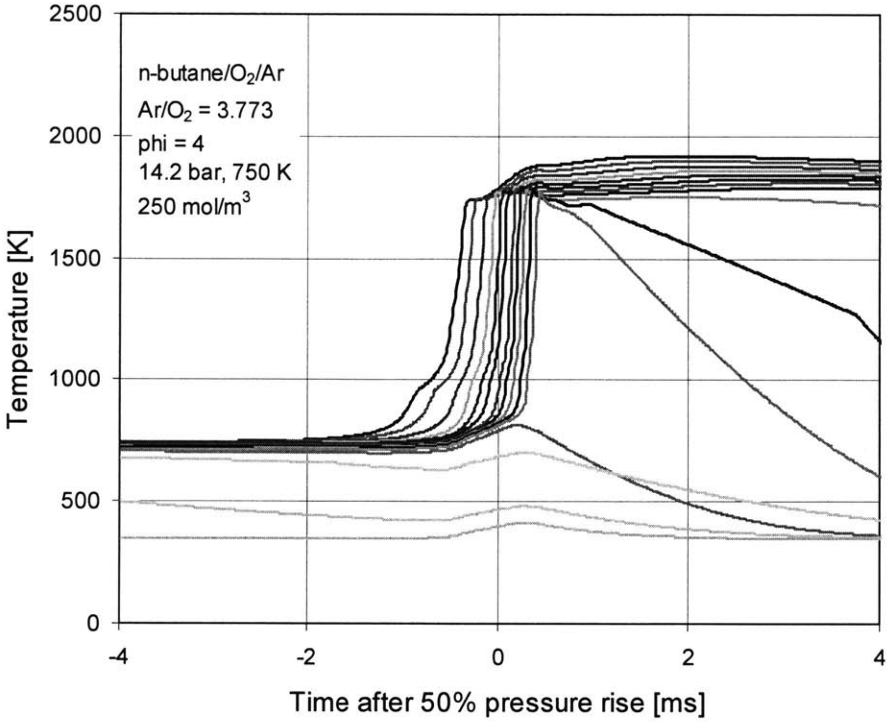

Figure 5.14 Temperature history predictions with multizone model

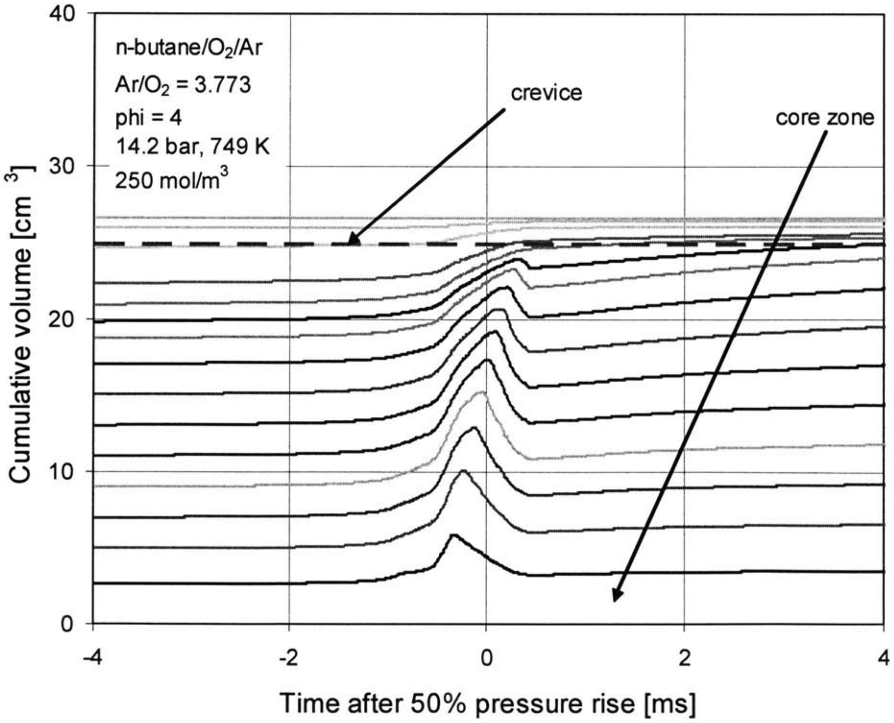

Figure 5.15 Cumulative volume history predictions with multizone model

As already shown in Figure 5.13, the correlation between the experimental and the predicted maximum pressure is fairly good when the multizone model is employed. Figure 5.17 shows this correlation for most tests conducted for the purpose of this study. As opposed to the prediction obtained with the singlezone model and shown in Figure 5.3, the multizone model can sufficiently predict the maximum pressure observed experimentally under most conditions studied. The improved agreement is mostly attributed to the fact that the multizone model allows for flow into the crevice.

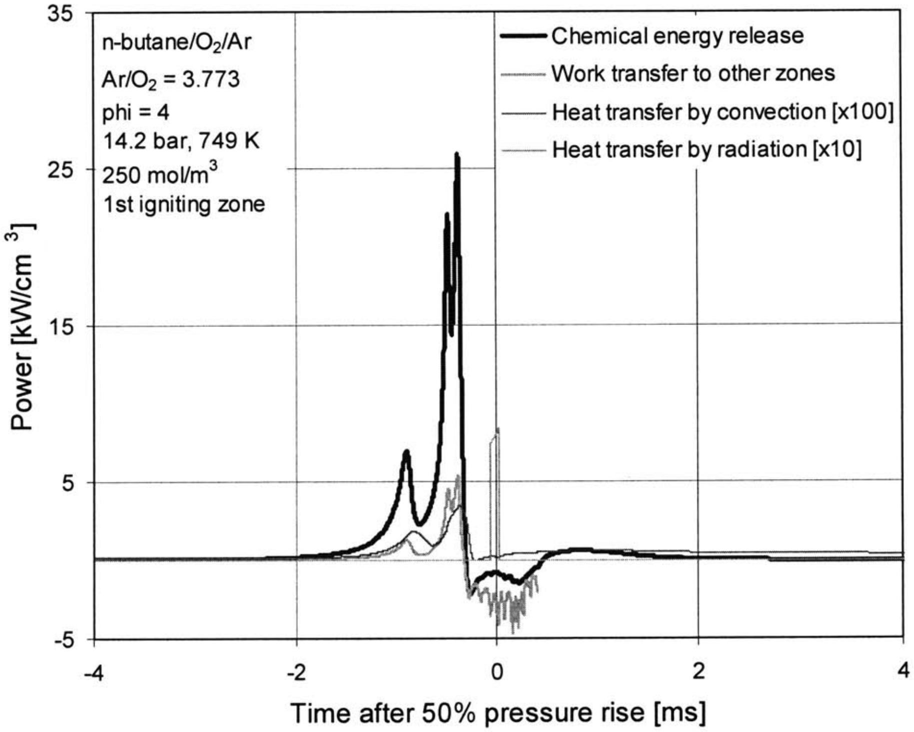

Figure 5.16 Chemical energy release, work transfer and heat transfer by convection and radiation of the first igniting zone as predicted by the multizone model.

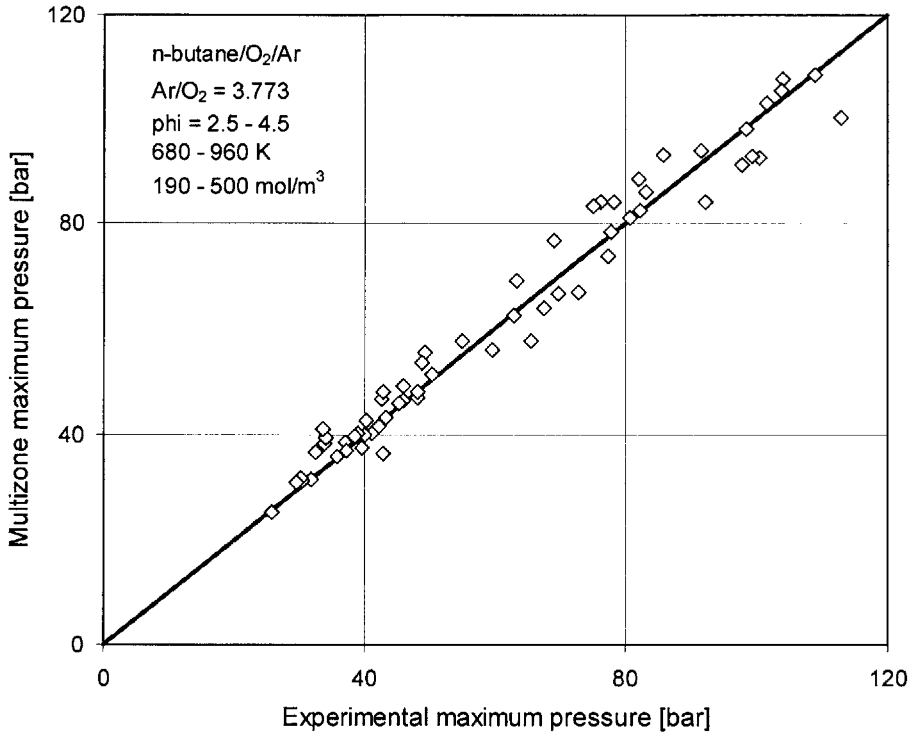

Figure 5.17 Maximum pressure correlation between multizone model predictions and experiments for most conditions tested.

The temperature stratification assumed by the multi-zone model improves significantly the agreement between the experimental and predicted 20-80% combustion time constant. However as Figure 5.13 suggests, the agreement for the 5%-20% combustion time constant does not improve much. This is mostly apparent when comparing Figure 5.1 and Figure 5.18, which show the correlations of both combustion time constants for all tests studied with the single and multizone models respectively. It is believed that the discrepancy in the 5%-20% combustion time constant is related to the chemical kinetic model itself rather than the temperature stratification and the multiple ignition timings. During the very early stage, heat release is mostly determined by kinetics and the model behaves as in the singlezone approach, while at later stages the heat release is governed by temperature stratification and therefore the multizone approach gives a better prediction. To support this argument, different temperature-mass distributions were tested that would give a heat release history as close as possible to the experimental one keeping the chemical kinetic model intact. Such distribution (assuming again 15 zones) is shown in Figure 5.8 with closed symbols. Even though CFD calculations cannot be precise and a certain amount of simplifications need to be made, the distribution required at the end of compression for perfect heat release agreement is very unlikely to occur. Such mass-temperature distribution implies the existence of a very small amount of mass at very high temperature compared to the rest of the core. Therefore the details of the chemical kinetic model need to be addressed more extensively.

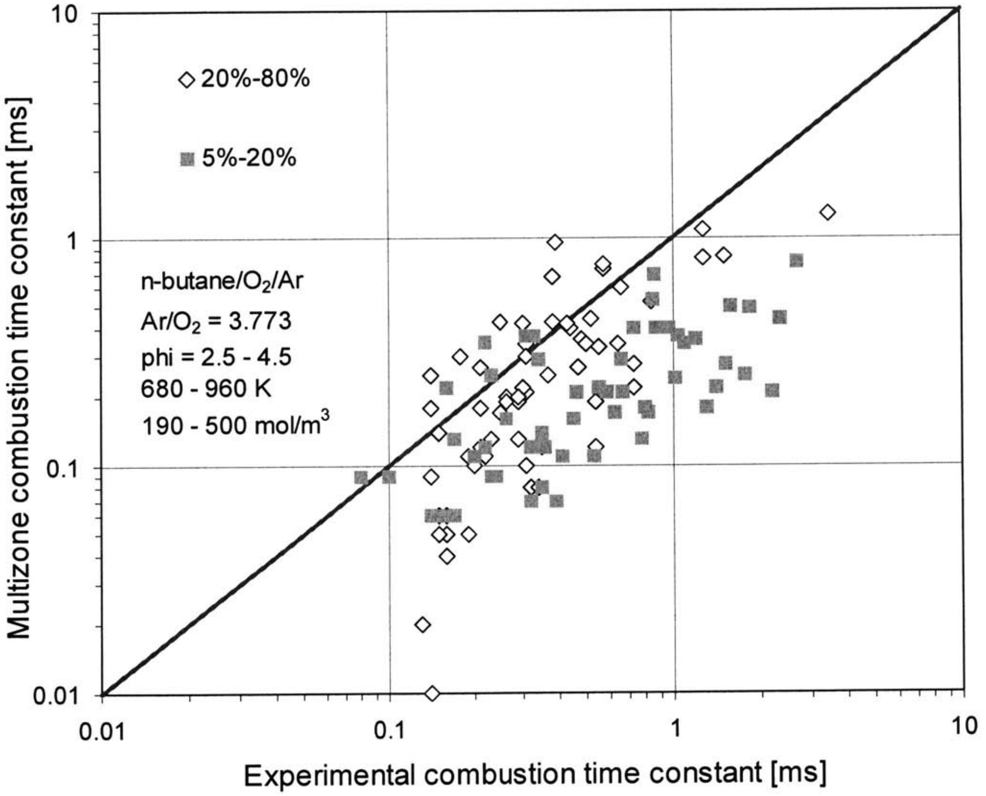

Figure 5.18 Combustion time constant correlation between multizone model predictions and experiments for all conditions tested.

5.6 Chemical kinetic Model Sensitivity Analysis

As already discussed in the introduction, most of the chemical kinetics models have been tested against ignition delay data and no further validation for heat release rates have been reported. This is particularly true for the fuel-rich mixtures and high-pressure conditions employed in this study. Since it has been previously reported that chemical pathways might actually change under different conditions [104], a detailed analysis was carried out to investigate how the heat release critical pathways change under high-pressure conditions as a fuel-lean mixture becomes fuel-rich. The sensitivity analysis was performed by multiplying the pre-exponential factor of the rate constant of certain reactions by 2, while keeping the equilibrium constant the same, and then calculating the percent change in the 20%- 80% combustion time constant. This combustion time constant, which describes the rate of heat release right after hot ignition (HOOH decomposition), gives a more generic picture of the chemical pathways involved under lean and rich mixtures. The 5%-20% time constant on the other hand, depends a lot on the specific temperature regime since the kinetics are governed a lot by the ignition delay chemistry. Therefore, to safely draw some preliminary conclusions about heat release rates, the sensitivity of the 20%-80% combustion time constant was thoroughly studied. The compression conditions employed for this analysis were 750 K and 14.2 bar (case studied also in Figure 5.13) and the fuel-air equivalence ratio was set to 4 (fuel-rich case) and 0.4 (fuel-lean case). The reactions that exhibited the highest sensitivity are shown in Figure 5.19.

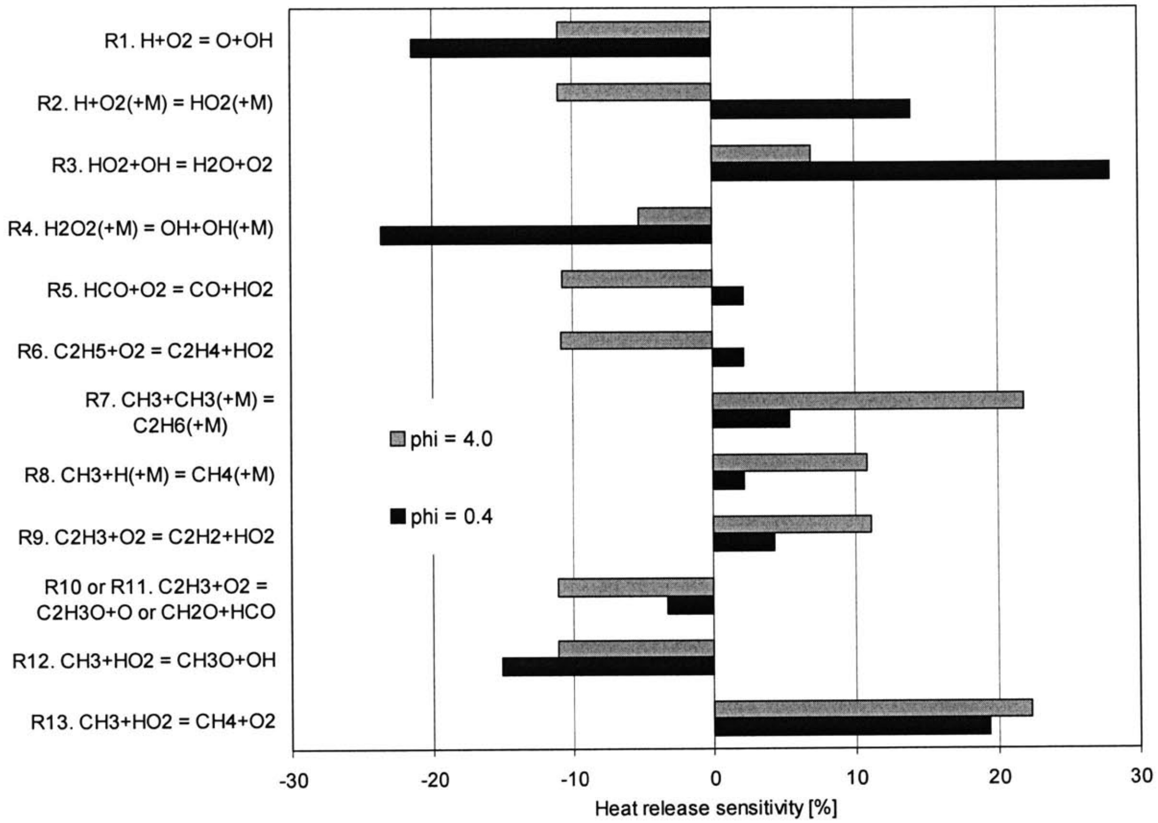

Figure 5.19 Ignition delay sensitivity analysis of n-butane/Ar/O_2 mixture (Ar/O_2 = 3.773) for 250 mol/m^3 and 750 K.

In the high-temperature, low-pressure combustion of fuel-lean hydrocarbon mixtures, R1 is the most important chain branching reaction. Along with O+H_2 and OH+H_2, it consumes one H-atom and it produces three. At higher pressures and especially at early stages when temperatures are not very high, R2 competes with R1 and slows down the rate. This is occurring because R2 along with HOO recombination and HOOH decomposition consumes two H-atoms and produces two OH radicals turning chain branching to chain propagation. Therefore, for high-pressure, fuel-lean mixtures these reactions compete. However, both reactions accelerate the oxidation of rich mixtures because in this case R2 could be part of chain branching along with fuel+HOO and HOOH decomposition, as already explained in Chapter 4. This is a significant reason why fuel-rich mixtures oxidize faster than fuel-lean mixtures at high pressures. Reactions R3 and R4 turn out to be more crucial under fuel-lean conditions and since they involve radical recombination and decomposition, they decelerate and accelerate the rate respectively. Reactions R5 and R6 were found to feed the system with significant amounts of HOO especially during the early stages of combustion. For the reasons explained earlier, HOO is mostly important under fuel-rich conditions hence, these reactions accelerate the oxidation rate only when significant amounts of fuel are included. Reactions R7 and R8 are important methyl radical (CH_3) sinks. Since CH_3 concentration is high only under fuel-rich conditions, these reactions do not have a substantial impact when the mixture is fuel-lean. The alternative channels of C_2H_3+O_2 (reactions R9-R11), has drawn a lot of attention in previous studies. Mebel et al. [113] suggested that the dominant path is pressure dependent and as pressure increases the formation of the relatively stable $C_2H_3O_2$ (not included in the LLNL model) is becoming important. Hughes et al. [114] proposed the total omission of R10 and R11, which would slow down the rate substantially but there is evidence that routes other than C_2H_2+HOO exist. Since R10 and R11 lead to active radical formation, increasing the rate of competition reaction R9, decelerates the overall rates. The impact of these reactions on the mechanism is mostly apparent for fuel-rich mixtures because then C_2H_3 concentration is higher. The competition between the possible routes of CH_3+HOO (R12 and R13), seems to largely govern the rate of energy release. R12 leads to two very reactive radicals while R13 to recombination, which is one of the most important sinks of HOO radicals under the conditions tested. Overall, the sensitivity analysis performed here implied that at least at high pressures the critical chemical pathways for heat release are different for fuel-lean and fuel-rich mixtures. In particular, the production and consumption of HOO and CH_3 especially for rich mixtures governs the rate of heat release.

For the purpose of this study a literature review was made on the reaction rate constants of all reactions exhibiting the higher sensitivity. The rate constants of

CH_3+CH_3(+M), CH_3+H(+M), C_2H_5+O_2, HOOH(+M) were updated according to the recommendations of Baulch et al. [115] and of HCO+O_2 according to Hsu et al. [116]. Finally, it was found out that in order to improve the rate of heat release agreement between model and experiments, the rates of both CH_3+HOO possible routes should be similar. This resulted in an increase of the rate of R13, which is a HOO and CH_3 sink by a factor of 5. The reactions with the rate constants used in the LLNL kinetic model and the updated ones used in this study are reported in Appendix C. Figure 5.20 shows then the pressure history prediction against the experimental data for the case described in Figure 5.13. The multizone model performs much better during the main heat release but if the rate of CH_3+HOO increases, the agreement improves considerably also in the early stage of combustion. Figure 5.20 show the agreement of the both combustion time constants for all tests carried out in this study if the two CH_3+HOO channels have similar rates. The agreement is definitely much better when compared to the multizone model with the default LLNL chemistry. Even though this modification is not based on previous experimental or theoretical study, it is suggested that the different channels of CH_3+HOO need to be revisited because such modification improves the agreement significantly. The rate of heat release is very sensitive to these paths and their relevant contribution may not remain unchanged for the extreme conditions of very fuel-rich, high-pressure conditions used in this study.

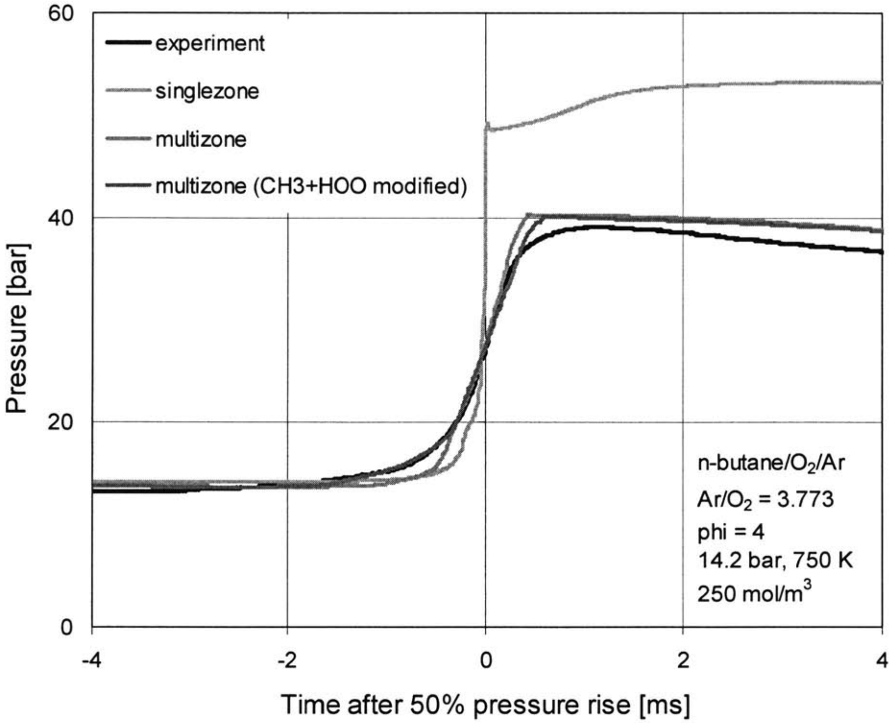

Figure 5.20 Pressure history prediction with single- and multizone model with the modified CH_3+HOO rate constant along with the corresponding experimental data.

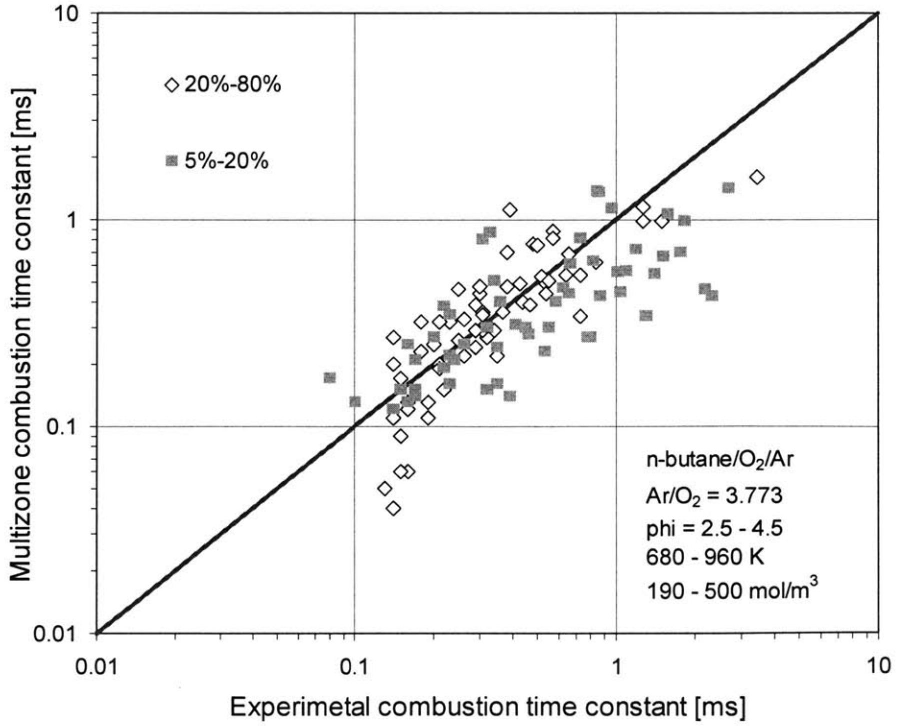

Figure 5.21 Combustion time constant correlation between multizone model predictions with the modified CH_3+HOO rate constant and experiments for most conditions tested.

Chapter 6

Soot Formation Study

6.1 Introduction

Understanding soot chemistry is one of the major challenges in combustion research. Despite essential progress in understanding single phenomena, no comprehensive theory or models with consistent predictive capabilities over a wide range of conditions are currently available. It is the conversion of hydrocarbon fuel molecules containing a few carbon atoms into an agglomerate of some million carbon atoms that complicates the process. This project focuses exactly on this transition: from the gas phase to the particulate phase. This stage is critical because it includes all chemical processes involved during the formation of the first aromatic ring, soot precursors and incipient soot particles that determine to a large extent further growth and final soot yield. This study is one of the very first attempts to look into the fundamental details of this early soot formation stage under high-pressure and fuel-rich conditions. Since these conditions are found locally in diesel engines at the location where soot is speculated to start forming, the goal of this study is to shed some light in the underlying fundamental mechanisms and motivate future efforts in mixing and fueling strategy of diesel engines for lower engine-out PM emission levels.

As already stated in Chapter 3, where typical soot rate data obtained with the RCM were briefly reviewed, soot starts forming very fast. The initial rate for most of the available observation time exhibited an exponential pattern and a soot time constant could be defined. Even though the combustion chamber became opaque shortly after particle soot inception, the great resolution during that early stage allowed for unambiguous interpretation of the soot time constant trends. It is one of the objectives of this study to determine the sensitivity of this soot time constant to critical combustion parameters like temperature, pressure, fuel-air equivalence ratio and also fuel structure. The onset of soot formation with respect to heat release could be also clearly studied. With the exemption of experiments at conditions close to the soot formation threshold, the final soot yield could not be determined with the optical methods employed in this study. However, scrapping the soot off the combustion chamber walls after the experiment and weighing the collected sample gave a good approximation of the final soot yield. Even though no sophisticated techniques were used, the 95% confidence level of such method was approximately ±5 %.

Final soot yield, and especially soot time constant data that describe the conversion of big molecules to soot particles, are valuable reference data for detailed soot formation modeling. A model like that is put together in this study by combining existing kinetic models reported in the literature. It is the goal of this project to test the predictive capability of the model against the data so that the former can sufficiently describe the underlying chemistry. A thorough model sensitivity analysis is performed in the next chapter aiming to identufy the most critical chemical pathways leading to soot.

6.2 Experimental Results

6.2.1 Soot time constant

Some typical experimental results of initial soot formation rates, obtained with the LOS absorption technique, were shown in Chapter 3. Soot yield was plotted versus time for two different compression volume concentrations (190 and 250 mol/m^3), while all other conditions were kept constant ($T_{comp,core} = 765\,\mathrm{K}$, $\phi = 3$). Even though the rates and the final soot yields were quite different (0.1622 ms/13.7% and 0.0546ms/17.2% respectively), both cases exhibited a similar exponential (autocatalytic) soot growth trend. The lower-concentration mixture data, where the available observation time of soot formation was longer, suggested that the rate started to slow down at the later stage of the process.

The sensitivity of the soot time constant, which can be obtained from the exponential soot growth rates observed initially under almost all conditions studied, to total volume concentration and core temperature for $\phi = 3$ is presented in Figure 6.1. Soot was observed for less fuel-rich mixtures too, but the soot time constant could not be clearly defined under all conditions, therefore, no data for these cases are presented here. The results obtained for even richer mixtures, $\phi = 4$ and $\phi = 4.5$, are shown in Figure 6.2 and Figure 6.3 respectively.

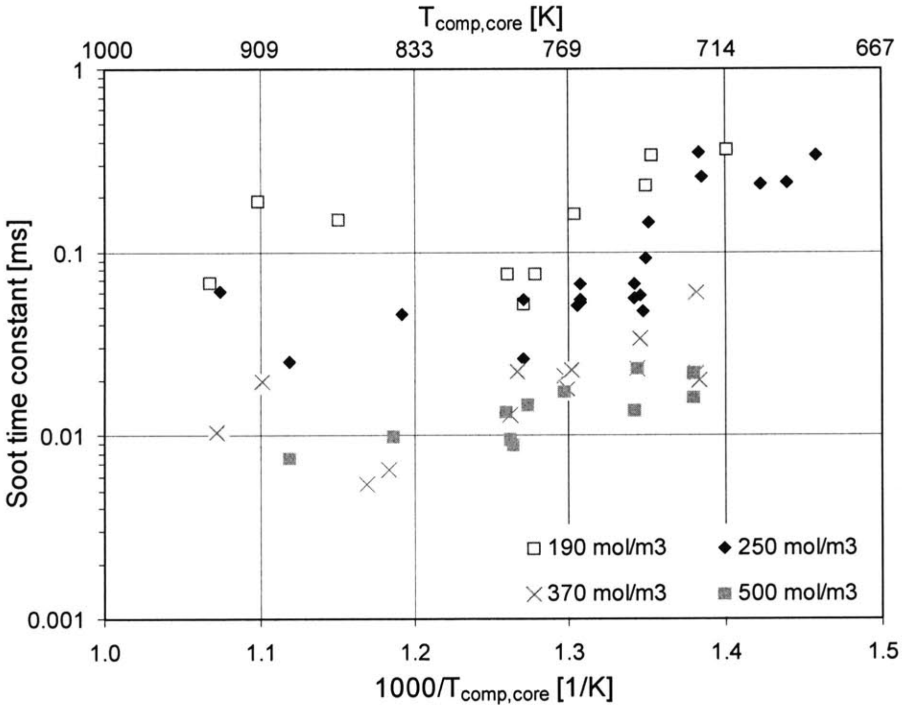

Figure 6.1 Soot time constant experimental data of n-butane/Ar/O_2 mixtures (Ar/O_2=3.773) for $\phi = 3$.

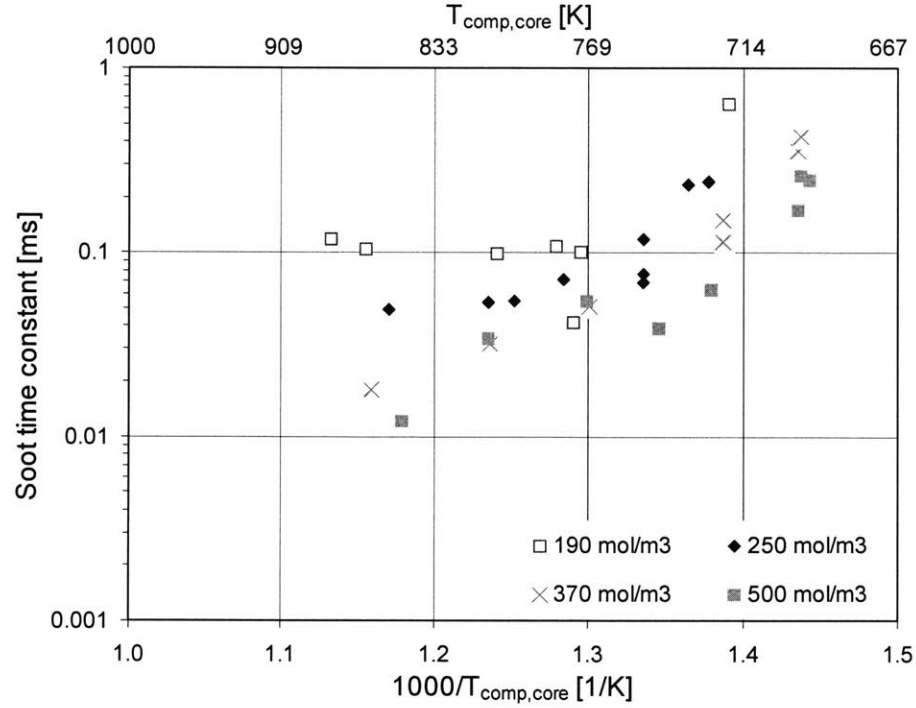

Figure 6.2 Soot time constant experimental data of n-butane/Ar/O_2 mixtures (Ar/O_2=3.773) for $\phi = 4$.

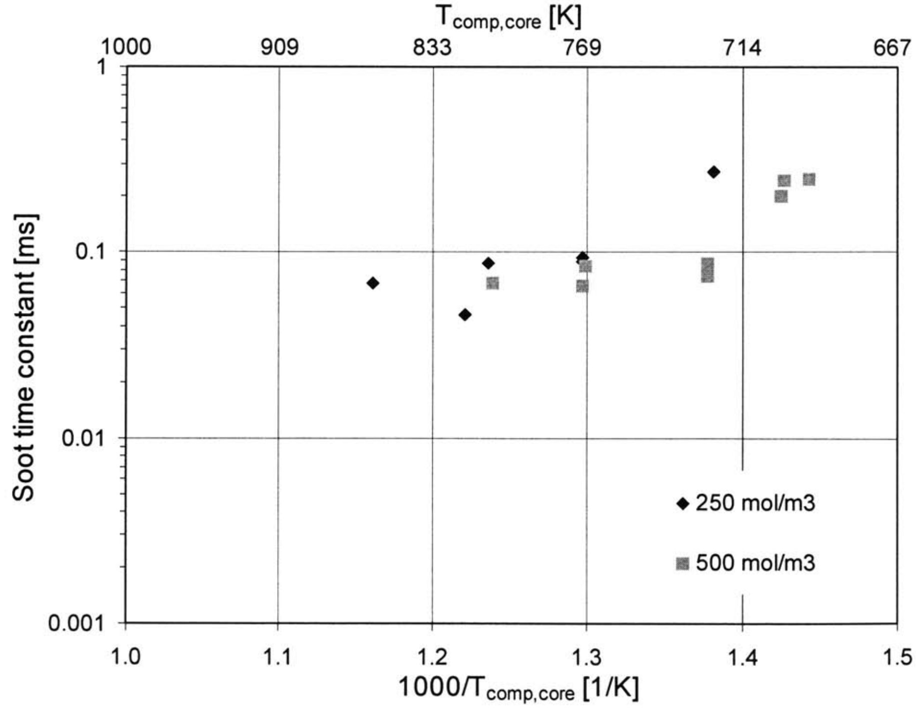

Figure 6.3 Soot time constant experimental data of n-butane/Ar/O_2 mixtures (Ar/O_2=3.773) for $\phi = 4.5$.

Since the sensitivity of soot time constant to temperature is fairly high, all data are plotted in Arrhenius form, where the trends can be more clearly studied. The trend of soot time constant with temperature is similar to ignition delay studied in Chapter 4. However, the effect of temperature is not as strong. For instance, the soot time constant drops by less than a factor of 2 for $\phi = 3$ and 500 mol/m^3 when the temperature increases by 150 K, while the corresponding drop in ignition delay is close to a factor of 50. The rapid soot formation rate with increasing temperature reflects the tendency for fast fuel molecule decomposition and soot precursors formation and growth. Since these processes need to overcome an energy barrier, high temperature can act, at least initially, in favor without though necessarily increasing the final soot yield, which is the outcome of competition among formation, dissociation and oxidation of soot precursors. The impact of temperature on these processes may be similar but formation comes first and it may dominate at the early stages. The total volume concentration, which scales with pressure, seems to accelerate initial soot formation rates as well. Even though pressure dependent chemical reactions critical to soot chemistry cannot be excluded, rapid rates are most likely attributed to high species concentrations. Since the effect of fuel-air equivalence ratio on soot time constant cannot be clearly observed in the figures above, data at $T_{comp,core} = 770\,\text{K}$ for total volume concentrations of 250 and 500 mol/m^3 are reported in Figure 6.4. It is evident that for both volume concentrations the soot formation rate becomes slower as the mixture gets richer. A similar trend was observed by Miyamoto et al. [27] in an optically accessible diesel engine, where the effects of ignition lag on soot formation were studied. By decreasing the ignition lag, the author found out that the apparent soot formation rates decreased, even though the final soot yield increased, and he attributed that behavior to local fuel-rich mixtures (which could not be measured though) resulting from insufficient mixing time. At first glance this is surprising because the final amount of soot is actually higher for richer mixtures (to be shown below). Even though changes in the reaction network and soot chemistry cannot be excluded, one possible explanation for this behavior could be the different temperature environment at the onset of soot formation. All data points shown in Figure 6.4 correspond to the same temperature at the end of compression but the totally different mixtures result in very different temperature histories during combustion. Consequently, less fuel-rich mixtures lead to higher temperatures which could then accelerate the initial soot formation rates. To illustrate this, Figure 6.4 shows also the corresponding maximum temperatures obtained with the multizone model described in Chapter 5. Decreasing the fuel-air equivalence ratio from 5 to 3, results in more than 500 K temperature rise, which could accelerate the initial soot formation rates substantially. Therefore, even though these data were produced by retaining the same compression temperature, which governs the ignition delay, the soot chemistry seems to be affected by the temperature history during combustion or possibly the maximum combustion temperature. This is discussed in detail later in this chapter.

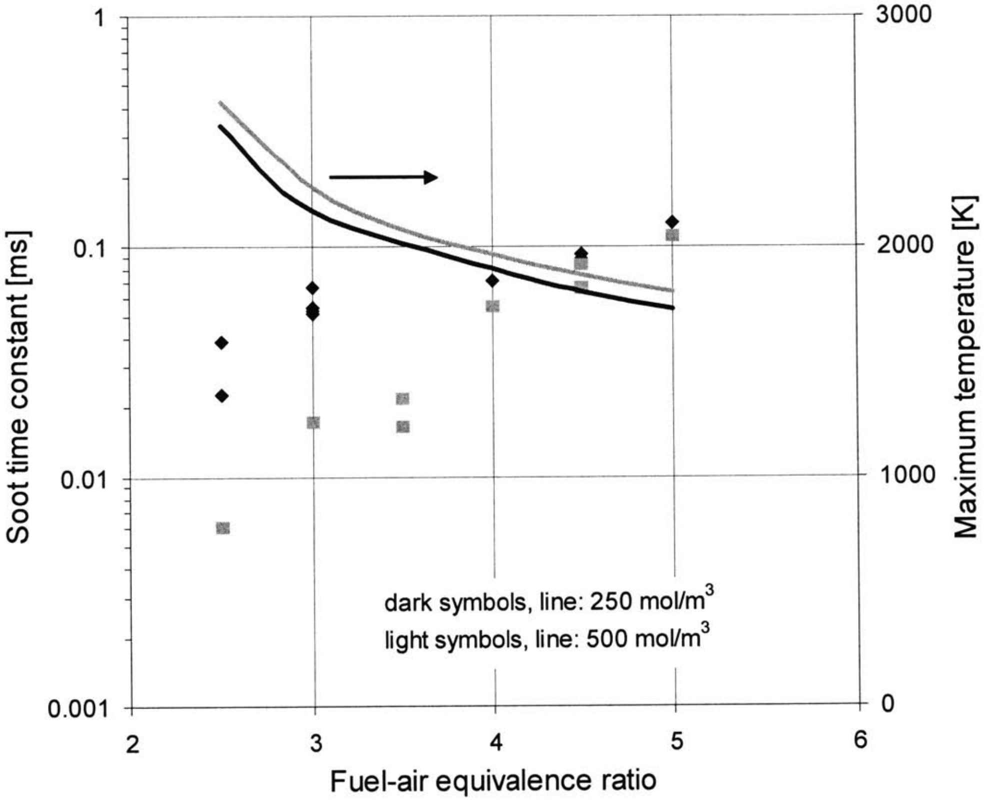

Figure 6.4 Soot time constant experimental data and maximum temperature calculation of n-butane/Ar/O_2 mixtures (Ar/O_2=3.773) for $T_{comp, core}$ = 770 K.

6.2.2 Soot yield

As already stated above, under most conditions tested, the optical technique employed in this study could not provide any information about the final soot yield. Even though such data might not be as useful as the initial soot rates for understanding the chemistry of particle inception, they could provide some insight into the temperature and mixture effects on the amount of fuel carbon converted to soot. Figure 6.5 shows the fuel-air equivalence effect on the soot yield for the same compressed core temperature and for two different volume concentrations.

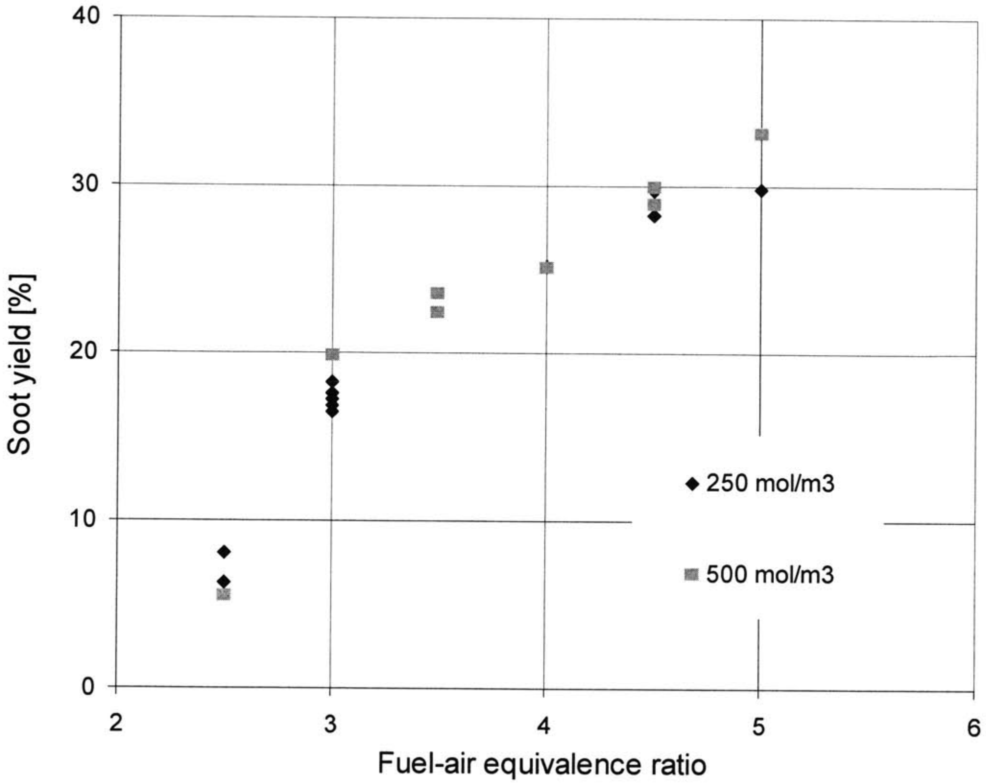

Figure 6.5 Soot yield experimental data of n-butane/Ar/O_2 mixtures (Ar/O_2=3.773) for $T_{comp,\,core}$ = 770 K.

Note that since soot yield is a quantity reduced to the amount of carbon in the fuel initially introduced into the combustion chamber, all data points of volume concentration collapse into a single line. As expected, the higher the amount of fuel relative to oxygen, the higher its conversion to soot. Interestingly, these soot yield figures are comparable to those obtained under the very different environment of shock tubes, where the soot formation rates are totally different [43]. According to Figure 6.5, the soot yield for $\phi = 5$ and maximum temperature 1750-1800K (see Figure 6.4), is ~30%. Kellerer et al. [43] measured soot yields between 25-35% for the same fuel-air equivalence ratio and similar temperatures. It was also found experimentally (and can be extrapolated from the data) that the soot formation threshold under the conditions tested was around $\phi = 2$ or slightly less. For n-butane, this corresponds C/O ratio $\phi_c = 0.62$ (assuming conversion to CO_2 and

H_2O) or $\psi_c = 0.89$ (assuming conversion to CO and H_2O). This suggests higher sooting tendency for n-butane compared to the findings of the study done by Glassman in a simple premix flame, where it was found $\psi_c \cong 1.1$ [117]. That C/O ratio would then correspond to $\phi \cong 2.48$, conditions under which significant amounts of soot were observed. Even though the temperature environment between these two studies is similar, the pressure employed here is much higher and it could affect the soot formation kinetics to a direction of shifting soot formation threshold towards lower fuel-air equivalence ratios. As already demonstrated in Figure 6.4, even though the conditions before combustion commences are similar for all the data points, the temperature history and especially the maximum temperatures may vary by more than 500 K. Plotting then the data against the calculated maximum temperature may give a different perspective. This is done in Figure 6.6, where most of the data obtained in this study are presented. It is evident that the effects of fuel-air equivalence ratio and temperature on soot yield are coupled. Then, the trends shown in Figure 6.5 may be biased by temperature. From the experimental point of view, it is a challenge to keep the same temperature history for totally different mixtures for all other conditions constant. Changing the diluent itself or the diluent/O_2 ratio (used 3.773 in this study, like in air) could potentially help but the former would require unreasonable thermal properties to cover the whole temperature range, while the latter would entirely change the combustion regime (very different collision frequencies). From a computational perspective though, introducing artificial diluents with convenient thermal properties, is possible. Such analysis, where the temperature and fuel-air equivalence ratio effects are uncoupled, is carried out in the next chapter.

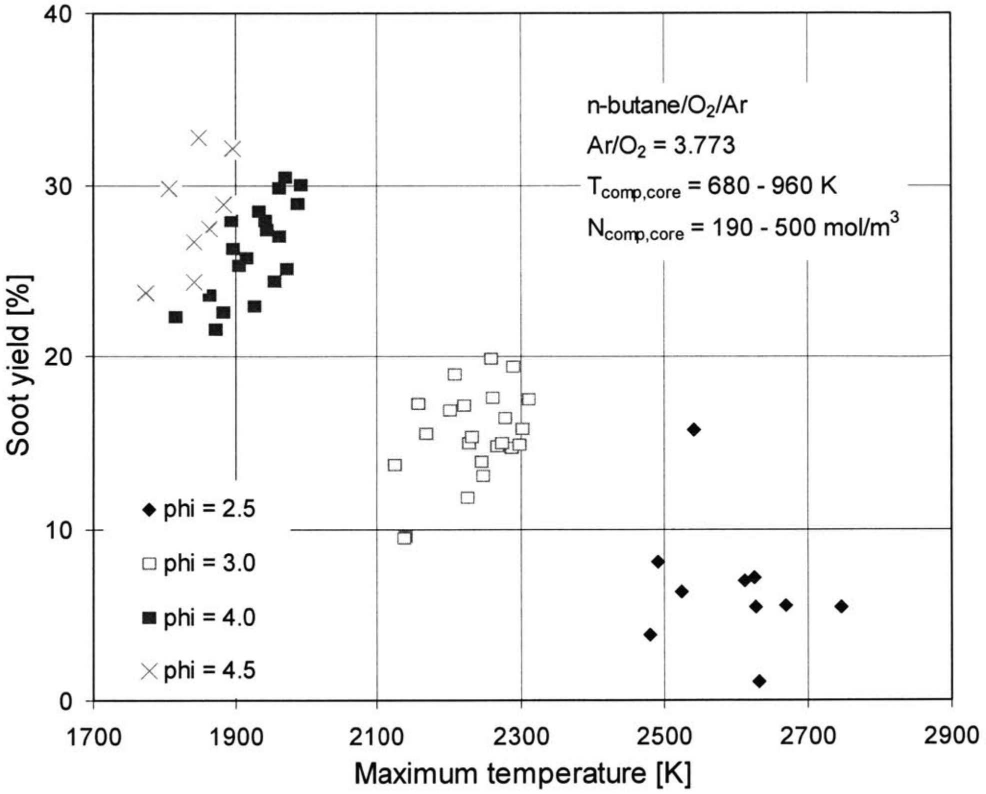

Figure 6.6 Soot yield experimental data versus calculated maximum temperature for most conditions tested.

6.2.3 Fuel structure effects

The fuel used in most of the experiments in this study was n-butane, which is a simple paraffin. Being in gas phase under ambient conditions, n-butane facilitates the mixture preparation process and its relatively simple chemical structure allows for detailed chemical kinetic modeling. Even though paraffins constitute a substantial fraction of the diesel fuel, there are hundreds of other species with completely different structure. The aromatic content in diesel fuel usually exceeds 20% by mol, while other additives like oxygenates and nitrates or peroxides (CN improvers), which are believed to suppress soot and accelerate autoignition respectively, are also typically included. In this study certain amounts of aromatics, oxygenates and nitrates where used to represent the diesel fuel better and investigate the sensitivity of soot formation to fuel structure.

Toluene has been suggested in the literature as a surrogate for describing combustion of aromatics in diesel fuels. It is a convenient fuel because it has the simplest molecular structure of all alkylated benzenes (so there are available kinetic models), it has significant vapor pressure at room temperature so that mixture preparation is facilitated. It is also fairly easy to compression-ignite. The impact of aromatic fuel structure on soot formation was studied by adding certain amounts of toluene in the fuel (0 to 40% by mol), while keeping compressed volume concentration and core temperature constant. The soot yield trends and the corresponding maximum temperatures are shown in Figure 6.7 with open symbols and dotted line respectively for $\phi = 3.5$. Unlike the case studied above, maximum temperature varied only slightly (~50 K across the entire range) and soot yield data could be safely interpreted on the basis of fuel structure only. Soot yield is increasing steadily as the aromatic content in the fuel increases with a rate of approximately 1% per 1% of increase of toluene in the fuel by mol. Similar trends were reported previously in the literature by Kwon et al. [118], who measured engine-out PM levels using fuels of very well-known composition. Before interpreting these results though, one needs to take into account the fact that the definition of fuel-air equivalence ratio is a little vague when double-component fuels are used. The different stoichiometric C/O ratios (0.308 for n-butane versus 0.389 for toluene) results to different C/O ratio even though the fuel-air equivalence ratio is the same. For instance, when the amount of toluene in the fuel increases from 0% to 40% by mol, and fuel-air equivalence ratio is kept constant at 3.5, C/O ratio increases from 1.077 to 1.213. The mixture inherently then becomes richer. The closed symbols in Figure 6.7 represent the soot yield data obtained if the fuel-air equivalence ratio is adjusted so that C/O ratio remains constant as the aromatic content in the fuel increases. Interestingly, the soot yield does not increase with toluene concentration in the fuel, while temperature stays roughly the same. This finding suggests that the chemical structure of the parent fuel molecules does not necessarily play a critical role in the soot formation process. On the other hand, the carbon relative to the available oxygen atoms seem to govern the sooting tendency of a mixture. This conclusion is consistent with the conjecture that during fuel decomposition most fuel molecules break down to simple structures with 2 or 3 carbon atoms and the original identity of fuel molecules is lost. Even though this theory may hold for simple aromatic molecules like toluene, stable polyaromatics that exist in diesel fuel may not entirely decompose and they may actually contribute more to the formation of soot particle precursors than paraffins. The different behavior of mono-aromatics and poly-aromatics in combustion and especially in soot formation has been also reported elsewhere [118]. Figure 6.8 shows the soot time constant trends for increasing aromatic content in the fuel. No particular trend is observed even though there seems to be a maximum for small aromatic concentrations. The fact that the two different fuels have different ignition characteristics, drawing conclusions from the initial soot formation rate may lead to errors. As already stated above, the soot time constant reflects the rate at which soot precursors evolve into soot particles, hence for very similar temperature fields, soot formation rates are not expected to be very different.

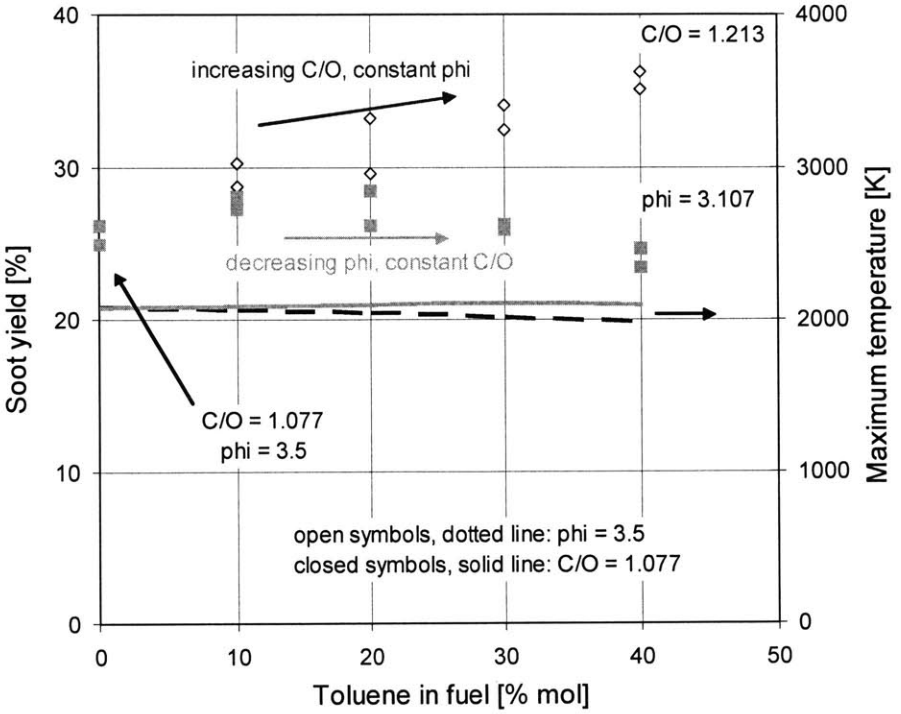

Figure 6.7 Soot yield experimental data and maximum temperature calculation of n-butane/toluene/Ar/O_2 mixtures (Ar/O_2=3.773) for $T_{comp,core} = 770\,K$, $N_{comp} = 500\,mol/m^3$.

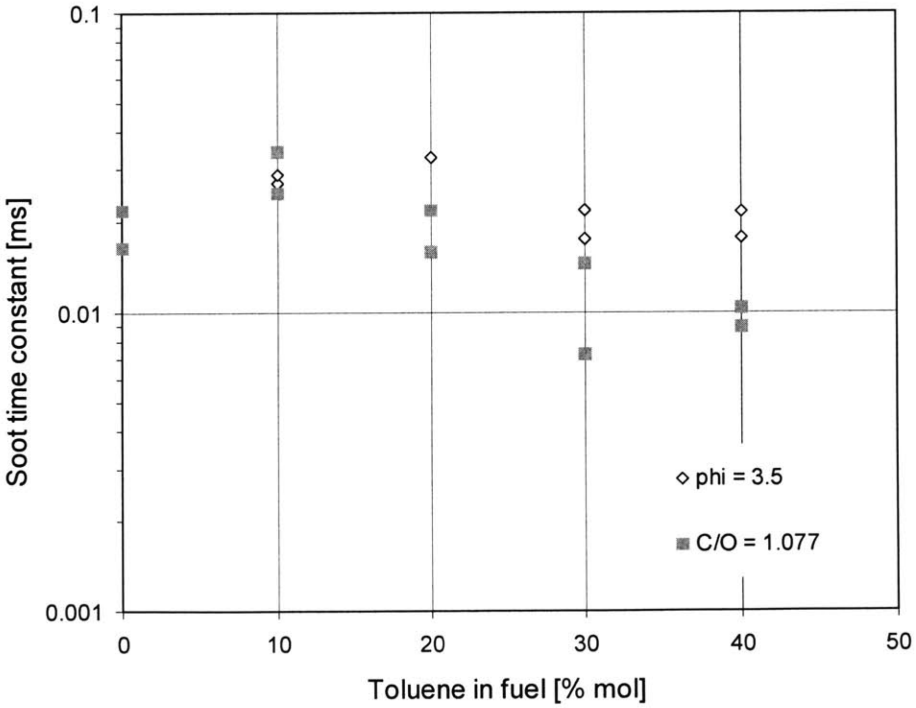

Figure 6.8 Soot time constant experimental data of n-butane/toluene/Ar/O_2 mixtures (Ar/O_2=3.773) for $T_{comp,core} = 770\,K$, $N_{comp} = 500\,mol/m^3$.

DME is an oxygenate fuel that has drawn the attention of many researchers in the diesel engine community [13, 102]. The fact that it is gaseous under ambient conditions and it has simple chemical structure, which encourages chemical kinetic modeling, were some of the reasons for including it the test matrix of this study. DME, as an oxygenate, is a very appealing fuel in the diesel engine community because of its ability to suppress soot formation. It has been suggested that the number of C-C bonds is reduced and species concentrations, like C2H2, responsible for the formation of aromatic species become lower [102]. Also the C-O bond is very strong and under most conditions even high temperatures generated during combustion cannot tear it apart [119]. Therefore, all carbon atoms attached to oxygen atoms are "reserved" and they do not participate to the soot formation process. To assess the effects of oxygenate fuels on soot formation, certain amounts of DME were added to n-butane (0 to 100% by mol) while keeping compressed core temperature and volume concentration constant. The open symbols and dotted line of Figure 6.9 represent the soot yield and maximum temperature as a function of the amount of oxygen in the entire fuel by mass. Without changing the thermal environment substantially, DME is very effective soot inhibitor. As also reported by Miyamoto et al. [120], for approximately 30% of oxygen in the fuel by mass, soot is entirely suppressed even though the overall mixture is fuel-rich. To reach 30% of oxygen in the fuel though, DME should constitute more than 90% of the fuel by mol. For similar reasons explained above, the C/O ratio drops significantly for the same fuel-air equivalence ratio as oxygenate is introduced in the fuel. Looking at the closed symbols of Figure 6.9, which corresponds to constant C/O ratio, it is evident that DME still suppresses soot with a slightly lower rate though. Despite the non-negligible temperature changes in this case, it is speculated that DME's mechanism for suppressing soot formation is mostly chemical in origin rather than thermal by "reserving" one or sometimes both carbon atoms attached to its oxygen. Figure

6.10 shows the soot time constant trends for increasing aromatic content in the fuel. For the reasons explained above no particular trend is observed and especially at high DME concentrations the amount of soot was too low and definition of soot time constant was not possible.

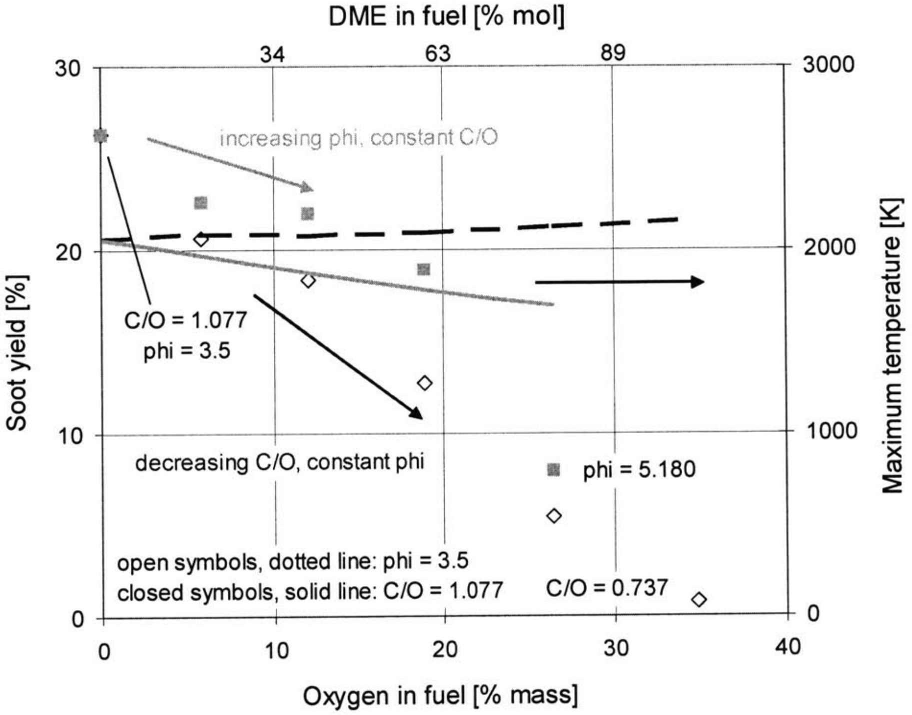

Figure 6.9 Soot yield experimental data and maximum temperature calculation of n-butane/ DME/Ar/O_2 mixtures (Ar/O_2=3.773) for $T_{comp, core} = 715\,K$, $N_{comp} = 450\,mol/m^3$.

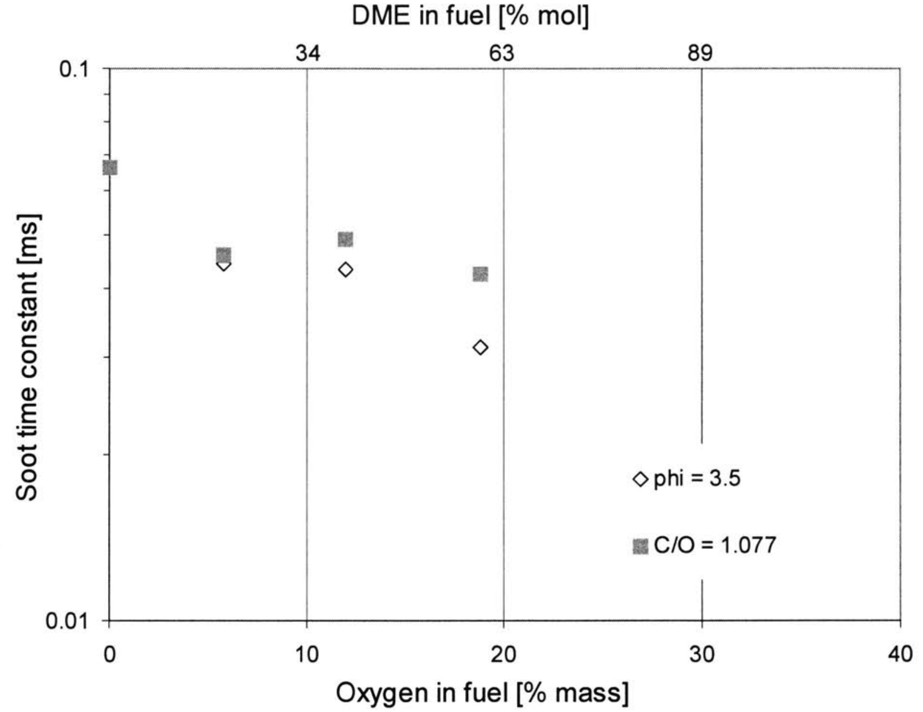

Figure 6.10 Soot time constant experimental data of n-butane/DME/Ar/O_2 mixtures (Ar/O_2=3.773) for $T_{comp,core} = 715\,\mathrm{K}$, $N_{comp} = 450\,\mathrm{mol/m^3}$.

CN improvers are sometimes used as additives in diesel fuel in order to shorten the ignition lag affecting noise, performance and emissions. Typical CN improvers are nitrates, like EHN, and peroxides, like di-tertiary butyl peroxide. Their concentration in the diesel fuel typically does not exceed 1000 ppm. Due to the complexity of diesel combustion, the impact of such additive on engine-out PM levels is not obvious. Most data reported in the literature have shown that CN improvers could actually increase the soot emission levels from a diesel engine [118]. The mechanism for this trend lies in the way combustion proceeds and the location and timing of soot formation. For shorter ignition delays, the spray does not have a lot of time to mix with the surrounding air and as a result the premixed zone becomes even more fuel-rich. Hence, soot formation is enhanced and engine-out PM levels increase, if subsequent oxidation is not particularly different. In this project, since mixing and chemistry are entirely decoupled, chemical effects, if any, of CN improvers can be clearly studied. To this extent, the base fuel, n-butane, was doped with very small amounts of EHN (0 to 1.5%) that does not have any impact on the energetics of the system (maximum temperature remains the same). For 1% EHN, the ignition delay dropped from 14 to 4 ms for conditions at the end of compression of 700 K, 450 mol/m^3 and $\phi = 4.5$. The soot yield data are depicted in Figure 6.11. As expected, final soot yield levels are independent of the presence of EHN, which does not seem to affect, at least, directly the soot chemistry. However, EHN does not only shorten the ignition delay, but also the combustion duration. Consequently, the initial soot formation rates increase significantly as Figure 6.12 presents, with possible implications in a diesel engine environment where competing processes simultaneously occur.

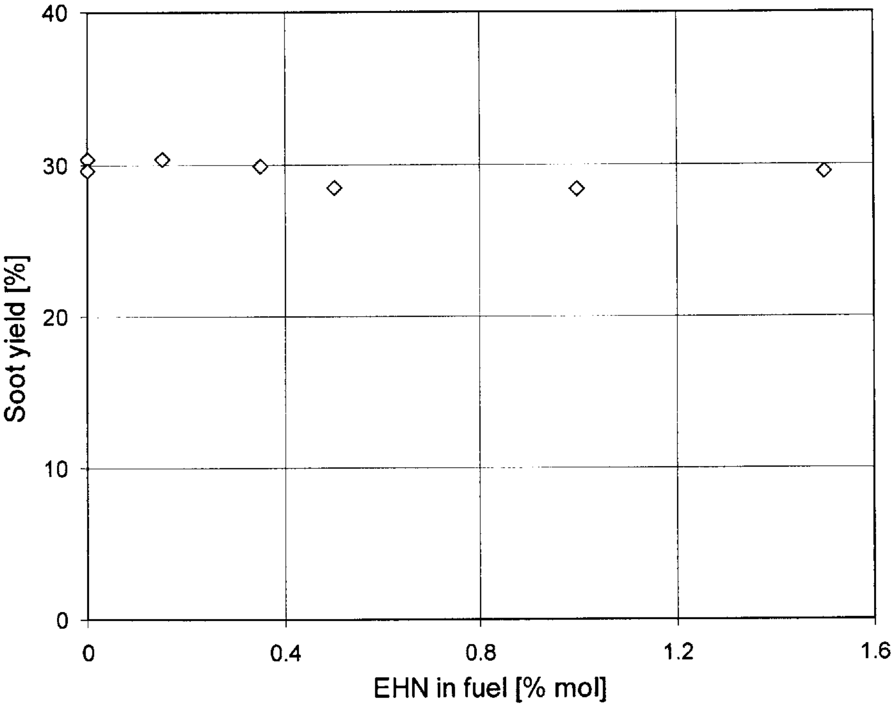

Figure 6.11 Soot yield experimental data of n-butane/EHN/Ar/O$_2$ mixtures (Ar/O$_2$=3.773) for $\phi = 4.5$, $T_{comp,core} = 700\,\mathrm{K}$, $N_{comp} = 450\,\mathrm{mol/m^3}$.

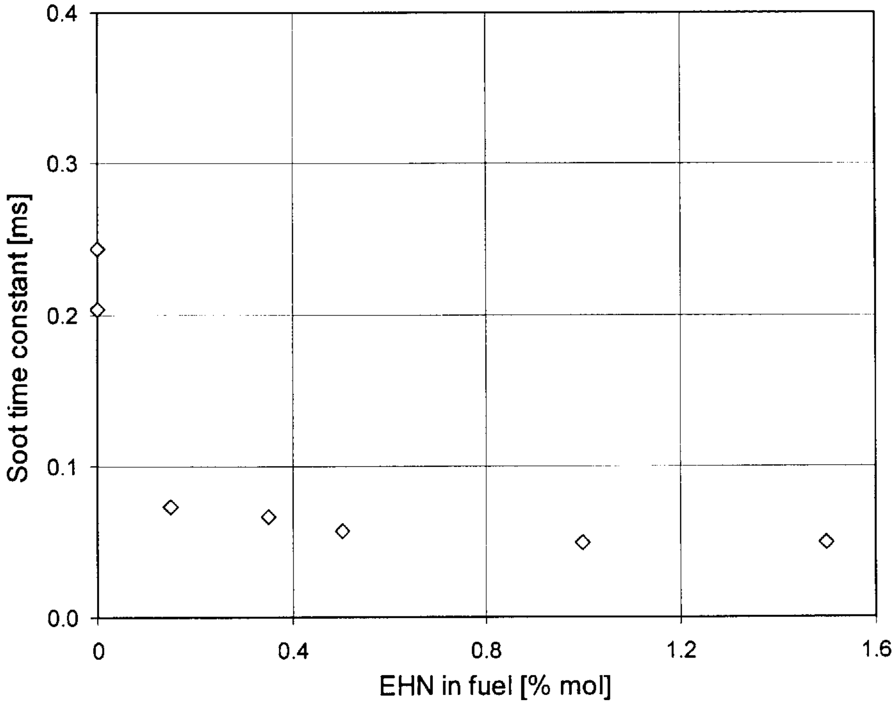

Figure 6.12 Soot time constant experimental data of n-butane/EHN/Ar/O_2 mixtures (Ar/O_2=3.773) for $\phi = 4.5$, $T_{comp,core} = 700\,\mathrm{K}$, $N_{comp} = 450\,\mathrm{mol/m^3}$.

6.2.4 Onset of soot formation

The most important feature of the experimental and optical setups employed in this study, is the very good resolution of the data at the early stages of soot formation. This capability of the setup provided valuable information during the transition from gas to particulate phase and identified the initial exponential soot growth trend. In addition, the timing of soot formation onset relative to the heat release can be determined. Even though the distinction between soot particles and big molecules is somewhat arbitrary, as already discussed in detail in Chapter 3, soot in this studied is defined the species absorbing light at 632.8 nm. To be more precise, the first 10% of light absorbed is not considered, as it accounts for noise and possible absorption by big gas-phase molecules. Under typical conditions tested, this amount of light would correspond to sootyield of less than 0.05%. Figure 6.13 shows the details of soot formation onset relative to pressure rise, which can be thought of as energy release, under typical conditions of the current study. To be able to compare different tests, zero was set the time that pressure increase reaches 50% of its maximum value. Interestingly, soot starts forming relatively early, when less than 30% of heat has been released, which corresponds to 0.24 ms before 50% pressure rise. However, if the findings of Chapter 5 are taken into account, this picture is not surprising. Due to the thermal stratification at the end of compression of the RCM, 30% of pressure rise does not correspond to 30% temperature rise in the core zones. Figure 6.14 shows the simulated temperature field and pressure with the multizone model described in Chapter 5. It is evident that for 30% pressure rise (which corresponds to 0.22 ms before 50% pressure rise and very close to the experiment), the core zone has almost burned completely, the next 2-3 zones have already ignited and temperatures in the combustion chamber can locally reach 1700 K. Under these conditions soot formation in the core zone could be possible but the details are discussed extensively when the experimental data are compared to the modeling results in the next section.

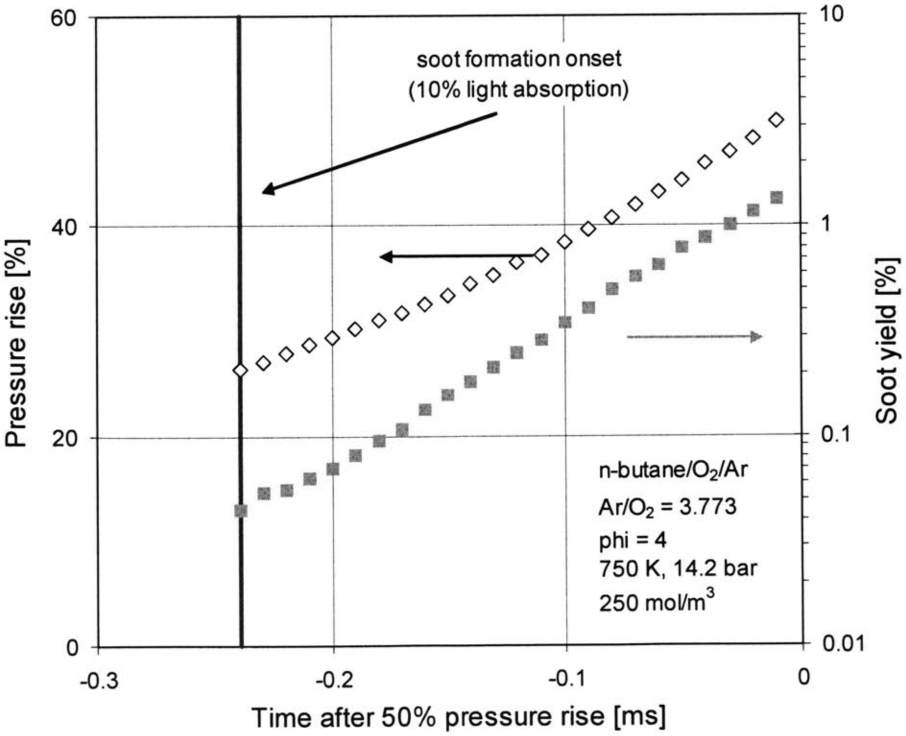

Figure 6.13 Details of early soot formation relative to pressure rise under typical conditions.

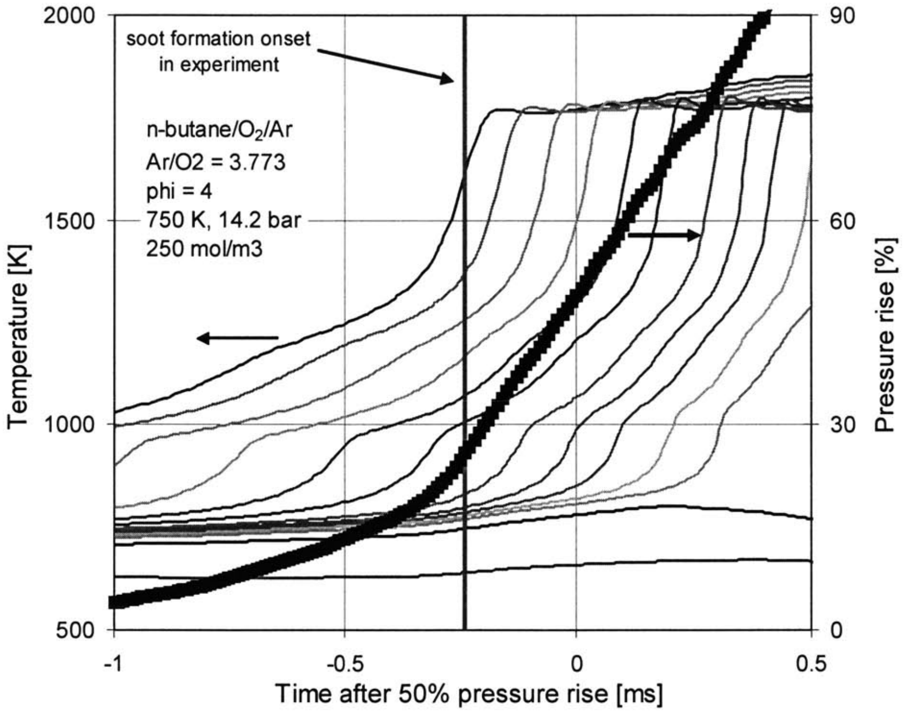

Figure 6.14 Simulation of temperature field and pressure with the multizone model under typical conditions.

It has been reported that temperature is a critical parameter for the onset of soot formation [121]. Combustion generated energy must increase temperature above a certain limit before reactions leading to soot particles can occur at appreciable rates. Even though measuring temperature in such environment is not an easy task and due to thermal stratification local temperatures may not be very accurately calculated, the effect of temperature on soot formation onset was studied here in a relevant sense. Figure 6.15 shows initial soot formation data under typical conditions for 3 different core temperatures at the end of compression: 740 K, 780 K and 800 K. Surprisingly, lowering the compression temperature, and therefore all temperatures in the combustion chamber, moves soot onset to earlier times with respect to heat release. If temperature is the only parameter determining the onset of soot formation for a certain mixture, then the trend shown in Figure 6.15 must have been reversed. In other words, the lower the initial temperature the higher the heat release required for forming soot. Since this is not observed in this study another factor besides temperature must also play a catalytic role during the early soot formation stages. This parameter could be time. Along with soot data, Figure 6.15 shows also the corresponding ignition delay times. As expected, lowering the temperatures, ignition delay increases for the non-NTC regime. This simple observation implies that even though the temperatures are a little lower (50 K), there is much more time available for chemistry to proceed (3.72 ms) before actual ignition occurs. Hence, the fact that the mixture at lower temperature stays at these temperatures for longer periods of time facilitates soot formation when ignition starts. The correlation between ignition delay and onset of soot formation under different conditions is depicted in Figure 6.16. There is a clear trend under most conditions. At very short ignition delays, temperature effects are also important and the impact of time is not clear.

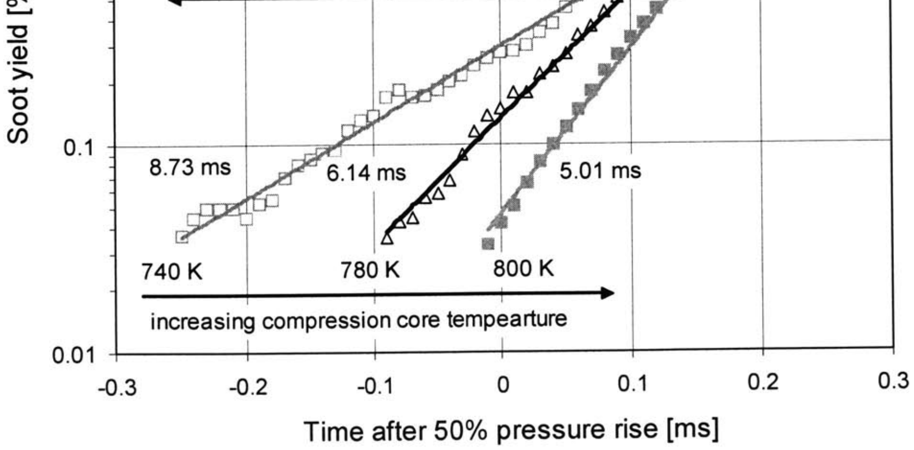

Figure 6.15 Initial soot formation experimental data of n-butane/Ar/O_2 mixtures (Ar/O_2=3.773) for N_{comp} = 250 mol/m3 and $\phi = 4$.

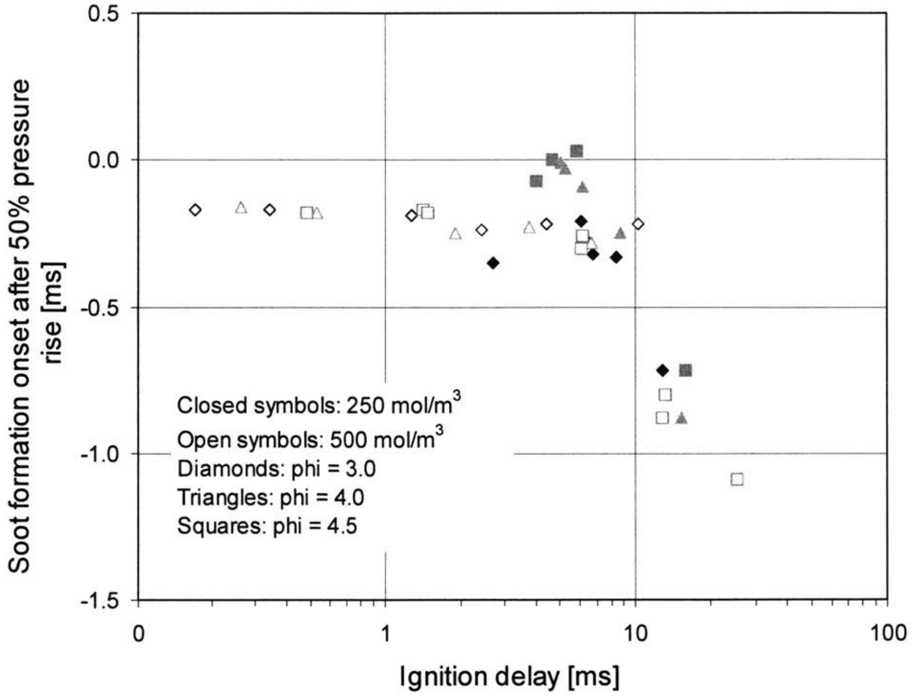

Figure 6.16 Ignition delay and onset of soot formation correlation (experimental data) of n-butane/Ar/O_2 mixtures (Ar/O_2=3.773).

To uncouple completely temperature and ignition delay effects, a CN improver was used. The base fuel was doped with small amounts of EHN, which chemically shortens the ignition delay, while all other conditions were kept constant. The results are shown in Figure 6.17. The figure shows clearly the critical role of time in soot formation chemistry regardless thermal effects.

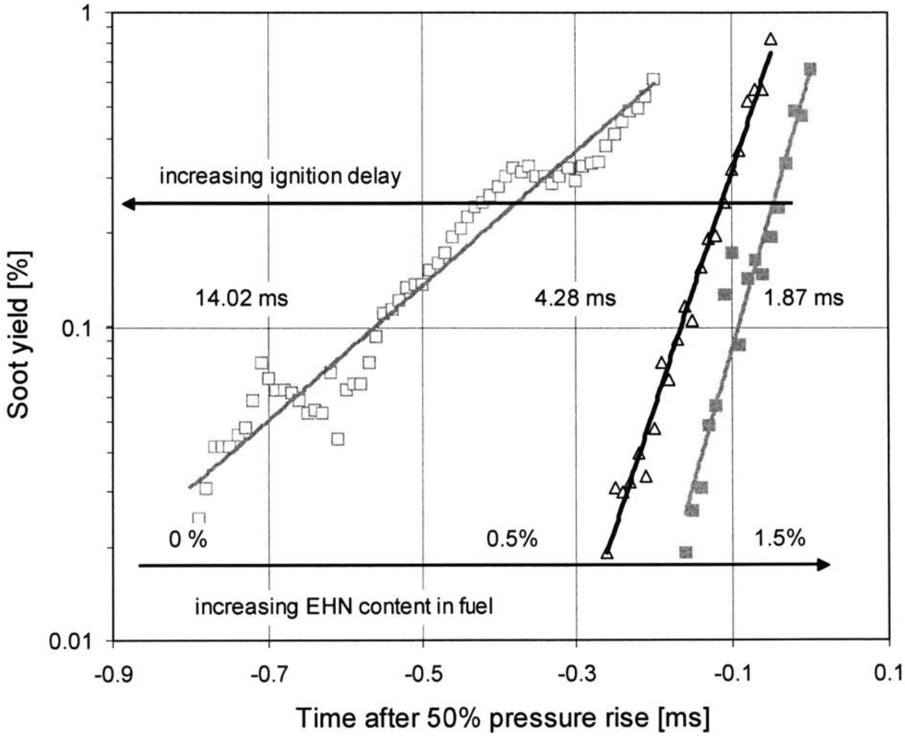

Figure 6.17 Effect of EHN on soot formation onset of n-butane/Ar/O_2 mixtures (Ar/O_2=3.773) for $\phi = 4.5$, $T_{comp,core} = 700$ K, $N_{comp} = 450$ mol/m^3.

6.3 PAH Growth and Soot Models

Since this project focuses on fundamental understanding of soot formation mechanisms, detailed chemical kinetics were chosen over empirical soot relationships for the modeling study. As already explained in the ignition delay and heat release studies, the LLNL chemical kinetic mechanism was used for the base chemistry of hydrocarbons. The oxidation mechanisms of toluene and DME also developed by LLNL were included, so that the effects of aromatics and oxygenates on soot formation could be also studied. This long mechanism was coupled with the PAH growth and soot models developed at MIT by Richter et al. [51, 54] resulting to a very extensive model of 498 species and 5734 reactions (not including the DME and toluene chemistries). A schematic of the entire chemistry code and its sub-models are depicted in Figure 6.18.

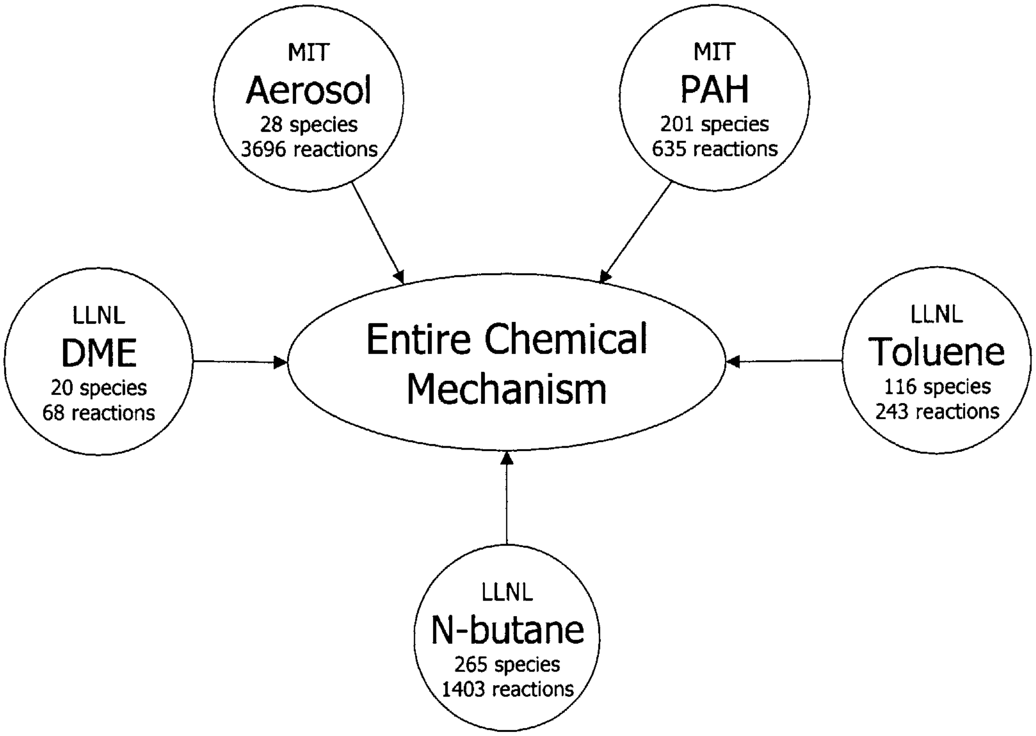

Figure 6.18 Sub-models of entire chemical kinetic code.

The PAH growth model encompasses most of combustion community's current knowledge of aromatic ring formation from paraffins and subsequent growth up to $C_{30}H_{10}$. In this mechanism and under the investigated conditions, C_3H_3 and C_5H_5 recombinations were found to be the dominant paths to the formation of the first and second aromatic ring respectively. Further PAH growth is mostly governed by the HACA mechanism but the contribution of small PAH as building blocks is also considered. Oxidation of selected PAH, like naphthalene ($C_{10}H_8$), pyrene ($C_{16}H_{10}$), benzopyrene ($C_{20}H_{12}$) and anthanthracene ($C_{22}H_{12}$), for which rate data can be found in the literature, is also included. Figure 6.19 illustrates the most important chemical pathways of the PAH growth model. One of the uncertainties of this model are the thermal properties of these big molecules, which affect not only the specific heat behavior but also the chemical equilibrium constant that determines the relationship between forward and backward reaction rates. Density-functional theory (DFT) calculations followed by vibrational analysis gave an estimate for the thermodynamic data of species up to 4 rings, while molecular mechanics gave the estimates for the properties of larger species. The fact that this detailed reaction network describing the formation and depletion of PAH, exhibited reasonable correlations with past experimental data obtained in low pressure, premixed, laminar, one-dimensional flames encouraged its use in this study. More details of the model and agreement with experimental data for simple flames can be found in [65].

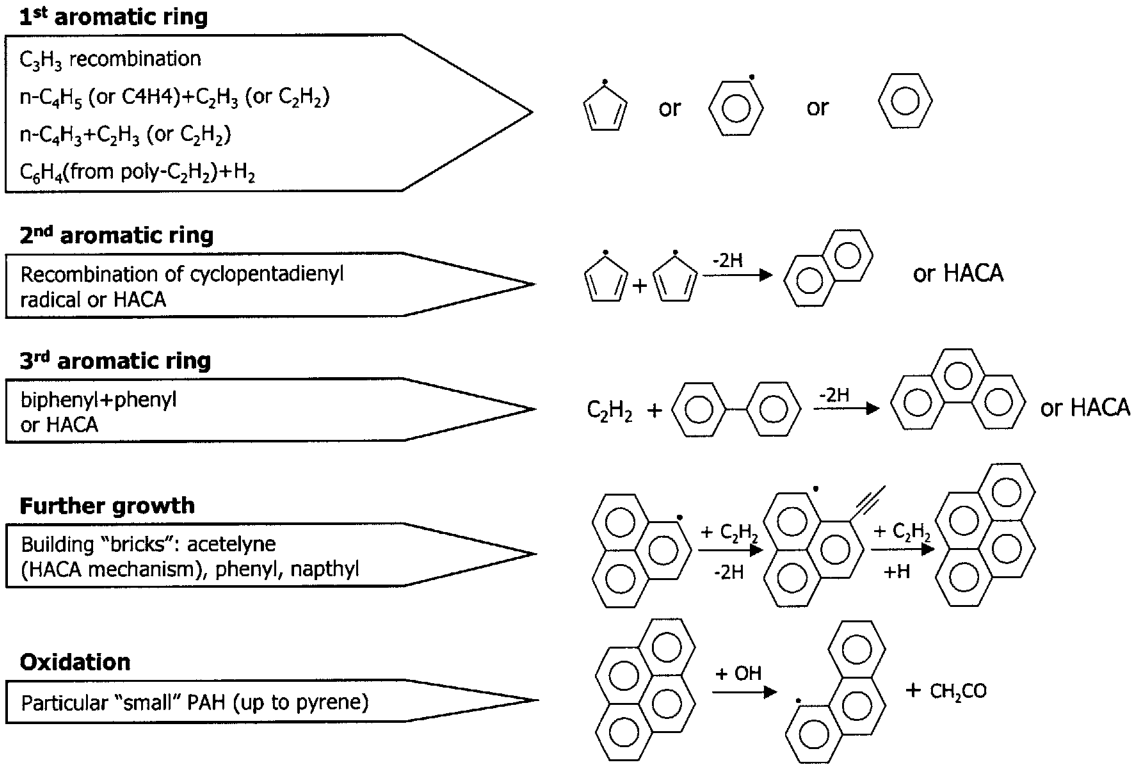

Figure 6.19 Most important chemical pathways of PAH growth model.

Modeling the formation and depletion of PAH gives an insight into the pathways that would eventually lead to soot particles because PAH are thought to be key intermediates in soot formation. In order to have a clear picture of the entire process though, several research groups extended the gas phase chemistry mechanism to particle formation at the expense of increasing complexity and computational effort. To overcome the difficulties involved, many past modeling efforts separated PAH growth and soot formation into two distinct processes [53, 122]. Even though such approach provided even further insight into the underlying critical processes, it is evident that PAH growth and soot formation do overlap and uncoupling them may lead to insufficient description of the underlying chemistry involved. The soot model used in this study, which is described in detail by Richter et al. in [54], combined gas phase and aerosol (soot particles) chemistry together in single-stage computations. To deal with the quickly increasing number of possible species of similar mass and of isomers of identical molecular formula, the sectional approach introduced by Pope et al. [123] and further developed by Kronholm [124] was used. In this technique, the particle ensemble is divided into classes (BINs) covering a certain mass range and is represented by a given average number of carbon and hydrogen atoms. In order to account for the increasing number of species, BIN mass range was not kept constant but continuously increased by a factor of 2 for the next BIN. Also, assuming spherical structures and constant particle density of 1.8 g/cm^3 (a little lower than graphite), a particle diameter for each BIN could be defined[1]. Finally, based on previously reported experimental data, H/C ratios were chosen to decrease with increasing particle size [19]. Table 6.1 summarizes the definition of each BIN and their characteristics. Since the number of atoms of a particular element in some BINs is larger than 999, the Chemkin-II interpreter was modified accordingly in this study.

---

[1] The diameter is calculated by the relationship: $\rho\frac{\pi}{6}d^3 = \frac{W}{N_A}$

Table 6.1 Definition of BINs in soot model.

BIN number	Molecular weight [amu]	H/C	Diameter [nm]
1	201 - 400	0.5	0.85
2	401 - 800	0.5	1.07
3	801 - 1600	0.5	1.34
4	1601 - 3200	0.435	1.69
5	3201 - 6400	0.371	2.13
6	6401 - 12800	0.339	2.68
7	12801 - 25600	0.308	3.37
8	25601 - 51200	0.292	4.24
9	51201 - 102400	0.276	5.35
10	102401 - 204800	0.261	6.73
11	204801 - 409600	0.245	8.48
12	409601 - 819200	0.229	10.69
13	819201 - 1638400	0.214	13.46
14	1638401 - 3276800	0.198	16.96

The biggest particle in this model, which corresponds to BIN14 has average molecular weight more than 2 million, H/C ratio less than 0.2 and diameter around 17 nm. These figures are consistent with the elementary carbon-based soot particles found in the diesel exhaust [1, 60]. This study stops particle growth at 17 nm, even though the original soot model extended to particles with diameter up to 70 nm, because it would be computationally very expensive, potential errors in thermal and kinetic properties become more important and experimental evidence suggested that substantial agglomeration would take place for particles larger than 20 nm resulting to non-spherical shapes. For the purpose of this study the thermal properties of soot particles have been estimated with Benson's group additivity method. Even though this calculation may inherently involve some approximations, the error concerns only the energy balance (heat capacitites of soot particles) and not the equilibrium constants because the entire aerosol model consists of irreversible reactions. Even the energy balance is speculated to be weakly affected because of the low molar concentration of soot under most conditions of interest.

The most appealing feature of the sectional approach is the similarity in the description and treatment of gas phase and aerosol chemistry. The aerosol chemistry equations can be written as chemical reactions with a rate constant close to that dictated by collision theory. For instance, if A is a soot particle (any BIN) the following reaction:

$$A+B\rightarrow\alpha C+\beta D$$

could represent surface growth if B is any gas phase growth species (PAH or C_2H_2) or coagulation if it is another soot particle. Species D is usually H_2 (for hydrogen balance since these processes lead to dehydrogenation) and α and β are the corresponding stoichiometric coefficients. The rate constant for this reaction is given by:

$$k=\gamma\cdot k_{collision}=\gamma N_A d^2\sqrt{\frac{8\pi K_B T}{\mu}}$$

where $k_{collision}$ depends on species A and B (reduced mass μ and equivalent diameter d) and temperature, while γ is the collision efficiency, i.e. the fraction of collisions leading to reactions, which is a free parameter and it is orders of magnitude higher than in gas phase chemistry and close to unity for large particles. A schematic overview of the soot formation sub-model is shown in Figure 6.20.

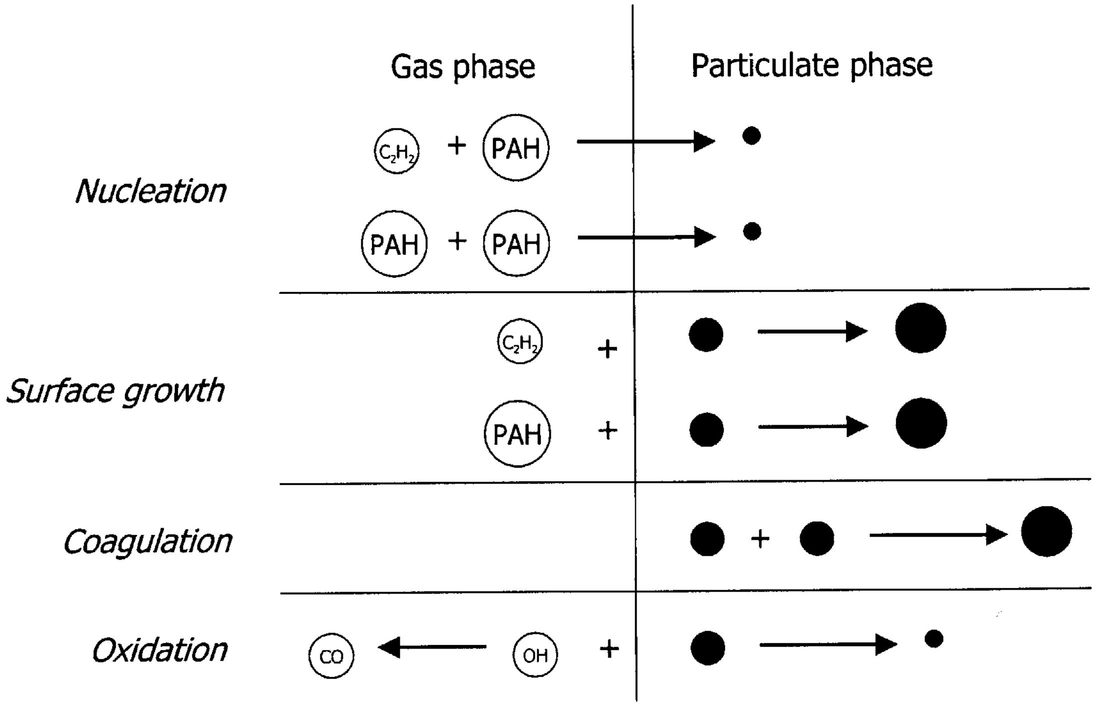

Figure 6.20 Overview of soot formation sub-model.

As this figure illustrates, even though the soot sub-model itself consists of thousands of reactions, the number of classes of reactions is fairly small. Then, even though each reaction has its own rate constant, which corresponds to different $k_{collision}$ there is only a limited number of collision efficiencies, which are the only free parameters in the model. Nucleation is considered the reaction between two gas-phase species resulting to a molecule with molecular weight high enough to be considered a young soot particle or an immediate soot precursor. Even though the distinction between a large PAH and the incipient soot particles is somewhat arbitrary, all results shown in the next paragraph have been derived assuming that all BINs are in the particulate phase. A thorough sensitivity analysis of this assumption was performed and is presented in the next section. Surface growth involves the reaction between a soot particle and a gas phase species and coagulation the reaction between two soot particles. Other reactions include soot oxidation, H-atom abstraction and addition and unimolecular H-atom loss from a soot particle. Note that all above reactions proceed only via a radical-molecule interaction and therefore H-atom abstraction from a soot particle or a PAH (from gas-phase chemistry) is essential to the model. Table 6.2 summarizes all classes of reactions and their respective collision efficiencies or rate constants. One of the big debates in the combustion community is the relative contribution of PAH and C_2H_2 both in the nucleation and surface growth process. Since this model includes all these routes, the relative contribution can be quantified and the agreement with the experimental data can be assessed. These issues are addressed in detail in the next chapter.

Table 6.2 Classes of reactions and collision efficiencies or rate constants of soot sub-model.

Reaction class	Representation	Rate constant or collision efficiency
Nucleation	$PAH_i^* + PAH_j^*(PAH_j)$	rate const. based on $C_6H_5 + C_6H_5(C_6H_6)$
	$PAH^* + C_2H_2$	rate const. based on $C_{10}H_7 + C_2H_2$
Surface growth	$BIN_i^* + PAH_j(PAH_j^*)$	$\gamma=0.1$
	$BIN_i + PAH_j^*$	$\gamma=0.1$
	$BIN_i^* + C_2H_2$	rate const. based on $C_{10}H_7 + C_2H_2$
Coagulation	$BIN_i^* + BIN_j^*(BIN_j)$	$i,j<5: \gamma=0.1,\ i,j\geq5: \gamma=1$
Oxidation	$BIN_i + OH(O)$	$i\leq4: \gamma=0,\ i>5: \gamma=0.2$
H abstraction (rev.)	$BIN_i + H(OH)$	rate const. based on $C_6H_6 + H$
H addition (rev.)	$BIN_i^* + H$	rate const. based on $C_6H_5 + H$

6.4 Modeling Results

6.4.1 Typical results and details

The soot formation model described above reflects the current knowledge base and understanding of the underlying chemistry. Being able to compare the predictions of this model to the valuable experimental data obtained at the critical transition stage from the gas to the particulate phase could be beneficial to the combustion community. First of all, the performance of the model and therefore the degree of current understanding of soot formation chemistry can be tested. As a result, not well-established parts of the model can be modified improving model's predictive capability. Moreover, insight into the critical chemical processes involved in soot chemistry can be gained. Due to experimental limitations such insight cannot be directly gained from the experimental data. Finally, a validated soot formation model can always be used as a predictive tool for designing combustion systems and lowering PM emission levels from diesel engines.

Before looking at the performance of the model and its predictive capability, it would be beneficial to understand the most important features of the model. Then, the trends could be readily interpreted and possible discrepancies with the experimental data better explained. Figure 6.21 represents a carbon diagram, which essentially shows the carbon distribution and temperature history during a typical fuel-rich combustion event for the core zone. Such diagram is very useful because carbon yield indicates the species to which carbon is tied up to, providing insight into the underlying chemical pathways. Before combustion starts all carbon is stored in the fuel molecules (100% carbon yield). Right after ignition, fuel molecules rapidly break down to small species, denoted as decomposition products. These products mostly consist of olefins and aldehydes of not more than 2 or 3 carbon atoms. At ~1300 K (where ~50% of the energy has been released) more than 90% of the fuel has been already consumed, and the rest of the carbon is stored in decomposition (~60%) and stable products (~30%). The most important decomposition products at this stage are ethylene, propylene, acetaldehyde and formaldehyde. The olefins store ~40% and the aldehydes ~15% of the total carbon. Because of the very fuel-rich environment not much CO_2 is produced and the stable products are mostly CO and CH_4 storing ~20% and ~7% of the total amount of carbon at this stage. At ~1800K when the total amount of energy has been released (subsequent temperature rise is due to compression from surrounding zones igniting at later times), the first soot precursors start forming. The decomposition products are consumed rapidly forming large amounts of C_2H_2 (~20%) and mono-aromatics (~8%), which are essentially benzene and phenyl-acetylene, while at the same time increasing the carbon stored in the stable products (~60%). Beyond that point, PAH start forming, storing ~5% of the carbon in the system before the first soot particles appear. After soot particle inception, the carbon stored in the soot particles increases rapidly consuming C_2H_2, PAH and mono-aromatics. At the end of the combustion event ~30% of the carbon is stored in soot (referred to as soot yield), ~50% in CO, ~5% in CH_4, ~4% in CO_2 and ~10% in C_2H_2. Looking closely at the carbon diagram the following points are worth noting:

- Soot starts forming late relative to the energy release. In this particular case incipient soot particles are not observed in the system before the total amount of energy is released. However, this observation does not necessarily imply that very high temperatures are needed for particle inception, as time is another important parameter as well. After ignition and before particle inception a series of chemical processes, like formation of C_2H_2, mono-aromatics and PAH, need to take place that require both energy and time.
- The first appearance of soot particles coincides with the maximum concentration of PAH. This observation is consistent with the critical role of PAH to particle inception. Experimental data from simple flat flame burners that have been reported in the literature also support this argument [17].
- The amount of carbon stored in C_2H_2 during soot formation is much higher than the carbon stored in PAH in spite of its lower molecular weight. In addition, the fact that C_2H_2 carbon yield drops significantly during the soot growth process indicates that C_2H_2 may be the dominant growth species. However, no general conclusion can be

drawn at this point. The relative contribution of PAH/C_2H_2 to surface growth is discussed in detail in Chapter 7.

- The significant amount of carbon stored in C_2H_2 (~10%) that does not take part in the soot growth process may be related to the decreased reactivity (collision efficiency) of aged particles with C_2H_2 as already reported in the literature [24].

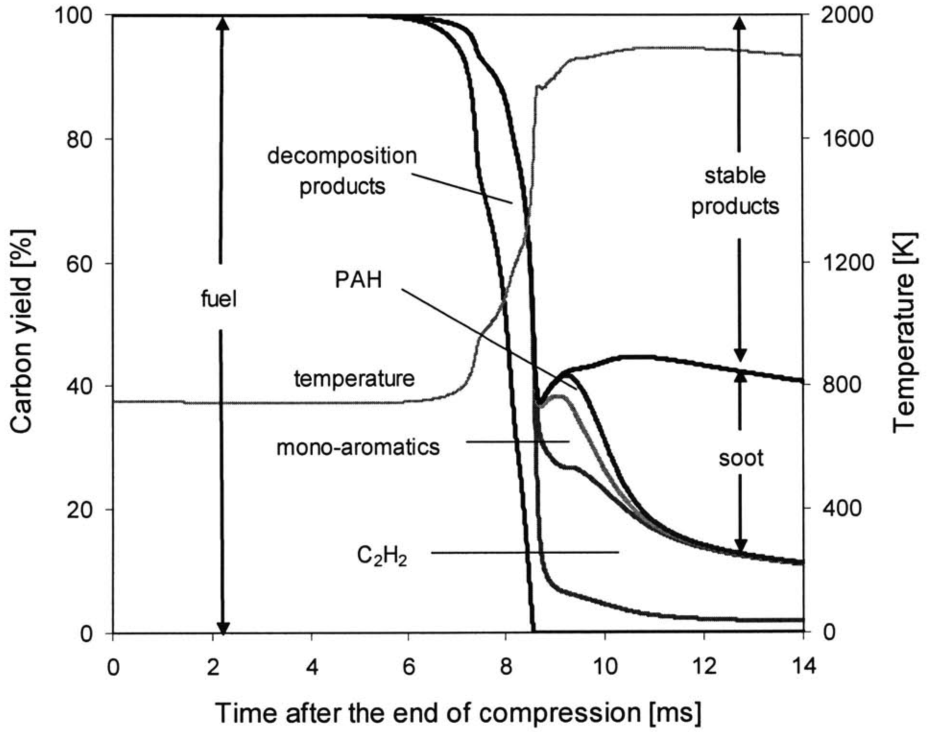

Figure 6.21 Carbon diagram and temperature history during combustion under typical conditions: n-butane/Ar/O_2 mixture (Ar/O_2 = 3.773), $\phi = 4$, $T_{comp,\,core} = 750$ K, $N_{comp} = 250$ mol/m^3 (core zone).

Figure 6.22 gives the details of soot particle distribution during the early stage of soot formation. In particular the evolution of soot yield, number density and volume-mean average diameter[1] are shown. The particle number density is governed by nucleation and coagulation rates. Right after particle inception, nucleation dominates and the number of particles increases rapidly while the diameter stays essentially constant at very low levels. At some point, the gaseous species concentrations have been reduced by the nucleation

---

[1] Calculated from: $\bar{v} = \sqrt[3]{\sum_i \frac{N_i d_i^3}{N}}$

process sufficiently that they tend to be adsorbed rather than to nucleate. At this stage the volume-mean particle diameter is less than 2 nm and the soot loading is very small (~5%) compared to its final value (~30%). With nucleation halted, all subsequent soot yield rise is due to surface growth, which is also partially responsible for the mean particle diameter rise. Due to the high particle number density right after nucleation, coagulation rates are high as collision frequencies are high and as a result, particle mean diameter increases. However, coagulation is relatively slow and the mean diameter still increases even after the final soot yield is reached. Interestingly, the time scale for the entire soot formation process is of the order of 5 ms, while the combustion event takes place in less than 1 ms. The first modeling results shown in Figure 6.22 are very encouraging because they reflect the current understanding of soot formation in combustion systems and they are in accordance, as least qualitatively, to the experimental data obtained in simple flames where sampling is possible. Note that the optical setup employed in this study focuses on the very early stage of soot formation where soot yield is less than 2%. According to Figure 6.22, this stage corresponds to the nucleation process, where the particle number density is close to its maximum and the mean diameter is less than 1.5 nm. A magnification of the early stage of soot formation for the case shown above is depicted in Figure 6.23. The data shown correspond approximately to the available range of the optical setup. It is evident that the multizone model reproduces the exponential soot growth trend observed by the experiments and a soot time constant can be also defined. On the same graph the corresponding singlezone model results are also shown. The trend is close to exponential and the rate is very similar to the one obtained with multizone model, unlike the combustion time constant that changed by more than an order of magnitude when the multizone model was introduced. This is encouraging because all uncertainties in the formulation of the multizone model does not seem to affect significantly the final outcome of the soot model.

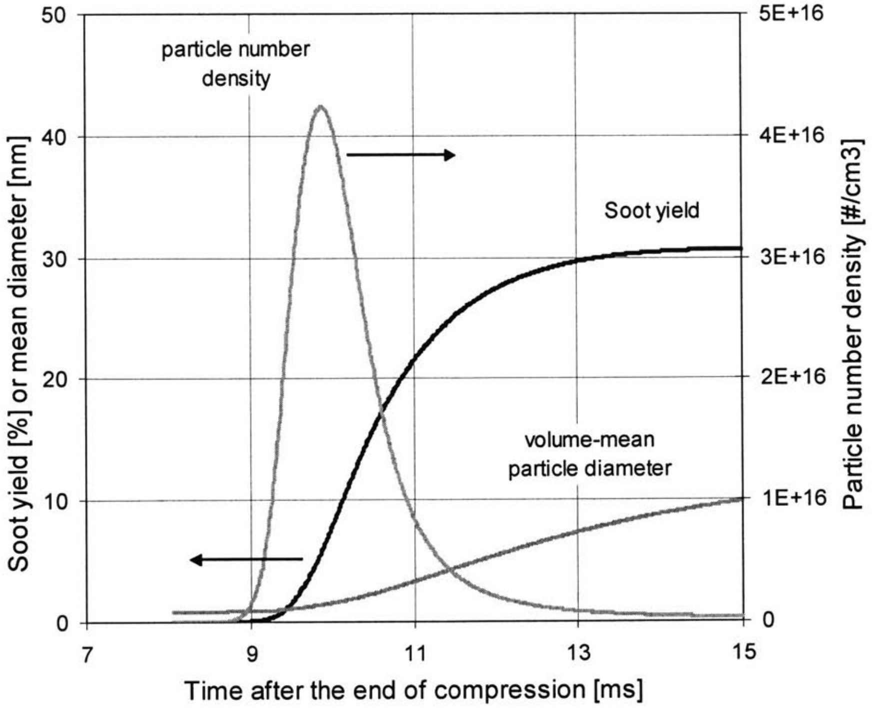

Figure 6.22 Details of soot particle distribution under typical conditions: n-butane/Ar/O_2 mixture (Ar/O_2 = 3.773), $\phi = 4$, $T_{comp,\,core}$ = 750 K, N_{comp} = 250 mol/m^3 (core zone).

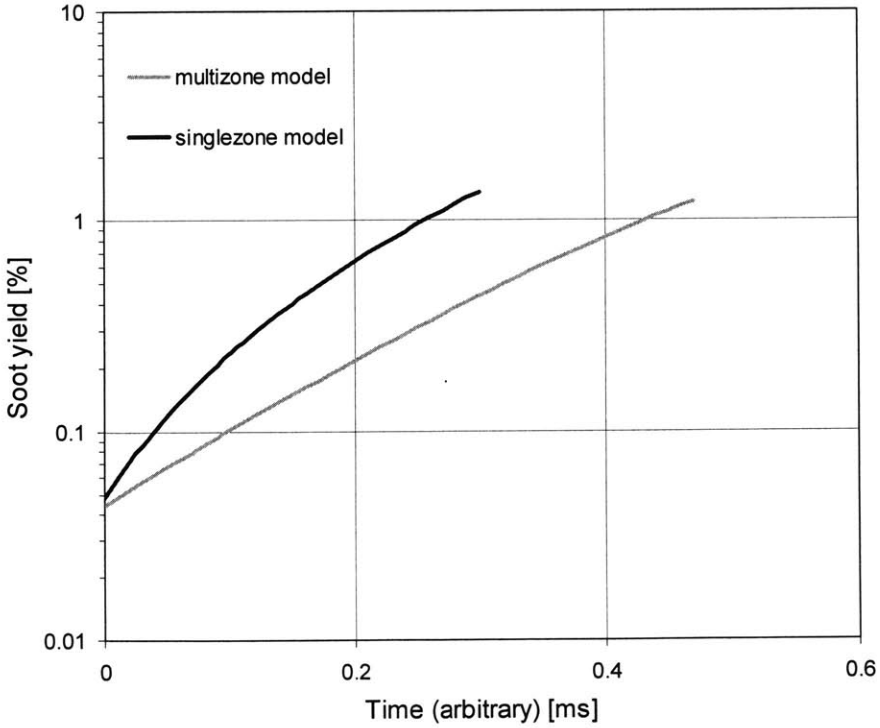

Figure 6.23 Simulation of the early stage of soot formation with the multizone and singlezone models under typical conditions: n-butane/Ar/O_2 mixture (Ar/O_2 = 3.773), $\phi = 4$, $T_{comp,\,core}$ = 750 K, N_{comp} = 250 mol/m^3.

6.4.2 Soot time constant and soot yield

The performance of the chemical kinetic model, as far as the main combustion characteristics are concerned, was reviewed in Chapters 4 and 5. The ignition delay was sufficiently well predicted, while the rate of heat release when coupled with CFD analysis gave reasonable agreement between model and experiments with minor adjustments to the original kinetics. In this section the performance of the composite multizone model, including all sub-models described in Figure 6.18 is assessed with regard to its predictive capability on initial soot formation rates and soot yield.

Figure 6.24 shows the correlation between experimental data and modeling results for $\phi = 4.5$ at different compressed core temperatures and total volume concentrations. The performance of the model at these highly fuel-rich mixtures is very encouraging. Soot time constant trends with temperature and volume concentrations are reproduced and the agreement is very satisfactory even on a quantitative basis.

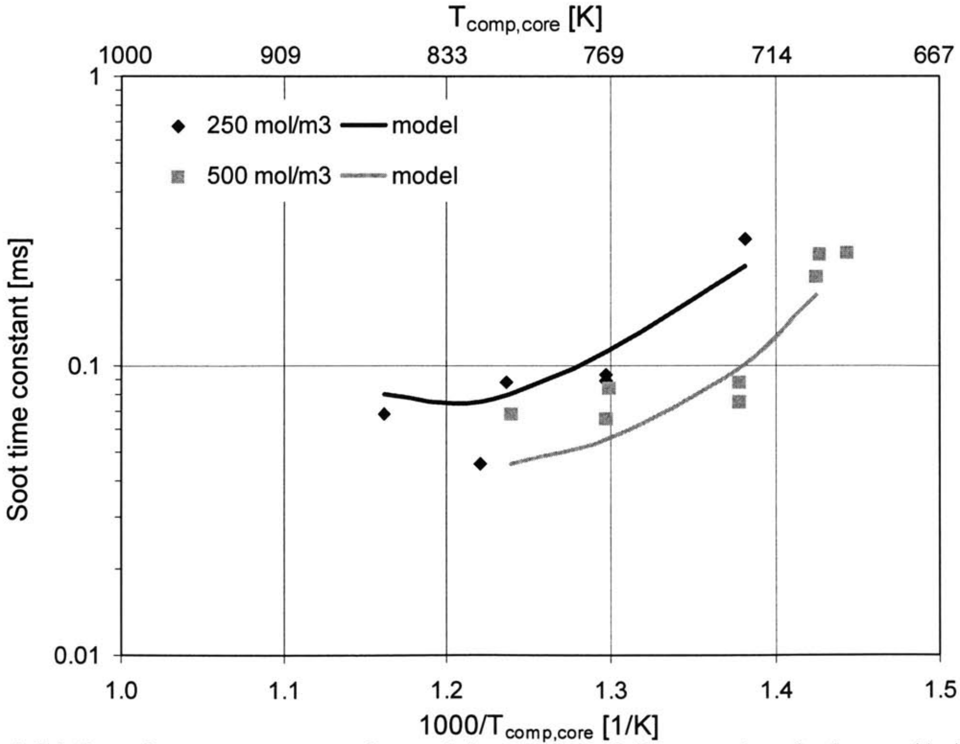

Figure 6.24 Soot time constant experimental data and modeling results of n-butane/Ar/O_2 mixtures (Ar/O_2=3.773) for $\phi = 4.5$.

However, this good correlation does not apply at less fuel-rich mixtures. Figure 6.25 shows the experimental and modeling trends of soot time constant with fuel-air equivalence ratio for a fixed compressed core temperature of 770 K at two different volume concentrations. The correlation is reasonably good for mixtures of fuel-air equivalence ratio between 4 and 5 and it deteriorates for less fuel-rich mixtures. Nevertheless, the experimentally observed trend of increasing soot formation rates as the mixtures becomes less fuel-rich, is reproduced by the model and as explained above it must be due to the higher temperatures reached for these mixtures. For fuel-air equivalence ratios below 3, the soot levels predicted by the model are so low that no soot time constant can be defined. This discrepancy between model and experiments at the threshold of soot formation can be more clearly seen when correlating soot yield data.

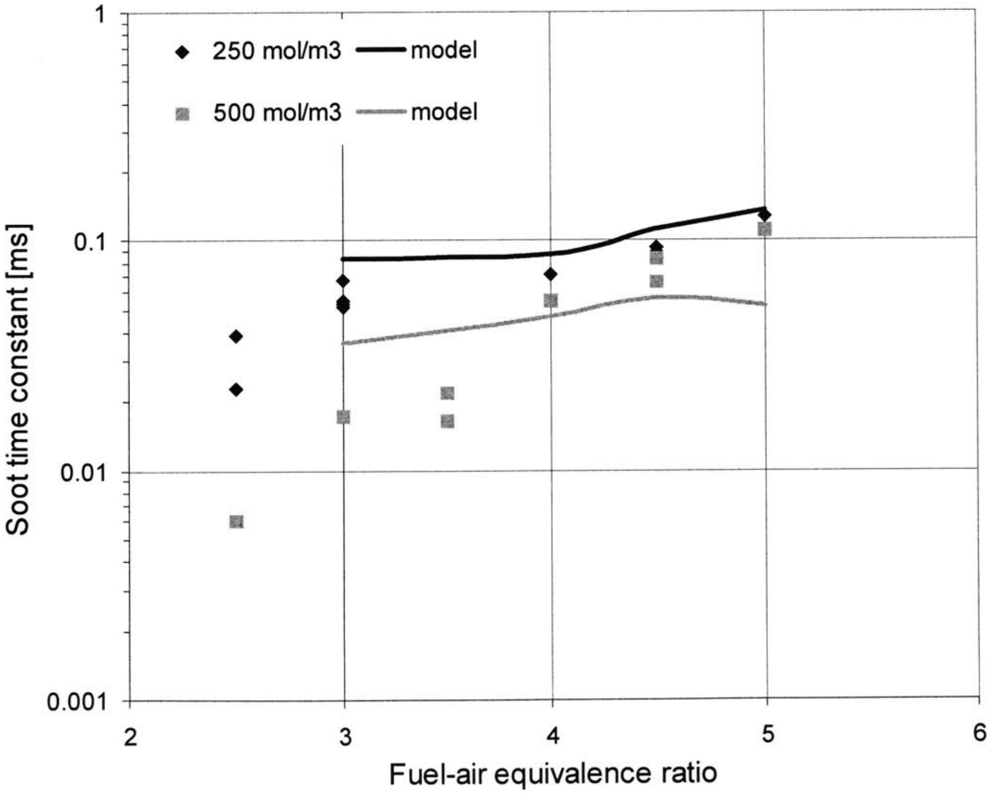

Figure 6.25 Soot time constant experimental data and modeling results of n-butane/Ar/O_2 mixtures (Ar/O_2=3.773) for $T_{comp, core}$ = 770 K.

Figure 6.26 shows this correlation for the same conditions of Figure 6.25. The overall agreement between model and experiment is reasonably good. The model is capable of predicting the increasing soot yield with fuel-air equivalence ratio without any significant impact of volume concentration. There is however a slight overprediction of soot yield for very fuel-rich mixtures and more significantly underprediction at less fuel-rich mixtures. This defficiency of the model is of particular interest because a very important piece of information to the combustion and especially to the diesel engine community, is the definition of soot formation thresholds. Under the conditions tested here, soot was observed experimentally at $\phi \cong 2$, while the model predicts that the threshold is at $\phi \cong 2.5$. This discrepancy could be attributed to poor temperature calculation, which affects soot yield as shown in the next chapter, to uncertain thermal properties of critical species, which may change equilibrium of important chemical pathways leading to soot, or to the aerosol dynamics code, which affects directly the soot chemistry. The sensitivity of the model to all these factors is extensively discussed in the next chapter.

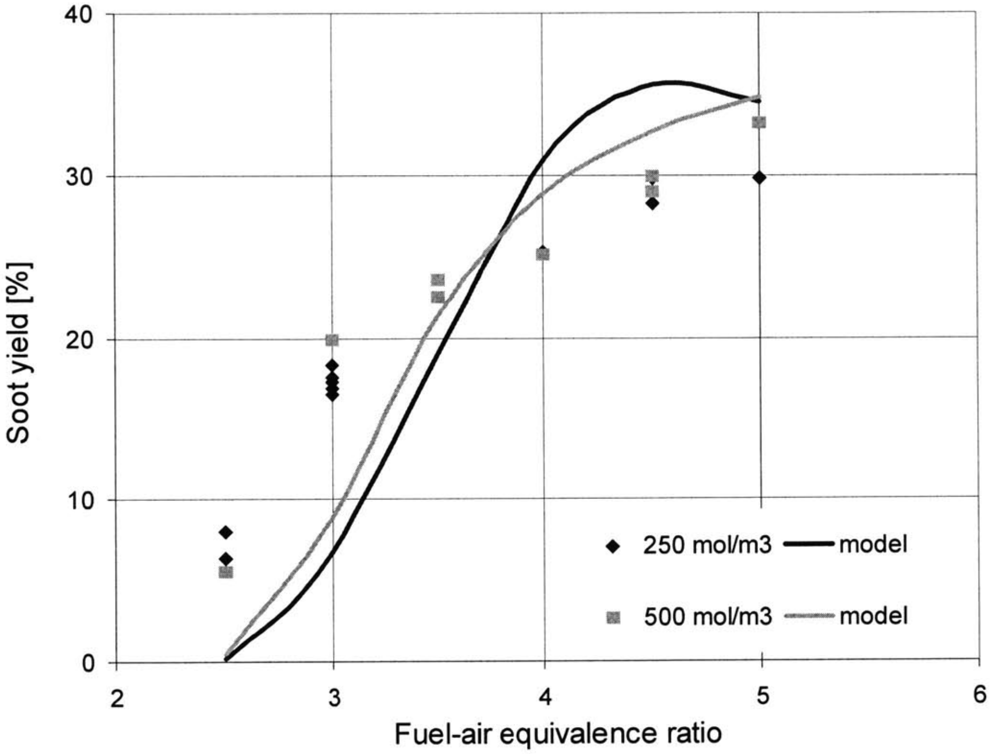

Figure 6.26 Soot yield experimental data and modeling results of n-butane/Ar/O_2 mixtures (Ar/O_2=3.773) for $T_{comp, core}$ = 770 K.

6.4.3 Aromatics and oxygenates

Modeling a combustion system with detailed chemistry requires relying on the literature for most kinetic and thermal data describing hundreds of reactions and numerous species. Since adding the soot chemistry introduces many new unknown parameters in the system, this study focused on simple fuels, where their chemistry is relatively well understood. Therefore, n-butane was used as the base fuel in this study. In order to asses the effects of fuel structure on soot formation and acquire a more complete picture, experiments were conducted with different fuels as well. Toluene and DME were used as additives and their effects on soot yield and soot time constant were discussed above. Even though to develop a model including toluene and DME chemistry introduces some more uncertainties, the correlation between experimental data and this composite model regarding soot time constant and soot yield predictions is briefly discussed in this section.

Figure 6.27 and Figure 6.28 show the experimental data and modeling results for soot time constant and soot yield respectively when toluene is added to the base fuel. As the aromatic content in the fuel increases, both fuel structure and temperature history have an impact on the soot time constant. The model predictions of the experimental trends are very encouraging. The non-monotonic trend of the soot time constant is believed to be due to the competition between higher sooting tendency of toluene and its lower maximum temperatures. The trends of soot yield with increasing aromatic content are also reproduced but the model seems to overpredict toluene contribution to soot formation mechanisms. Even though when keeping the C/O ratio constant the effects are smaller, the model cannot reproduce the negligible effect of toluene in the soot formation process.

In Figure 6.29 and Figure 6.30 the corresponding trends when adding DME to the base fuel are depicted. For high DME concentrations, the soot levels are low and the soot time constant cannot be easily defined. However, at least for the DME concentrations shown, the model captures the experimental trends reasonably well. More importantly, the model is capable of predicting the soot yield trends, which have been also reported in the literature. For ~30% of oxygen in the fuel by mass, almost no soot is generated even for fuel-rich mixtures. The model also performs well when the C/O ratio is constant where the drop in soot yield is not that fast (actually the model predicts a slight rise) with increasing the DME content in the fuel. The very fast drop ~15% oxygen in fuel by mass, must be related to temperature drop in the mixture, as Figure 6.9 suggests. The effects of temperature on soot formation are discussed extensively in the next chapter.

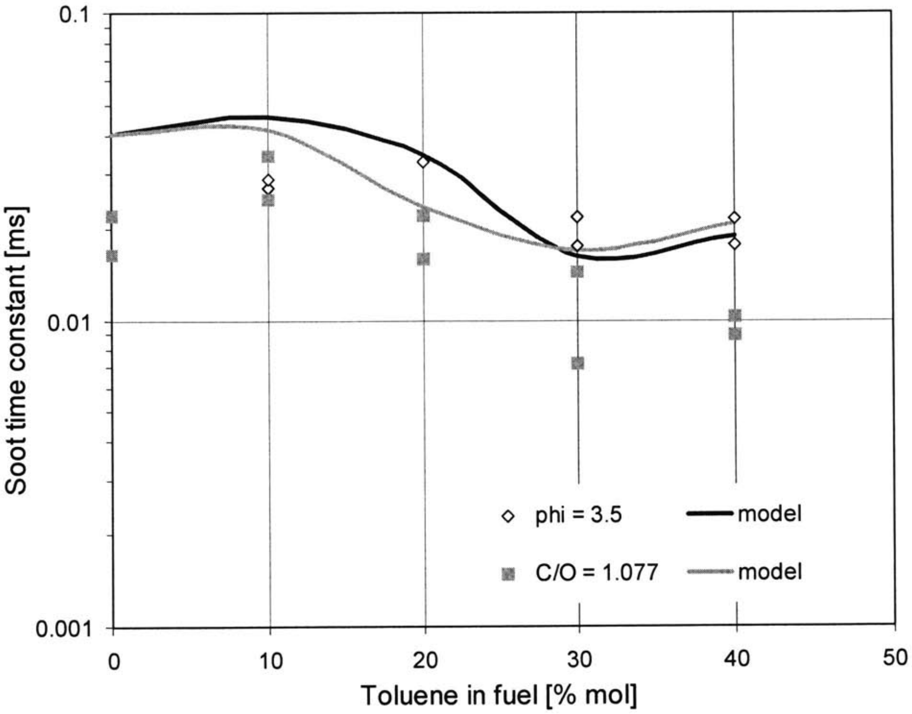

Figure 6.27 Soot time constant experimental data and modeling results of n-butane/toluene/Ar/O_2 mixtures (Ar/O_2=3.773) for $T_{comp, core} = 770\,K$, $N_{comp} = 500\,mol/m^3$.

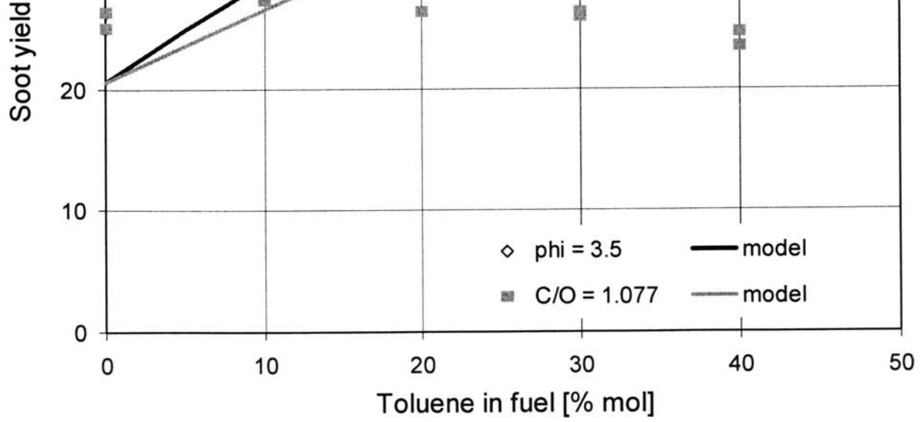

Figure 6.28 Soot yield experimental data and modeling results of n-butane/toluene/Ar/O_2 mixtures (Ar/O_2=3.773) for $T_{comp, core} = 770\,K$, $N_{comp} = 500\,mol/m^3$.

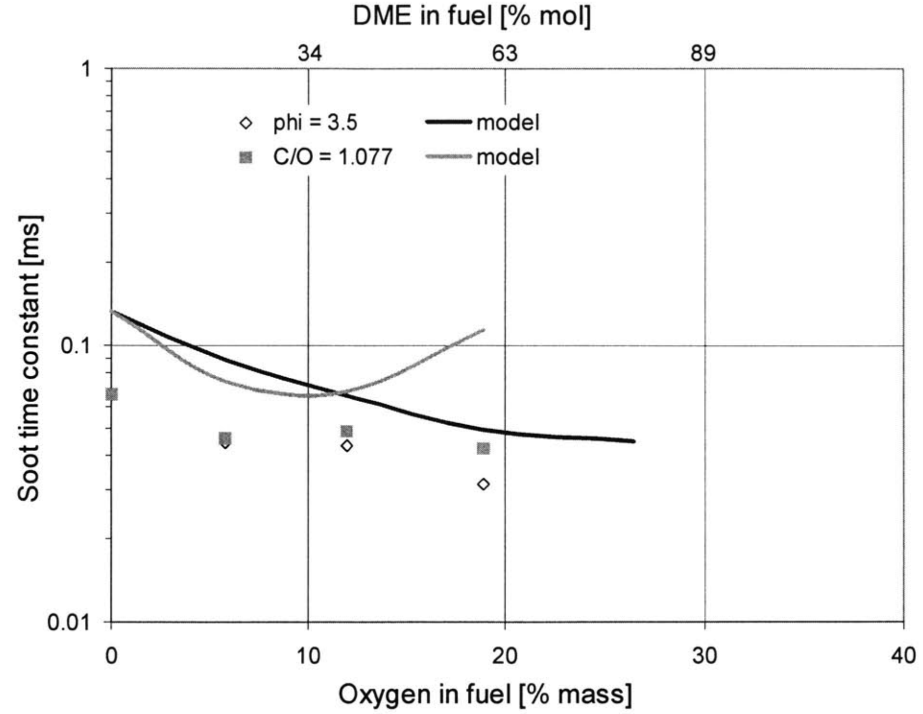

Figure 6.29 Soot time constant experimental data and modeling results of n-butane/DME/Ar/O_2 mixtures (Ar/O_2=3.773) for $T_{comp,core}$ = 715 K, N_{comp} = 450 mol/m^3.

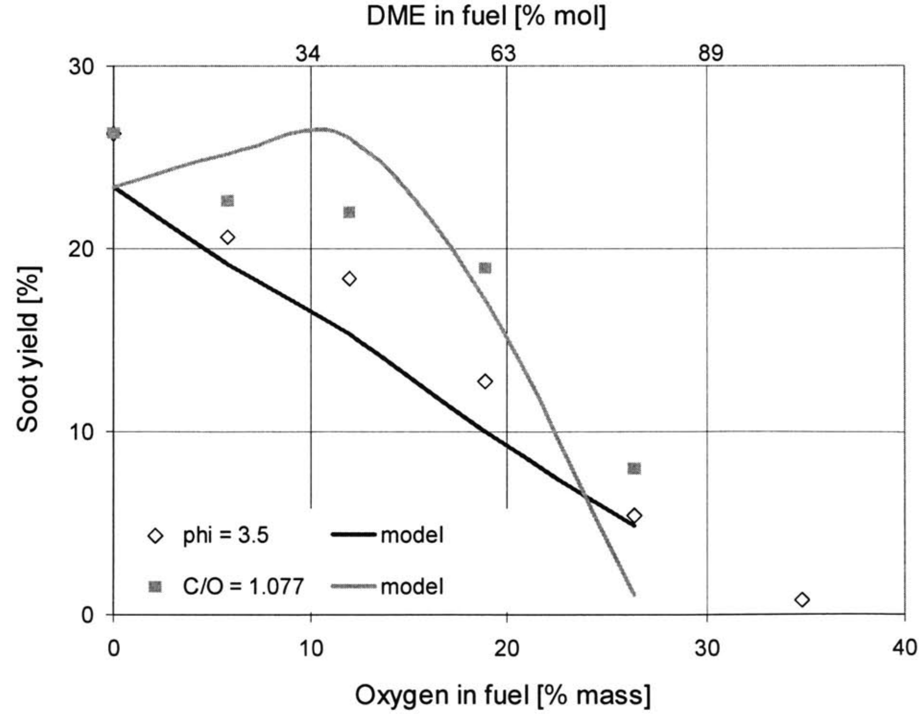

Figure 6.30 Soot yield experimental data modeling results of n-butane/DME/Ar/O_2 mixtures (Ar/O_2=3.773) for $T_{comp,core}$ = 715 K, N_{comp} = 450 mol/m^3.

6.4.4 Onset of soot formation

When discussing the experimental results in Section 6.3.4, special attention was given at the onset of soot formation. It was shown that along with temperature, time is a critical parameter that determines when soot starts forming relative to the energy release. Temperature is important because energy barriers need to be overcome for reactions to take place and time because forming critical intermediates is a time-consuming process. Even though time is affected by temperature, these two parameters are not entirely dependent. Experimental data reported in Section 6.3.4 showed that longer ignition delays shifted soot formation onset consistently earlier relative to the energy release, i.e. to lower temperatures. This is a very interesting trend that the model is also able to reproduce to some extent as Figure 6.31 suggests. This graph is similar to Figure 6.16 but instead of experimental data, the modeling results are plotted. The trend is similar however, the effect of ignition delay, which represents the time a mixture remains at high temperatures, on soot formation onset is not as dominant as in the experiments.

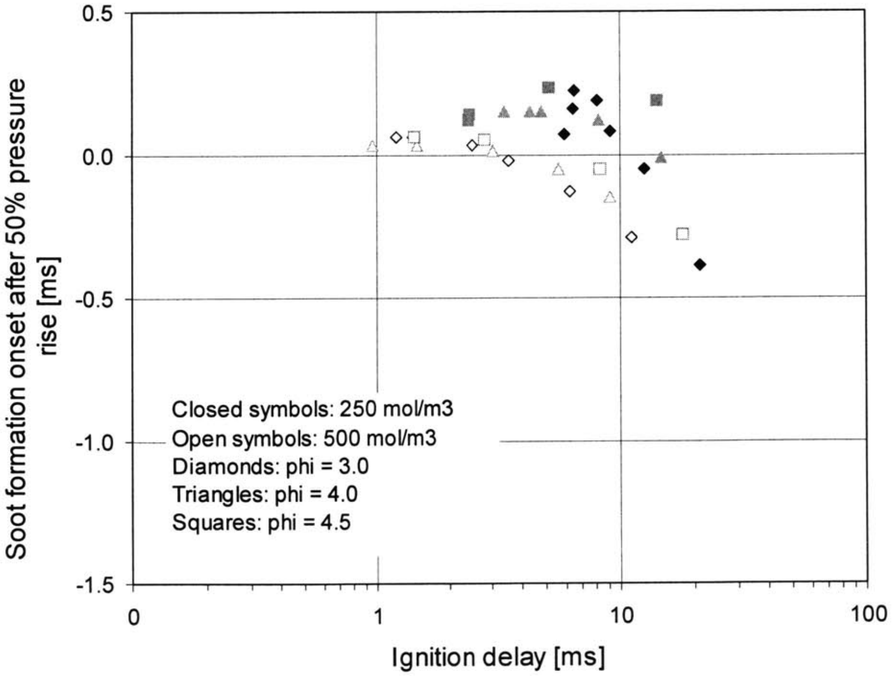

Figure 6.31 Ignition delay and onset of soot formation correlation (both modeling results) of n-butane/Ar/O_2 mixtures (Ar/O_2=3.773).

Despite the fact that the model reflects the impact of ignition delay on the onset of soot formation observed in the experiments, the absolute timing of soot formation onset relative to the energy release is consistently predicted at later times. Comparing Figure 6.16 and Figure 6.31, it is apparent that all experimental data points are shifted lower in the graph, which implies that soot formation onset occurs at earlier times than in the model. Note that the higher spread of the experimental data points is just due to inaccuracies in ignition delay prediction, which is not of particular concern at this point. The fact that soot onset i spredicted to start later than in the experiment is clearly seen in Figure 6.32. Defining as soot all species larger than 7 aromatic rings (BIN1 and higher, as described in Section 6.3), the model predicts the formation of the first soot particles to occur 0.37 ms later than in the experiments. As shown in the graph, this discrepancy is too high to be explained by experimental variability. If PAH with 3 aromatic rings and higher are also absorbing light, then the model could explain the experimental data. However, as discussed in Chapter 3, there is no evidence of such small species to absorb light in that wavelength, which is also proved by observing light luminosity starting at the same time with absorption. Moreover as Figure 6.32 indicates, the shape of soot growth rates are a little different because soot and PAH have different formation mechanisms. On the other hand, the employed laser light is more likely to be absorbed by even larger species (e.g. 1600 amu and higher), which would increase the discrepancy even more. To summarize, possible reasons for the observed discrepancy in soot formation onset between model and experiments and their potential contribution are the following:

- Experimental repeatability: extensive testing suggested that the repeatability does not exceed ±0.06 ms, which cannot explain the discrepancy
- Experimental error: tests have been conducted with different mixture preparation strategies (allowing for sufficient mixing before the start of compression), sampling

frequencies and data acquisition filtering and the results obtained were within the experimental repeatability.

- Higher temperature non-uniformities: apart from not being predicted by detailed CFD analysis, the predicted rate of pressure rise is closely matched with the experimental data, so thermal stratification should not be an issue any more.
- PAH absorption: To explain the experimental data small PAH with 3 aromatic rings should absorb the red light and there is no experimental or theoretical evidence for this.

Hence, the most possible reason for this discrepancy is the chemistry related to soot formation. A detailed sensitivity analysis of the soot model is performed in the next chapter giving more insight into the critical chemical processes leading to soot formation and how thay may differentiate for different temperatures and fuel-air equivalence ratios.

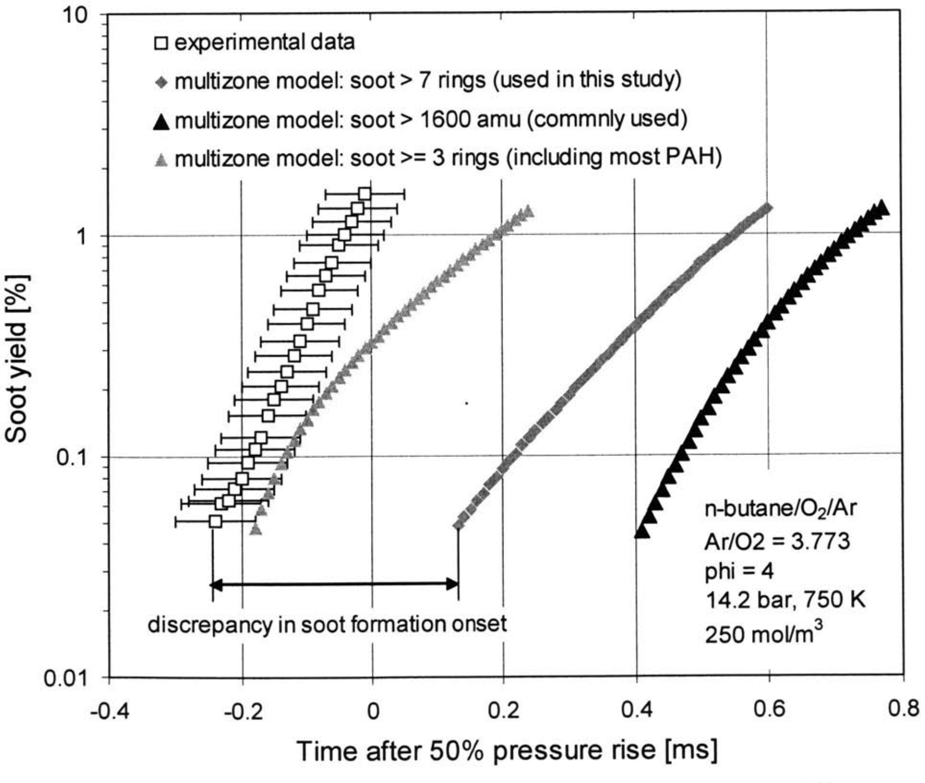

Figure 6.32 Comparisons of soot formation onset between experiment and different models under typical conditions.

Chapter 7

Soot Formation Model Sensitivity Analysis

7.1 Introduction

The soot formation chemistry is a very complicated process and developing a comprehensive kinetic model may require thousands of reactions and hundreds of species. Apart from uncertainties in chemistry, the complexity of all physical processes (temperature non-uniformities, heat transfer, flow into the crevice and so on) involved in any experimental system, like the RCM, obscure data interpretation and require substantial modeling efforts. Therefore, the correlation between experimental data and modeling results shown in the previous chapter is considered very encouraging.

In this chapter an extensive sensitivity analysis of the composite model leading to soot particles is performed. The major benefit of these models is that extreme conditions of temperatures and fuel-air equivalence ratios, which most experimental setups can hardly achieve, can be clearly studied giving valuable information. Particularly in this study the sensitivity of soot formation rate and soot yield to temperature, fuel-air equivalence ratio and certain chemical pathways is investigated. Such analysis aims to provide insight into the fundamental chemical processes leading to soot formation under various conditions pertinent to diesel engine operation. Questions in soot formation theory like the relative contribution of PAH and C_2H_2 on soot inception and surface growth processes that has caused major debates within the combustion community for many years, are extensively studied in this chapter. Understanding the most important pathways and identifying the critical species are the key steps in controlling engine-out PM levels. In addition, this approach gives the opportunity to study the reasons for poor agreement between modeling results and experimental data at soot formation onset and for less fuel-rich mixtures. The findings could be valuable for further model developments in the future.

7.2 Chemical Pathways and Fuel-Air Equivalence Ratio

In this section critical chemical pathways for soot formation are identified. Their impact on model predictions is evaluated and the correlation with the experimental data regarding the soot time constant and soot yield is discussed. In particular, the sensitivity of soot formation to the following chemical channels was investigated:

- *Formation of the first aromatic ring.* One scenario assumed that the first aromatic ring does not decompose (irreversible step) and the other, that the single-ring aromatics do not oxidize. Then, the conjecture that under some conditions the formation of the first aromatic ring is a "bottleneck" in the whole process could be evaluated.
- *Soot particle inception.* The impact of PAH coalescence as opposed to PAH growth due to C_2H_2 leading to the incipient soot particles is assessed. These two different channels are blocked one at a time and soot formation rates are calculated.
- *Surface growth of soot particles.* The relative contribution of different growth species like PAH and C_2H_2 during particle surface growth, which significantly increases soot loading, is determined. Similarly to the above case, each channel is blocked at a time.
- *Particle coagulation.* Even though coagulation does not directly affect the soot mass, its potential to change the kinetics in the system is examined. To clearly observe this trend, particle coagulation is halted and the effects are recorded.
- *Soot and PAH oxidation.* Regardless the fuel-rich environment, oxidation of large species and soot particles does take place especially with OH. The role of oxidation in the chemical kinetic model is evaluated by not allowing it to occur.

- *Thermal properties of C_2H_2.* C_2H_2 has long been recognized as a soot precursor playing a critical role in PAH growth, soot particle inception and surface growth. The sensitivity of model predictions to the thermal properties of C_2H_2 is studied by decreasing the standard entropy of formation by 2 cal/mol/K (original value: 48 cal/mol/K). This change is expected to prevent the species formed by C_2H_2, like PAH, from decomposing, by increasing the equilibrium constant of the relevant reactions at a given temperature and shifting the equilibrium towards the formation of larger aromatic species and eventually soot.

The sensitivity analysis was performed under $T_{comp,core} = 770\,\mathrm{K}$ and $N_{comp} = 500\,\mathrm{mol/m^3}$ for $\phi = 3$ and $\phi = 4.5$. Even though the compression core temperature is the same, the temperature history during soot formation is different because of the different fuel-air equivalence ratio. As a result, the maximum temperatures achieved in each case were 2260 K and 1882 K respectively. The modeling results (bars) along with the experimental data (lines) of soot yield and soot time constant are summarized in Figure 7.1 and Figure 7.2 respectively, where the base model corresponds to zero sensitivity. As already stressed out in the previous chapter, unlike less fuel-rich mixtures, the experimental data under fuel-rich conditions correlate well with the base model (within 15%) for both soot yield and soot time constant.

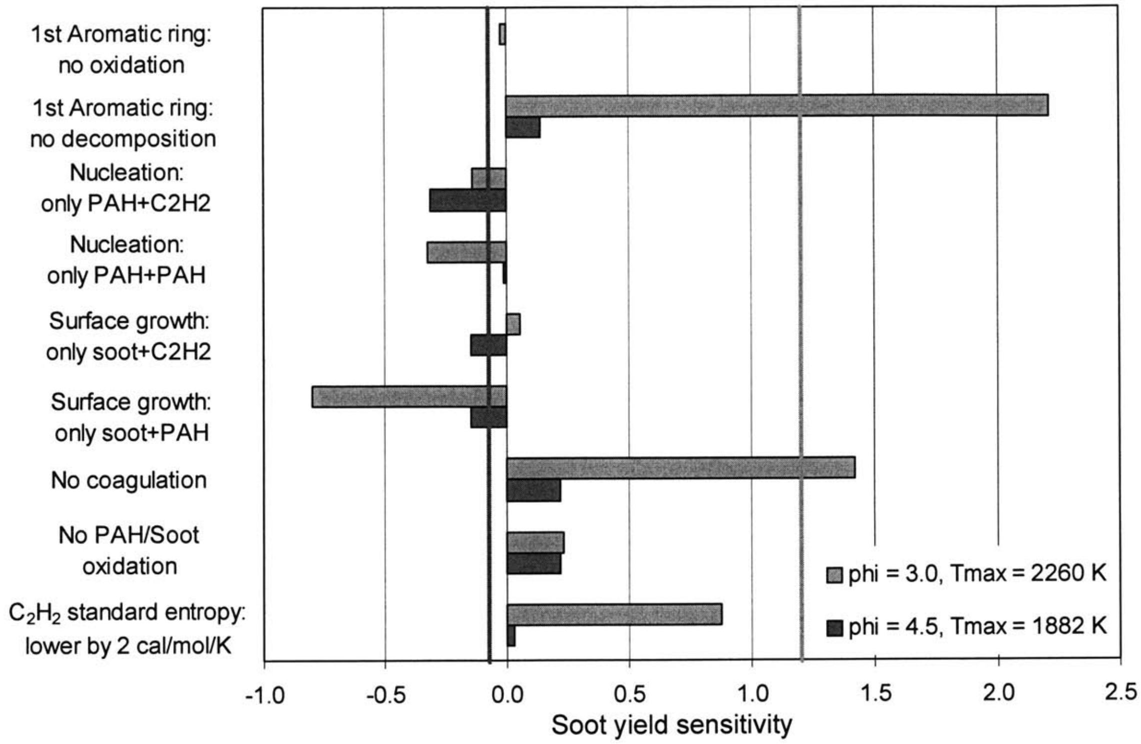

Figure 7.1 Soot yield sensitivity analysis and experimental data for $T_{comp, core} = 770$ K and $N_{comp} = 500$ mol/m^3.

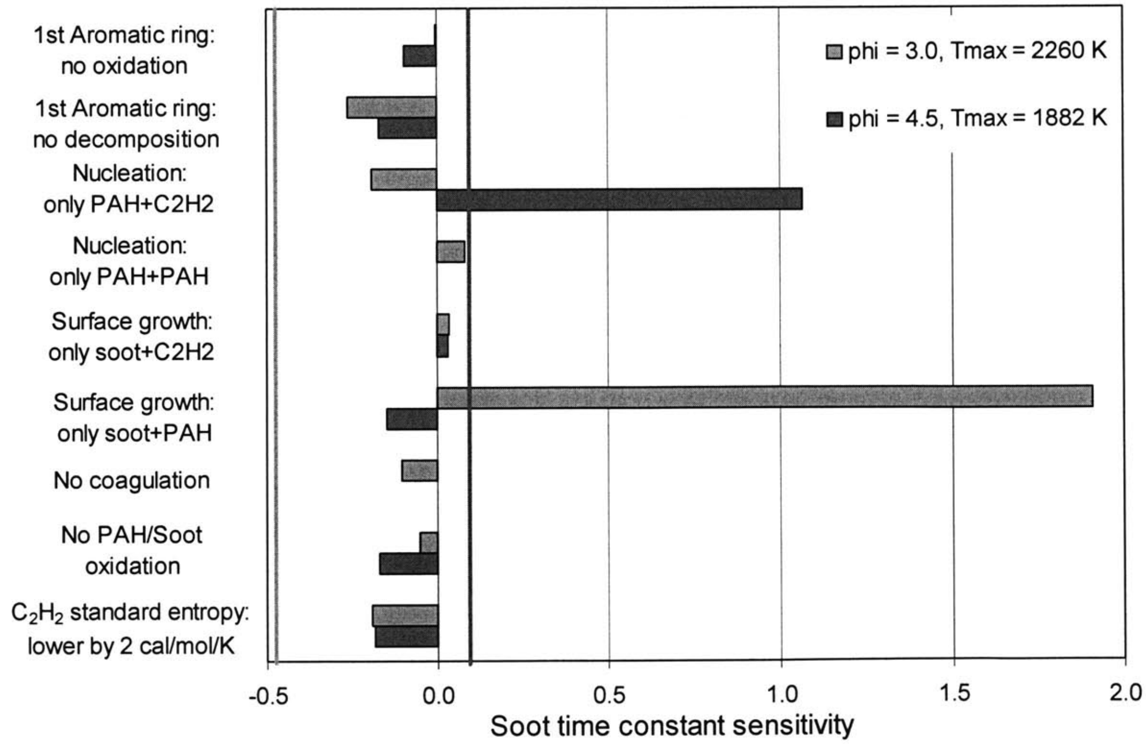

Figure 7.2 Soot time constant sensitivity analysis and experimental data for $T_{comp, core} = 770$ K and $N_{comp} = 500$ mol/m^3.

The oxidation of the first aromatic ring has only a modest effect on soot yield and soot time constant for both operating conditions tested. Conversely, assuming that no decomposition takes place, both the soot yield and rate of soot formation increase. The impact is much more predominant for less fuel-rich mixtures at high temperatures because under these conditions aromatic rings become thermodynamically unstable limiting the formation of soot. The agreement with the data becomes better at these conditions and worse at richer mixtures and lower temperatures. The relative importance of PAH coalescence and PAH-C_2H_2 reactions on soot particle inception depends on the operating conditions. For lower temperatures and very fuel-rich mixtures PAH coalescence governs entirely the soot nucleation process. No sensitivity of both soot yield and soot time constant is observed under these conditions as long as the PAH-PAH channel remains active. On the other hand, for higher temperatures, less fuel-rich mixtures the PAH-C_2H_2 channel significantly contributes to soot nucleation and when omitted soot yield drops by ~20% compared to ~40% when the PAH-PAH channel is omitted. Interestingly, under these conditions blocking the PAH-PAH route, soot time constant decreases because then C_2H_2 is exclusively used for nucleation rather than formation of higher PAH species. Since the soot time constant describes the early stage of soot formation and therefore the nucleation rates, it shows higher sensitivity than the soot yield results. Similarly to soot nucleation, the relative roles of PAH and C_2H_2 as surface growth species are determined by the operating conditions. Under less fuel-rich and high-temperature conditions surface growth is exclusively determined by C_2H_2, while the contribution of PAH and C_2H_2 under for rich mixtures at lower temperatures is approximately the same for the final soot yield. As already stated above, coagulation may not be able to affect directly the final soot yield, however, it could change the kinetics of the system significantly. Blocking coagulation the number of particles in the system increases substantially, which more than offsets the drop of collision theory rate constant due to smaller diameters. Therefore, the higher collision frequencies between soot particles and PAH/C_2H_2 increases the soot yield. This is clearly depicted in Figure 7.1, especially for higher temperatures, where collision frequencies increase even more. Since coagulation proceeds at very modest rates during soot nucleation, as already shown in Figure 6.22, the soot time constant is barely affected by coagulation. Soot and PAH oxidation have modest impact on soot yield and soot formation rate for both conditions tested. Blocking oxidation completely, results in less than 25% changes, which implies that some uncertainty in oxidation rates have minor effect on the model. Even though the thermal properties of C_2H_2 are known with accuracy (±0.5 cal/mol/K), a sensitivity analysis was performed regarding its standard entropy of formation. Since C_2H_2 is a very important species in the soot formation process, error propagation from uncertainties in its thermal properties are evaluated. As Figure 7.1 and Figure 7.2 show, changing the standard entropy of formation of C_2H_2 by 2 cal/mol/K has a significant impact on model results and especially on soot yield. Higher amounts of soot are formed and the model predictions come closer to the experimental data. This finding implies the necessity for even better estimation of the thermal properties of species critical in soot formation.

In Figure 7.1 and Figure 7.2 the critical chemical pathways for soot formation were identified and a sensitivity analysis was performed to evaluate their contribution to mixtures with different fuel-air equivalence ratios. Even though the same compression conditions were used, the resulting maximum temperature was different making data interpretation ambiguous. The observed trends of the sensitivity analysis could be attributed to either different fuel-air equivalence ratios or maximum temperatures. To assess the fuel-air equivalence ratio impact alone on the sensitivity analysis results shown above, the maximum temperature was fixed to around 1870 K by changing the diluent of the less fuel-rich mixture. In particular, an artificial diluent with higher heat capacity was used while keeping the diluent/O_2 ratio the same so that collision frequencies are the same. A similar sensitivity analysis was performed and the results are shown in Figure 7.3 and Figure 7.4. Note that the richer case ($\phi = 4.5$, $T_{max} = 1882\,K$) was also shown in Figure 7.1 and Figure 7.2. It is evident from Figure 7.3 that the sensitivity of soot yield to different chemical channels, critical to soot formation, is similar for both fuel-air equivalence ratios ($\pm 20\,\%$). Conversely, the sensitivity of soot time constant to chemical pathways shown in Figure 7.4, exhibit some differences for highly and less fuel-rich mixtures under the temperature regime tested. Soot surface growth by PAH is accelerated for fuel-rich and decelerated for less fuel-rich mixtures. This must be attributed to the fact that under less fuel-rich mixtures C_2H_2 concentration is higher and surface growth is mostly based on it. Also, due to higher PAH concentrations, highly fuel-rich mixtures are more sensitive to PAH oxidation and C_2H_2 entropy of formation, which is mostly responsible for building up large PAH. On the other hand, it is apparent that for the temperature regime tested nucleation is governed exclusively by PAH coalescence for both mixture types. As already stated above, the sensitivity analysis trends regarding the soot yield are similar for very rich and less rich mixtures. This implies that the different trends observed in Figure 7.1 must be attributed to different temperature regimes. The sensitivity of soot formation to temperature is studied in detail in the next section.

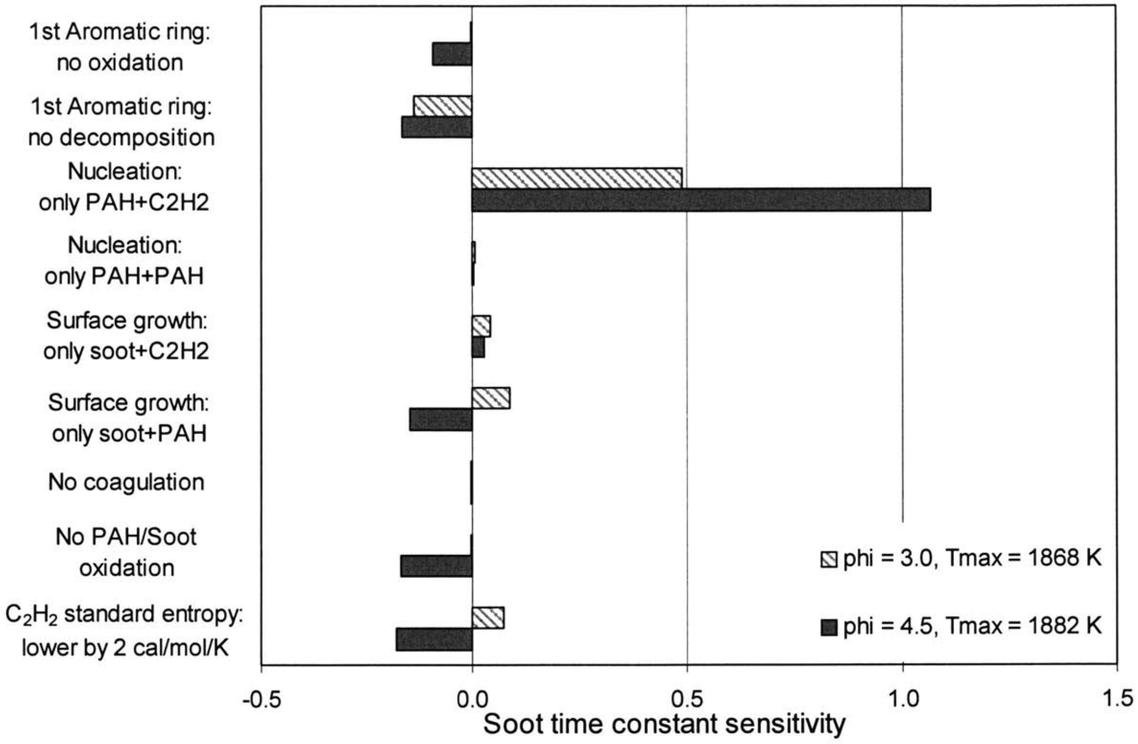

Figure 7.3 Soot yield sensitivity analysis for $T_{comp,\,core}$ = 770 K and N_{comp} = 500 mol/m^3 for similar maximum temperatures.

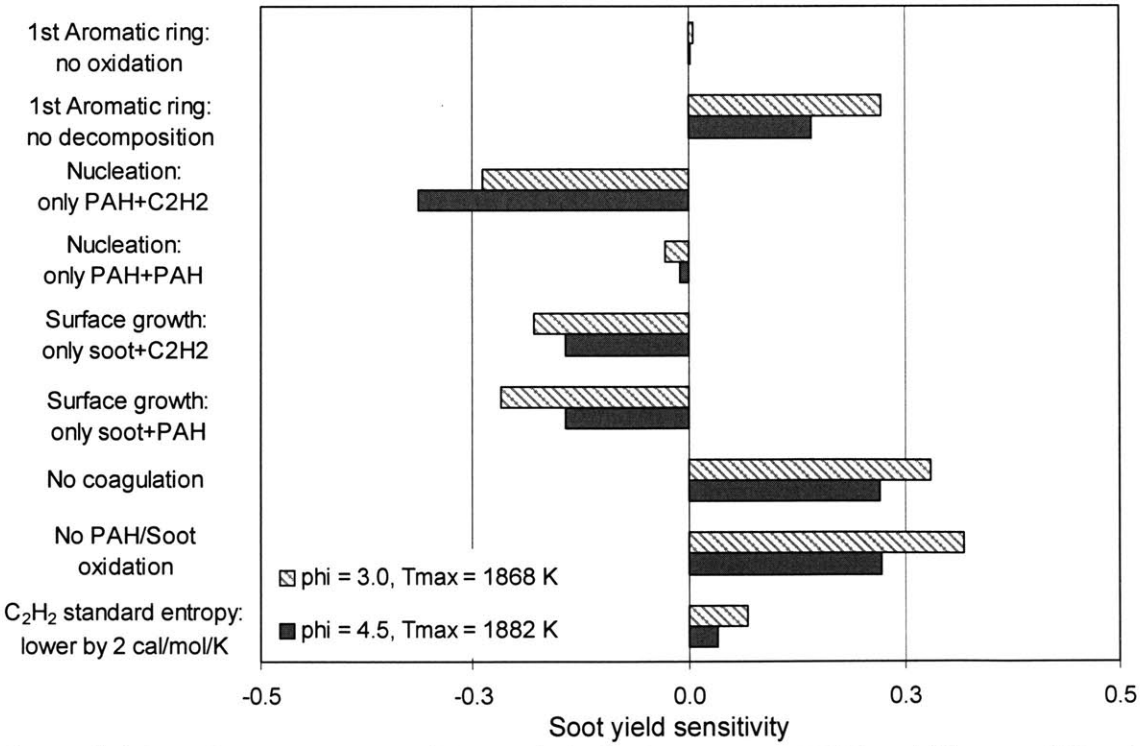

Figure 7.4 Soot time constant sensitivity analysis for $T_{comp,\,core}$ = 770 K and N_{comp} = 500 mol/m^3 for similar maximum temperatures.

7.3 Chemical Pathways and Temperature

Both experimental data and modeling results showed higher soot yield levels for higher fuel-air equivalence ratios. Despite the fact that it is not surprising, one cannot exclusively attribute this trend to the mixture itself since the temperature regime seems to change significantly as well. According to Figure 6.5 soot yield increases from ~5% to ~35% when the fuel-air equivalence ratio goes from 2.5 to 5.0 for the same compression temperature but then the maximum temperature (calculated in Figure 6.4) drops from ~2600K to ~1800K. Unless the effect of temperature on soot formation is well-established, no safe conclusions can be drawn about the impact of fuel-air equivalence ratio. Keeping similar temperatures at the end of combustion across the whole range of fuel-air equivalence ratios cannot be simply achieved by modifying compression temperature, since its range is limited between 700-900K. Alternatively, a mixture with low specific heats to balance out the high heat capacity of the fuel for richer mixtures would be required. This could be achieved either by modifying the diluent to oxygen ratio or changing the diluent itself. The former approach, which is widely used in shock tube studies, would result in much less frequent collisions between reacting molecules (due to low fuel concentration) and lower heat release for richer mixtures, that could potentially change the soot formation regime. The latter approach on the other hand, affects only the thermal environment[1]. However, there are not that many inert gases with so different heat capacities to cover the entire desirable range. Even though studying the effects of temperature alone involves practical challenges in a laboratory environment, it is a much simpler task to accomplish computationally. Hence, in this study artificial diluents with the desirable specific heats were employed to investigate temperature effects alone on soot formation. At this point only the soot yield trends with temperature were studied. Figure 7.5 shows some typical trends.

---

[1] Collision efficiency changes in three-body reactions are considered to have a minor effect.

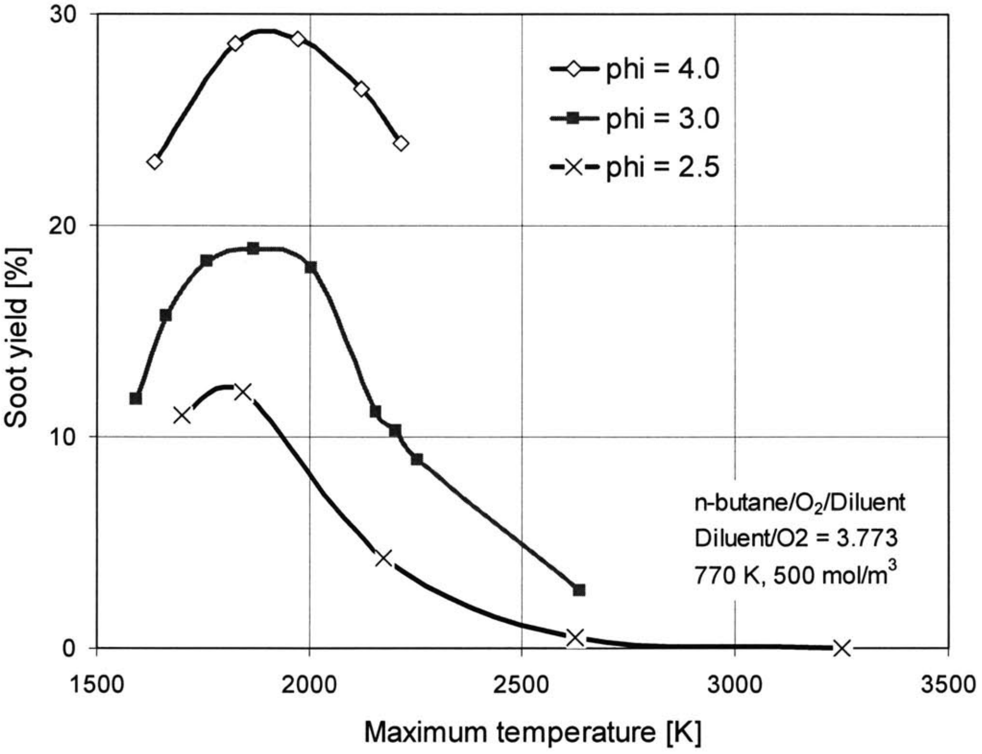

Figure 7.5 Modeling results of temperature effects on soot yield

The model predicts a bell-shape dependence of soot yield on temperature. This trend has been previously reported in the literature by both experimental [43-46] and computational studies [49, 56] under different conditions and it is encouraging that the model reproduces this behavior. There is a pronounced maximum in soot yield with temperature between 1800K and 2000K, which seems to shift slightly to lower temperatures as the mixture becomes less fuel-rich. These modeling results can explain the continuously decreasing slope of soot yield with fuel-air equivalence ratio observed experimentally and depicted in Figure 6.5. According to the calculations of Figure 6.4, the temperature dropped, bringing the soot yield to the lower temperature bound of the bell. Furthermore, the trend for fuel-air equivalence ratio of 2.5 suggests that the soot formation threshold changes significantly with temperature. This observation implies that a possible error in temperature calculation could be the reason for model's inability to predict soot for such mixtures. A more extensive discussion of these discrepancies is following in Section 7.4.

Frenklach et al. [49] conjectured that the competition between kinetic and thermodynamic factors is responsible for this bell-shape behavior of soot yield with temperature. In particular, he argued that decomposition reactions are rate limited at low temperatures and at higher temperatures aromatic radicals, which are key intermediates, are not stable and they decompose before building up to form soot particles. At very high temperatures, fragmentation of even single-ring aromatics is suggested. In this study, a more extensive analysis identifying also the dominant chemical pathways under different temperatures is performed in order to interpret the trend depicted in Figure 7.5.

The sensitivity analysis was carried at typical conditions of this study: $\phi = 3$, $N_{comp} = 500\,\mathrm{mol/m^3}$, $T_{comp,core} = 770\,\mathrm{K}$ using different diluents resulting in different temperatures after the end of combustion. These temperatures were chosen so that the entire range of soot formation dependence on temperature was included. The results are summarized in Figure 7.6. Note that the base model results were previously reported in Figure 7.5. Two temperatures (~1600K and ~2150K respectively) correspond to similar soot levels (~11.5%) and an intermediate temperature (~1850K) to maximum soot yield (~19%). The sensitivity of soot yield to critical chemical channels of soot chemistry at different temperature regimes is shown in Figure 7.6 and it is discussed below:

- At higher temperatures the soot yield is limited by the competition of formation and fragmentation of soot precursors. The intermediate species, like PAH, leading to soot particles are not thermodynamically stable at these high temperatures and they decompose to smaller species containing 2 or 3 carbon atoms, which readily oxidize. At very high temperatures the fragmentation reactions of these species are so severe that decomposition is practically taking place at even the first-ring level. This is clearly shown in Figure 7.6, where if no single-aromatic decomposition is assumed, soot levels steadily go up with temperature, while oxidation of the single-ring aromatics has minor impact even at high temperatures. Also, soot and PAH oxidation has only a modest effect on the model results and the trend is very similar for the entire temperature regime.

- Conversely, at lower temperatures the soot yield is kinetically limited. Soot formation rates are very slow and when the characteristics of a physical system, like finite reaction time and heat transfer, are taken into account, soot levels diminish substantially. Therefore, soot yield increases if critical processes like soot nucleation and/or H-atom abstraction from soot particles (so that they can readily react with gaseous surface growth species) are occurring at considerably higher rates (pre-exponential factor increased by an order of magnitude in Figure 7.6). Unlike the higher temperature regime, sensitivity to single-ring decomposition is minor implying that thermodynamics is not limiting soot formation at these temperatures.
- Since different factors are responsible for limiting soot yield at different temperature regimes, soot formation mechanisms do change, as expected, across the entire temperature range. For higher temperatures thermodynamic instability of intermediate species limits PAH concentrations and C_2H_2 is mostly responsible for soot surface growth. As Figure 7.6 suggests, removing the soot-PAH channel has minor impact on the final soot yield, which drops by more than a factor of 3 if the soot-C_2H_2 route is blocked. Conversely, at lower temperatures C_2H_2 concentration is lower because it contributes to PAH formation, which are now much more stable. According to Figure 7.6, blocking the soot-PAH pathway under these conditions is detrimental for soot yield, without though the contribution of the soot-C_2H_2 route becoming negligible. Based on the results of the sensitivity analysis performed in this study for n-butane

and $\phi = 3$, the relative contribution of PAH and C_2H_2 to soot surface growth as a function of temperature, is shown graphically in Figure 7.7. The calculation is performed in a fairly simple-minded way assuming that blocking each chemical channel for surface growth, the other route is not considerably affected. This analysis is just an illustration of the relative contribution of PAH and C_2H_2 on surface growth, which has long been a field of major debate within the combustion community. PAH are responsible for 2/3 and C_2H_2 for 1/3 of surface growth at lower temperatures, while at higher temperatures C_2H_2 is the only surface growth species. The negative values of PAH contribution at very high temperatures reflect the fact that PAH inhibit soot growth by consuming C_2H_2 for their own growth without them contributing to soot growth but subsequently decomposing to small species that can readily oxidize.

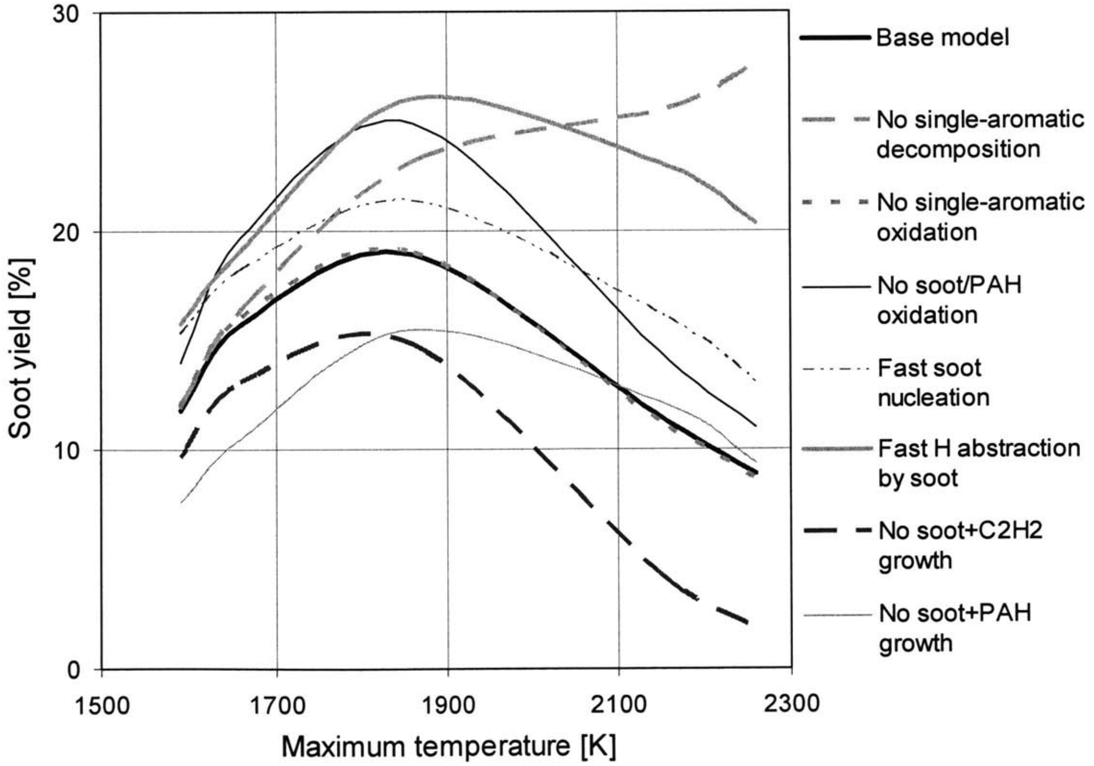

Figure 7.6 Sensitivity analysis of soot yield to critical chemical channels of soot chemistry for different temperature regimes at typical testing conditions: n-butane/O_2/Ar, Ar/O_2 = 3.773, $\phi = 3$, $T_{comp,\,core} = 770$ K, $N_{comp} = 500$ mol/m^3.

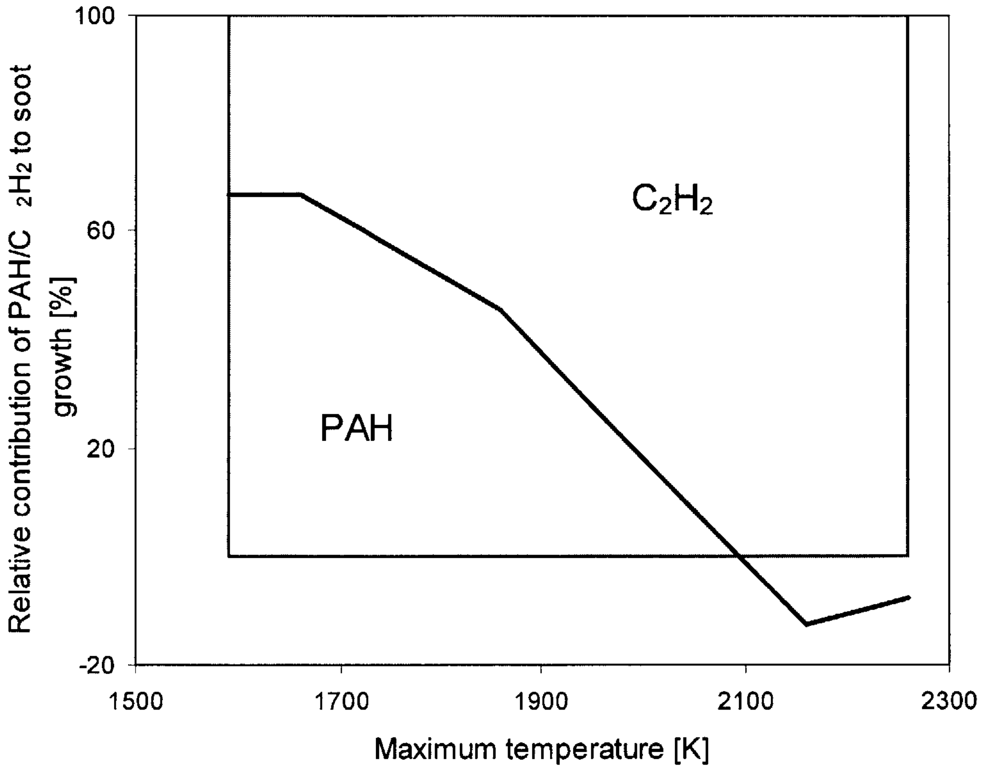

Figure 7.7 Relative contribution of PAH and C_2H_2 to soot surface growth as a function of temperature at typical testing conditions: n-butane/O_2/Ar, Ar/O_2 = 3.773, $\phi = 3$, $T_{comp,core} = 770$ K, $N_{comp} = 500$ mol/m^3.

Despite the fact that soot yield reaches very similar soot levels (~11.5%) at two different temperatures (~1600K and ~2150K), the different soot formation mechanisms imply that the composition of gas-phase species after combustion is very likely to be different. A very illustrative representation of carbon distribution during combustion and soot formation processes providing insight into the species that carbon atoms are stored in, is given by carbon diagrams. A typical diagram was shown in Figure 6.21 and the corresponding details of particle distribution in Figure 6.22. The carbon diagrams along with particle distribution details and temperature evolution for the above two cases, which produce similar soot levels are shown in Figure 7.8 and Figure 7.9 respectively. The most important observations are summarized below:

- The time scale of soot evolution is very different, even though combustion proceeds at comparable rates for both cases. At lower temperatures the soot formation is very slow lasting for tens of milliseconds, while at higher temperatures final soot yields are reached within a couple of milliseconds. This is an important point if residence time is short and competing processes are taking place simultaneously, like in a diesel engine.

- Even though both cases exhibit similar final soot levels, at higher temperatures the amount of carbon oxidized to CO (CO_2 and CH_4 are also part of the stable products but their carbon yield is typically less than 10%) is around 90%, while at lower temperatures less than 75%. In the latter case a significant amount of carbon is tied up to PAH, single-ring aromatics and species with 2 or 3 carbon atoms, which are fairly stable not being able to oxidize or contribute significantly to soot growth. Hence, the lower temperature regime favors the formation of hydrocarbons, which are kinetically limited and cannot form soot, while at higher temperatures a higher fraction of carbon is oxidized.
- It is also worth noting that the particle size distribution is not the same for different temperatures, despite similar soot yield levels. At higher temperatures the particle number density is around 30 times smaller than that at lower temperatures. Consequently, shortly after ignition the average diameter almost reaches its maximum value of 16 nm (see Table 6.1), which is considerably larger than the 1.5 nm diameter particles observed when most of the soot is formed at lower temperatures. This observation in conjuction with recent findings about health effects of smaller particles [3] may have significant implications about the desirable operating regime of a combustion system.

To summarize, the fact that soot yield levels can be the same for totally different temperature regimes, does not imply that the underlying chemical processes are similar. At higher temperatures large hydrocarbon species contributing to soot formation and growth are not stable and they decompose to smaller species that can be readily oxidized. At lower temperatures though, these species are very stable and even though they may not form soot, at least right away, they "reserve" a significant amount of carbon that cannot be oxidized. Soot formation in this case is slower but these hydrocarbon species, mostly PAH, are formed relatively fast, within the time scales of typical combustion systems, like a diesel engine. The high concentrations of these species, which are considered carcinogenic, along with the large number densities and small average diameters of soot particles at lower temperatures, raise questions about the merits of low-temperature, fuel-rich combustion concept, which has been recently proposed simultaneously low soot and NO_x levels [56].

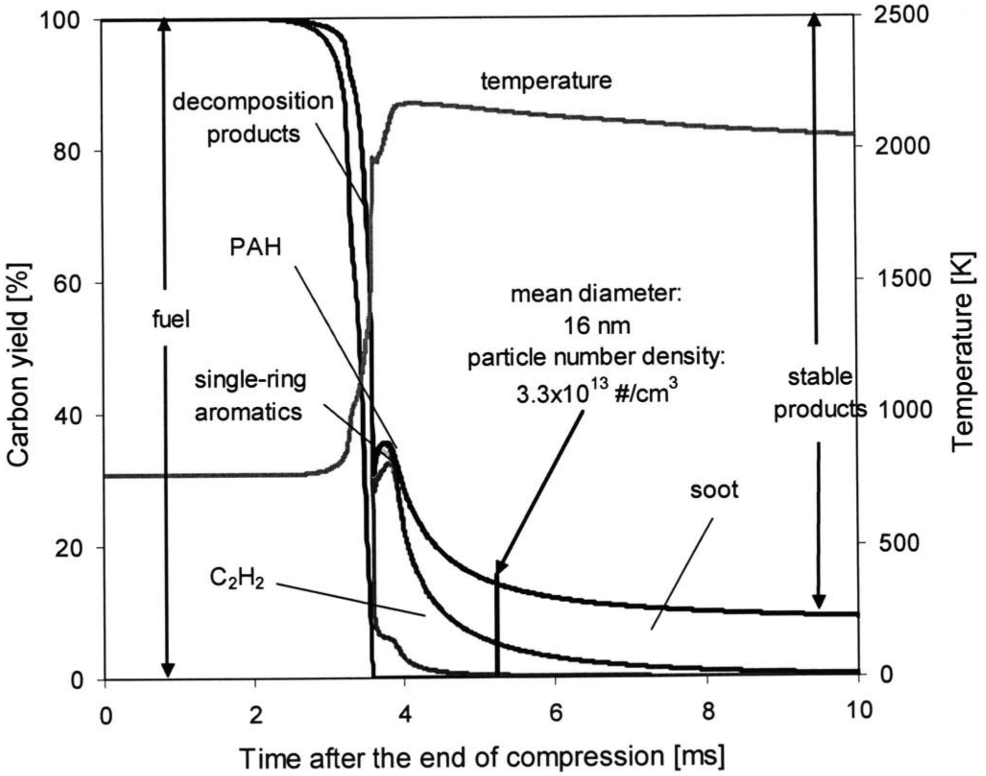

Figure 7.8 Carbon diagram, temperature history and particle size distribution for n-butane/O_2/Ar mixture ($Ar/O_2 = 3.773$) for $\phi = 3$, $T_{comp, core} = 770$ K, $N_{comp} = 500$ mol/m^3 and $T_{max} = 2150$ K.

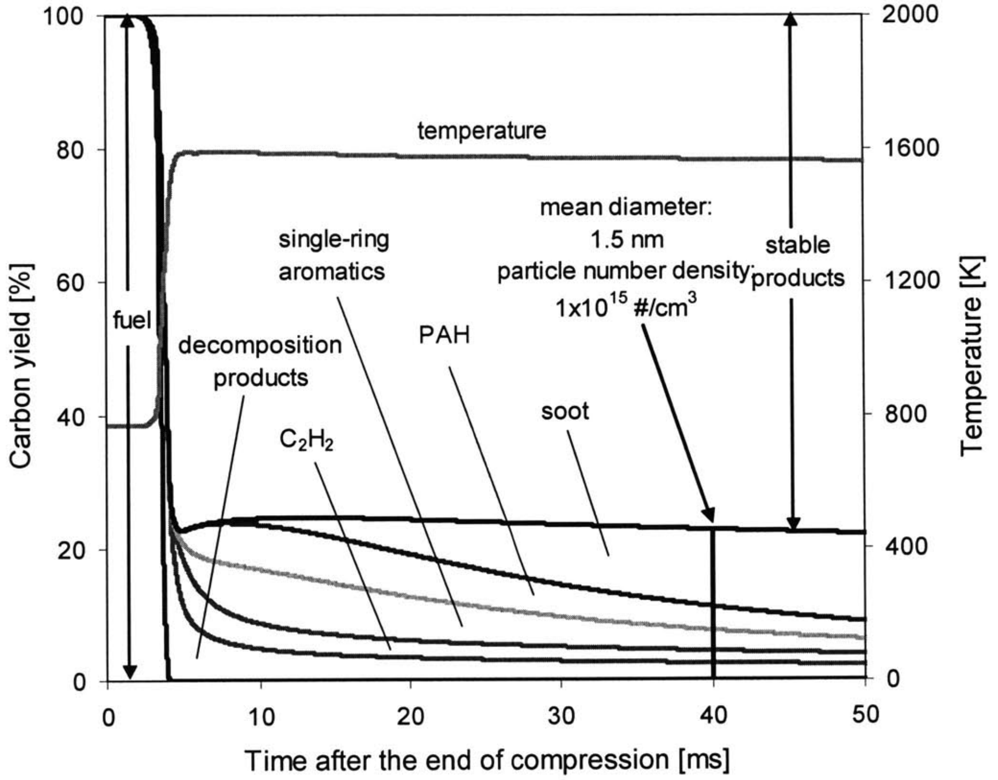

Figure 7.9 Carbon diagram, temperature history and particle size distribution for n-butane/O_2/Ar mixture (Ar/O_2 = 3.773) for $\phi = 3$, $T_{comp,\,core} = 770$ K, $N_{comp} = 500$ mol/m^3 and $T_{max} = 1600$ K.

7.4 Discussion of Model Discrepancies

The agreement between the experimental data and the modeling results presented in Chapter 6 is considered very encouraging especially if the complexities of the chemical and physical processes involved are taken into account. Despite the good correlation, the model failed to sufficiently predict the early onset of soot formation (relative to the heat release) observed in the experimental data and the soot formation threshold with regard to fuel-air equivalence ratio. In particular, the model predicted soot to start forming ~0.3 ms later than the experiments for very similar pressure traces and the soot formation threshold to occur at $\phi \cong 2.5$ instead of $\phi \cong 2$ under typical conditions.

The soot formation onset discrepancy was also discussed in Section 6.4.4, where a sensitivity analysis of all parameters, other than chemical, was performed. It was found that the discrepancy is highly unlikely to be attributed to factors like PAH absorption, CFD uncertainties and experimental errors. It is now speculated that chemistry or thermodynamic properties of critical species could be responsible for the disagreement. To illustrate this, Figure 7.10 compares the soot formation onset of experimental data with different chemical kinetic models. When assuming an order of magnitude higher soot nucleation rates for example, soot starts forming earlier relative to the heat release but not that much to explain the experimental data. Similar conclusions can be drawn if the standard entropy of formation of C_2H_2 was decreased by 2 cal/mol/K, which according to the literature though, is known more accurately than that. What is less accurately known though is the thermal properties of larger species like PAH. In Figure 7.10 instead of explicitly investigating the impact of their thermal properties, it is assumed that the PAH growth chemistry is irreversible, which implies that PAH are more stable. In that case soot formation onset shifts earlier relative to the heat release and closer to the experimental data implying that PAH properties are critical and more research efforts in this field should be performed. Irreversibility of the processes responsible for the formation of the first aromatic ring, on the other hand, does not seem to change the picture substantially under the conditions tested. Apart from uncertainties in the kinetics of soot formation chemistry and in the thermodynamic properties of critical species, the possibility of missing chemical channels leading to soot formation especially at the initial stages cannot be ruled out. For example, the carbon diagram in Figure 6.21, which corresponds to the conditions shown in Figure 7.10, predicts a considerable amount of carbon stored initially to decomposition products like olefins and aldehydes. Ethylene (C_2H_4), which stores more than 20% of the carbon at this stage, is considered a major soot precursor because it forms C_2H_2, which later contributes to soot particle inception and surface growth. If C_2H_4 could contribute to soot nucleation and growth directly, at least at these early stages, bypassing the time-consuming C_2H_2 formation, soot particle inception could take place faster. Even though explicit soot-C_2H_4 channels have not been reported in the literature, future studies are encouraged towards this direction due to the high concentration and reactivity of C_2H_4.

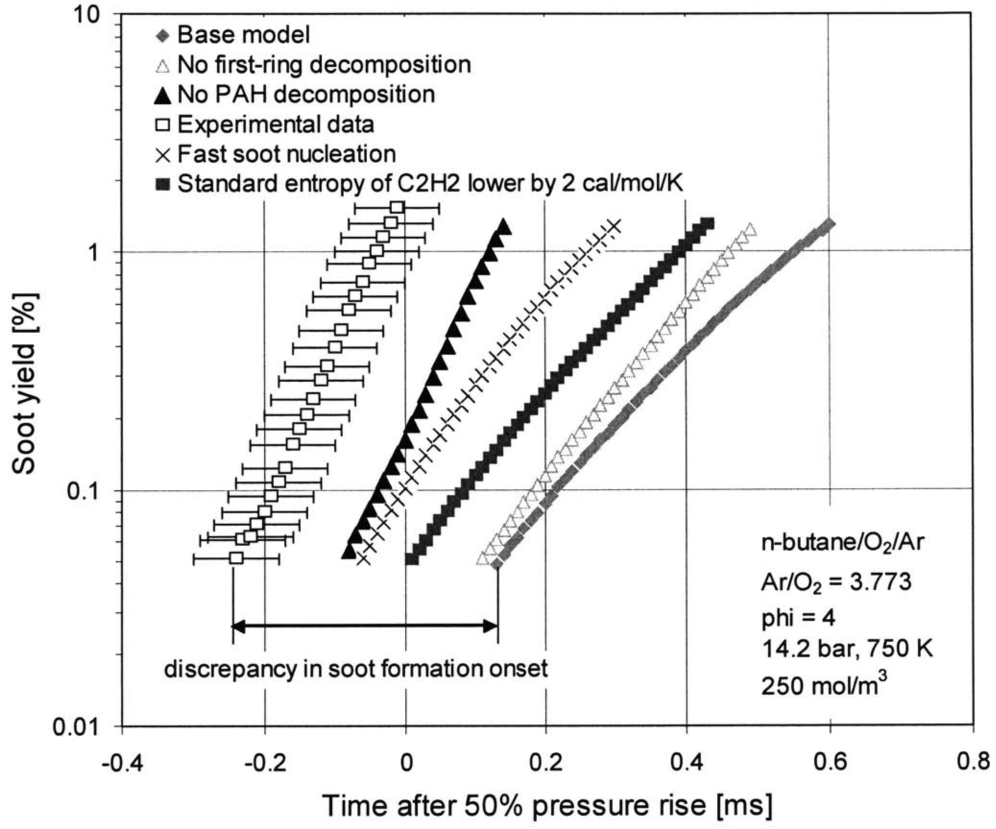

Figure 7.10 Comparisons of soot formation onset between experiment and different chemical kinetic models under typical conditions.

Comparing soot yield experimental data and modeling results in Section 6.4.2, it was found that the model could not predict any soot for $\phi \leq 2.5$. This discrepancy, which results from the competition between formation and fragmentation of soot precursors, can be mostly attributed to thermodynamics. As already stated in this chapter, decomposition of soot precursors or even species at the first aromatic ring level is responsible for limiting formation of soot at higher temperatures, which are reached for less fuel-rich mixtures, like when $\phi = 2.5$. To illustrate the impact of thermodynamics and kinetics on soot formation threshold, different scenarios were tested and the results are shown in Figure 7.11. It is evident that preventing decomposition of critical species, like single-ring aromatics or PAH, which implies different thermal properties, or even modifying C_2H_2 thermal properties favoring large species formation, result in soot levels closer to the experimental data. Conversely, faster nucleation rates[1], even though they would not be consistent with flame data [54], are still not enough to explain the experimental observations. The experimental and modeling results discrepancies cannot also be attributed to mixture uncertainties and/or temperature calculations. Figure 7.5 can be used to assess the degree of computational and/or experimental errors in order to achieve sufficient agreement between the model and the experiment. The experimentally obtained soot yield of the base model in Figure 7.11, which was also reported in Figure 7.5 ($\phi = 2.5$, $T_{max} = 2600\,K$, soot yield ~0.5%), was ~5.5%. It is apparent that errors of more than 500K in temperature calculation are required to explain the trends or equivalently the fuel metering system should produce mixtures with $\phi \geq 3$, instead of $\phi = 2.5$. These errors are much larger than the accuracy of temperature calculation and fuel metering system, therefore these factors can be excluded as potential contributors that to the observed discrepancies.

---

[1] A factor of 10 higher rates were assumed.

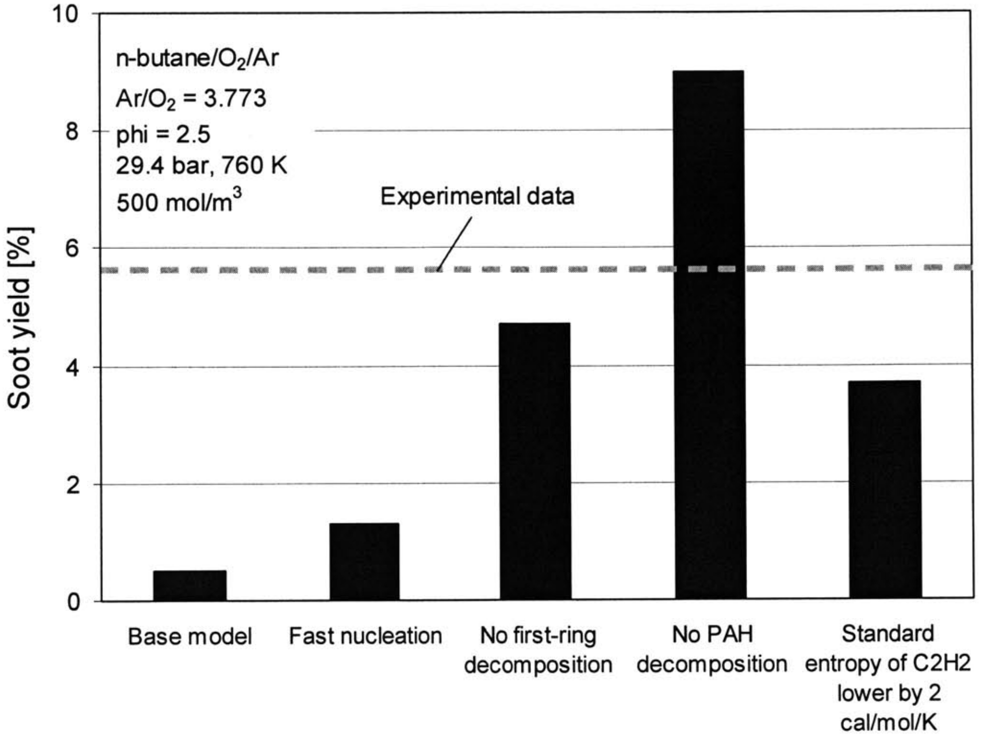

Figure 7.11 Sensitivity of soot formation threshold to different model scenarios under typical conditions.

To summarize, the discrepancies between experimental data and modeling results are most likely attributed to chemistry or thermodynamics. Experimental errors, soot definition and CFD uncertainties are not able to explain the trends. The thermodynamic properties of critical species for soot formation, like single-ring aromatics and especially PAH are uncertain and their impact on the soot chemistry was found to be fairly significant. Moreover, the possibility of missing chemical pathways leading to soot cannot be ruled out. As an example, it was mentioned that using C_2H_4 as a growth species during the early stages of soot formation could potentially lead to earlier soot formation relative to the heat release, as observed experimentally. It is very likely that a single amendment in the model, chemistry or thermodynamics, could possibly fix both discrepancies concerning soot formation onset and threshold.

Chapter 8

Summary and Discussion

8.1 Experimental and Diagnostic Method

Motivated by recent in-cylinder visualization experiments in diesel engines showing that soot starts forming in local fuel-rich regions during the premix burn, this study focuses on the fundamentals of fuel-rich combustion and soot formation. A new RCM with full optical access was designed and built in order to provide soot kinetics data under diesel engine conditions. The LOS absorption technique was employed to monitor the soot volume loading history during the course of combustion.

The RCM is a single-stroke piston/cylinder apparatus in which a uniform fuel-air mixture is rapidly compressed to a thermal environment similar to that of diesel engine operation. These conditions cannot be easily reproduced in typical laboratory scale experiments, like flat-flame burners or shock tubes, while data from diesel engines are difficult to interpret because of the uncertainty in local charge composition and thermal state. In a RCM, on the other hand, well-defined mixture composition (precise fuel-metering, single or double component fuels) and combustion environment (constant volume, uniform) can be realized so that there is unambiguous interpretation of the data. Since this study focuses on the chemical mechanisms leading to soot particles, mixing and chemistry were decoupled by introducing the mixture into the RCM premixed. The conditions at the end of the compression reflected the premixed burn of a diesel engine: 9-33 bar, 680-950K and $\phi = 2-5$. The repeatability of this RCM was remarkably good and the compression time was short (~15 ms) so that heat transfer and chemical reactions occurring before the end of compression were minimized.

The LOS absorption technique was chosen as a diagnostic method since it is relatively simple, non-intrusive and quantitative monitoring of soot formation was possible throughout the whole combustion event. The optics was properly set up in order to filter out noise originating from mechanical vibrations, beam steering, chemiluminescence and soot luminosity. Since the combustion chamber becomes opaque very quickly, information only during the early stages of soot formation could be obtained.

8.2 Fuel-rich combustion

To gain good insight into the soot chemistry, one needs to understand better fuel-rich combustion, which has not been extensively studied. This study investigates the oxidation characteristics of hydrocarbon fuels at high-pressure and fuel-rich conditions using the RCM and detailed chemical kinetic modeling. The ignition delay data augment the literature data under less fuel-rich conditions, while the heat release data shown here, are part of a very limited number of data reported in previous studies. In this study, a thorough sensitivity analysis identified the main oxidation pathways of fuel-rich mixtures and how they differentiate compared to better-established lean conditions.

The RCM has been extensively used for autoignition and knock studies in past research. The major conclusions drawn from this study about ignition delay of fuel-rich mixtures are summarized below:

- Modeling the RCM as a constant-volume, adiabatic and homogeneous system, is sufficient for prediction of ignition delays between 2 and 10 ms. Beyond that range pre end of compression reactions and heat transfer respectively, may introduce errors.
- Temperature shortens rapidly the ignition delay for lower and higher temperatures, while a weak NTC zone is observed at intermediate temperatures. Increase in pressure shifts the NTC zone to higher temperatures; this zone is hardly perceptible at

very high pressures. Fuel-air equivalence ratio enhances the reactivity of the mixture, especially at lower pressures. A two-stage autoignition behavior is clearly observed for less fuel-rich mixtures at lower pressures and intermediate temperatures.

- Toluene, having an alkylated benzene structure, lengthens the ignition delay, while DME shortens it due to its low octane number.
- All data trends can be explained with the low and high temperature paths of hydrocarbon oxidation often postulated in the literature. The detailed chemical kinetic mechanism proposed by LLNL was used and even though it underpredicted the ignition delays under almost all conditions by more than a factor of 3, it provided a fairly good qualitative agreement. The agreement became much better after two adjustments were made. The first concerns the low temperature mechanism (increase the activation energy of OOQOOH isomerization by 1.5 kcal/mol out of 25 kcal/mol) and the high temperature mechanism (increase the activation energy of H abstraction by the fuel with HOO by 3 kcal/mol out of 20 kcal/mol). The first modification has been also suggested in the literature while the second was found to be the only way to decrease the reactivity of the mixture at high temperatures only, since under fuel-rich mixtures this reaction is part of a chain-branching loop.

Employing such a simplistic singlezone approach for studying heat release rates in a RCM though, could lead to significant errors. The predicted rates were found to be more than an order of magnitude higher compared to the experiments. Summarizing the findings of the rate of heat release study, one could include the following points:

- Slow pressure rise in the RCM is mostly attributed to temperature stratification generated by the piston motion, which shears gas off the wall creating a roll up vortex. The lack of temperature uniformity rather than chemical kinetics determined the pressure rise especially when the ignition delay chemistry was very sensitive to temperature and the rates of heat release were very high. The extent of non-uniformities at the end of compression of a RCM depended on design variables, like bore to stroke ratio and crevice volume. For the particular design, CFD analysis showed that approximately 80% of the mass ranged within 50 K. Therefore, to study hydrocarbon chemistry after ignition in a RCM, one needs to couple fluid dynamics with chemical kinetics.

- Since no significant reactions took place during the course of compression, the problem in this study was solved sequentially. KIVA-3 predicted the temperature distribution at the end of compression and the chemical solver took over right after assuming 15 zones, which were treated as constant-mass well-stirred reactors with the restriction of constant total volume. This multizone model also included flow into the crevice and heat transfer by convection and radiation due to combustion-generated soot particles. The agreement between this model and the experimental data became much better both for heat release rate and maximum pressure. The temperature stratification improved the heat release agreement and the flow into the crevice the maximum pressure.
- A thorough sensitivity analysis on the chemical kinetic model was performed to identify the most important chemical pathways at high-pressure, fuel-rich conditions. It was found that the formation and consumption of HOO and CH_3 were particularly important under these conditions. Pathways like CH_3+CH_3, HCO+O_2, C_2H_3+O_2 and CH_3+HOO were critical under the conditions tested. Especially the multi-channel paths of C_2H_3+O_2 and CH_3+HOO, which have previously drawn the attention of research efforts, seemed to depend significantly on pressure and mixture composition. The agreement between the model and the experimental data improved significantly if the two alternative paths of CH_3+HOO, which are CH_4+O_2 (recombination)

and CH_3O+OH (branching), were forced to have similar rates. This involved the increase of the recombination channel rate constant by a factor of 5.

8.3 Soot Formation

The complexity of the soot formation process originates from the conversion of a hydrocarbon fuel molecule containing a few carbon atoms into an agglomerate of some million carbon atoms. This project is one of the first research efforts, which uses both experimental and computational tools, to fundamentally understand the transition from the gas phase to the particulate phase under conditions pertinent to diesel engine operation. The great resolution of the experimental technique provided valuable quantitative data and the detailed chemistry employed by the model sheded some light on the critical chemical channels leading to soot particles. Coupling gas-phase chemistry with aerosol dynamics and lumping species of similar molecular mass and classes of reactions using the sectional approach, proved to be a valuable tool for modeling the kinetics. The most striking observations and conclusions regarding soot formation chemistry are summarized below:

- Initial soot formation rates are exponential with a time constant of the order of 0.05 ms. This trend, which is also reproduced by the model, can be attributed to the "autocatalytic" nature of soot formation, since the higher the soot concentration, the larger the available surface area for gaseous species to condense on. The soot time constant depends on fuel-air equivalence ratio and strongly on temperature and pressure. Modeling results showed that soot formation is a time-consuming process that usually does not start before most of the energy is released (at least locally). Soot formation onset was found to occur earlier (relative to the heat release) for longer ignition delays due to the longer available time for chemistry. Since soot started forming at the thermal environment after the end of combustion, the slower soot formation rates for richer mixtures were mostly attributed to lower maximum temperatures rather than to different chemical pathways.

- The final soot yield, which was measured after the end of the combustion process, is a strong function of fuel-air equivalence ratio. Both experimental data and modeling results predicted soot levels between 5% and 35% for fuel-air equivalence ratio between 2.5 and 5 respectively. These soot yield levels were also observed in shock tube studies under totally different conditions. Soot yield increased by ~1%/1% of toluene in the fuel by volume for constant fuel-air equivalence ratio. If C/O ratio is kept constant though, soot levels exhibit negligible change with the addition of toluene, implying that the identity of parent fuel molecules during decomposition is lost. DME, on the other hand, suppressed soot formation very effectively. As also reported in the literature, ~30% oxygen in the entire fuel by mass prevents any formation of soot regardless fuel-air equivalence ratio. No change in soot yield was observed when the fuel was doped with small amounts of EHN, which is a typical CN improver used in diesel fuel to decrease ignition lag. Even though the kinetics do change, this observation implies that different PM levels from a diesel engine with the addition of combustion accelerators is mostly attributed to mixing rather than to chemistry characteristics.
- Soot yield is also a function of temperature reached after the end of combustion. The modeling part of the study reproduced the bell-shape dependence of soot to temperature, which was also reported in the literature by both experimental and computational studies. The competition between formation and fragmentation of soot precursors limits soot formation at higher temperatures. It was shown here that decomposition of species at even the first-ring level is possible leading to smaller species that readily oxidize at very high temperatures. At lower temperatures even

though soot precursors are thermodynamically stable, soot formation process is kinetically limited for the time scale of typical combustion systems. The highest soot yields are observed between 1800-2000K and under most conditions they drop by more than an order of magnitude for temperatures higher than 2500K or lower than 1500K.

- The bell-shape dependence of soot yield on temperature involves difficult chemical mechanisms leading to soot particle formation. It was found in this study that at high temperatures soot surface growth is exclusively realized through C_2H_2, while PAH have no contribution or even inhibit soot formation rates (since they consume C_2H_2 and then they decompose). At lower temperatures where PAH are thermodynamically stable, roughly 2/3 of soot growth is occurring through the PAH channel and 1/3 through C_2H_2. Soot particle inception, on the other hand, is mostly governed by PAH coalescence even though at high temperatures the contribution of C_2H_2 is remarkable (~33%). Apart from soot formation mechanisms fairly different composition of combustion products were observed across the entire temperature range studied. For similar soot levels the amount of carbon stored in PAH, single-ring aromatics and small hydrocarbons is ~10% at lower temperatures while they are almost zero at higher temperatures. Such species could eventually condense physically on soot particle surface at later stages of a practical combustion system, like in the exhaust of a diesel engine. This finding along with the observation that the average particle diameter is ~1.5 nm as opposed to ~16 nm at higher temperatures and the particle number density is higher by more than an order of magnitude, raises serious questions about the potential health effects of low temperature combustion regimes.
- Taking into account the complexity of soot formation chemistry and the physical processes involved in any combustion system, the agreement between experimental data

and modeling results is considered very encouraging. However, there are essentially two discrepancies: (a) the soot formation threshold was predicted at $\phi \cong 2.5$, while experimentally it was observed at $\phi \cong 2$ and (b) soot starts forming ~0.3 ms later relative to the heat release (for almost identical pressure histories) than in the experiments. A thorough sensitivity analysis showed that these discrepancies cannot be attributed to PAH light absorption, uncertainties in CFD calculations, experimental errors or temperature calculations. It was found that since the soot formation threshold is depending strongly on temperature, uncertainties in large species thermal properties, like PAH, could explain the soot formation threshold discrepancy. Increasing the thermodynamic stability of such species at higher temperatures could lead to the formation of soot particles even at lower fuel-air equivalence ratios. Thermal properties and PAH decomposition rates could also explain the discrepancy on soot formation onset. However, missing chemical channels in the soot formation model cannot be excluded. To illustrate this, 20% of carbon during decomposition is stored in ethylene, which later forms C_2H_2. If ethylene is considered directly as a growth species, soot formation process could potentially accelerate and occur earlier relative to the energy release.

8.4 Future Outlook

Fuel-rich combustion and combustion-generated soot particles have been a field of study for many years within the combustion community due to their significant environmental impacts, health concerns and industrial applications, like synthesis of carbonaceous material and recently fullerenes. This study, which combined experimental and computational techniques, aimed to shed some light into the fundamental chemical processes involved and give directions for new research areas related to soot formation chemistry. Some of these areas, which could be pursued with experimental methods are the following:

- *Definition of soot formation thresholds with regard to fuel-air equivalence ratio.* The sensitivity of the soot formation threshold to temperature and fuel structure, e.g. the aromatic and/or oxygenate content in the fuel, would be invaluable especially to diesel engine community. Such data, which could give insight to engine developers and help them devise engine and fuel strategies leading to lower PM emission levels, could be readily obtained in the well-controlled environment of the RCM.
- *Extension of soot evolution observation time.* The fuel-rich, high-pressure conditions employed in this study resulted in very high soot concentrations turning the combustion chamber opaque shortly after soot particle inception. Even though the transition from the gas to the particle phase was clearly studied, it would be interesting to observe a longer part of (if not the entire) soot evolution. This could be accomplished by employing different conditions (e.g. less fuel-rich, lower pressure, slightly diluted), or testing less sooting fuels (e.g. oxygenates), or shortening the beam path length (e.g. smaller cylinder bore), which would result in higher soot concentration for the same light attenuation.
- *Particle number density and diameter distribution determination.* The detailed chemical kinetic model predicted relatively slow coagulation and the average particle diameter increased very slowly after the total amount of energy was released. Since experimental data consisted only of soot volume, the above model prediction would be worthwhile to be tested experimentally. This could be accomplished by combining LOS absorption and scattering techniques and these data would be a valuable reference data set for further insight into the soot formation process and robust chemical kinetic modeling.

Further research efforts in soot formation modeling are summarized below:

- *Experiment-model discrepancies.* Even though the overall agreement between modeling results and experimental data is encouraging, there are still discrepancies discussed in Section 7.4. A thorough sensitivity analysis performed in this project excluded many factors from potentially contributing to these discrepancies, like PAH light absorption, CFD analysis, experimental errors and temperature calculations. It was found that modeling results are very sensitive to thermal properties of large species, like PAH, therefore future research efforts are encouraged to look more into accurate calculation of their properties. Also, other chemical pathways that could potentially lead to soot particles and are not included in this study could be investigated. For instance, soot-ethylene channels could possibly shift soot formation earlier relative to the heat release, as observed experimentally.
- *Further model improvements.* The current model defines classes of molecules covering certain mass ranges to which given numbers of carbon and hydrogen atoms have been assigned. Within a certain class, all species have the same properties regardless their origin or how they were formed. One model improvement would be the definition of carbonaceous material with different H/C ratios (i.e. degrees of curvature) of similar molecular mass and the description in the model of their formation based on thermodynamic and kinetic forces.
- *Model reduction.* Since the model used detailed chemistry to describe the oxidation-decomposition process of parent fuel molecules, PAH growth and soot, the chemical kinetic mechanism consists of hundreds of species and thousands of reactions (498 and 5734 respectively). This study has performed a very extensive sensitivity analysis on the critical chemical pathways for almost the entire mechanism and these findings could be used for significant model reduction keeping though its essential features. Such approach would be beneficial to the diesel engine community because

a simpler model coupled with CFD analysis could become a valuable design tool for the fueling-mixing strategy of a diesel engine that would lead to lower PM emission levels.

In the process of performing this study, insights were gained regarding fuel-rich combustion and RCM operation. Some future guidelines concerning these research fields are given here:

- *Fuel-rich combustion.* This research is one of the very limited number of studies that performed both experimental and computational work under high-pressure, fuel-rich conditions. Ignition delay and heat release rate data obtained in this study provided valuable information about the critical processes under fuel-rich conditions and how they differentiate compared to a lean mixture. Since most of the chemical kinetic models were validated under lean mixtures, recommendations are given here for the rates of certain reaction pathways, like CH_3+HOO and fuel+HOO, under fuel-rich conditions. Due to the high sensitivity of the mechanism to such reactions, future studies are encouraged to look into these reactions both computationally and experimentally.
- *RCM and thermal stratification.* The multizone model developed in this study utilized the temperature distribution predicted by CFD analysis. A sensitivity of design parameters, like the stroke and the crevice volume, on the calculated temperature profile at the end of compression was also performed. However, this work was done only computationally and experimental validation would be particularly useful for future designs. Towards this direction different pistons and compression ratios could be employed and the resulting compression pressure could be measured. Using optical methods, like scattering or laser induced fluorescence (LIF), through the transparent RCM head, temperature distribution during compression could be estimated.

Appendix A

Rapid Compression Machine

A.1 Operation Protocol

The RCM was designed at the Sloan Automotive Laboratory of MIT during the summer of the year 2000. It first operated compressing inert gases in February 2001, and combustion tests started in May 2001. A picture of the entire RCM setup is shown in Figure A.1. The footprint of the setup (not including gas bottles and data acquisition system) is ~2.2x1.6 m.

For each RCM test a series of steps must be followed. The protocol of operation along with general guidelines about RCM maintenance and operation are presented below.

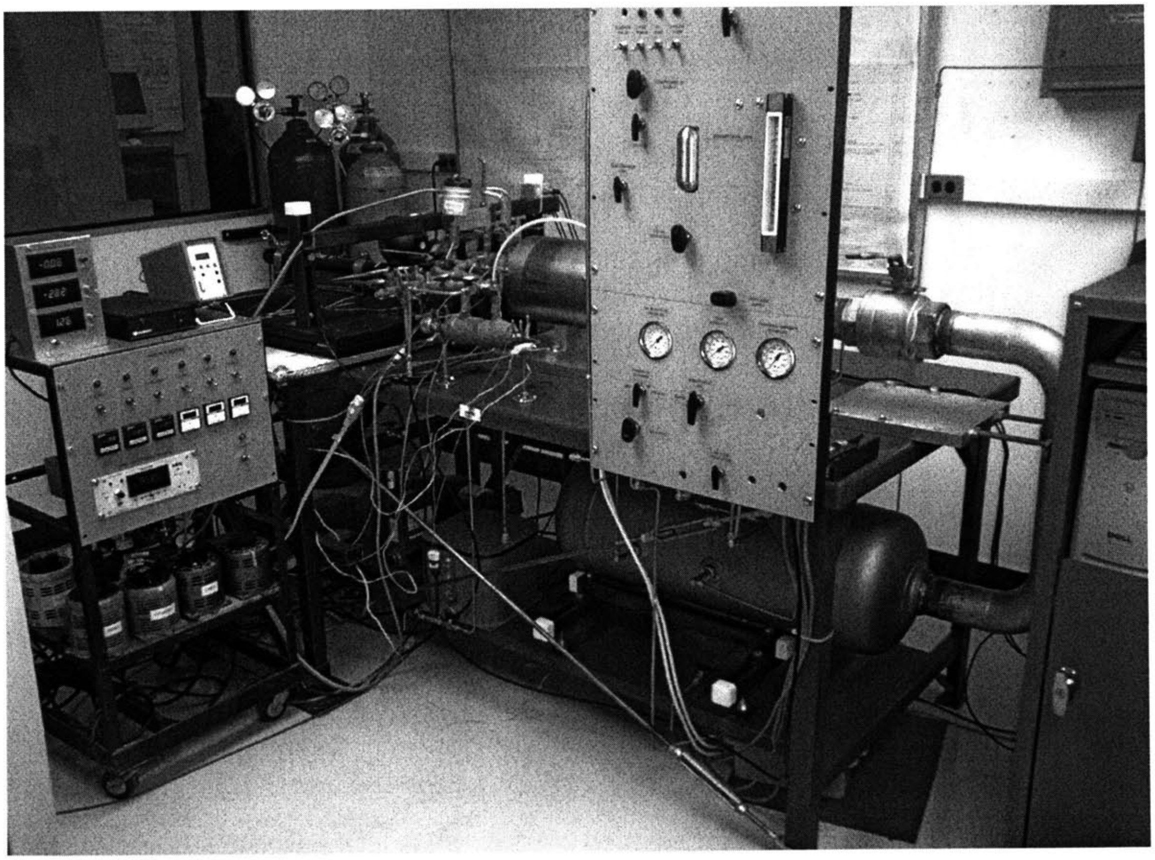

Figure A.1 The entire RCM setup.

Initial preparations

- *Oil level:* Check the oil level through the sight tube. It must be at the recommended level shown on the main panel. Use the oil pump and the oil flow regulation valve to pump more oil from the reservoir into the RCM. The oil supply valve must be open during oil pumping and closed right after pumping is over to prevent the oil from draining back to the reservoir. Keep solenoid valve open while pumping to avoid trapping air.

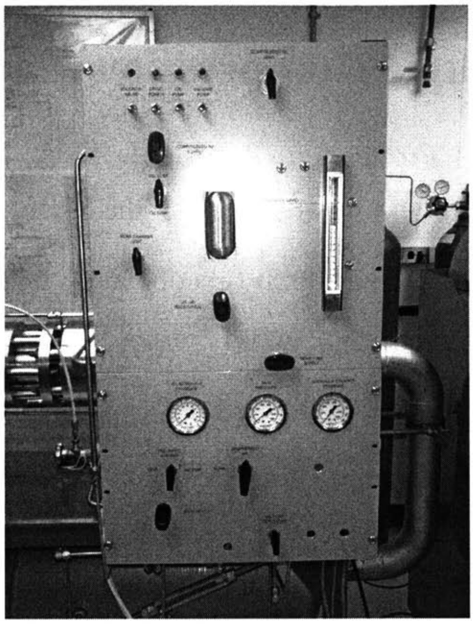

Figure A.2 Main panel.

- *Tank pressure:* Check pressure from the tank pressure gauge on the main panel. Driving pressure usually does not exceed ~250 psi, which results in ~15 ms compression time and it sustains combustion chamber pressures up to ~110 bar. Use the compressed air valve (left position) on the main panel to supply gas (usually N_2) to the tank from gas bottles or the valve on the tank to vent gas. The tank is designed for pressures up to 500 psi. The pressure relief valve on the tank is set to 450 psi. The tank leaks at a very slow rate (over periods of weeks).

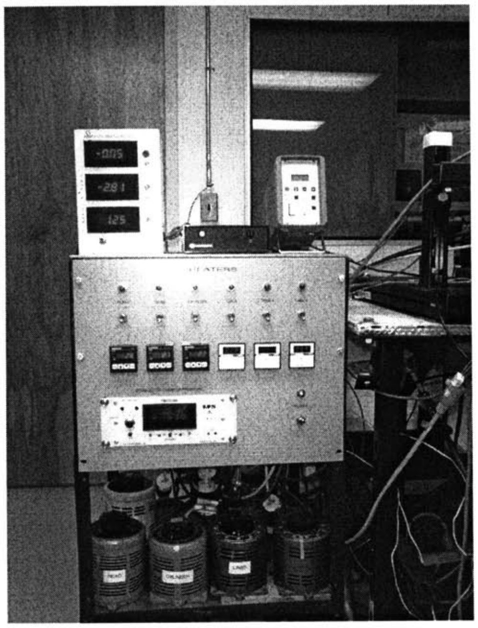

Figure A.3 Heating panel.

- *Heating system:* Used only when tests require temperatures before the compression higher than the ambient. There are 6 different electrical circuits: 3 for the RCM (combustion chamber, head and head plate), 2 for the fuel tanks and 1 for the fuel lines. All related controls (switches, temperature displays) are on the heating panel. Use variable power output controllers (located underneath the heating panel) to achieve even temperature rise. Do not exceed the maximum value marked on the controllers or the heaters may burn. Fuel lines do not need to reach to the desired temperature. Their temperature must be sufficiently higher than the fuel dew point though. It is recommended that they stay below 60^0C to avoid overheating of Baratron pressure sensor and valve seals damage.

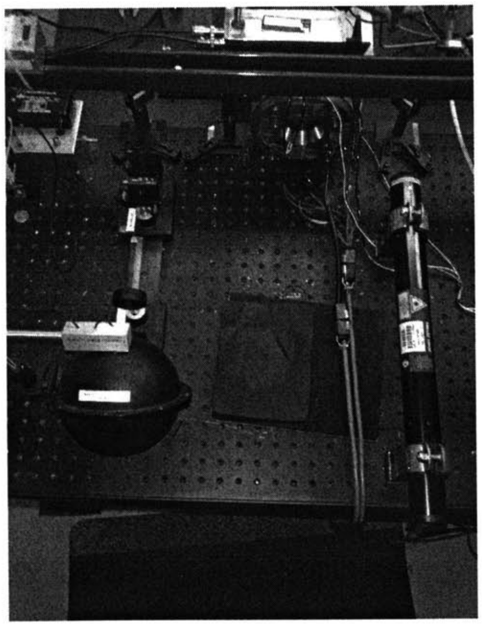

Figure A.4 Optical system

- *Optical system*: The He-Ne laser must be turned on ~15 minutes before the experiment in order to stabilize. If the PMT is used, the high voltage power supply can be turned on shortly before the experiment.
- *Piston position*: Apply vacuum at the back of the pneumatic piston, using the pneumatic chamber valve (right position) on the main panel (make sure the vacuum valve of the mixture preparation setup is closed), to bring

it all the way back and ensure good contact between the o-ring and the hydraulic chamber for sufficient sealing. Then, apply ~100 psi pressure at the hydraulic chamber to ensure good contact even after the combustion chamber is evacuated for mixture preparation (see below). Before opening the compressed N_2 supply valve, close the compressed N_2 vent, the rear chamber vent and sight tube supply valves.

Mixture preparation

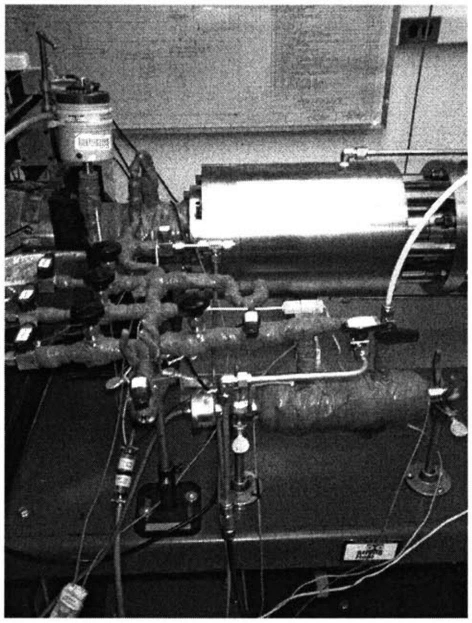
Figure A.5 Mixture preparation setup.

- *Combustion chamber:* Apply vacuum to the combustion chamber using the corresponding valve on the mixture preparation setup. Make sure the corresponding valve on the main panel is at its upright position and the vent valve on the mixture preparation setup is closed. Usually it takes less than ~5 minutes for good vacuum to be achieved. The Baratron pressure transducer drifts over time and when it is heated, so the zero point may be slightly lower or higher than 0 Torr. Testing that the vacuum pump is providing sufficient vacuum is recommended over periods of ~1 month if extensive testing is performed. Right after sufficient vacuum is achieved, close the vacuum valve and shut down the pump. Wait for 1-2 minutes to make sure that the vacuum is retained.

- *Mixture components introduction:* Introduce first the fuels, then the inert gases and finally the oxygen. For each mixture component follow the procedure described here: open the corresponding ball valve and then slowly the metering valve. As gas is introduced, watch the Baratron display (heating panel) and close the metering valve as soon as the required pressure is reached. Then close the ball valve. Introduce the mixture components slowly (~1 minute) and allow ~1 minute between each gas. Make sure that the final pressure is retained for at least ~2 minutes after the entire mixture is introduced and then close the ball valve attached to the combustion chamber.

Firing

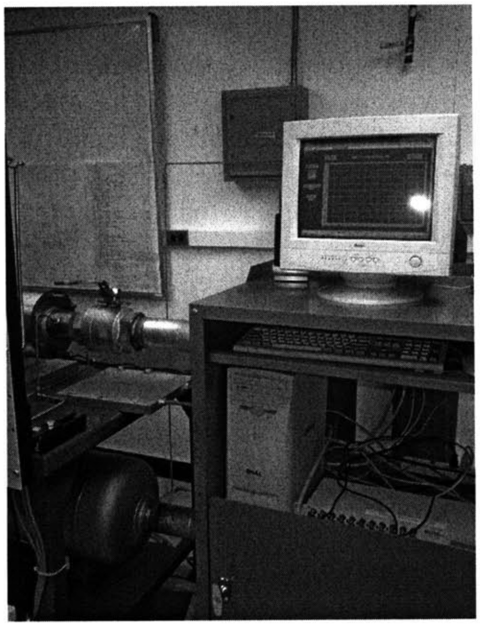

Figure A.6 Data acquisition system.

- *Force balance creation:* Pressurize the oil from ~ 100 psi to ~1500 psi by opening slowly the compressed N_2 supply valve. The area ratio between the hydraulic and the pneumatic piston is ~5, but for safety purposes, ~1500 psi pressure is recommended for ~250 psi driving pressure. Then, close the oil-N_2 separating valve and point the ball valve above the solenoid valve to oil damp. Turn the compressed air valve to bypass (right) and open the big ball valve behind the main panel. Turn the compressed air valve to supply (left) to compensate for pressure loss due to the higher volume and then turn it again to its upright position.
- *Force balance destruction:* Switch the pressure transducer to its operational mode and start the data acquisition system (for example RCM.VI in LabVIEW). Make sure that the 24VDC power supply is on and fire the RCM by switching momentarily the solenoid valve.

Shutting down

- Close the big ball valve behind the main panel and vent the pneumatic chamber (point corresponding valve to the left) and the gas that pressurized the oil (open compressed N_2 vent valve). While venting (it takes ~2 minutes if the valves are half open), turn the heaters off, cover the optics, reset the pressure transducer, vent the mixture preparation setup and save the data file. After venting is over, open slowly the oil-N_2 separation, sight tube supply and rear chamber vent valves. Also, point the ball valve above the solenoid valve to oil vent.

Combustion chamber cleanup

- *Disassembly:* Bring the piston all the way back by applying vacuum at the pneumatic chamber (point corresponding valve to the right). Then, open slowly the valve attached to the combustion chamber. After the combustion chamber has cooled down, take apart the combustion chamber by removing the 4 head bolts.
- *Cleanup:* Use lint-free paper and acetone to cleanup the combustion chamber from soot. Move the piston to the front to clean the piston head. To do so, pressurize slightly the pneumatic chamber by using the bypass of the compressed air valve (left position). Vent the chamber after the piston has reached its final position. During cleaning, pay particular attention to the crevices formed by the windows and the pressure transducer.
- *Assembly:* Before putting the combustion chamber together, bring the piston back by applying vacuum at the pneumatic chamber as described above. Then, clean again the cylinder liner. Finally, tighten the 4 combustion chamber bolts in 2-3 stages up to 70 ft.lb.

General guidelines when using the RCM

- *Stroke:* The maximum stroke is 8 in. Change the spacers behind the hydraulic chamber for shorter strokes. Spacers are for 7 in and 6 in strokes are provided. To avoid optics alignment, move the back of the RCM (push pneumatic chamber back) to change the stroke. Draining the oil first is recommended.
- *RCM oil:* Silicon oil is used due to its low vapor pressure and lower toxicity. Due to its high compressibility a small reservoir is used at the point of separation with the compressed gas (main panel). Spills can spread oil around due to its low surface tension. Pin-groove deceleration mechanism calculations were based on oil with 100 CS kinematic viscosity (Dow Corning 200 series was used). To drain the oil back to its reservoir, open the oil supply valve. To fill up the RCM with oil, evacuate the whole RCM from its highest point (compressed N_2 vent valve). Use a valve just downstream the oil reservoir and open it when sufficient vacuum has been created (~1 hour). Use the oil pump to help the oil fill up the RCM if it does not show up in the sight tube after ~20 minutes. Since a little oil escapes the hydraulic chamber after each test, oil must be provided with the oil pump into the RCM. Make sure that enough oil remains in the oil reservoir and no air is pumped.
- *Combustion chamber seal:* If vacuum cannot be sustained, the combustion chamber seal may not be sealing properly. It is essential not to damage the seal when inserting it in the combustion cylinder. Use the provided tool and sufficient amount of vacuum grease to insert a new seal properly. To do so, the combustion cylinder must be removed (after removing the cylinder head, holding brackets and detaching the mixture preparation setup).
- *Combustion chamber windows*: The combustion chamber windows are made of fused silica. A thin washer made of rubber (~0.015 in) is used to avoid window

cracking due to high combustion chamber pressures. The hollow bolts should not be tighten much and a copper washer is recommended between them and the rubber washers. Similar approach should be followed when using the head window.

A.2 RCM Schematics

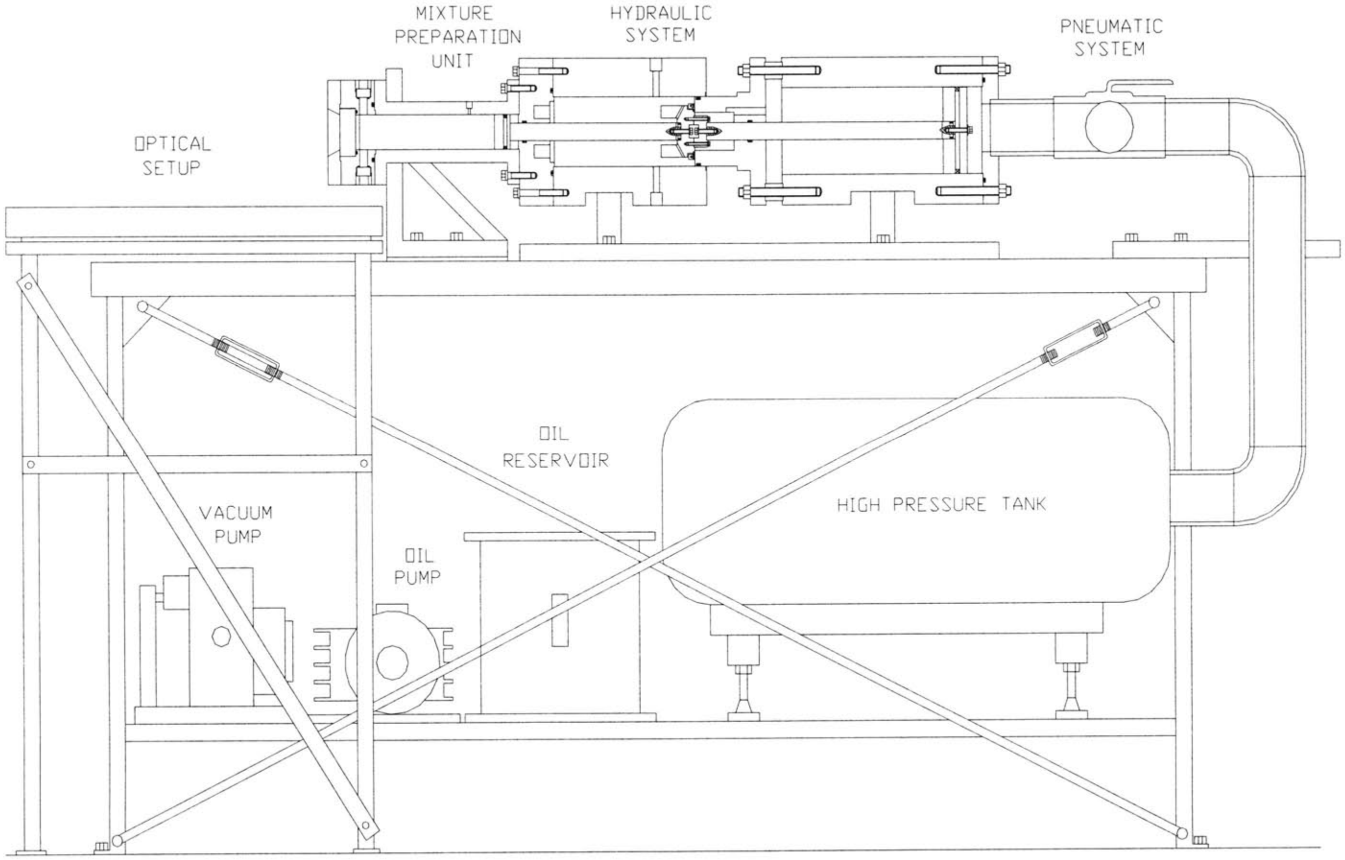

Figure A.1 RCM setup.

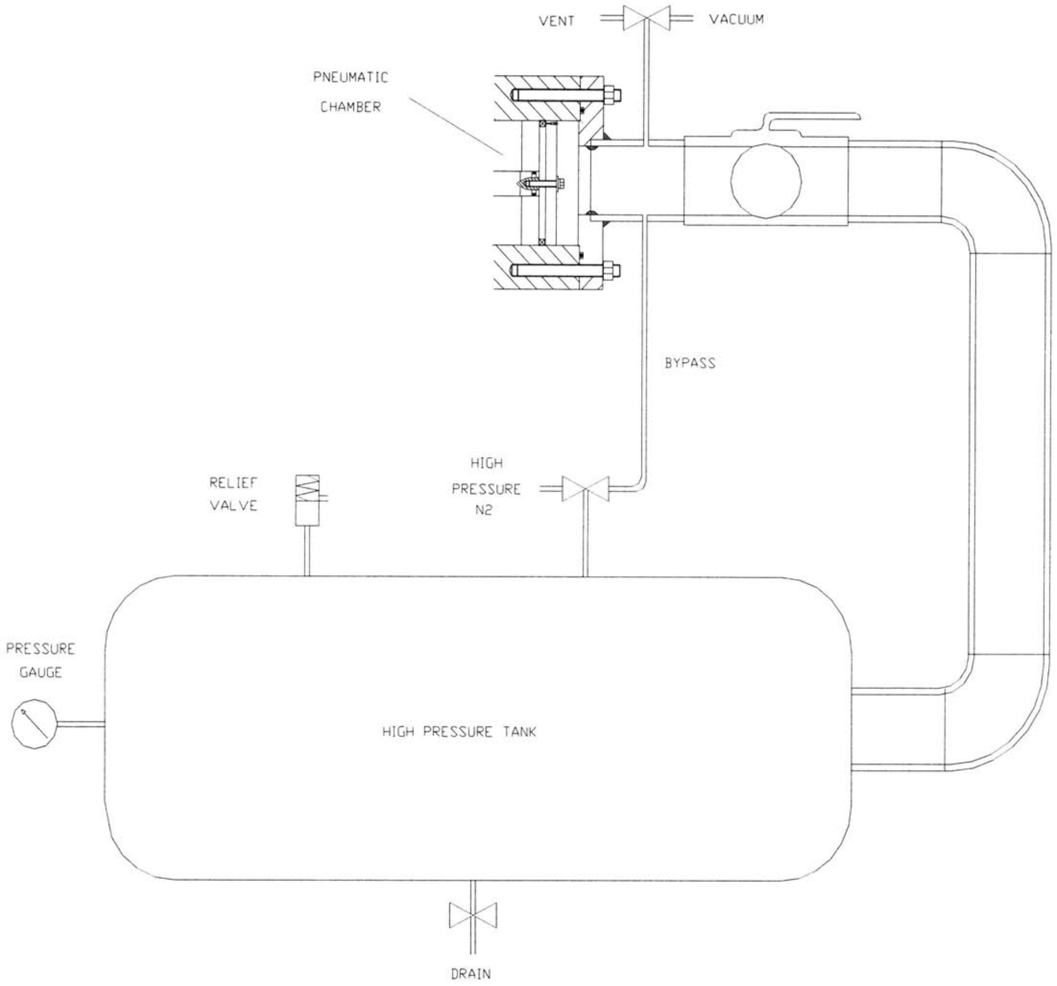

Figure A.2 Pneumatic (driving) system.

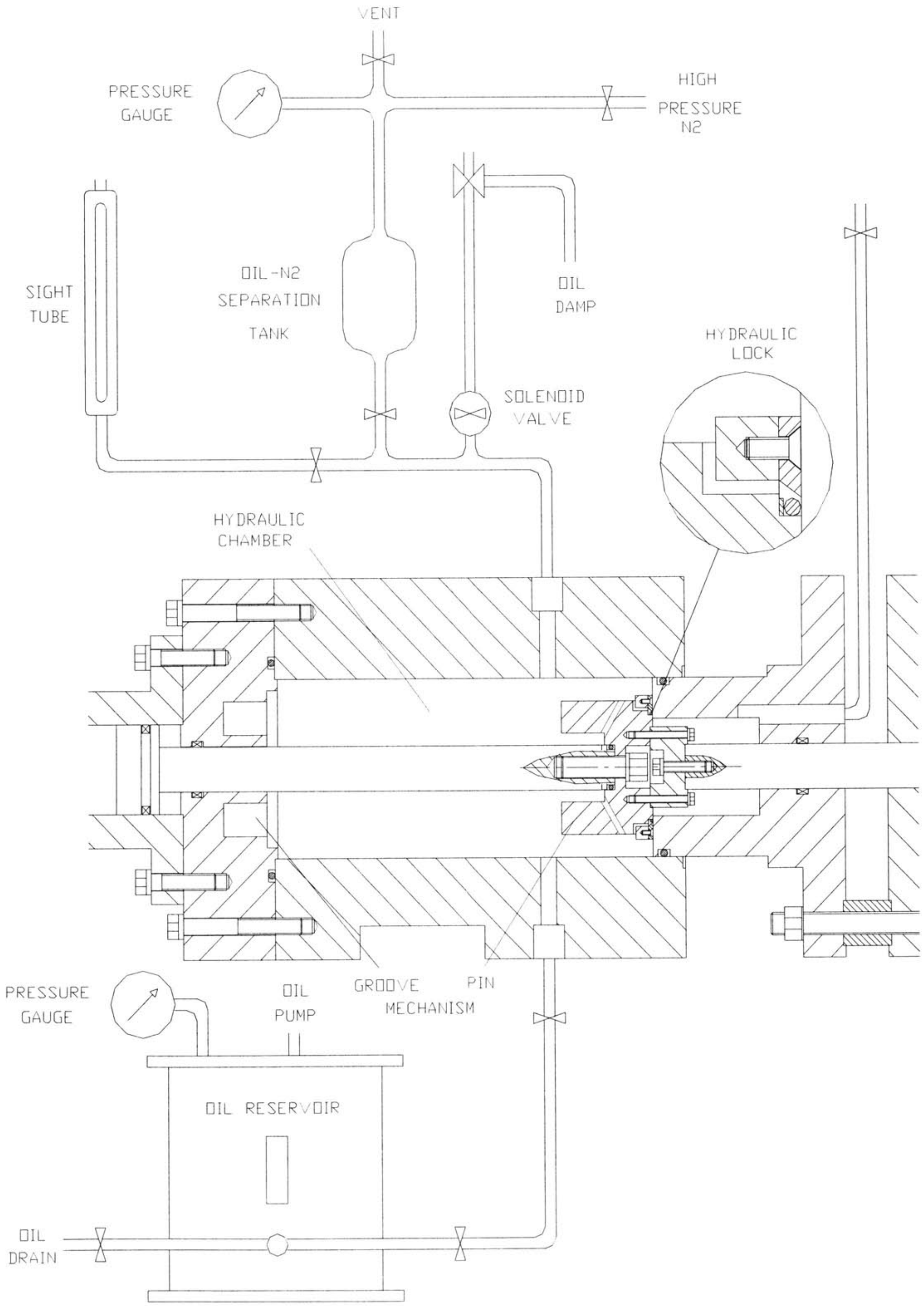

Figure A.3 Hydraulic (starting-stopping) system.

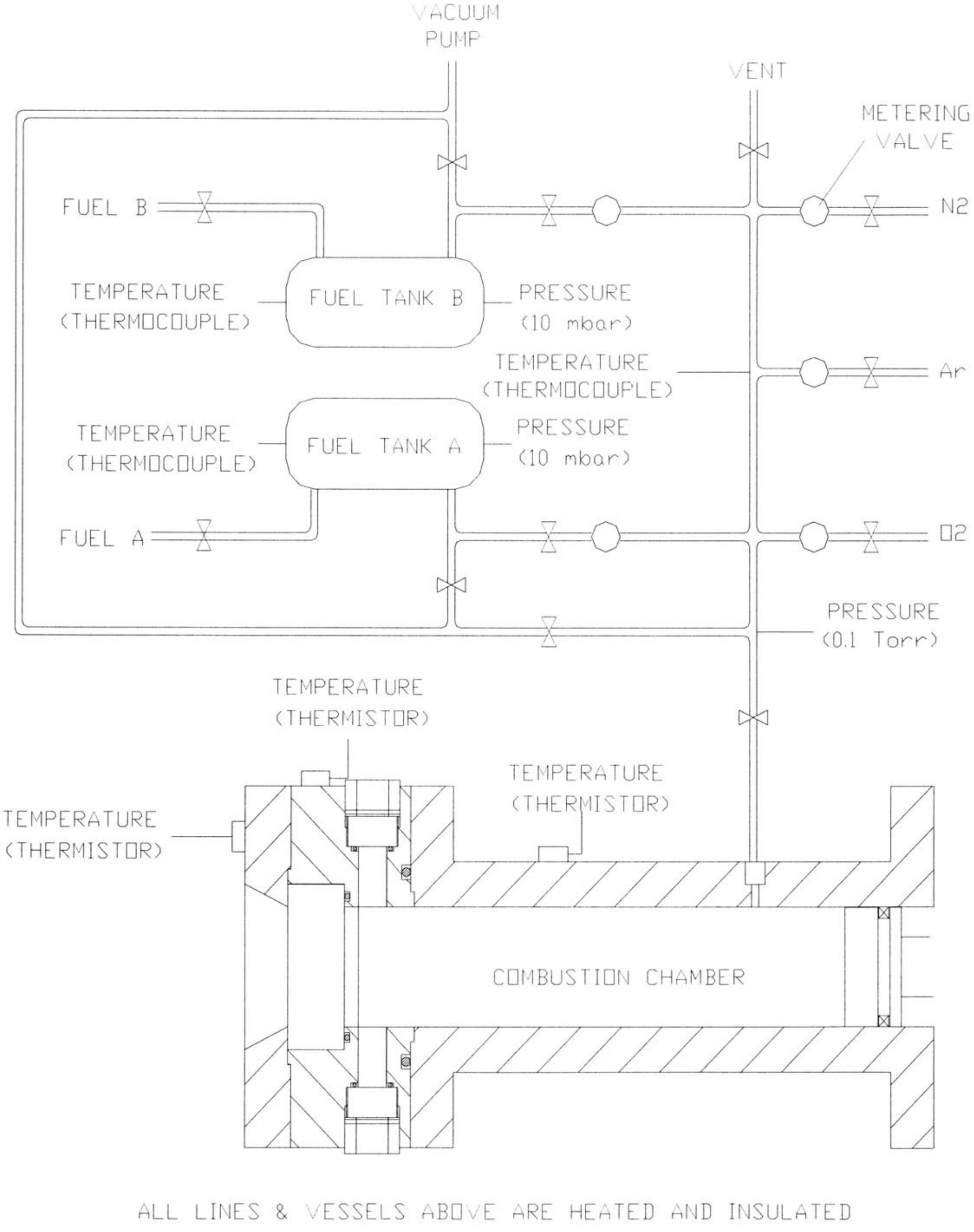

Figure A.4 Mixture preparation setup

A.3 Mechanical Drawings of RCM Parts

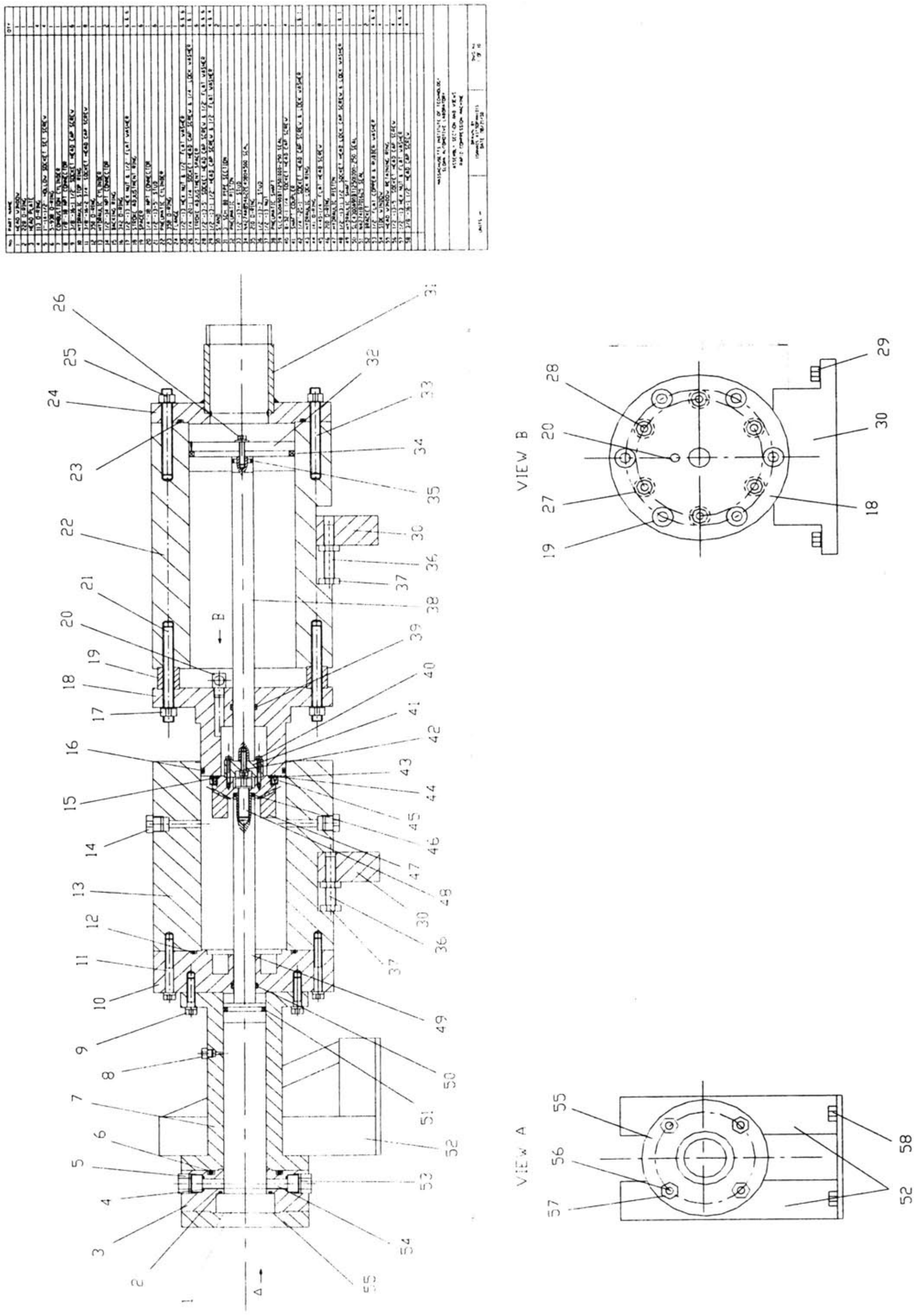

NO	PART NAME	QTY
1	HEAD WINDOW	1
2	228 O-RING	1
3	HEAD PLATE	1
4	113 O-RING	4
5	1"-14-1/2" HOLLOW SOCKET SET SCREW	4
6	S-938 O-RING	1
7	COMBUSTION CYLINDER	1
8	1/8"-18 NPT CONNECTOR	1
9	3/8"-16-1 1/2" SOCKET HEAD CAP SCREW	6
10	HYDRAULIC STOP RING	1
11	3/8"-16-2 3/4" SOCKET HEAD CAP SCREW	8
12	350 O-RING	1
13	HYDRAULIC CYLINDER	1
14	1/2"-14 NPT CONNECTOR	2
15	BACKING RING	1
16	342 O-RING	1
17	1/2"-13 HEX NUT & 1/2" FLAT WASHER	6 & 6
18	STROKE ADJUSTMENT RING	1
19	SPACER	6
20	1/4"-18 NPT CONNECTOR	1
21	1/2"-13-5" STUD	6
22	PNEUMATIC CYLINDER	1
23	358 O-RING	1
24	FLANGE	1
25	1/2"-13 HEX NUT & 1/2" FLAT WASHER	6 & 6
26	1/4"-20-1 1/4" SOCKET HEAD CAP SCREW & 1/4" LOCK WASHER	1 & 1
27	STROKE ADJUSTMENT SPACER	6
28	1/2"-13-5" SOCKET HEAD CAP SCREW & 1/2" FLAT WASHER	6 & 6
29	1/2"-13-1 1/2" HEAD CAP SCREW & 1/2" FLAT WASHER	4 & 4
30	STAND	2
31	3" SCH. 80 PIPE SECTION	1
32	PNEUMATIC PISTON	1
33	1/2"-13-4" STUD	6
34	[illegible] SEAL	1
35	210 O-RING	1
36	1/2"-13-2" STUD	2
37	1/2"-13 NUT	4
38	PNEUMATIC SHAFT	1
39	SLC4300[illegible]-250 SEAL	1
40	8-32-1 1/4" SOCKET HEAD CAP SCREW	4
41	SHAFT COUPLER	1
42	1/4"-20-1" SOCKET HEAD CAP SCREW & LOCK WASHER	1 & 1
43	HYDRAULIC LOCK RING	1
44	141 O-RING	1
45	4-40-1/4" FLAT HEAD CAP SCREW	8
46	210 O-RING	1
47	HYDRAULIC PISTON	1
48	1/2"-13-1 1/2" SOCKET HEAD LOCK CAP SCREW & LOCK WASHER	1 & 1
49	HYDRAULIC SHAFT	1
50	SLC4300[illegible]-250 SEAL	1
51	[illegible] SEAL	1
52	BRACKET	2
53	1/2" FLAT COPPER & RUBBER WASHER	4 & 4
54	SIDE WINDOW	4
55	HEAD WINDOW RETAINING RING	1
56	1/2"-13-5" SOCKET HEAD CAP SCREW	4
57	1/2"-13 HEX NUT & FLAT WASHER	4 & 4
58	3/8"-16-1 1/2" HEAD CAP SCREW	4

MASSACHUSETTS INSTITUTE OF TECHNOLOGY
SLOAN AUTOMOTIVE LABORATORY

ASSEMBLY SECTION AND VIEWS
RAPID COMPRESSION MACHINE

UNITS = in

DRAWN BY
IOANNIS KITSOPANIDIS
DATE [illegible]

DWG NO
[illegible]

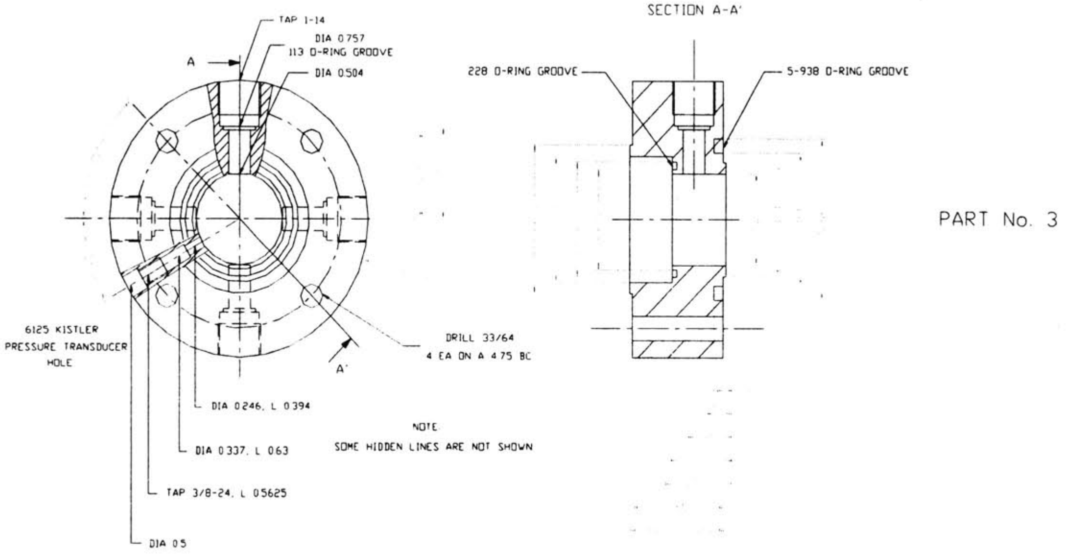

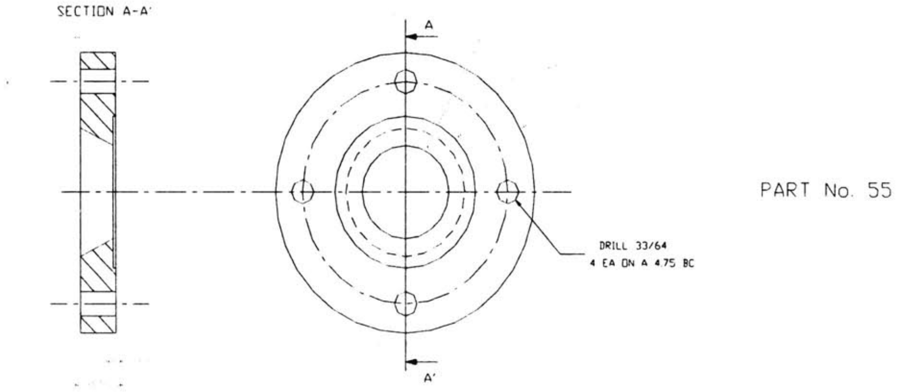

MASSACHUSETTS INSTITUTE OF TECHNOLOGY
SLOAN AUTOMOTIVE LABORATORY

PART No	PART NAME	QUANTITY
3	HEAD PLATE MATERIAL STEEL 11L17	1
55	HEAD WINDOW RETAINING RING MATERIAL STEEL 11L17	1

UNITS in	DRAWN BY IOANNIS KITSOPANIDIS DATE 08/21/00	DWG No 2 of 10

PART No. 43

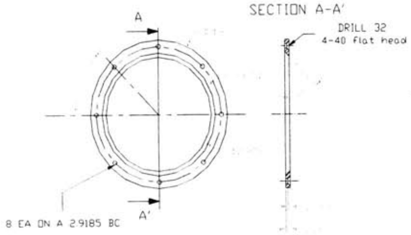

PART No. 1

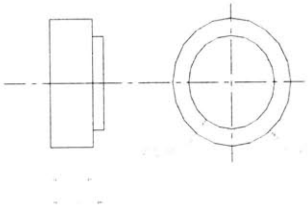

PART No. 54

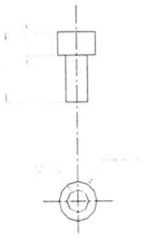

PART No. 19

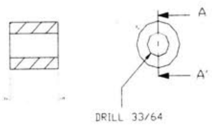

PART No. 41

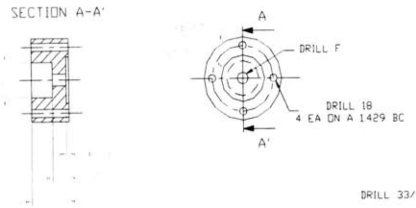

PART No. 30

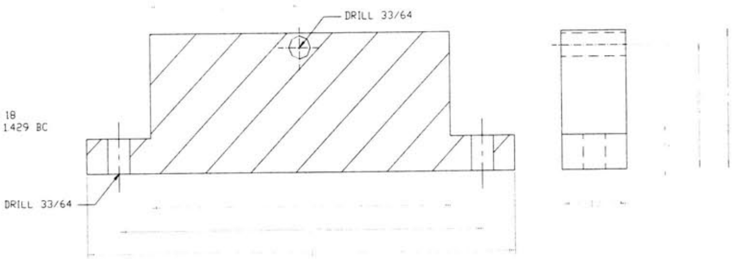

MASSACHUSETTS INSTITUTE OF TECHNOLOGY
SLOAN AUTOMOTIVE LABORATORY

PART No.	PART NAME	QUANTITY
30	STAND MATERIAL: ALUMINUM 6061-T6	2
43	HYDRAULIC LOCK RING MATERIAL: STEEL 11L17	1
1	HEAD WINDOW MATERIAL: FUSED SILICA	1
19	SPACER MATERIAL: STEEL 11L17	6
41	SHAFT COUPLER MATERIAL: STEEL 11L17	1
54	SIDE WINDOW MATERIAL: FUSED SILICA	4

UNITS: in	DRAWN BY IOANNIS KITSOPANIDIS DATE: 08/21/00	DWG No 3 of 10

PART No. 7

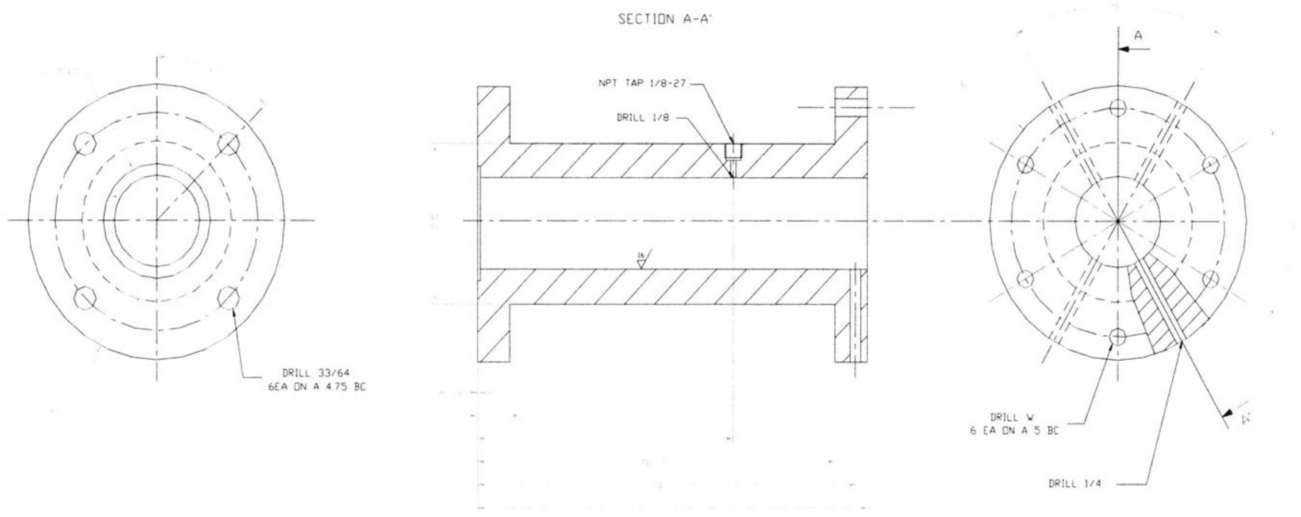

MASSACHUSETTS INSTITUTE OF TECHNOLOGY
SLOAN AUTOMOTIVE LABORATORY

PART No.	PART NAME	QUANTITY
7	COMBUSTION CYLINDER MATERIAL: STEEL 11L17	1
UNITS: in	DRAWN BY IOANNIS KITSOPANIDIS DATE: 08/21/00	DWG No. 4 of 10

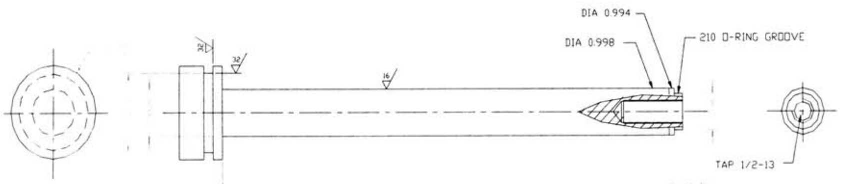

PART No. 49

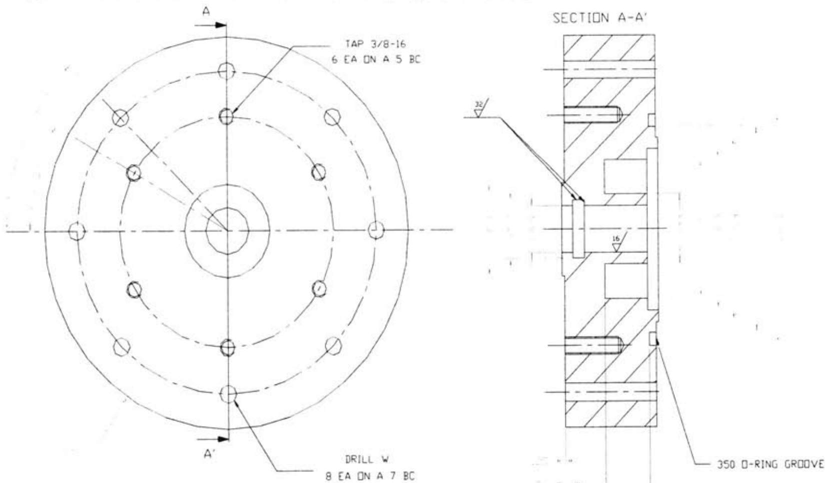

PART No. 10

NOTE:
HIDDEN LINES NOT SHOWN

MASSACHUSETTS INSTITUTE OF TECHNOLOGY SLOAN AUTOMOTIVE LABORATORY		
PART No.	PART NAME	QUANTITY
49	HYDRAULIC SHAFT MATERIAL: STEEL 11L17	1
10	HYDRAULIC STOP RING MATERIAL: STEEL 11L17	1
UNITS: in	DRAWN BY IOANNIS KITSOPANIDIS DATE: 08/21/00	DWG No 5 of 10

PART No. 13

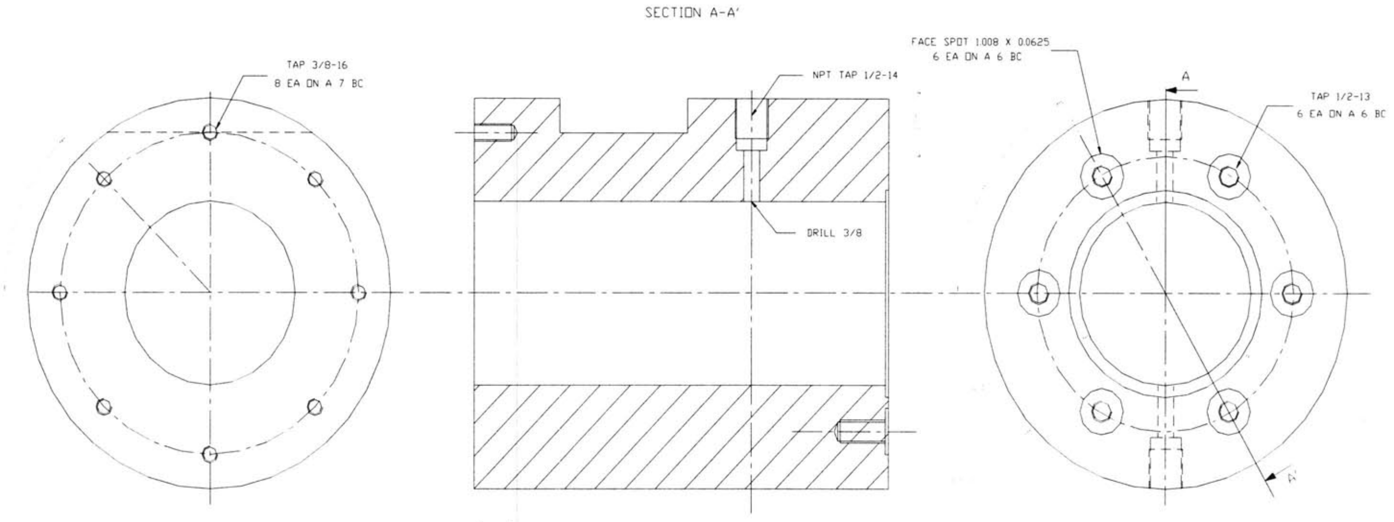

MASSACHUSETTS INSTITUTE OF TECHNOLOGY SLOAN AUTOMOTIVE LABORATORY		
PART No. 13	PART NAME HYDRAULIC CYLINDER MATERIAL: STEEL 11L17	QUANTITY 1
UNITS: in	DRAWN BY IOANNIS KITSOPANIDIS DATE: 08/21/00	DWG No. 6 of 10

PART No. 32

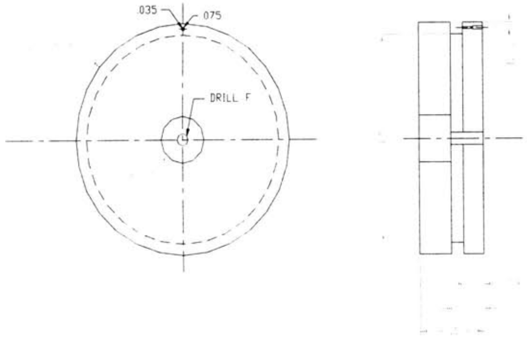

PART No. 27

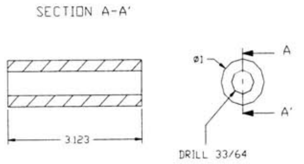

PART No. 47

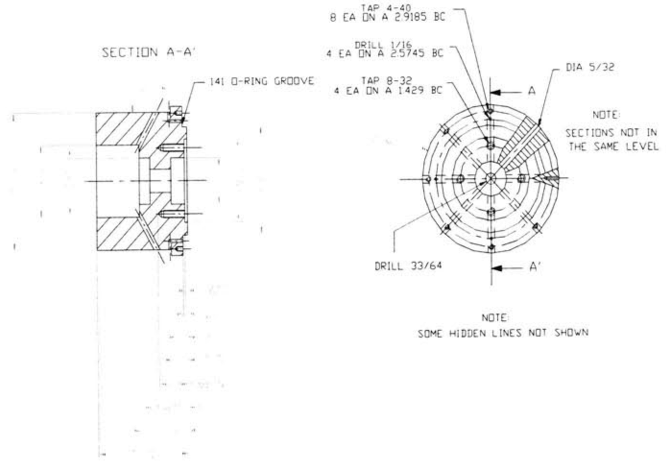

NOTE:
SECTIONS NOT IN THE SAME LEVEL

NOTE:
SOME HIDDEN LINES NOT SHOWN

MASSACHUSETTS INSTITUTE OF TECHNOLOGY
SLOAN AUTOMOTIVE LABORATORY

PART No.	PART NAME	QUANTITY
32	PNEUMATIC PISTON MATERIAL: ALUMINUM 6061-T6	1
27	STROKE ADJUSTMENT SPACER MATERIAL: STEEL 11L17	6
47	HYDRAULIC PISTON MATERIAL: STEEL 11L17	1

UNITS: in	DRAWN BY IOANNIS KITSOPANIDIS DATE: 08/21/00	DWG No 7 of 10

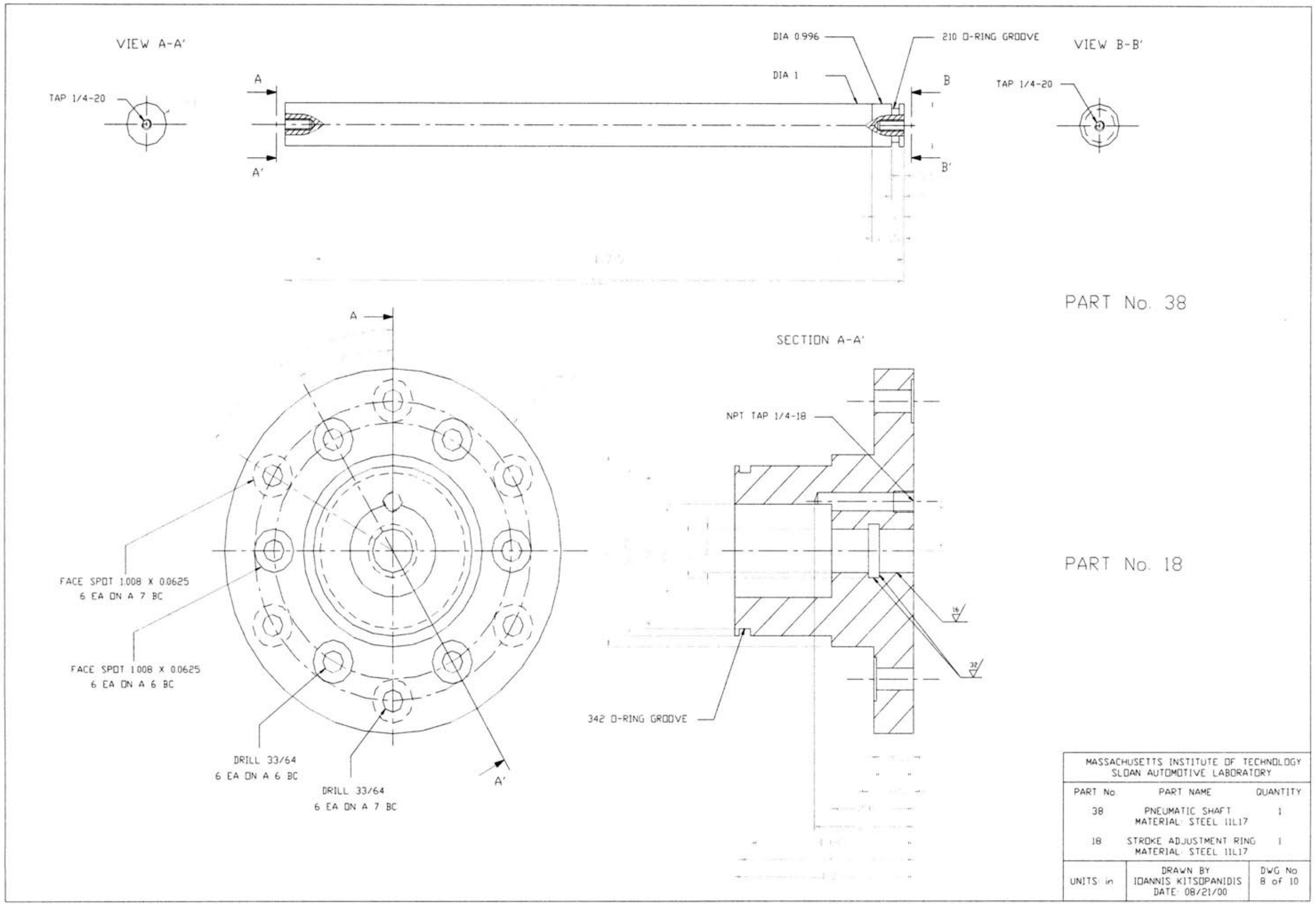

MASSACHUSETTS INSTITUTE OF TECHNOLOGY SLOAN AUTOMOTIVE LABORATORY		
PART No.	PART NAME	QUANTITY
38	PNEUMATIC SHAFT MATERIAL: STEEL 11L17	1
18	STROKE ADJUSTMENT RING MATERIAL: STEEL 11L17	1
UNITS: in	DRAWN BY IOANNIS KITSOPANIDIS DATE: 08/21/00	DWG No 8 of 10

PART No. 22

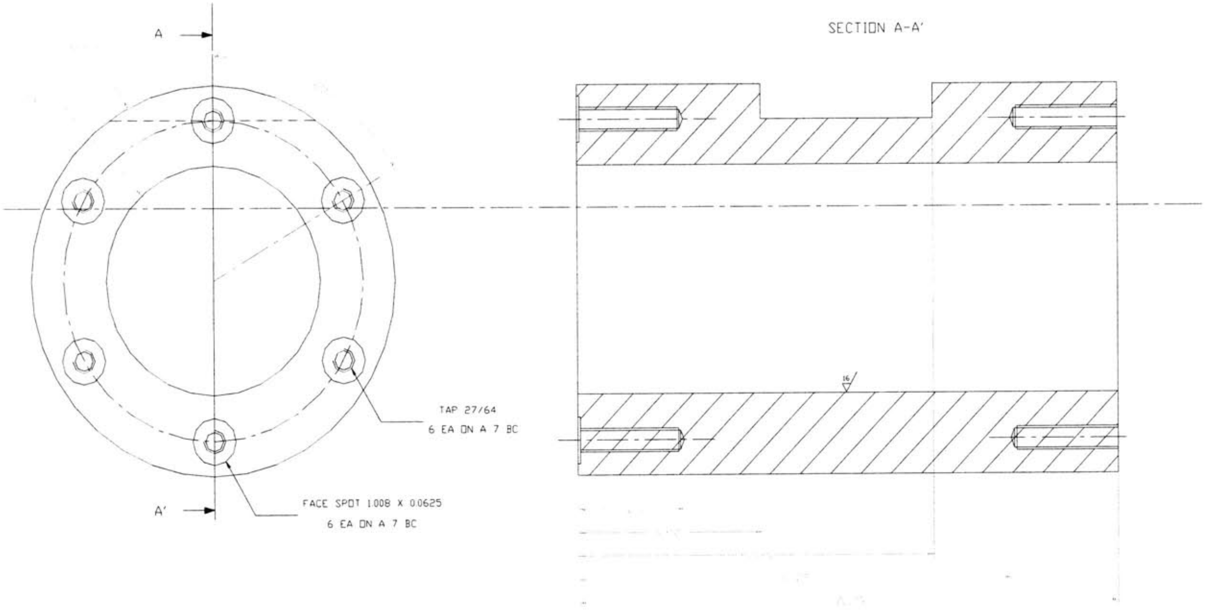

MASSACHUSETTS INSTITUTE OF TECHNOLOGY SLOAN AUTOMOTIVE LABORATORY		
PART No 22	PART NAME PNEUMATIC CYLINDER MATERIAL: STEEL 11L17	QUANTITY 1
UNITS: in	DRAWN BY IOANNIS KITSOPANIDIS DATE: 08/21/00	DWG No 9 of 10

PART No. 15

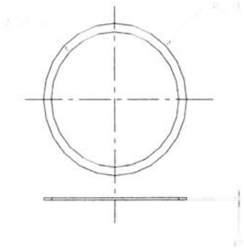

PART No. 24

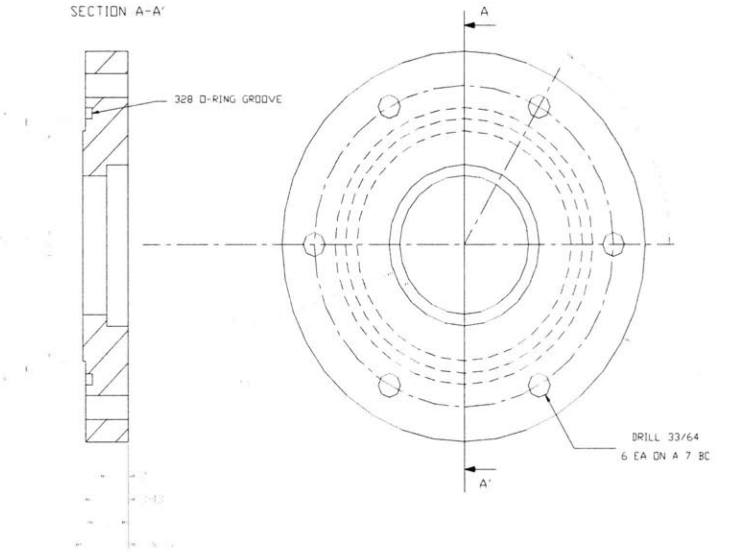

MASSACHUSETTS INSTITUTE OF TECHNOLOGY
SLOAN AUTOMOTIVE LABORATORY

PART No.	PART NAME	QUANTITY
15	BACKING RING MATERIAL: ALUMINUM 6061-T6	1
24	FLANGE MATERIAL: STEEL 11L17	1

UNITS: in	DRAWN BY IOANNIS KITSOPANIDIS DATE: 08/21/00	DWG No 10 of 10

Appendix B

Temperature Field at the End of Compression

The temperature field at the end of compression of the RCM is largely dependent on the combustion chamber geometry. A CFD analysis using KIVA-3 was performed in order to investigate the major design parameters that affect the degree of temperature stratification at the end of compression. It was found that there are essentially two parameters, which are closely related, that contribute to the resulting temperature field: the stroke and the crevice volume. The higher the stroke, the larger the roll-up vortex generated by the piston motion, which scrapes the boundary layer off the cold walls. Then, to achieve thermal uniformity at the end of compression, a larger crevice volume is required in order to contain the resulting vortex. As Figure B.1 shows, when the combustion chamber contains no crevice, the predicted temperature field is more non-uniform, while the maximum pressure and temperature are higher: 23.2 bar, 842 K (21.2 bar, 822 K for the case shown in Figure 5.6). Conversely, for shorter stroke the thermal environment becomes more uniform since the vortex is smaller and can be better contained in the crevice, which had the same volume. The maximum pressure and temperature are lower (19.1 bar, 798 K) because of the higher heat transfer due to large surface to volume ratio. This case is depicted in Figure B.2.

To design a crevice that could contain the entire vortex, it must be:

$$V_{crevice} \geq V_{vortex}$$

$V_{vortex} \sim \bar{\delta}_w \cdot L \cdot D$, where L is the stroke, D the bore and $\bar{\delta}_w$ is the entire boundary layer at the conditions next to the wall:

$$\bar{\delta}_w = \frac{\int_0^{t_{comp}} \delta_w dt}{t_{comp}}$$

where $\delta_w \geq \sqrt{\alpha_w t}$, where $\alpha_w \sim 2 \times 10^{-6}$ m^2/s for air at 300 K and 10 bar (average conditions inside the crevice). Then, for approximately 15 ms compression time:

$$\bar{\delta}_w \geq \frac{2}{3}\sqrt{\alpha_w t_c} \sim 0.1 mm$$

Then, $V_{vortex} \sim 2$ cm^3, while for this particular RCM design $V_{crevice} \sim 0.8$ cm^3.(~3.1 % of the combustion chamber at the end of compression).

The analysis performed in this study found that if the crevice volume was increased by a factor of 5 (approximately double the vortex volume), almost the entire vortex would be contained inside the crevice resulting in a more uniform temperature field. This is shown in Figure B.3. Consequently, the maximum pressure and temperature are lower: 18.2 bar and 784 K. Larger crevice than the vortex is required because, unless crevices are designed with high surface to volume ratio, the contained gas may not stay very close to wall temperatures.

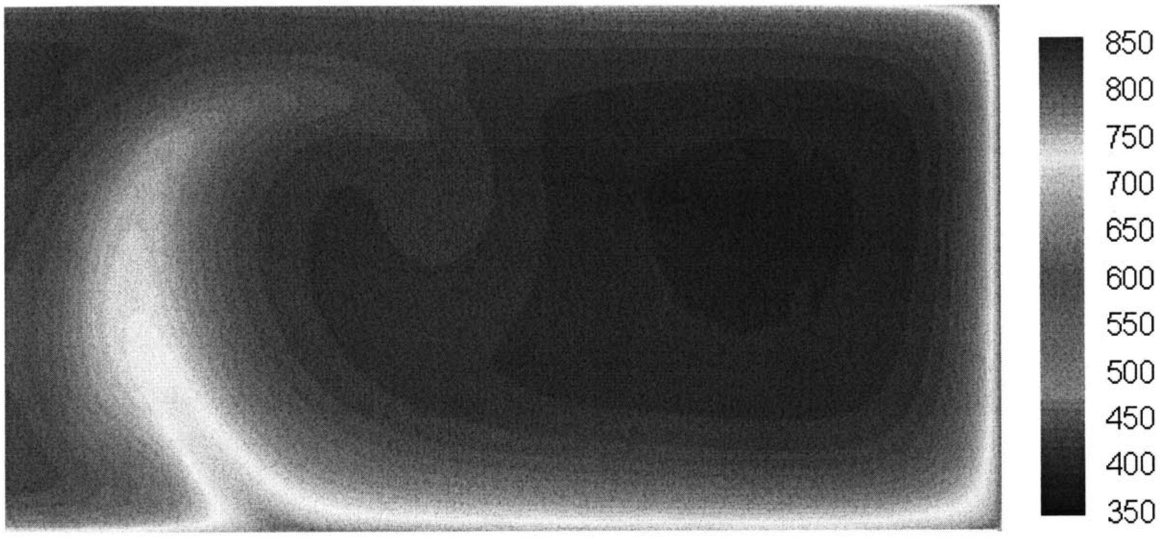

Figure B.1 KIVA-3 prediction of temperature field at the end of compression for the RCM design without crevice.

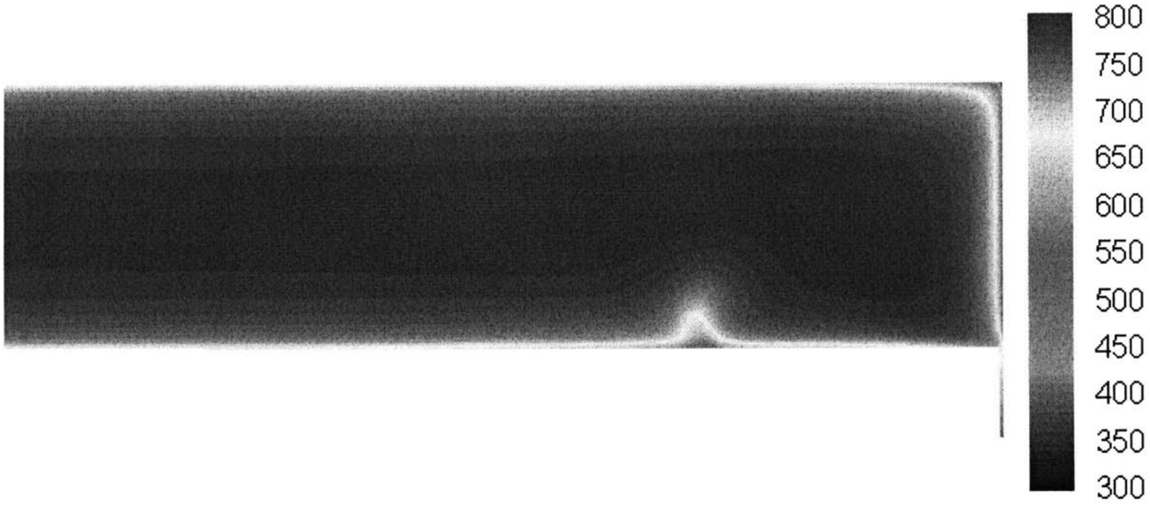

Figure B.2 KIVA-3 prediction of temperature field at the end of compression for the RCM design with half stroke and half clearance height (same compression ratio).

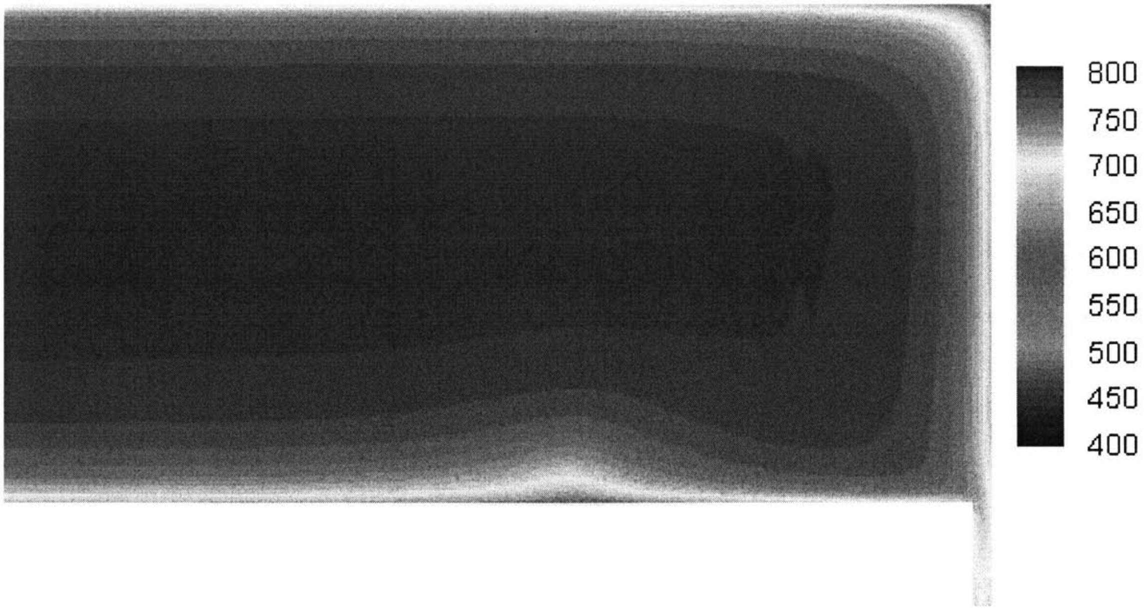

Figure B.3 KIVA-3 prediction of temperature field at the end of compression for the RCM design with larger crevice volume by a factor of 5.

Appendix C

Reactions with Updated Rate Constants

Table C.1: Reactions with modified rate constants[a]

Reaction	A	n	Ea	Reference
$CH_3+CH_3(+M)=C_2H_6(+M)$ (low)	9.214e16 1.135e36	-1.17 -5.246	6.358e2 1.705e3	[91]
	3.61e13 3.63e41	0 -7	0 2.762e3	[115], this study
$CH_3+H(+M)=CH_4(+M)$ (low)	2.138e15 3.31e30	-0.4 -4	0 2.108e3	[91]
	2.11e14 1.76e24	0 -1.8	0 0	[115], this study
$C_2H_5+O_2=C_2H_4+HOO$	1.22e30	-5.76	1.01e4	[91]
	1.02e10	0	-2.185e3	[115], this study
$OH+OH(+M)=HOOH(+M)$ (low)	1.236e14 3.041e30	-0.37 -4.63	0 2049	[91]
	7.4e13 2.3e18	-0.37 -0.9	0 -1.7e3	[115], this study
$HCO+O_2=CO+HOO$	7.58e12	0	4.1e2	[91]
	1.55e4	2.38	-1.526e3	[116], this study
$CH_3+HOO=CH_4+O_2$	3.6e12	0	0	[91]
	1.8e13	0	0	this study
$CH_3+HOO=CH_3O+OH$	1.1e13	0	0	[91], this study

a. reaction rates in cm^3 mol cal units, $k = AT^n \exp\left(\frac{Ea}{RT}\right)$

References

1 Heywood, J.B., Internal Combustion Engine Fundamentals, McGraw-Hill, New York, 1988.

2 Bowman, C.T., *Energy Combust. Sci.*, Vol. 1, p.33-45, 1975

3 Miller, F.J., Gardner, D.E., Graham, J.A., Lee Jr, R.E., Wilson, W.E., Bachmann, J.D., *J. Air Pollut. Control Assoc.*, 1979, 29:610-615.

4 "National Ambient Air Quality Standards for Particulate Matter; Final Rule," Federal Register, Vol. 62, p. 38652, 1997.

5 Concawe Website, http://concawe.be/

6 DieselNet Website, http://dieselnet.com/

7 Schubiger, R., Bertola, A., and Boulouchos, K., *Soc. Automotive Eng.*, SAE Paper 2001-01-3497, 2001.

8 Leet, J.A., Simescu, S., Froelund, K., Dodge, and L.G., Roberts, C.E., *Soc. Automotive Eng.,* SAE Paper 970873, 1997.

9 Khair, M.K., *Soc. Automotive Eng.*, SAE Paper 2003-01-2303, 2003.

10 Johnson, T.V., *Soc. Automotive Eng.*, SAE Paper 2004-01-0070, 2004.

11 Alleman, T.L., and McCormick, R.L., *Soc. Automotive Eng.*, SAE Paper 2003-01-0763, 2003.

12 Yoshimoto, Y., Onodera, M., and Tamaki, H., *Soc. Automotive Eng.*, SAE Paper 2001-01-1807, 2001.

13 Hallgren, B.E., and Heywood, J.B., *Soc. Automotive Eng.*, SAE Paper 2001-01-0648, 2001.

14 Grieco, W.J., Lafleur, A.L., Swallow, K.C., Richter, H., Taghizadeh, K., and Howard, J.B., *Proc. Combust. Inst.* 27 (1998) 1669-1675.

15 Howard, J.B., Wersborg, B.L., and Williams, G.C., *Faraday Symp. Chem. Soc.* No.7 (1973) 109-119.

16 Wersborg, B.L., Howard, J.B., and Williams G.C., in *Fourteenth Symposium (International) on Combustion,* The Combustion Institute, Pittsburg, 1973, p. 929-940.

17 Wersborg, B.L., Fox, L.K., and Howard, J.B., *Combust. Flame*, 24: 1-10, 1975.

18 McKinnon, J.T., and Howard, J.B., in *Twenty-Fourth Symposium (International) on Combustion*, The Combustion Institute, Pittsburg, 1992, p. 965-971.

19 Harris S.J., and Weiner, A.M., *Combust. Sci. Technol.*, 31: 155-167, 1983.

20 Harris S.J., and Weiner, A.M., *Combust. Sci. Technol.*, 32: 267-275, 1983.

21 Harris S.J., and Weiner, A.M., *Combust. Sci. Technol.*, 38: 75-87, 1984.

22 Harris S.J., and Weiner, A.M., in *Twenty-Second Symposium (International) on Combustion*, The Combustion Institute, Pittsburg, 1988, p. 333-342.

23 Weiner, A.M., and Harris, S.J., *Combust. Flame*, 77: 261-266, 1989

24 Harris S.J., and Weiner, A.M., *Combust. Sci. Technol.*, 72: 67-77, 1990.

25 D'Alessio, A., Di Lorenzo, A., Sarofim, A.F., Beretta, F., Masi, S., and Venitozzi, C., in *Fifteenth Symposium (International) on Combustion*, The Combustion Institute, Pittsburg, 1975, p. 1427-1438.

26. Hanisch, S., Jander, H., Pape, T., and Wagner, H.G., in *Twenty-Fifth Symposium (International) on Combustion*, The Combustion Institute, Pittsburg, 1994, p. 577-584.

27 Miyamoto, N., Ogawa, H., Goto, N., and Sasaki, H., *Soc. Automotive Eng.*, SAE Paper 900640, 1990.

28 Wiartalla, A., Backer, H., and Durnholz, M., *Soc. Automotive Eng.*, SAE Paper 950233, 1995.

29 Hentschel, W., and Richter, J.U., *Soc. Automotive Eng.*, SAE Paper 952517, 1995.

30 Pungs, A., Pischinger, S., Backer, H., and Lepperhoff, G., *Soc. Automotive Eng.*, SAE Paper 2000-01-1999, 2000.

31 Song, K.H., Lee, Y., and Litziger, A., *Soc. Automotive Eng.*, SAE Paper 2000-01-2794, 2000.

32 Kocis, D., Song, K.H., Lee, Y., and Litziger, A., *Soc. Automotive Eng.*, SAE Paper 2000-01-2795, 2000.

33 Senda, J., Choi, D., Iwamuro, M., Fujimoto, H., and Asai, G., *Soc. Automotive Eng.*, SAE Paper 2002-01-0893, 2002.

34 Dec, J., zur Loye A.O., and Siebers, D.L., *Soc. Automotive Eng.*, SAE Paper 910224, 1991.

35 Dec, J., *Soc. Automotive Eng.*, SAE Paper 920115, 1992.

36 Dec., J., and Espey, C., *Soc. Automotive Eng.*, SAE Paper 922307, 1992.

37 Dec., J., and Espey, C., *Soc. Automotive Eng.*, SAE Paper 950456, 1995.

38 Dec, J., and Kelly-Zion P.L., *Soc. Automotive Eng.*, SAE Paper 2000-01-0238, 2000.

39 Tree, D., and Dec, J., *Soc. Automotive Eng.*, SAE Paper 2001-01-1296, 2001.

40 Musculus, M.P., Dec, J., and Tree, D.R., *Soc. Automotive Eng.*, SAE Paper 2002-01-0889, 2002.

41 Muller, A., and Wittig, S., *Eighteenth International Symposium on Shock Waves*, 1991, p.759.

42 Wittig, S., Muller, A., and Lester, T.W., *J. Chem. Phys.*, 468-474, 1990.

43 Kellerer, H., Muller, A., Bauer, H.J., and Wittig, S., *Combust. Sci. Technol.*, 113: 67-80, 1996.

44 Kellerer, H., Koch, R., and Wittig, S., *Combust. Flame*, 120: 188-199, 2000.

45 Parker, T.E., Foutter, R.R., and Rawlins, W.T., *J. Chem. Phys.*, 481-486, 1990.

46 Bauerle, S., Karasevich, Y., Slavov, S., Tanke, D., Tappe, M., Thienel, T., Wagner, H.G., in *Twenty-Fifth Symposium (International) on Combustion*, The Combustion Institute, Pittsburg, 1994, p. 627-634.

47 Leung, K.M., Lindstedt, R.P., and Jones, W.P., *Combust. Flame*, 87: 289-305, 1991.

48 Harris, S.J., Weiner, A.M., and Ashcraft, C.C., *Combust. Flame*, 64: 65-81, 1986.

49 Frenklach, M., Clary, D.W., Gardiner Jr., W.C., and Stein, S.E., in *Twentieth Symposium (International) on Combustion*, The Combustion Institute, Pittsburg, 1984, p. 887-901.

50 Wang, H., and Frenklach, M., *Combust. Flame*, 110: 173-221, 1997.

51 Richter, H., Grieco, W.J., and Howard, J.B., *Combust. Flame*, 119: 1-22, 1999.

52 Marinov, N.M., Pitz, W.J., Westbrook, C.K., Vincitore, A.M., Castaldi, M.J., Senkan, S.M., and Melius, C.F., *Combust. Flame*, 114: 192-213, 1998.

53 D'Anna, A., Violi, A., D'Alessio and Sarofim, A.F., *Combust. Flame*, 127: 1995-2003, 2001.

54 Richter, H., Granata, S., Green, W.H., and Howard, J.B., P*roc. Combust. Inst.* 30 (2004), in press.

55 Appel, J., Bockhorn, H., and Frenklach, M., *Combust. Flame*, 121: 122-136, 2000.

56 Akihama, K., Takatori, Y., Inagaki, K., Sasaki, S., and Dean, A.M., *Soc. Automotive Eng.*, SAE Paper 2001-01-0655, 2001.

57 Kamimoto, T., and Bae, M-h., *Soc. Automotive Eng.*, SAE Paper 880423, 1988.

58 Smith, O.I., *Prog. Energy Combust. Sci.*, vol. 7, p. 275-291, 1981.

59 Haynes, B.S., and Wagner, H.G., *Prog. Energy Combust. Sci.*, vol. 7, p. 229-273, 1981.

60 Baumgard, K.J. and Johnson, J.H., *Soc. Automotive Eng.*, SAE Paper 960131, 1996.

61 Amann, C.A., and Siegla, D.C., *Aerosol Sci. Technol.*, 1: 73-101, 1982.

62 Allen, J.O., Dookeran, N.M., Smith, K.A., Sarofim, A.F., Taghizadeh, K., and LafleurA.L., *Environ. Sci. Technol.*, 1996, 30: 1023-1031.

63 Bockhorn, H., Soot Formation in Combustion: Mechanisms and Models. Berlin: Springer, 1994.

64 Richter, H., and Howard, J.B., *Prog. Energy Combust. Sci*, 26: 565-608, 2000.

65 Richter, H., and Howard, J.B., P*hys. Chem. Chem. Phys.*, 2002

66 Graham, S.C., in *Sixteenth Symposium (International) on Combustion*, The Combustion Institute, Pittsburg, 1976, p. 663.

67 Kamimoto. T., and Kobayashi, H., *Prog. Energy Combust. Sci.*, 1991, Vol. 17, p.

163-189.

68 Dec, J., *Soc. Automotive Eng.*, SAE Paper 970873, 1997.

69 Flynn, P.F., Durrett, R.P, Hunter, G.L., zur Loye, A.O., Akinyemi, O.C., Dec, J.E., and Westbrook, C.K., *Soc. Automotive Eng.*, SAE Paper 1999-01-0509, 1999.

70 Affleck, W.S., and Thomas, A., *Proc. of Instn. Mech. Engr.*, 183: 36, 1968.

71 Park, P., and Keck, J.C., *Soc. Automotive Eng.*, SAE Paper 900027, 1990.

72 Griffiths, J.F., Jiao, Q., Kordylewski, W., Schreiber, M., Meyer, J., and Knoche, K.F., *Combust. Flame*, 93: 303-315, 1993.

73 Minetti, R., Ribaucour, M., Carlier, M., Fittschen, C., and Sochet, L. R., *Combust. Flame* 96:201-211, 1994.

74 Jones, A.R., *Prog. Energy Combust. Sci.*, 25: 1-53, 1999.

75 Chang, H., and Charalampopoulos, T.T., *Proc. R. Soc. Lond. A*, 430: 577-591.

76 Lee, S.C., and Tien, C.L., in *Eighteenth Symposium (International) on Combustion,* The Combustion Institute, Pittsburg, 1981, p. 1159-1166.

77 Gaydon, A.G., The Spectroscopy of Flames, 2nd Ed., Chapman and Hall, London, 1974.

78 Dec, J., Espey, C., *Soc. Automotive Eng.*, SAE Paper 982685, 1998.

79 Vaglieco, B.M., Merola, S.S., D'Anna, A., and D'Alessio, A., J. *Quant. Spectr. Rad Transf.,* 73: 443-450, 2002.

80 Bjorseth, A., Handbook of polycyclic aromatic hydrocarbons, M. Dekker, New York, 1985.

81 Tanaka, S., Ayala, F., Keck, J.C., and Heywood, J.B., *Combust, Flame*, 132: 219-239, 2003.

82 Lee, D., Hochgreb, S. and Keck, J.C., *Soc. Automotive Eng.* SAE Paper 932755, 1993.

83 Kojima, S., and Suzuoki, T., *Combust. Flame*, 92: 254-265, 1993.

84 Griffiths, J.F., Halford-Maw, P.A., and Rose, D.J., *Combust. Flame*, 95: 291-306, 1993.

85 Minetti, R., Carlier, M., Ribaucour, M., Therssen, E., and Sochet, L.R., *Combust. Flame*, 102: 298-309, 1995.

86 Ciezki, H.K., and Adomeit, G., *Combust. Flame*, 93: 421-433, 1993.

87 Vermeer, D.J., Meyer, J.W., and Oppenheim, A.K, *Combust. Flame* 18: 327-336, 1972.

88 Coats, C.M., and Williams, A., in *Seventeenth Symposium (International) on Combustion*, The Combustion Institute, Pittsburg, 2000, p. 611-621.

89 Callahan, C.V., Held, T.J., Dryer, F.L., Minetti, R., Ribaucour, M., Sochet, L.R., Faravelli, T., Gaffuri, P., and Ranzi, E., in *Twenty-Sixth Symposium (International)*

on Combustion, The Combustion Institute, Pittsburg, 1996, pp. 739-746.

90 Dagaut, P., Reuillon, M., and Cathonnet, M., *Combust. Flame* 101: 132-140, 1995.

91 Curran, H.J., Gaffuri, P., Pitz, W.J., and Westbrook, C.K., *Combust. Flame*, 129:253-280, 2002.

92 Pitz, W.J., Seiser, R., Bozzelli, J.W., Seshadri, K., Chen C.J., Da Costa, I., Fournet, R., Billaud, F., Battin-Leclerc, F., and Westbrook, C.K., in *Thirtieth Symposium (International) on Combustion*, The Combustion Institute, Pittsburgm 2004, p.

93 Kaiser, E.W., Wallington, T.J., Hurley, M.D., Platz, J., Curran, H.J., Pitz, W.J., Westbrook, C.K., *J. Phys. Chem. A*, 2000.

94 Kee, R.J., Rupley, F.M., and Miller, J.A., CHEMKIN II: A FORTRAN Chemical Kinetics Package for the Analysis of Gas-Phase Chemical Kinetics, SANDIA Report SAND89-800B, 1989.

95 Clarkson, J., Griffiths, J.F., Macnamara, J.P., and Whitaker, B.J., *Combust. Flame*, 125:1162-1175, 2001.

96 Desgroux, P., Gasnot, L., and Sochet, L.R., *Appl. Phys. B* 61, 69-72, 1995.

97 Westbrook, C.K., Curran, H.J., Pitz, W.J., Griffiths, J.F., Mohamed, C., and Wo, S.K., in *Twenty-Seventh Symposium (International) on Combustion*, The Combustion Institute, Pittsburg, 1998, p. 371-378.

98 Cox, R. A., and Cole, J.A., *Combust. Flame*, 60:109-123, 1985.

99 Hu, H., and Keck, J.C., *Soc. Automotive Eng.*, SAE Paper 872110, 1987.

100 Tanaka, S., Ayala, F., and Keck, J.C., *Combust. Flame* 133:467-481, 2003.

101 Westbrook, C.K., in *Twenty-Eighth Symposium (International) on Combustion*, The Combustion Institute, Pittsburg, 2000, p. 1563-1577.

102 Curran, H.J., Fisher, E.M., Glaude, P.A., Marinov, N.M., Pitz, W.J., Westbrook, C.K., Layton, D.W., Flynn, P.F., Durrett, R.P., zur Loye, A.O., Akinyemi, O.C., and Dryer, F.L., *Soc. Automotive Eng.*, SAE Paper 2001-01-0653, 2001.

103 Westbrook, C.J., Pitz, W.J., Boercker, J.E., Curran, H.J., Griffiths, J.F., Mohamed, C., and Ribaucour, M., in *Twenty-Nineth Symposium (International) on Combustion, The Combustion Institute*, Pittsburg, 2002, p. 1311-1318.

104 Westbrook, C. K, and Dryer, F.L., *Prog. Energy Combust. Sci.* 10, 1 (1984).

105 Bittner, J. D., and Howard, J.B., in *Eighteenth Symposium (International) on Combustion, The Combustion Institute*, Pittsburgh, 1980, p.1105.

106 Griffiths, J.F., and Whitaker, B.J., *Combust. Flame* 131: 386-399, 2002.

107 Lee, D., and Hochgreb, S., *Combust. Flame* 114: 531-545, 1998.

108 Amsden, A., KIVA-3: "A KIVA Program with Block-Structured Mesh for Complex Geometries", Los Alamos National Laboratory Report, LA-12503-MS, 1993.

109 Aceves, S.M., Martinez-Frias, J., Flowers, D.L., Smith, J.R., Dibble, R.W., Wright,

J.F., and Hessel, R.P., *Soc. Automotive Eng.*, SAE Paper 2001-01-3612, 2001.

110 Yelvington, P.E., and Green, W.H., *Soc. Automotive Eng.*, SAE Paper 2003-01-1092, 2003.

111 Annand, W.J.D., in Afgan, N., and Beer, J.M., (eds.), Heat Transfer from Flames, Chap. 24, John Wiley, 1974.

112 Modest, M. F., Radiative Heat Transfer, 2nd Ed., Academic Press, 1993.

113 Mebel, A.M., Diau, W.G., Lin, M.C., and Morokuma, K., *J. Am. Chem. Soc.*, 1996, 118: 9759-9771.

114 Hughes, K.J., Turanyi, T., Clague, A.R., and Pilling, M.J., *Int. J. Chem. Kinet.*, 2001, 33, 513-538.

115 Baulch, D.L., Cobos, C.J., Cox, R.A., Frank, P., Hayman, G., Just, Th., Kerr, J.A., Murrells, T., Pilling, M.J., Troe, J., Walker, R.W., and Warnatz, J., *Combust. Flame* 98: 59-79, 1994.

116 Hsu, C.C., Mebel, A.M., and Lin, M.C., *J. Chem. Phys.*, 105(6), 2346-2352, 1996.

117 Glassman, I., in *Twenty-Second Symposium (International) on Combustion*, The Combustion Institute, Pittsburg, 1988, p. 295-311.

118 Kwon, Y., Mann, N., Rickeard, D.J., Haugland, R., Ulvund, K.A., Kvinge, F., and Wilson, G., *Soc. Automotive Eng.*, SAE Paper 2001-01-3522, 2001.

119 Glaude P.A., Pitz, W.J., and Thomson, M.J., 2003 Fall Meeting of the Western States Section of the Combustion Institute, UCLA, 2003.

120 Miyamoto, N., Ogawa, H., Nurun, N.M., Obata, K., Arima, T., *Soc. Automotive Eng.*, SAE Paper 980506, 1998.

121 Kitamura, T., Ito, T., Senda, J., and Fujimoto, H., *Soc. Automotive Eng.*, SAE Paper 2001-01-1262, 2001.

122 Frenklach, M., and Wang, H., in *Twenty-Third Symposium (International) on Combustion*, The Combustion Institute, Pittsburg, 1990, p. 1159-1566.

123 Pope, C.J., and Howard, J.B., *Aerosol Sci. Technol.*, 27: 73-94, 1997.

124 Kronholm, D.F., *PhD Thesis*, Massachusetts Institute of Technology, Cambridge, MA, 2000.

4534-31